

Design and Synthesis of Cyclometallated Iridium Molecular Probes with Targeted Image-Guided Therapeutic Capabilities for Cancer Management

by

SHAMJITH S.

10CC18A39018

A thesis submitted to the
Academy of Scientific & Innovative Research
for the award of the degree of
DOCTOR OF PHILOSOPHY
in
SCIENCE

Under the supervision of
Dr. KAUSTABH KUMAR MAITI



**CSIR-National Institute for Interdisciplinary
Science and Technology (CSIR-NIIST),
Thiruvananthapuram – 695 019**



**Academy of Scientific and Innovative Research
AcSIR Headquarters, CSIR-HRDC Campus
Sector 19, Kamla Nehru Nagar,
Ghaziabad, U. P. – 201 002, India**

September 2023

Dedicated to My,

Achan and Amma...

CSIR-National Institute for Interdisciplinary Science and Technology



(NIIST)

Council of Scientific and Industrial Research (CSIR)
Industrial estate P.O., Thiruvananthapuram- 695019
Kerala, India




Dr. Kaustabh Kumar Maiti
Senior Principal Scientist
Chemical Sciences and Technology Division


Tel: 0471-2515475
Mob: +91-8547761544
e-mail: kkmaiti@niist.res.in
kkmaiti29@gmail.com

29th September 2023

CERTIFICATE

This is to certify that the work incorporated in this Ph.D. thesis entitled, “*Design and Synthesis of Cyclometallated Iridium Molecular Probes with Targeted Image-Guided Therapeutic Capabilities for Cancer Management*”, submitted by *Mr. Shamjith S.* to the Academy of Scientific and Innovative Research (AcSIR) in fulfillment of the requirements for the award of the Degree of *Doctor of Philosophy in Sciences*, embodies original research work carried out by the student. We further certify that this work has not been submitted to any other University or Institution in part or full for the award of any degree or diploma. Research materials obtained from other sources and used in this research work have been duly acknowledged in the thesis. Images, illustrations, figures, tables, etc., used in the thesis from other sources, have also been duly cited and acknowledged.


Shamjith S. 29/09/23


Dr. Kaustabh Kumar Maiti 29/09/23
(Supervisor)

STATEMENTS OF ACADEMIC INTEGRITY

I Shamjith S., a Ph.D. student of the Academy of Scientific and Innovative Research (AcSIR) with Registration No. 10CC18A39018 hereby undertake that, the thesis entitled “*Design and Synthesis of Cyclometallated Iridium Molecular Probes with Targeted Image-Guided Therapeutic Capabilities for Cancer Management*” has been prepared by me and that the document reports original work carried out by me and is free of any plagiarism in compliance with the UGC Regulations on “*Promotion of Academic Integrity and Prevention of Plagiarism in Higher Educational Institutions (2018)*” and the CSIR Guidelines for “*Ethics in Research and in Governance (2020)*”.

September 29, 2023

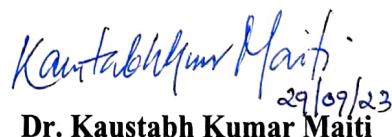
Thiruvananthapuram


Shamjith S. 29/09/23

It is hereby certified that the work done by the student, under my supervision, is plagiarism-free in accordance with the UGC Regulations on “*Promotion of Academic Integrity and Prevention of Plagiarism in Higher Educational Institutions (2018)*” and the CSIR Guidelines for “*Ethics in Research and in Governance (2020)*”.

September 29, 2023

Thiruvananthapuram


Dr. Kaustabh Kumar Maiti 29/09/23

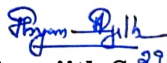
DECLARATION

I, Shamjith S., AcSIR Registration No. 10CC18A39018 declare that my thesis entitled, ***“Design and Synthesis of Cyclometallated Iridium Molecular Probes with Targeted Image-Guided Therapeutic Capabilities for Cancer Management”*** is plagiarism-free in accordance with the UGC Regulations on *“Promotion of Academic Integrity and Prevention of Plagiarism in Higher Educational Institutions (2018)”* and the CSIR Guidelines for *“Ethics in Research and in Governance (2020)”*.

I would be solely held responsible if any plagiarised content in my thesis is detected, which is violative of the UGC regulations 2018.

September 29, 2023

Thiruvananthapuram


Shamjith S. 29/09/23

ACKNOWLEDGEMENTS

I have great pleasure in expressing my deep sense of gratitude to Dr. Kaustabh Kumar Maiti, my thesis supervisor, for suggesting the research topic and for his constant guidance, endearing care, valuable support and encouragement, leading to the successful completion of this work.

I wish to thank Dr. C. Anandharamakrishnan and Dr. A. Ajayaghosh, present and former Director of the CSIR-National Institute for Interdisciplinary Science and Technology, Thiruvananthapuram, for providing me with the necessary facilities for carrying out the work.

I also extend my sincere thanks to:

- ✓ *Dr. V. Karunakaran, Dr. C. H. Suresh, and Dr. R. Luxmi Varma, present and former AcSIR co-ordinators.*
- ✓ *Dr. Joshy Joseph, Dr. Ravi Shankar L. and Dr. Priya S., Doctoral Advisory Committee (DAC) members and the whole AcSIR faculty for the successful completion of the course work.*
- ✓ *Dr. K V Radhakrishnan, Dr. P. Sujatha Devi, and Dr. R. Luxmi Varma, present and former Head of the Division, Chemical Sciences and Technology Division (CSTD).*
- ✓ *Dr. A. Kumaran, Dr. L. Ravi Sankar, Dr. B. S. Sasidhar, Dr. Sunil Varughese, Dr. Jubi John, and Dr. Adarsh Ashok, Scientists of the Organic Chemistry Section, for their help and support extended to me.*
- ✓ *Mr. Kiran Mohan & Mr. Robert Philip for TEM analysis, Mrs. Saumini Matthew for NMR, Mrs. Viji S., for mass spectral analyses, Dr. Joshy George for ICPMS analysis, Ms. Drishya Elizabeth for AFM analysis.*
- ✓ *Dr. Manu M. Joseph, Dr. Jyothi B. Nair, and Dr. Vishnu Priya Murali. for their timely suggestions and help.*
- ✓ *Dr. Achuthan C Ragavamenon, Amala Cancer Research Center Thrisur, for the animal experiments*
- ✓ *Dr. Jesny S, Dr. Dhanya Viswam, Dr. K S. Devaky, Ms. Praveena V P, Ms. Janeena, Ms. Shaija P B, Mrs. Ajimol P., Mr. Sarunkumar, Dr. Lekaha, Prof. Neena M, Prof. Jyothi, Mrs. Bhanumathi, and Dr. Anilkumar G, and all my beloved teachers at every stages of my academic career.*

- ✓ *Dr. S. Maniganda, Dr. Susan Alex, Dr. Varsha Karunakaran, Dr. Sujai P T, Dr. Saranya G, Dr. Ramya A N, Dr. Arya J S, Dr. Dhanya R., Dr. Sreedevi P, Dr. Biji M Mr. Madhukrishnan M., Ms. Vidyalekshmi M.S.Ms. Chandana R., Ms. Shamna K., Mr. Jerin Ms. Alisha, Ms. Anuja, Mr. Vimal Kumar, Ms. Sreedevi D., Mr. Shihashammed, Ms. Deepika S, Ms. Anjitha Ajith, Ms. Anusree, Ms. Kavya, Ms. Reshma and Ms. Anjitha U.M., my group members for their love, friendship and support.*
- ✓ *Special thanks to Ms. Fathima T S, Ms. Shamna, Ms. Shana, Mr. Arun Mantas, and Mr. Balagopal, my M.Sc project students*
- ✓ *Dr. Dhanya SR, Dr. Sajin Francis, Dr. Ranjitha J., Dr. Vishnu K. Omanakuttan, and Ms. Rajimol P R, for their encouragement and support.*
- ✓ *Special thanks to Dr. Neethu S, Mr. Syamkrishnan, and Ms. Nishna N for their wholehearted support during my toughest time*
- ✓ *Mr. Muhammad M, Mr. Ashin M, Dr. Sujith Vijayan, Mr. Rahul P, Dr. Prajeesh K V, My housemates for their constant support*
- ✓ *Thanks to Mr. Akhil M.G., Ms. Suja, Ms. Amrutham Linet and Remya G.S. for their support*
- ✓ *Ms. Megha Paul, Ms. Anusha, Ms. Roopasree, Ms. Shibna, Ms. Susanna, Ms. Sheba, Ms. Drishya, Mr. Christin Sam, and Mr. Anoop*
- ✓ *Mr. Merin and Ms. Aswathi for conducting the AcSIR procedures*
- ✓ *Former and present members of CSTD and friends at CSIR-NIIST, for their help and support.*
- ✓ *All my teachers for their encouragement at different stages of my academic career.*
- ✓ *University Grants Commission, Government of India, for Research fellowship.*

I am deeply and forever indebted to my parents Mr. K.M. Shanmughan and my mother Vijayamma P., my brothers Shijith and Shineeth, my wife Keerthana, and her father Benny, mother Sheeja and sister Karthika and my friend Sanjai Saji for their constant source of love, inspiration, and blessings. Above all, I thank the Almighty for all the blessings showered upon me.

Shamjith S.

TABLE OF CONTENTS

Certificate		i
Statements of Academic Integrity		ii
Declaration		iii
Acknowledgments		iv
Table of Contents		vi
List of Abbreviations		ix
Preface		xvii
CHAPTER 1	Harnessing Molecular Probes for Personalized Theranostics: The Recent Development on Activatable Photodynamic Therapy	1-70
	Abstract	1
1.1	Introduction	2
1.2	Fluorescent molecular probes	4
1.2.1	Turn-On Fluorescent Probes	5
1.2.2	Turn-Off Fluorescent Probes	11
1.2.3	Ratiometric Fluorescent Probes	15
1.2.4	Limitations of Organic Fluorescent Probes	19
1.3	SERS-based molecular probes	20
1.4	Transition Metal complexes for bio applications	25
1.4.1	Imaging applications of Iridium complexes	27
1.4.2	Theranostic applications of Iridium complexes	35
1.5	Harnessing Light to Heat: Photodynamic Effect as Innovative Approaches in Cancer Treatment	36
1.5.1	Photodynamic Therapy	37
1.5.2	Shining Light on Photodynamic Therapy: The Power of Photosensitizers	39
1.5.3	Iridium Complexes: A Beacon of Hope in PDT	41
1.5.4	Activatable Photosensitizers in Photodynamic Therapy: From Bench to Bedside	49
1.6	Objectives and methodologies for the present investigation	59
1.7	References	60

CHAPTER 2	NADH-Depletion Triggered Energy Shutting with Cyclometalated Iridium (III) Complex Enables Bimodal Luminescence-SERS Sensing and Photodynamic Therapy	71-104
	Abstract	71
2.1	Introduction	72
2.2	Results and discussion	73
2.2.1	Design and synthesis of quinolone appended iridium complex	73
2.2.2	Photophysical assessment and activation of QAIC by NADH.	76
2.2.3	NADH homeostasis by QAIC under cellular physiology.	79
2.2.4	Evaluation of photo-oxidation of NADH by QAIC.	83
2.2.5	Photo-reduction of cytochrome c by QAIC and NADH	84
2.2.6	Switching-off PeT to PDT during NADH sensing by QAIC.	85
2.2.7	PDT evaluation by the activated N-QAIC in cells	87
2.3	Conclusion	90
2.4	Experimental section	90
	References	101
CHAPTER 3	GSH-depletion Assisted Chemo dynamic Therapy Followed by NIR-laser Induced Combined Phototherapy Towards Triple-negative breast cancer	105-148
	Abstract	105
3.1	Introduction	106
3.2	Results and discussion	110
3.2.1	Synthesis and characterization of singlet oxygen delivery system	111
3.2.2	Photophysical evaluation of singlet oxygen delivery system	112
3.2.3	Synthesis of the Photothermal Agent	116
3.2.4	MnO ₂ coating of the nano construct for tumor microenvironment responsive activation	119
3.2.5	Synthesis of targeting peptide to target S-GRP-78	122
3.2.6	Formulation of the Theranostic nano construct (TNC)	123
2.2.7	<i>In-Vitro</i> Imaging Studies	124
3.2.8	<i>In-Vitro</i> Therapeutic Assessment	131
3.2.9	<i>In-Vivo</i> studies	134
3.2.9.1	<i>In-Vivo</i> – toxicity profiling of TNC	135
3.2.9.2	Sub-acute toxicity	136
3.3	Conclusion	138
3.4	Experimental Section	139
3.5	References	146

CHAPTER 4	Harnessing Hydrogen Sulphide-Induced Activation for Site-Specific Photodynamic Therapy: Disrupting Glycolysis as a Strategy for Selective and Enhanced Anticancer Effects	149-187
	Abstract	149
4.1	Introduction	150
4.2	Result and Discussion	152
4.2.1	Design and synthesis of P-NBD	152
4.2.2	Unlocking of P-NBD to activated PS P-OH by Hydrogen Sulphide (H ₂ S)	155
4.2.3	Conformation of In-Vitro activation through Fluorescence and SERS imaging of H ₂ S in SKBR3 cells.	159
4.2.4	Untangling Mitochondrial Co-localization: Revealing Subcellular Relationships	162
4.2.5	Modulation of Glycolytic Metabolism in SKBR3 Cells through Endogenous H ₂ S Depletion using P-NBD Treatment	163
4.2.6	Activatable Photodynamic effect of P-NBD and singlet oxygen generation	165
4.2.7	Establishing the apoptotic potential of activated P-NBD in the cellular milieu	167
4.2.8	SERS tracking of apoptotic events in the cellular milieu	171
4.3	Conclusion	173
4.4	Experimental section	173
4.5	References	183
	Abstract of the Thesis	189
	List of Publications	191-192
	List of Posters Presented in Conferences	192-193

List of Abbreviations

AA	Amino acid
AcOH	Acetic acid
AFM	Atomic force microscopy
Ag	Silver
AIE	Aggregation induced emission
Ala	Alanine
Arg	Arginine
ATP	Adenosine triphosphate
AuNP	Gold nanoparticle
AuNR	Gold nanorod
Bel 7702	Benign human liver cell line
BODIPY	4,4-Difluoro-4-bora-3a,4a-diaza- <i>s</i> -indacene
BSA	Bovine serum albumin
ca.	Approximately
CathB	Cathepsin B
CCD	Charge-coupled device
CDCl ₃	Deuterated chloroform
CHCl ₃	Chloroform
CH ₃ COOH	Acetic acid
CH ₃ CN	Acetonitrile
CHO	Chinese Hamster Ovary cell line
CK	Cytokeratin
cm	Centimeter
CO	Carbon monoxide
CO ₂	Carbon dioxide
COCl ₂	Cobalt chloride

Cys	Cysteine
D-A-D	Donor-acceptor-donor
DCM	Dichloromethane
DCF	2', 7'-dichlorofluorescein
DCFDA	2', 7'-dichlorofluorescein diacetate
DIC	N, N'-diisopropylcarbodiimide
DIPEA	Diisopropyl ethylamine
DLA	Dalton's lymphoma ascites
DLS	Dynamic light scattering
DMEM	Dulbecco's modified eagle's medium
DMF	Dimethyl formamide
DMSO	Dimethyl sulphoxide
DNA	Deoxyribonucleic acid
DOX	Doxorubicin
DPBF	1,3-diphenylisobenzofuran
DTT	Dithiothreitol
eq.	equivalent
EDC	N-(3-(dimethylamino)-propyl)-N'-ethylcarbodiimide
EDTA	Ethylenediamine tetraacetic acid
EGFR	Epidermal growth factor receptor
EPO	Endoperoxide
ESIPT	Excited state intramolecular proton transfer
ESR	Electron spin resonance
<i>et al.</i>	<i>Et alii/alia</i>
EtOH	Ethanol
FA	Folic acid
FAB	Fast atom bombardment
FBS	Fetal bovine serum
FITC	Fluorescein isothiocyanate
FKC	Phenylalanine-Lysine-Cysteine

FR	Folate receptor
FRET	Fluorescence resonance energy transfer
g	gram
Glu	Glutamic acid
Gly	Glycine
GM	Goppert Mayer
GSH	Glutathione
GSSG	Glutathione-disulfide
h	Hour
$h\nu_{\text{ex}}$	Excitation energy
$h\nu_{\text{em}}$	Emission energy
H69AR	Multidrug resistant lung cancer cell line
H9C2	Murine myoblast cell line
H-bonding	Hydrogen bonding
HBTU	(2-1H-benzotriazo-1-yl)-1,1,3,3-tetramethyluronium hexafluorophosphate
HCl	Hydrochloric acid
Hcy	Homocysteine
HeLa	Human cervical cancer cell line
HEPES	4-(2-hydroxyethyl)-1-piperazineethanesulfonic acid
HepG2	Human liver hepatocellular carcinoma cell line
HL-7702	Hepatic immortal cell line
H ₂ O	Water
H ₂ O ₂	Hydrogen peroxide
HOBt	Hydroxybenzotriazole
Hp	Hematoporphyrin
HRMS	High resolution mass spectrometry
HRP	Horseradish peroxidase
HSA	Human serum albumin
H ₂ S	Hydrogen sulphide
H ₂ SO ₄	Sulphuric acid

Hz	Hertz
IAEC	Institutional Animal Ethics Committee
ICPMS	Inductively coupled plasma mass spectrometry
ICT	Intramolecular charge transfer
Ile	Isoleucine
ip	Intra-peritoneal
Ir	Iridium
IR	Infrared
<i>J</i>	Coupling constant
K ₂ CO ₃	Potassium carbonate
KI	Potassium iodide
KMnO ₄	Potassium permanganate
<i>k</i> _{obs}	Observed rate constant
L	Litre
Leu	Leucine
LNCaP	Human prostate adenocarcinoma cells
LOD	Limit of detection
LPA	α -lipoic acid
M	Molar
M ⁺	Molecular ion peak
MCF7	Human breast cancer cells
MDA-MB231	Epithelial human breast cancer cells
MDM2	Mouse double minute protein
MES	2-(<i>N</i> -morpholino)ethanesulfonic acid
MeOH	Methanol
MES	2-(<i>N</i> -morpholino)ethanesulfonic acid
MLCT	Metal to ligand charge transfer
MMP	Matrix metalloproteinase
MnO ₂	Manganese oxide
MST	Mean survival time
MTT	3-(4,5-dimethylthiazolyl-2)-2,5-diphenyltetrazolium bromide

min	Minutes
mL	Millilitre
mm	Millimeter
mM	Millimolar
mmol	Millimoles
mol	Mole
mp	Melting point
Na ₂ CO ₃	Sodium carbonate
NaD(P)H	Nicotinamide adenine dinucleotide phosphate hydrogen
NaH	Sodium hydride
Nap	Napsin
Na ₂ SO ₄	Sodium sulfate
NEM	<i>N</i> -ethyl maleimide
NHS	<i>N</i> -hydroxysuccinimide
NH ₄ PF ₆	Ammonium hexafluorophosphate
NIR	Near-infrared
nm	Nanometer
nM	Nanomolar
Nm ⁻¹	Newton per meter
NMM	<i>N</i> -methylmaleimide
NMR	Nuclear magnetic resonance
NPs	Nanoparticles
ONOO	Peroxynitrite
O ₂	Molecular oxygen
¹ O ₂	Singlet oxygen
PBS	Phosphate buffered saline
PDT	Photodynamic therapy
PEG	Polyethylene glycol
PET	Photoinduced electron transfer
PET	Positron emission tomography
PFC	Perfluorocarbon

pH	Hydrogen ion concentration at logarithmic scale
Phe	Phenyl alanine
pKa	Acid dissociation constant at logarithmic scale
pmol	Picomolar
ppm	Parts per million
Pro	Proline
PS	Photosensitizer
PSA	Prostate specific antigen
Pt	Platinum
PTT	Photothermal therapy
RhB	Rhodamine B
Rh110	Rhodamine 110
ROS	Reactive oxygen species
rpm	Revolutions per minute
rt	Room temperature
Ru	Ruthenium
S ²⁻	Sulphide anion
S ₀	Ground electronic state
S ₁	Lower electronic excited state
S ₁ *	Higher electronic excited state
s	Seconds
SDS	Sodium dodecyl sulphate
sec	Seconds
SERS	Surface enhanced Raman scattering
SiO ₂	Silica
SOSG	Singlet oxygen sensor green
SPECT	Single photon emission computed tomography
str.	Stretching
T	Temperature
TEM	Transmission electron microscopy
TFA	Trifluoroacetic acid

THF	Tetrahydrofuran
TICT	Twisted intramolecular charge transfer
TIS	Triisopropyl silane
TME	Tumor microenvironment
TMS	Tetramethylsilane
Tyr	Tyrosine
US	Ultrasound
UV	Ultraviolet
v	Volume
Vis	Visible
WI38	Normal human diploid fibroblasts
Zn ⁺²	Zinc (II)
δ	Chemical shift
°C	Degree Celsius
Φ_F	Fluorescence quantum yield
ν_{em}	Frequency of emission
ν_{ex}	Frequency of excitation
μg	Microgram
μm	Micrometer
μM	Micromolar
ε	Molar extinction coefficient
λ_{abs}	Wavelength of absorption
λ_{ex}	Wavelength of excitation
λ_{em}	Wavelength of emission

PREFACE

One significant challenge in the field of biomedicine is the relatively slow progress in developing new bioanalytical methods and instrumentation. Among the various detection techniques available, optical assays are highly valuable for precise tracking of biomarkers, which play a crucial role in disease diagnosis, therapy administration, and therapy effectiveness monitoring. The concept of theranostics, which combines therapy with diagnostics, holds great potential for advancing translational research and clinical applications. Photodynamic therapy (PDT) represents a non-invasive approach to treating cancer, utilizing photosensitizers and light to selectively eliminate specific cells, particularly cancer cells. PDT offers several advantages over conventional cancer treatments, including minimal harm to surrounding healthy tissues and the ability to maintain low systemic toxicity. Typically, photosensitizers used in PDT can be activated by specific light wavelengths, initiating photochemical reactions that produce reactive oxygen species (ROS) responsible for damaging cancer cells. Moreover, PDT has the potential to stimulate an immune response against cancer cells, providing long-lasting protection against the disease. However, PDT does have some limitations, such as limited light penetration in tissues, modest selectivity for cancer cells, and the possibility of photosensitizer-induced skin sensitivity. Ongoing research aims to overcome these limitations by developing improved photosensitizers with enhanced properties, such as better tissue penetration, increased selectivity for cancer cells, and reduced skin sensitivity. Additionally, investigations are underway to explore combination therapies, such as combining PDT with chemotherapy or immunotherapy.

One promising approach within PDT is activatable photodynamic therapy (a-PDT), which employs photosensitizing agents that can be selectively activated in response to specific triggers. This approach allows precise targeting of the treatment to specific tissues or cells of interest, minimizing the risk of harm to healthy tissue. In a-PDT, the photosensitizing agent is modified to remain inactive until triggered by a specific stimulus, such as particular wavelengths of light, changes in pH or temperature, or the presence of specific molecules and enzymes. Once activated, the agent generates reactive oxygen species that specifically destroy the targeted cells or tissues. This approach offers greater control over the timing and location of the treatment.

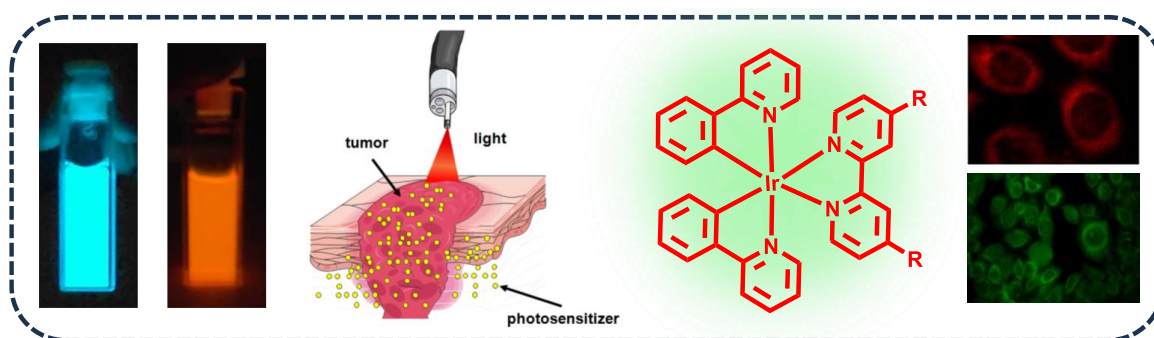
In the context of a thesis, the **first chapter** provides an overview of recent advancements in PDT, including the use of metal complexes as photosensitizing agents and their potential in diagnostic and theranostic applications. This chapter also discusses small molecule-based optical probes, photosensitizers, and their biological applications based on existing literature.

Chapter 2 focuses on the design and synthesis of a cationic cyclometallated Ir(III) complex using a quinoline-appended bipyridine as an auxiliary ligand for targeted activation through nicotinamide adenine dinucleotide-reduced (NADH). This complex, known as QAIC, serves as a molecular probe in surface-enhanced Raman spectroscopy (SERS) and fluorescence techniques to assess the state of endogenous NADH. The activation of QAIC through NADH triggers changes in SERS and luminescence, with remarkable sensitivity for NADH detection. Additionally, this chapter explores the potential of QAIC as a photosensitizer to generate singlet oxygen and its role in obstructing photo-induced electron transfer (PeT) and producing NAD radicals.

Chapter 3 discusses the design and development of a multifunctional photosensitizer complex, Ir-Nap, for theranostic applications. Ir-Nap is designed to achieve PDT in hypoxic tumors by generating singlet oxygen through heat-triggered cycloreversion of endoperoxides. This theranostic construct combines photothermal therapy (PTT) and PDT for enhanced cancer cell damage. To protect the medication from circulation damage, a tumor environment-responsive MnO₂ coating is applied. Additionally, a cancer-targeting peptide is incorporated for active cancer cell targeting, resulting in a powerful triple therapeutic approach.

In **Chapter 4**, a cyclometallated iridium complex is developed as an H₂S-activatable photodynamic agent to trigger H₂S depletion-assisted PDT in cancer cells. This complex exhibits a PDT-OFF state and weak photoluminescence until it encounters H₂S, which activates the photodynamic process. The complex shows high selectivity for H₂S and effectively converts it into a highly active PDT agent. This approach not only enhances photodynamic efficiency but also reduces the concentration of H₂S in cells, leading to decreased ATP levels and increased susceptibility of treated cells to apoptosis during PDT. This novel approach holds promise for revolutionizing cancer treatment.

Harnessing Molecular Probes for Personalized Theranostics: The Recent Development on Activatable Photodynamic Therapy



Abstract

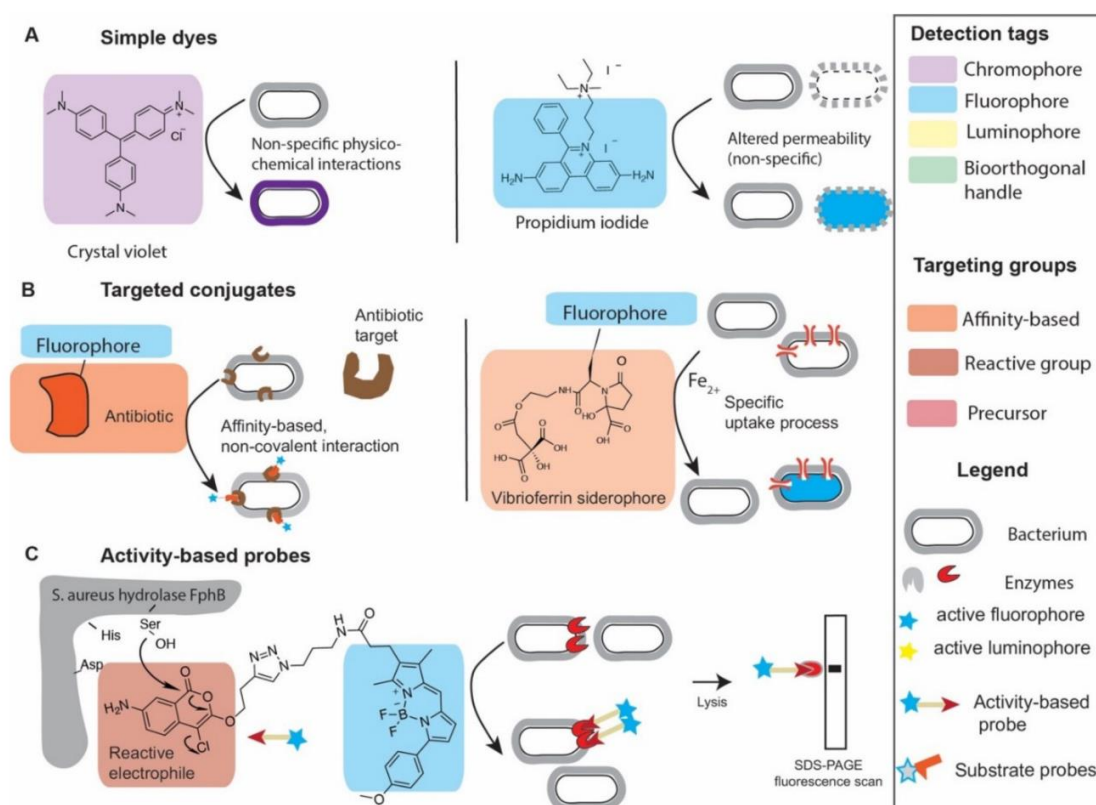
A major bottleneck in biomedicine is the limited pace of the development of new bioanalytical methods and instrumentation. Among the various detection methods available, optical assays provide accurate tracking of biomarkers, which can be utilized as targets for disease diagnosis, route of administration of therapeutic payload, and its effective monitoring. Theranostics is an approach that integrates therapy with diagnostics and possesses immense potential in translational research in clinical settings. Photodynamic therapy (PDT) is a non-invasive cancer treatment modality that employs photosensitizers and light to selectively destroy cancer cells of interest. It is a prevalent modality that can be easily integrated with diagnostic modalities. PDT offers several advantages over conventional cancer therapies, including minimal damage to surrounding healthy cells and tissue and enabling the maintenance of low systemic toxicity. Typically, photosensitizers used in PDT can be activated by specific wavelengths of light, initiating photochemical reactions that generate reactive oxygen species (ROS) responsible for damaging cancer cells. Furthermore, PDT has the potential to trigger an immune response against cancer cells, providing long-term protection against the disease. However, PDT also presents some limitations, such as limited tissue penetration of light, modest selectivity for cancer cells, and the possibility of photosensitizer-induced skin sensitivity. Research on overcoming these limitations by developing new photosensitizers with improved properties, such as enhanced tissue penetration, increased selectivity for cancer cells, and reduced skin sensitivity is a challenging interest in this field of research. Moreover, investigations

are underway to explore combinational therapies, such as combining PDT with chemotherapy or immunotherapy. Activatable photodynamic therapy (a-PDT) is a form of PDT that employs photosensitizing agents capable of being selectively activated in response to specific stimuli. This approach enables accurate targeting of the treatment to particular tissues or cells of interest, thereby reducing the risk of harm to the healthy tissue. In a-PDT, the photosensitizing agent is modified to remain inactive until triggered by a specific stimulus, such as the light of a particular wavelength, alterations in pH or temperature, or the presence of specific molecules and enzymes. Upon activation, the agent generates reactive oxygen species that specifically destroy the targeted cells or tissues. This approach enables precise targeting of the treatment, thereby minimizing damage to healthy tissue. Additionally, it provides greater control over the timing and location of the treatment.

1.1 Introduction

In the dynamic landscape of scientific exploration, the realm of molecular probes emerges as a pivotal cornerstone, affording scientists the means to delve into the intricate microcosm of molecules, cells, and biological processes. Molecular probes, commonly referred to as luminescent or fluorescent dyes, are ingenious molecules endowed with the remarkable capability to change their behavior under specific conditions. This exceptional property has ushered in a revolutionary era across various domains, spanning from biochemistry and cell biology to medicine and materials science.¹ The narrative of molecular probes encapsulates ingenuity, innovation, and their profound implications in and unraveling the enigmas of life at the molecular scale. At its essence, a molecular probe is a molecule characterized by a distinctive structure that can be selectively directed towards a specific molecule or cellular constituent of interest. These probes manifest in a diverse array of forms, each meticulously tailored to serve designated roles in research and diagnostic applications.² Among them, fluorescent molecules stand as the most recognizable type of molecular probe. By absorbing light energy at a specific wavelength and subsequently re-emitting it at a longer wavelength, these molecules generate a characteristic luminescence that is both detectable and quantifiable.³ This intrinsic trait has been adroitly harnessed to scrutinize a myriad of biological phenomena, encompassing the tracking of designated proteins within living cells and the comprehension of gene expression dynamics. Within the sphere of molecular biology, molecular probes have bequeathed researchers an unprecedented vantage point to visualize cellular mechanisms in real time.⁴ As an illustrative example, a scientist can affix a fluorescent probe to a protein of interest, thereby enabling the meticulous tracing of its

movements, interactions, and localization within a cell. This paradigm has engendered groundbreaking revelations into fundamental biological processes, including cellular division, signal transduction, and intracellular trafficking.⁵ Furthermore, molecular probes have facilitated the exploration of maladies at the molecular stratum, thereby empowering researchers to disentangle the molecular substrates underpinning disorders such as cancer, neurodegenerative diseases, and infectious ailments.² The applications of molecular probes transcend the confines of cellular biology. Within the medical domain, these probes have evolved into indispensable entities for diagnostics and imaging.



Scheme 1.1: (a) Schematic representation of different types of molecular probes and their strategy of sensing. Figures adapted from reference 7

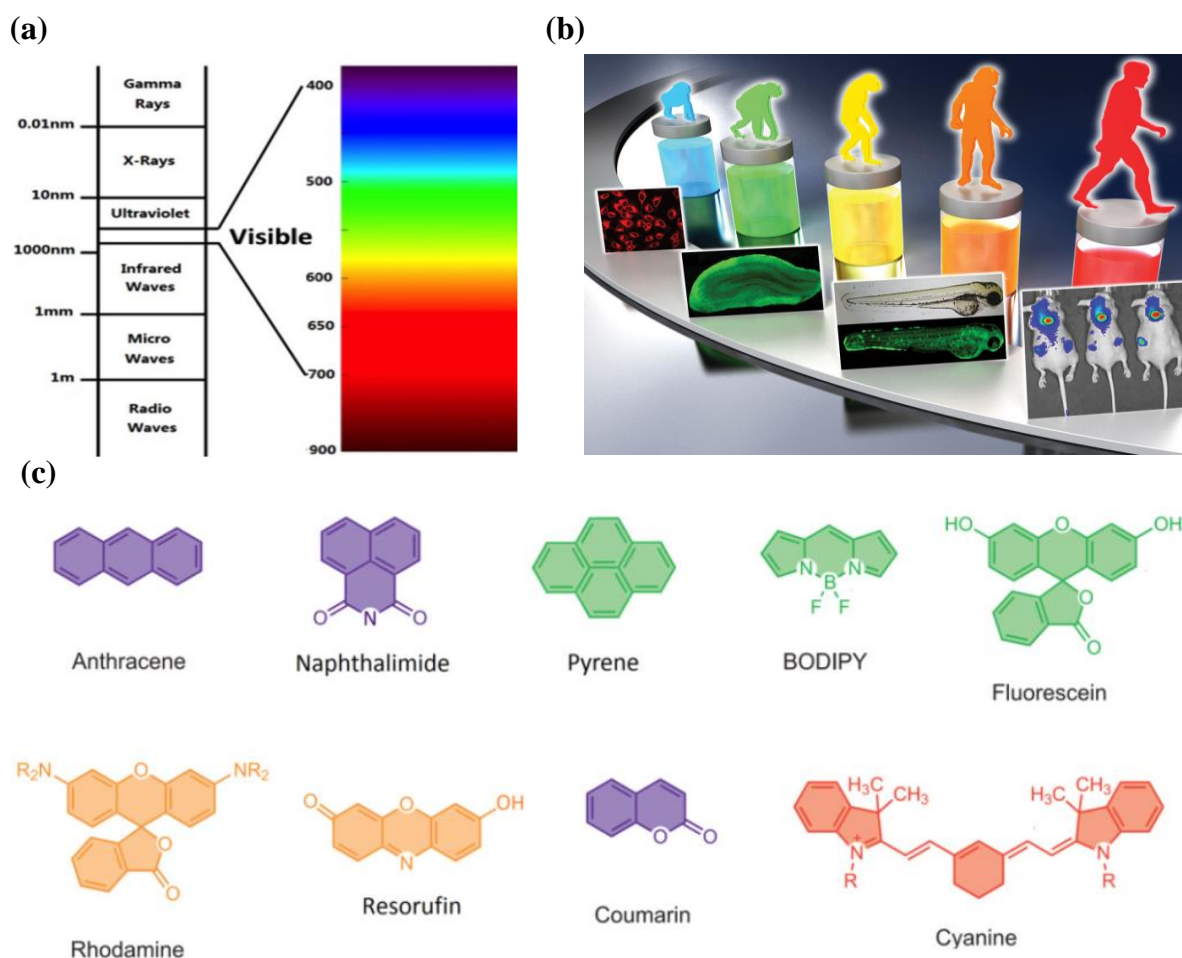
Techniques such as fluorescence microscopy, positron emission tomography (PET), and magnetic resonance imaging (MRI) have undergone transformation through the assimilation of molecular probes, culminating in the non-invasive visualization of tissues and organs with unparalleled precision.^{2,6} For instance, in the arena of cancer diagnosis, molecular probes can selectively target and accentuate specific tumor markers, thus assisting clinicians in the early detection and accurate staging of the ailment (**Scheme 1.1**).⁷ Moreover, the advancement of personalized medicine has been substantially expedited by molecular probes, as they facilitate the identification of distinct molecular targets that steer treatment modalities.^{8,9} The realm of materials science has also borne the imprint of

molecular probes. These probes are not confined solely to biological milieus; they have permeated the realm of material investigation, encompassing polymers, nanoparticles, and nanocomposites.^{10,11} By tethering luminescent or fluorescent probes to these materials, researchers are equipped to monitor their behaviors, interactions, and structural metamorphoses. This avenue has kindled prospects for crafting advanced materials endowed with tailored traits, including heightened conductivity, enhanced mechanical robustness, and responsiveness to external stimuli. As with any scientific progression, the evolution of molecular probes has been accompanied by challenges. The design of probes characterized by high specificity and minimal perturbation is a multifaceted endeavour, as the molecular milieu within living organisms is both intricate and dynamic. Researchers must adeptly engineer these probes to ensure their fidelity in reflecting the biological or chemical processes under scrutiny. Furthermore, the potential toxicity and photostability of these probes necessitate thorough evaluation, particularly when contemplating their *in vivo* applications.¹² Gazing forward, the horizon of molecular probes portends even more remarkable discoveries. Advancements in nanotechnology have yielded nanoscale probes capable of penetrating deep within tissues, thereby unfurling novel vistas for *in vivo* imaging and diagnostics. Moreover, the convergence of molecular probes with nascent technologies such as artificial intelligence and machine learning could inaugurate a paradigm shift in the analysis and interpretation of the intricate data precipitated by these probes. This synergy has the potential to expedite the identification of disease biomarkers, streamline drug development endeavours, and engender a profound comprehension of intricate biological systems.^{13,14}

1.2 Fluorescent molecular probes

Fluorescent molecular probes constitute a groundbreaking advancement in molecular imaging and biological research. These intricately designed molecules have the unique ability to emit fluorescent light when exposed to specific light wavelengths. This exceptional trait enables precise observation of biological processes in controlled settings and living organisms. A notable feature of these probes is their versatility, as they can be customized to target specific biomolecules like proteins, nucleic acids, and ions.¹⁵ This tailored approach provides deep insights into cellular dynamics. Crafting these probes requires a solid grasp of fluorescence principles and molecular interactions (**Scheme 1.2**). By selecting suitable fluorophores and optimizing their spectral properties, researchers can create probes with enhanced brightness, resistance to light-induced degradation, and reduced background interference.¹⁶ Furthermore, the progress of advanced imaging

techniques such as confocal microscopy and super-resolution microscopy has expanded the potential of these probes. These methods allow the investigation of biological events and structures with unprecedented precision in time and space. Consequently, these probes are employed extensively, from deciphering gene expression patterns and identifying protein locations to untangling cellular communication pathways and exploring neurobiology intricacies.^{17,18}



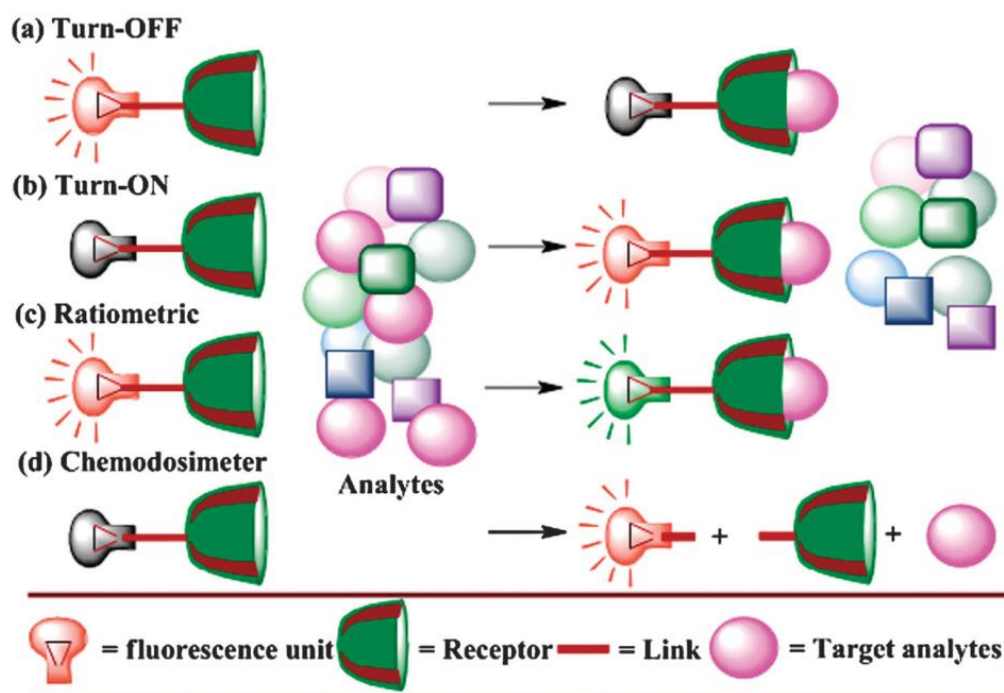
Scheme 1.2: (a) Electromagnetic spectra highlighting the visible region. (b) The action of a molecular probe from *In-Vitro* to the *In-Vivo* level. (c) Structure of common organic fluorophores used for making sensors. Figures adapted from references 16 and 17.

The continual improvement of fluorescent molecular probes promises to uncover more mysteries in the realm of biology. This trajectory offers invaluable insights for both fundamental scientific knowledge and practical applications like early disease detection and personalized medical treatments.

1.2.1 Turn-On Fluorescent Probes

Turn-on fluorescent probes represent a revolutionary breakthrough in the field of molecular sensing and imaging. These specially designed molecules initially exhibit minimal

fluorescence but undergo a remarkable transformation upon interacting with a specific target substance. This interaction leads to a change in their structure or a chemical reaction, resulting in a significant increase in fluorescence intensity.^{19,20} This distinct behavior offers significant advantages over traditional fluorescent probes, enabling highly sensitive and selective detection of target molecules within complex biological or environmental samples. The central innovation of turn-on fluorescent probes lies in their ability to remain inactive until they come into contact with their intended target (**Scheme 1.3**).²¹



Scheme 1.3: Schematic representation of various types of fluorescent sensors and their mode of action Figures adapted from references 21.

This characteristic reduces background signal and undesired interference, enhancing the accuracy of detection by improving the signal-to-noise ratio. These probes can be customized to identify a wide range of substances, including metal ions, biomolecules, enzymes, pH variations, and even specific disease indicators. This adaptability has brought about a transformative impact across various domains, ranging from biomedical studies to environmental surveillance.²⁰

Chang and colleagues developed a fluorescent probe named BA-Resa.²² This probe utilizes a two-step reaction and is built upon a Resazurin core. In this modified version, the Resazurin detector contains a boronic acid group that specifically binds to the carbohydrate section's diol motif. This boronic acid interacts with ribose from NADH, reducing the distance between them and facilitating hydride transfer. The carbohydrate part of NADH

selectively binds to the probe's boronic acid motif. Once the boronic acid recognizes this interaction, the detector core is reduced by NADH through a hydride transfer process, resulting in the restoration of the molecule's fluorescence. The Resazurin part acts both as a fluorescence activator and a recognition site. To expedite the sensing process by minimizing the spatial gap, the initial step involves the coupling of the boronic acid in BA-Resa with the ribose in NADH (Figure 1.1).

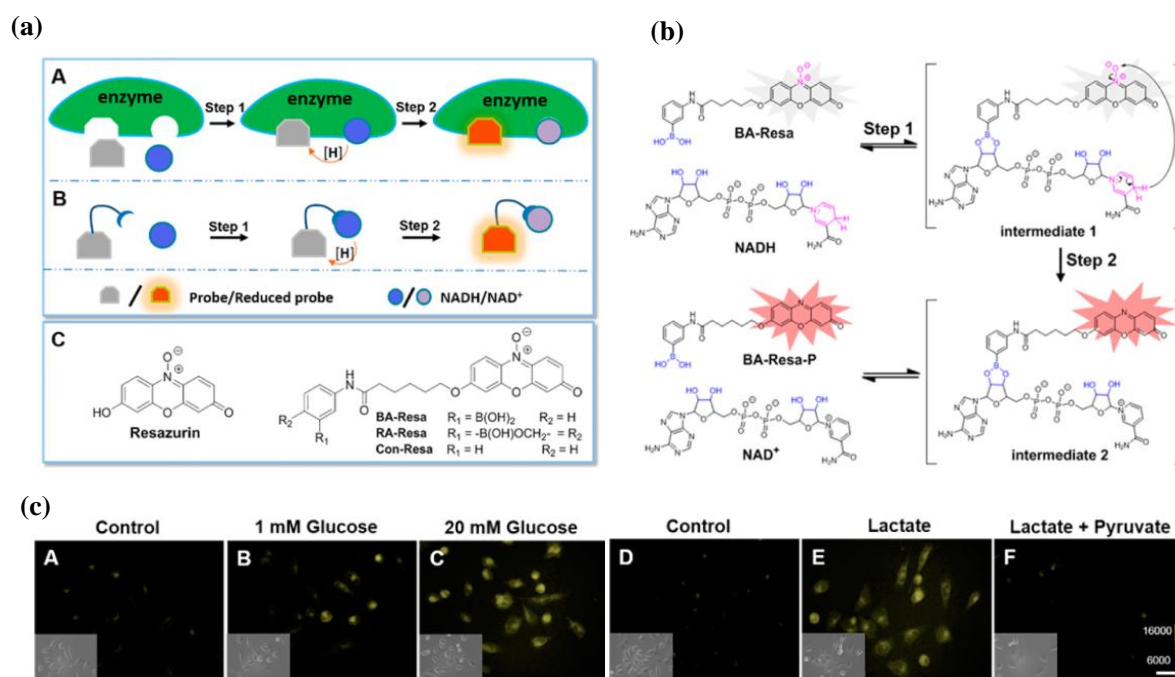


Figure 1.1: (a) Scheme of the enzyme-catalysed NADH sensing process. (b) The molecular structure of probe and sensing mechanism. (c) The fluorescence intensity of BA-Resa in live OSCC cells pre-treated with 1 and 20 mM Glucose along with lactate and pyruvate. Figures adapted from references 22

Subsequently, the probe receives active hydrogen from NADH in the second step, promoting the formation of highly fluorescent products while decreasing the weakly fluorescent BA-Resa. In a buffer solution with a pH of 9.5, the fluorescence intensity consistently increases, peaking at a wavelength of 575 nm with a shift from the original 620 nm.

Joo *et al.* have introduced a new fluorescent probe 1 (Figure 1.2). designed to target mitochondria and measure NADPH levels in live cells in real-time.²³ This innovative probe utilizes a pyridinium-based reactive site for NAD(P)H and a red-emitting dicyanoisophorone with a mitochondria-targeting triphenyl phosphonium cation. The initial state of the probe, due to its conjugated electron acceptor-acceptor system, lacks fluorescence. However, upon interaction with NAD(P)H, the pyridinium moiety undergoes

reduction, resulting in the formation of an electron donor-acceptor system ($1 + H$) with conjugation, leading to strong fluorescence emission. The lipophilic triphenyl phosphonium group allows the probe to accumulate within the mitochondrial matrix of live cells. Despite having low initial fluorescence, probe 1 exhibited vivid red fluorescence at 615 nm upon the addition of NADH (2 mM) to a solution containing 10 μM of the probe, and this fluorescence increased over time (Figure 1.2).

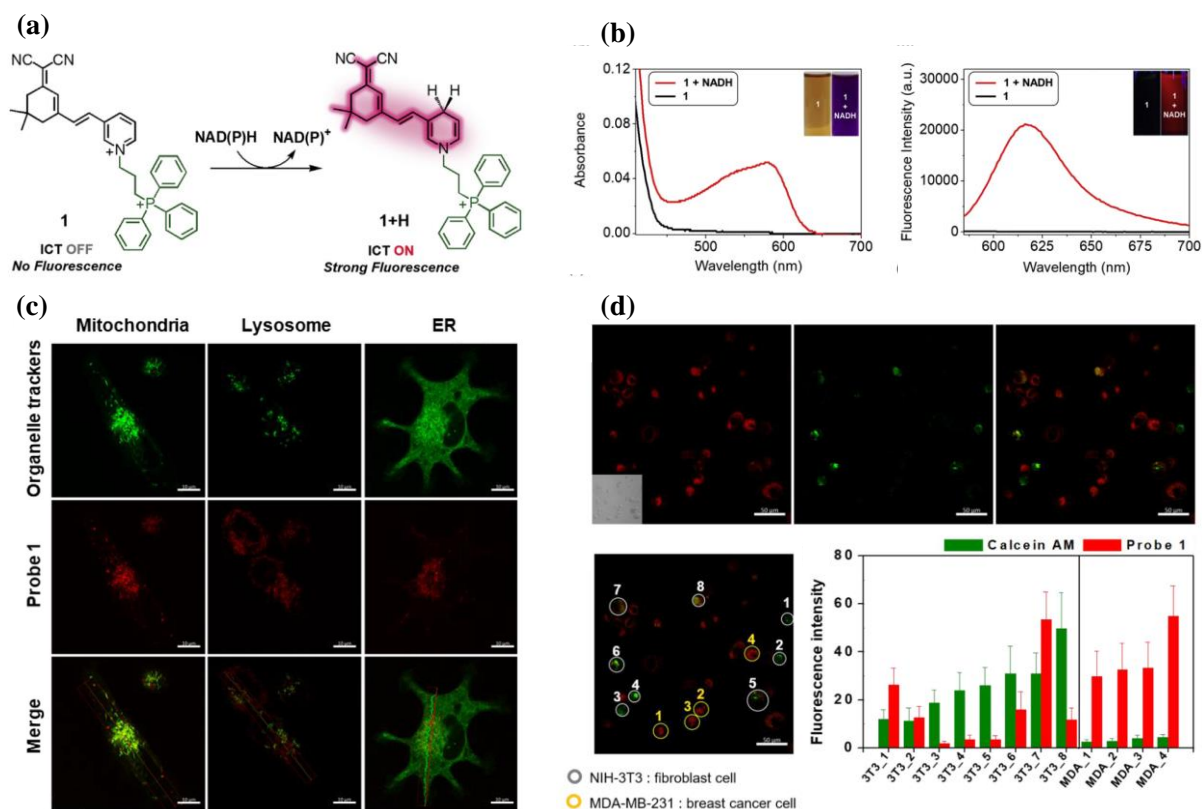


Figure 1.2: (a) The structure and NADH and NADPH sensing mechanism of probe 1. (b) The UV-visible and fluorescence changes associated with probe 1 upon reaction with NADPH. (c) Fluorescence images of intracellular localization of the probe through ER, Mito and Lyso trackers in MDA-MB-231 cells. (d) NIH-3T3 cells were exposed to Calcein AM for 30 min, and afterward, they were combined with MDA-MB-231 cells for a 24-hour period. The cell mixture was subjected to probe 1 and fluorescent signal strengths were measured within individual cells by analyzing fluorescence images of live MDA-MB-231 and NIH-3T3 cells. Figures adapted from references 23

In a recent study by Zhang *et al.*, an innovative approach has been introduced for the sensitive detection of hydrogen sulfide (H_2S) using a unique colour and fluorescence turn-on probe. The strategy involves modifying a naphthalimide fluorophore by attaching a H_2S -cleavable component, specifically a 2,4-dinitrobenzene sulfonyl group.²⁴ This modified fluorophore is then linked to a hydrophilic polyethylene glycol (PEG) chain, resulting in the creation of the fluorescent probe named probe 1. The clever design of probe 1 incorporates a fascinating mechanism that allows its fluorescence to be activated upon

interaction with H₂S. In the absence of H₂S, a phenomenon called photoinduced electron transfer (PET) leads to fluorescence quenching between the fluorophore and the detecting component. However, when exposed to H₂S, the 2,4-dinitrobenzene sulfonyl group undergoes cleavage, enabling the fluorophore's hydroxyl and naphthylamide units to interact and restore an intramolecular electron-donating and withdrawing system.

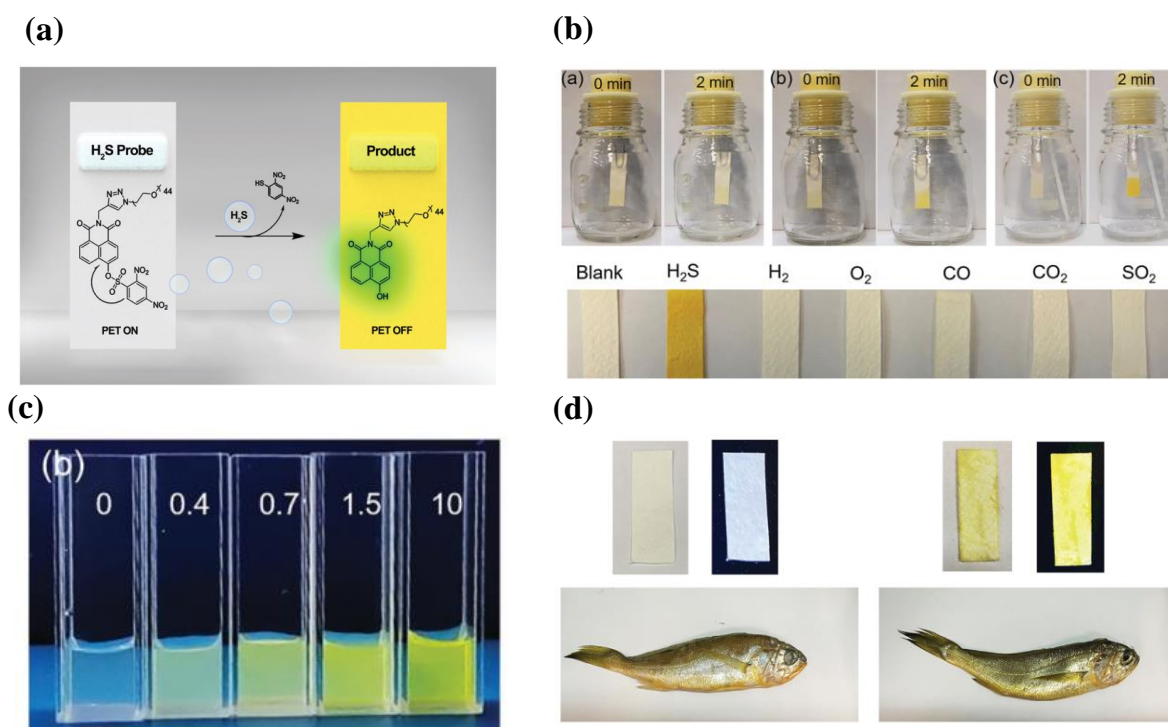


Figure 1.3: (a) The structure and H₂S sensing mechanism of probe. (b) Photographs of probe papers exposed to H₂S gas at concentrations of 25, 100, and 500 ppm for a duration of 2 minutes. Additionally, images of probe papers designed for detecting gases with a concentration of 100 ppm after they were exposed to these gases for 2 minutes. (c) Describe the visual outcomes when Probe 1 (5 μM) is exposed to various concentrations of NaSH. (d) Identification of H₂S from yellow croaker fish storage under conditions of -20°C with paper strip along with images of the fish. Figures adapted from references 24

This interaction results in a considerable enhancement of fluorescence emission, producing a strong yellow fluorescence. Notably, this fluorescence "turn-on" response demonstrates a linear correlation with H₂S concentration (Figure 1.3). In another study, Spiegel and colleagues showcased a noteworthy development involving a BODIPY-based turn-on fluorescent probe, denoted as MBo, designed for proficiently detecting methyl glyoxal. This probe, initially dimmed in fluorescence, is designed with a diamino structure.²⁵ Upon interaction with methyl glyoxal, it undergoes a reaction to create a compound adduct, resulting in vivid green fluorescence emission. Remarkably this innovative probe MBo, can be utilized for the direct assessment of methyl glyoxal concentrations within plasma or serum. The ease with which MBo allows for the quantification of MGO levels and

visualization of its presence within living cells carries substantial potential as a groundbreaking advancement in clinical diagnostics (**Figure 1.4**). Duan and his research team introduced an innovative fluorescent probe labeled as Probe 1 meticulously designed to proficiently identify the presence of cadmium ions (Cd^{2+}) both in solution and within living cells. This probe comprises a BODIPY fluorophore intricately connected to a cadmium-sensing component, enabling it to form intricate complexes with Cd^{2+} ions.

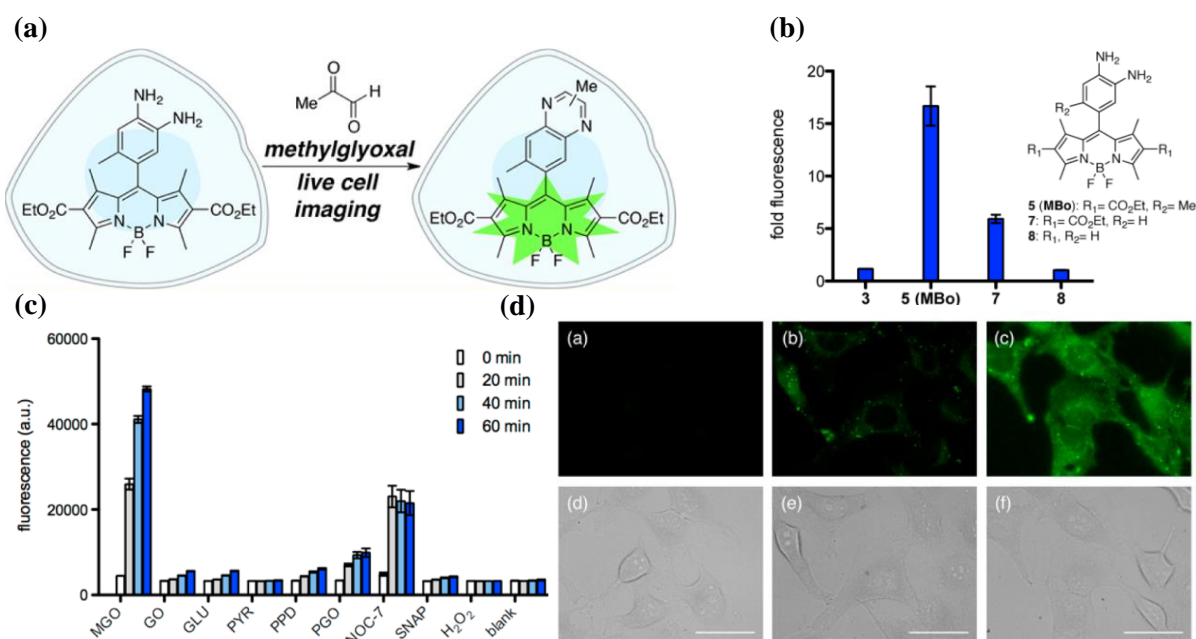


Figure 1.4: (a) The structure and MGO sensing mechanism of probe molecule. (b) Fold change of fluorescence intensity of ester substituent compare to the other substituents. (c) Selectivity of the probe towards MGO over other analytes. (d) The intracellular sensing of MGO in HeLa cells. Figures adapted from references 25

Initially, when the probe is in its free form, it exhibits feeble fluorescence due to a cleverly designed Photoinduced Electron Transfer (PET) mechanism, effectively quenching the fluorescence from the polyamide segment to the BODIPY fluorophore. Upon the introduction of Cd^{2+} ions into the probe solution, several remarkable transformations take place. A fresh absorption peak emerges at 562 nm, while the peak at 578 nm diminishes, with an interesting isosbestic point observed at 566 nm. Most significantly, the fluorescence intensity at 570 nm experiences a staggering 195-fold increase, accompanied by a quantum yield surge reaching an impressive value of approximately 0.3. Furthermore, this sensor exhibits a striking sensitivity to Cd^{2+} , detecting even minute concentrations as low as 6×10^{-7} M, which results in a substantial upsurge in fluorescence intensity.²⁶

1.2.2 Turn-Off Fluorescent Probes

On the other side, Turn-off fluorescent probes, also known as fluorescence quenching-based probes, play a pivotal role in both scientific and biomedical domains. They serve the critical function of reducing their fluorescence intensity upon encountering a particular target analyte, making them indispensable in various fields such as biological sensing, clinical diagnostics, and imaging.²⁷ In the realm of biological research, these turn-off fluorescent probes are of immense value for precisely identifying specific biomolecules like proteins, nucleic acids, ions, or metabolites. They facilitate the observation of intricate cellular processes, the identification of disease markers, and the tracking of essential molecules within biological specimens. The meticulous design of turn-off fluorescent probes is paramount to their functionality. These probes are carefully crafted with recognition elements that engage with the target analyte, triggering a quenching mechanism that diminishes fluorescence. Different quenching mechanisms, such as Photoinduced Electron Transfer (PET), Förster Resonance Energy Transfer (FRET), and Collisional Quenching, are employed based on the particular application's requirements.

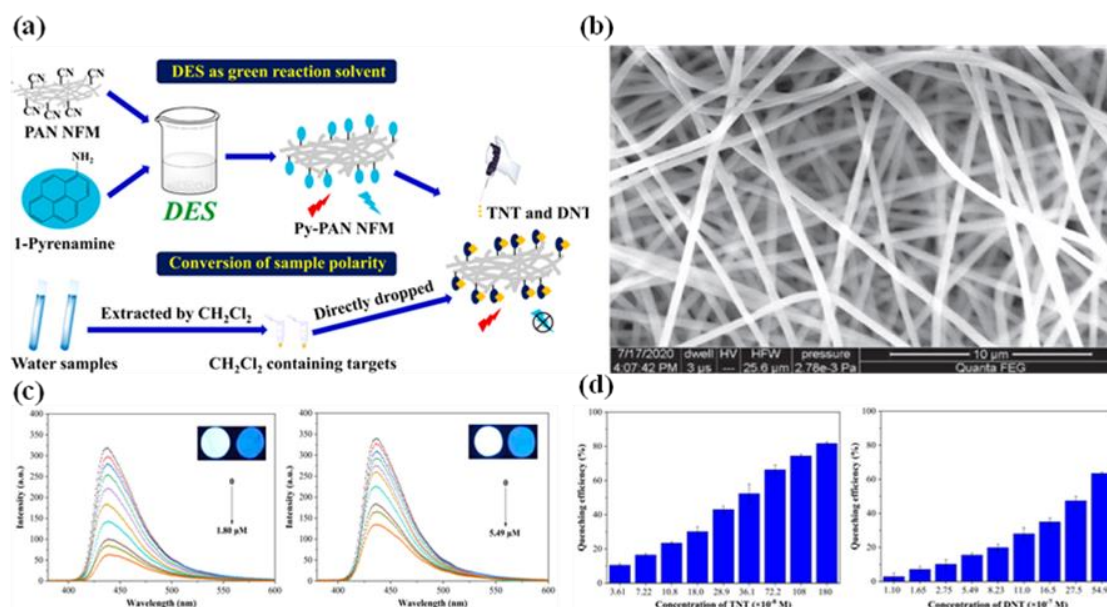


Figure 1.5: (a) Schematic representation of the preparation of the sensing construct. (b) SEM image of the construct. (c) Alterations in the fluorescence intensity of Py-PAN NFM when exposed to different concentrations of TNT. (d) Quenching efficiencies of the construct as a result of exposure to different TNT concentrations. Figures adapted from references 28

Cao and colleagues conducted a study where they explored the potential of pyrene-functionalized polyacrylonitrile fiber (Py-PAN) as a sensor for detecting 2,4-dinitrotoluene (DNT) and 2,4,6-trinitrotoluene (TNT).²⁸ They put forth a theoretical framework to explain how the fluorescence of Py-PAN is quenched in the presence of these explosives. Their

research revealed that the energy difference between the highest occupied molecular orbital (HOMO) of Py-PAN and the lowest unoccupied molecular orbital (LUMO) of DNT and TNT was smaller compared to the gap between the HOMO and LUMO of Py-PAN itself. This reduced energy gap facilitated the transfer of excited electrons from Py-PAN to DNT and TNT. The authors proposed that this electron transfer might occur through the formation of a donor-acceptor complex between Py-PAN and the explosives, driven by π - π interactions, ultimately leading to the quenching of fluorescence (FL).²⁹ Additionally, they noted that the FL decay curves of Py-PAN were unaffected when DNT or TNT were present. Based on these findings and the linear relationship observed in the Stern-Volmer plots, they suggested that the quenching mechanism likely involved a process referred to as photoinduced electron transfer (**Figure 1.5**).

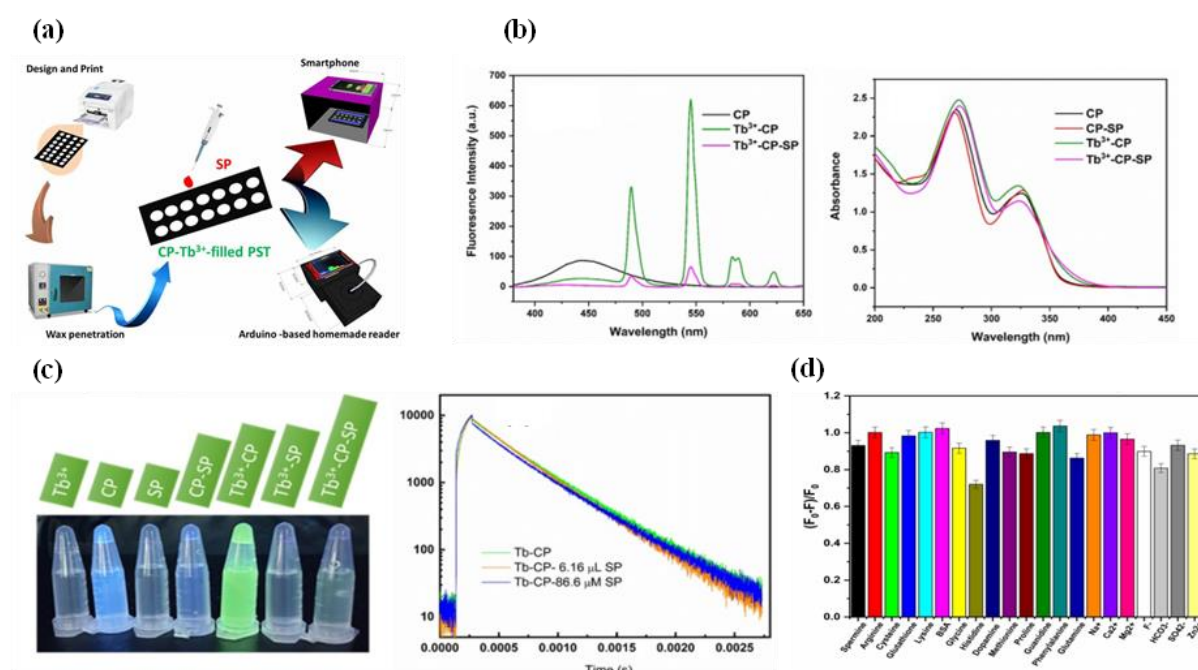


Figure 1.6: (a) Schematic representation of the preparation of the sensing construct. (b) Fluorescence and absorbance of the constructs (c) Observe alterations in sample colors when exposed to a UV lamp emitting light at a wavelength of 365 nm and the lifetime curves of three different samples. (d) In the presence of 0.1 mM SP and 1 mM of another compound, the available interferences of the $(F_0 - F)/F_0$ ratios of CP-Tb³⁺. Figure adapted from reference 30

In their research, Lee and their team devised an innovative spermine sensor employing the complex of ciprofloxacin-Tb³⁺.³⁰ This complex formation hinged on the connection between carboxylic acid and ketone groups, resulting in a crucial fluorescence signal. The coordination between ciprofloxacin and Tb³⁺ played a pivotal role in shaping this complex. However, the introduction of spermine disrupted this coordination due to its positive charge, consequently disbanding the complex and causing a decline in fluorescence. To

substantiate their findings, the scientists conducted a thorough analysis of various spectra, including absorption spectra for both the complex and ciprofloxacin, alongside excitation/emission spectra for Tb^{3+} ions. Furthermore, they delved into FL lifetime curves. Drawing from these experimental outcomes, the researchers postulated that dynamic quenching stood as the underlying mechanism behind the observed fluorescence quenching in the sensor (**Figure 1.6**).

Roy *et al.*, employed cysteine-conjugated MoS_2 (Cys- MoS_2) quantum dots as a stimulus to facilitate the imaging of cancer cells with folate receptor overexpression. Specifically, they observed that the emission signal emitted by Cys- MoS_2 at a wavelength of 444 nm rapidly diminished upon the introduction of folic acid (FA).³¹

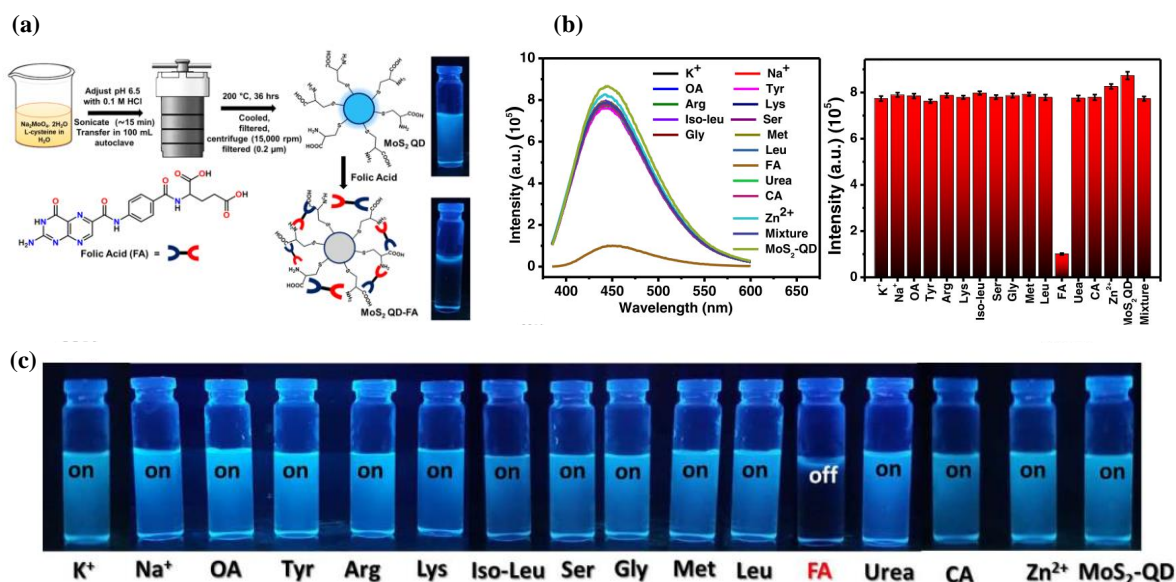


Figure 1.7: (a) Schematic representation of the preparation of MoS_2 -QD. (b) Selectivity of the construct towards FA over other analytes. (c) Photographs showing the turn-off of the MoS_2 -QD with FA over other relevant analytes. Figure adapted from reference 31

The rapid decrease in emission intensity was attributed to the formation of a complex between FA and Cys- MoS_2 , primarily driven by electrostatic interactions between the two components. Importantly, this interaction led to a reduction in the emission intensity of Cys- MoS_2 , without causing any noticeable shift in the peak wavelength. To quantitatively assess the degree of quenching in this system, the researchers calculated the quenching constant (KSV) using the Stern-Volmer equation. The results of this analysis confirmed that the MoO_2 /FA system exhibited strong and effective complexation, providing valuable insights into the underlying molecular interactions in this bioimaging approach (**Figure 1.7**). Ramamurthy and colleagues conducted a study in which they developed a series of chemosensors based on amido thiourea-linked acridine dione compounds for the purpose

of detecting Hg^{2+} ions.³² These compounds exhibited strong fluorescence emission at around 440 nm, primarily due to an Intramolecular Charge Transfer (ICT) process occurring from a nitrogen atom within the ring to the carbonyl center of the acridine dione moiety. Upon the introduction of Hg^{2+} ions, a notable decrease in the fluorescence signal was observed. The reduction in emission intensity can be ascribed to an intramolecular Photoinduced Electron Transfer (PET) process occurring from the aniline moiety towards the acridinedione fluorophore. This change in fluorescence can be employed as a means to detect the presence of Hg^{2+} ions in a given sample. Moreover one particular molecule referred to as 1e, demonstrated effectiveness in the *In-Vitro* two-photon imaging of Hg^{2+} . This suggests its potential utility in imaging applications for detecting Hg^{2+} ions in biological settings.

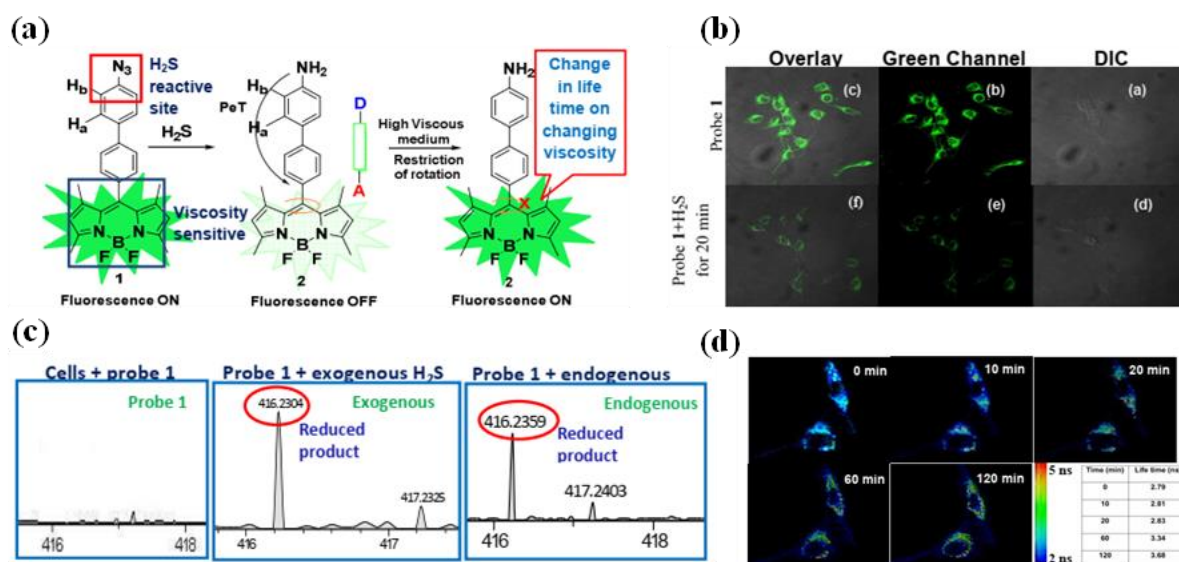


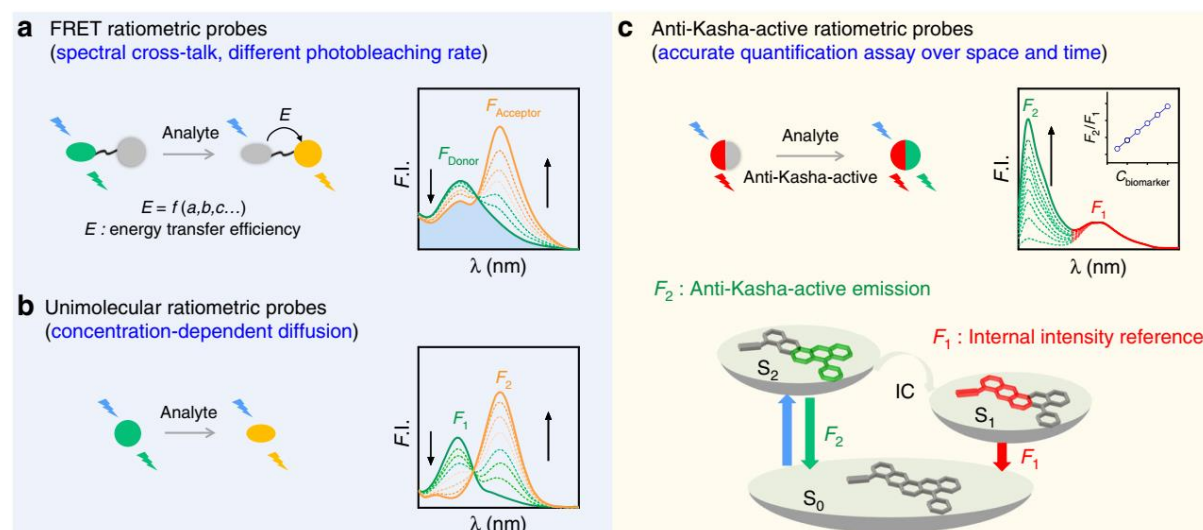
Figure 1.8: (a) The structure and H₂S, viscosity sensing mechanism of probe 1. (b) Fluorescence images of intracellular localization of the probe in C6 cells. (c) Analysing the intracellular mass changes resulting from the reduction of probe 1 through H₂S. (d) Fluorescence lifetime imaging of C6 cell lines showing apoptosis induced by probe 1 with H₂S. Figure adapted from reference 33

Manoj *et al.*, recently published a significant study introducing an innovative fluorescent probe based on BODIPY. This new probe serves a dual function by not only detecting hydrogen sulfide (H₂S) but also enabling the visualization of apoptosis triggered by H₂S.³³ What makes this probe particularly intriguing is its distinctive behavior of fluorescence "turn-off" in response to H₂S exposure. This behavior can be explained by the Photoinduced Electron Transfer (PET) process, where electrons move from the nitrogen atom towards the BODIPY component. Understanding this phenomenon is crucial in deciphering how the probe senses H₂S. Significantly, this sensor exhibits impressive selectivity for H₂S, making it an excellent tool for monitoring H₂S-induced cellular apoptosis. This application holds

immense potential in the realm of biomedical research, offering valuable insights into the cellular mechanisms involved in H₂S-induced apoptosis (**Figure 1.8**).

1.2.3 Ratiometric Fluorescent Probes

Ratiometric fluorescence probes represent a highly advanced category of tools used in chemical and biological sensing. They bring a new level of precision and reliability to the measurement of analyte concentrations and the characterization of specific attributes. Unlike traditional single-wavelength fluorescence probes, these cutting-edge probes rely on comparing emission intensities or ratios across two distinct wavelengths, which greatly improves the accuracy and trustworthiness of the measurements. Conventional single-wavelength fluorescence probes often face limitations that hinder their usefulness in precise scientific and analytical settings. These probes rely solely on the intensity of emitted light at one wavelength, making them vulnerable to various sources of error, such as fluctuations in instrument settings, photobleaching, and variations in sample properties.³⁴



Scheme 1.4: Developing ratiometric probes entails devising tactics that involve analysing distinct characteristics. Figure adapted from reference 34

In contrast, ratiometric fluorescence probes represent a significant advancement in sensing technology. By utilizing two distinct wavelengths, these probes take advantage of comparative analysis (**Scheme 1.4**)³⁴. They detect changes in fluorescence emissions induced by analytes by calculating the ratio of intensities at carefully chosen wavelengths. This clever approach not only reduces the impact of external factors but also provides researchers with a high level of confidence in the accuracy of their measurements.

Saranya and her colleagues have introduced a novel ratiometric fluorescent probe named Sq, which holds significant promise for measuring thiol levels *In-Vitro*.³⁵ This innovative

probe was applied to quantify imbalances in glutathione (GSH) levels at different stages of apoptosis in *In-Vitro* models, marking a pioneering approach for real-time apoptosis monitoring. Sq exhibits substantial alterations in both its absorption and emission spectra when it interacts with biothiols. Specifically, the addition of GSH results in a decrease in absorption at 670 nm, accompanied by the appearance of a new absorption band at 400 nm. Similarly, as GSH is added in increasing amounts, a new emission band at 560 nm emerges with a quantum yield of 0.12, while the near-infrared (NIR) emission at 690 nm is quenched.

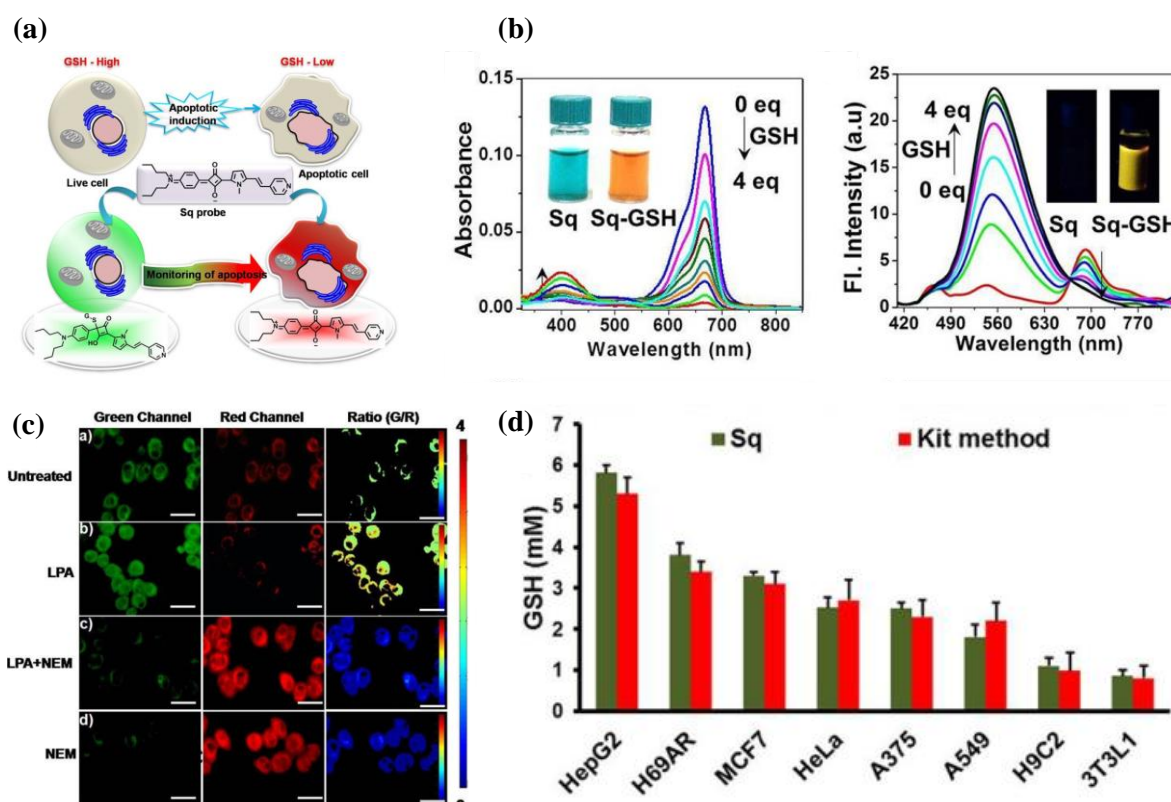


Figure 1.9: (a) The structure and GSH sensing mechanism of Sq. (b) Absorption and emission changes of Sq with different concentrations of GSH. (c) Ratiometric Fluorescence images of intracellular localization of the probe in HepG2 cells. (d) Comparison of GSH levels in different cells via Kit method and by Sq probe. Figure adapted from reference 35

These changes in the spectral properties are attributed to the activation of Sq's initially inactive fluorophore through a chemical process involving the Michael addition reaction of thiol to the cyclobutene ring within the squaraine moiety. This reaction forms the foundation for Sq's ratiometric sensing mechanism, enabling the quantification of thiols (Figure 1.9). Cho *et al.*, introduced a highly innovative two-photon fluorescent chemodosimeter, denoted as SSH-Mito, which demonstrates remarkable capabilities for the ratiometric sensing of thiols. This sophisticated probe is composed of several key components, including a 6-(benzo[d]thiazol-2-yl)-2-(N,N-dimethylamino)naphthalene

moiety serving as the two-photon active fluorophore.³⁶ Additionally, it features a strategically positioned disulfide group, designed as the thiol-cleavage site, and incorporates a triphenyl phosphonium salt moiety, carefully chosen for its mitochondrial targeting properties. Upon encountering thiols, this disulfide bond undergoes cleavage, leading to a fascinating and visually distinguishable ratiometric fluorescence response. This response is characterized by a shift in emission color from blue to yellow, and it can be attributed to the pronounced Intramolecular Charge Transfer (ICT) effect taking place within the probe's molecular framework.

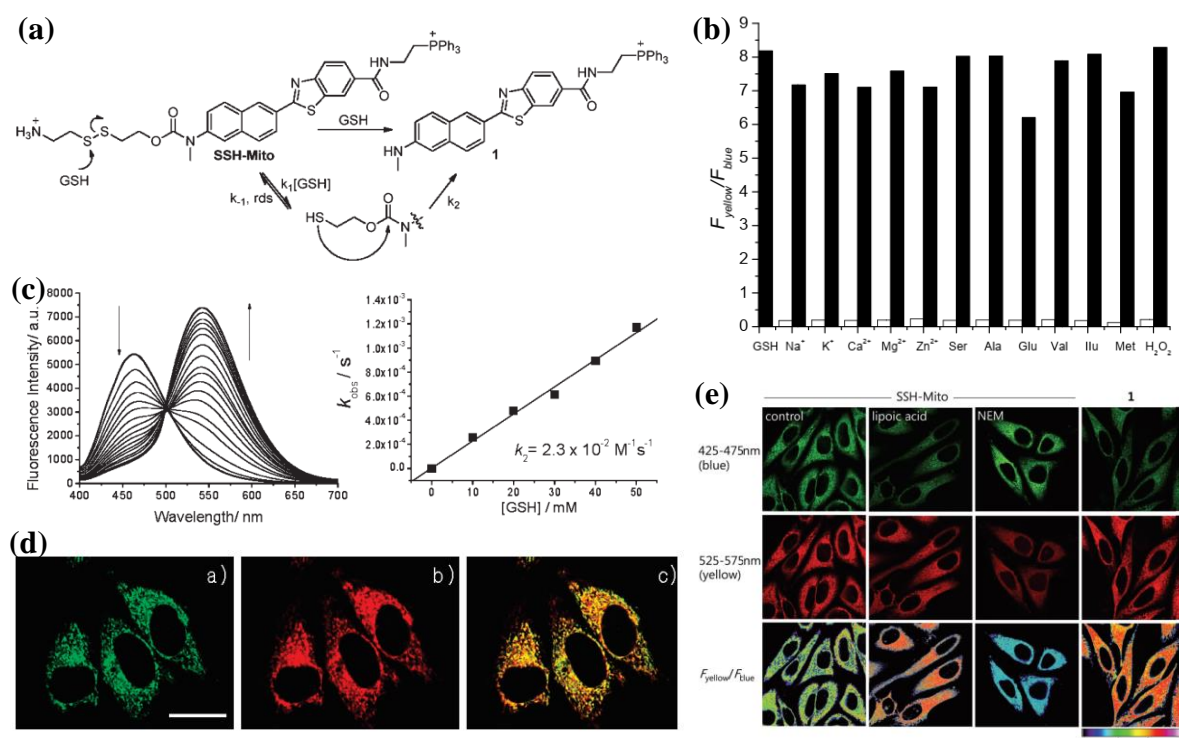


Figure 1.10: (a) The structure and GSH sensing mechanism of SSH-Mito. (b) Selectivity of SSH-Mito towards GSH. (c) The ratiometric fluorescence changes with different amounts of GSH. (d) Intracellular colocalization of SSH-Mito in mitochondria through confocal imaging. (e) Ratiometric imaging in cellular level through confocal imaging. Figure adapted from reference 36

This chemodosimeter has been successfully employed by the authors to visualize mitochondrial thiol levels in live cells, as well as in living tissues, even at considerable depths ranging from 90 to 190 μm (Figure 1.10). In another study, Yang *et al.*, achieved the successful development of a ratiometric fluorescent sensor designed to selectively detect glutathione (GSH) while discriminating it from cysteine (Cys) and homocysteine (Hcy).³⁷ This innovative sensor operates based on a mechanism involving the rapid displacement of chloride ions by thiolate groups. What sets this sensor apart is its ability to distinguish GSH from Cys and Hcy, which can be attributed to the amino group present in Cys and Hcy. This amino group replaces the thiolate group, leading to the formation of amino-substituted

BODIPY, which exhibits distinct photophysical properties compared to sulfur-substituted BODIPY formed during the reaction with GSH. This unique reaction mechanism serves as a clear discriminator for GSH, setting it apart from other thiols. Upon reacting with GSH, the sensor undergoes changes in its emission spectrum. Initially, the emission peak at 556 nm gradually diminishes, concurrently giving rise to a new peak at 588 nm.

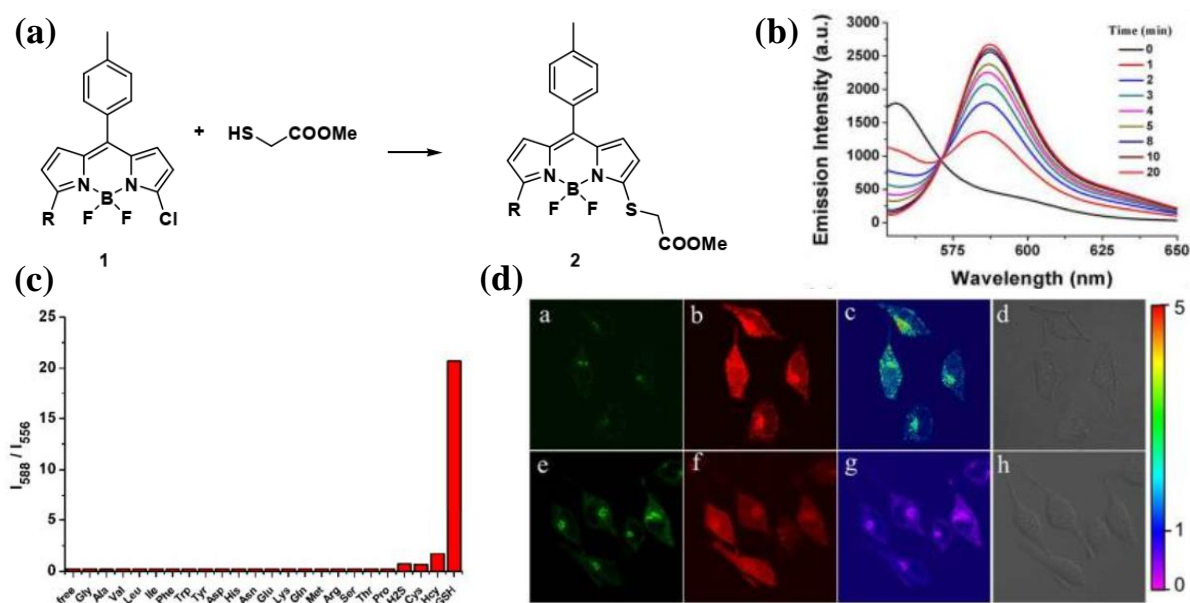


Figure 1.11: (a) The structure and sensing mechanism of 1. (b) The ratiometric fluorescence changes with different amounts of GSH. (c) Selectivity of 1 to GSH over other analytes. (d) Ratiometric imaging in the cellular level through fluorescence imaging. Figure adapted from reference 37

It's important to note that these spectral changes are specific to GSH and not observed with other thiols, thanks to the particular reaction pathway involving the amino group. This selectivity and unique reaction mechanism make this sensor a promising tool for the specific detection of GSH in complex biological or chemical systems (**Figure 1.11**).

In a separate study, Chang and colleagues introduced a novel two-photon ratiometric fluorescent probe named MITO-CC designed for the detection of peroxynitrite (ONOO^-), utilizing a Förster resonance energy transfer (FRET) mechanism. This probe exhibited remarkably swift response kinetics towards ONOO^- , displaying both high sensitivity and outstanding selectivity, even in the presence of other reactive sulfur species (RSS).³⁸ In spectrofluorometric experiments, when ONOO^- was absent, MITO-CC emitted strongly at 651 nm and displayed a weaker characteristic emission at 473 nm due to its coumarin component. However, upon gradual addition of ONOO^- in the concentration range from 0 to 7.5 μM , the emission at 651 nm almost vanished, accompanied by a significant intensification of the coumarin emission, causing the solution's fluorescence color to shift

from red to bluish-green. Notably, this yielded a substantial 93-fold increase in the fluorescence ratio (I_{473}/I_{651}), demonstrating a linear relationship over the entire ONOO⁻ concentration range (**Figure 1.12**). Furthermore, this probe was effectively utilized to perform ratiometric imaging of ONOO⁻ within mitochondria in live cells. It also allowed for the visualization of subtle fluctuations in ONOO⁻ levels within an inflamed pathological environment, marking the first successful application of two-photon fluorescence confocal microscopy for this purpose.

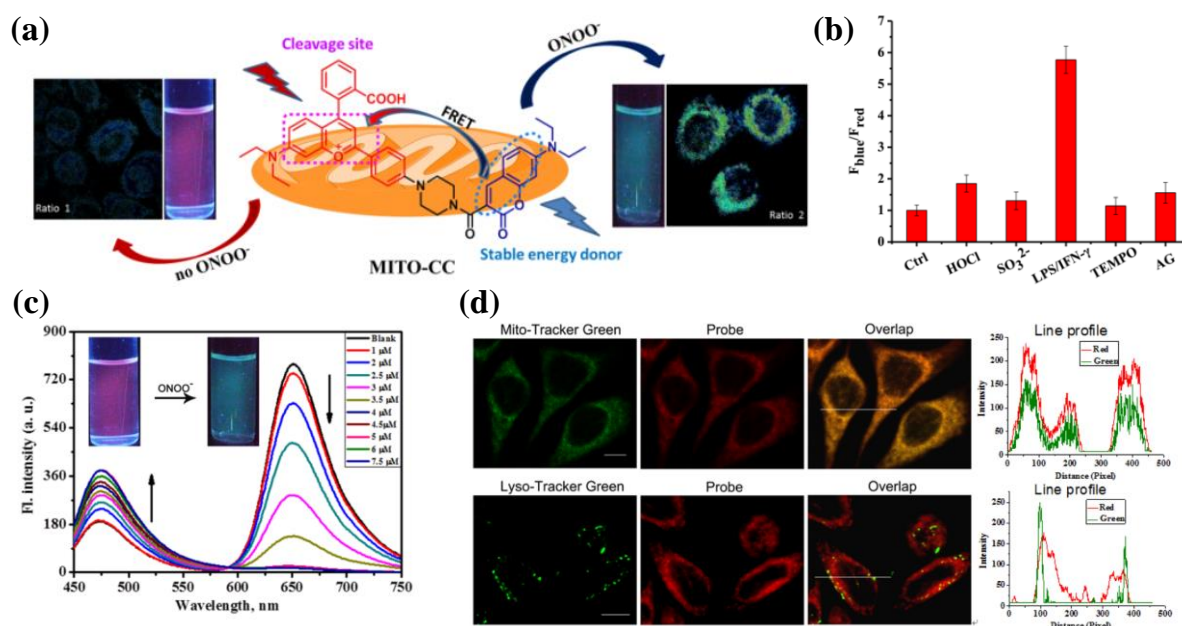


Figure 1.12: (a) The structure and peroxynitrite sensing mechanism of MITO-CC. (b) Selectivity of MITO-CC to peroxynitrite over other analytes. (c) Fluorescence changes associated with varying concentrations of peroxynitrite. (d) Intracellular colocalization of MITO-CC in mitochondria through confocal imaging. Figure adapted from reference 38

1.2.4 Limitations of Organic Fluorescent Probes

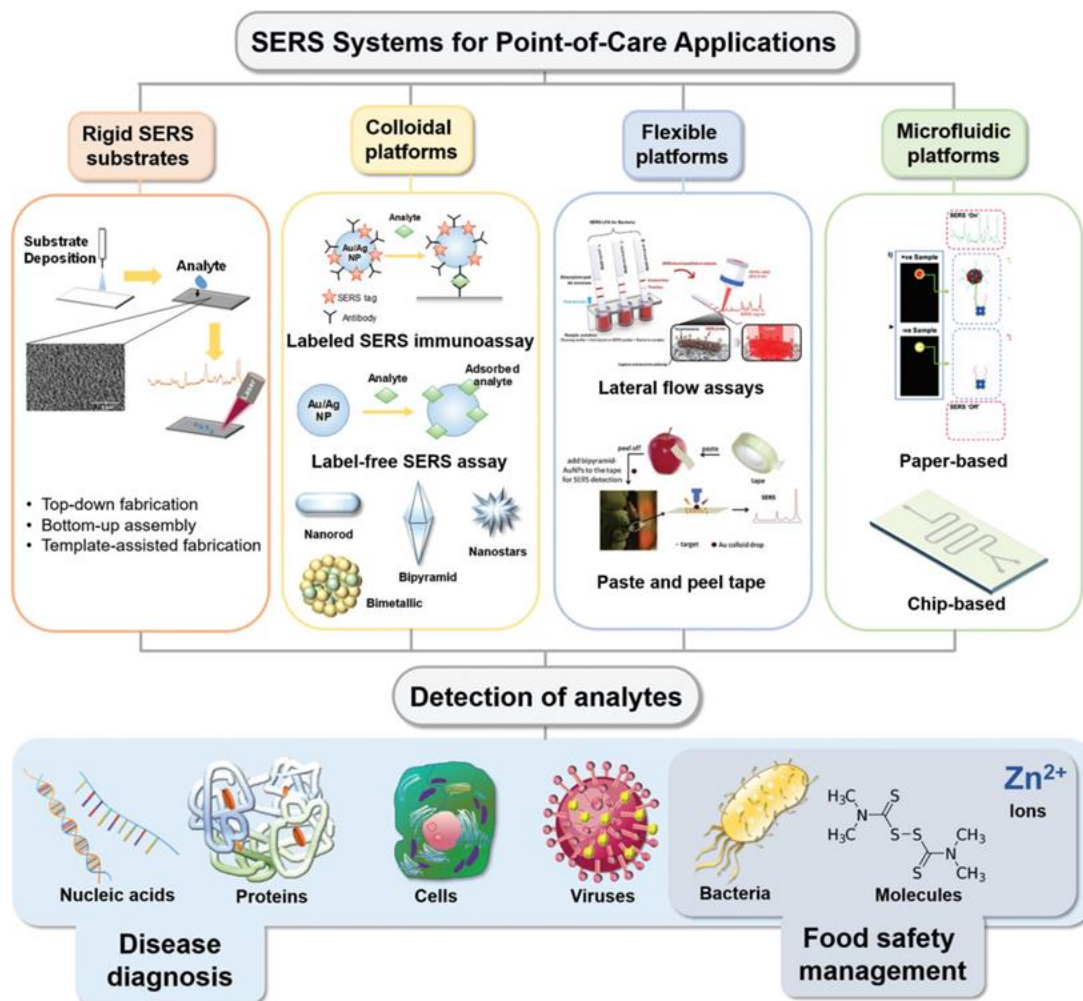
Organic fluorescent probes play an indispensable role across various scientific fields, thanks to their unique ability to emit light in response to specific conditions or targets. However, like any technology, they have their fair share of drawbacks that researchers must carefully consider. A significant challenge is photobleaching, where intense light exposure leads to irreversible fading of fluorescence. This limitation can restrict their suitability for long-term imaging studies. Additionally, organic fluorophores are often sensitive to environmental factors such as pH, temperature, and oxygen levels, which can affect their stability and reliability.³⁹ Spectral overlap among the emission spectra of different probes can complicate distinguishing multiple targets in the same experiment. Furthermore, the limited number of distinct colors and the bulkiness of certain organic fluorophores can

hinder multiplexing and target access in specific applications. Concerns regarding cellular penetration, toxicity, and environmental impact underscore the need for caution. The potential toxicity of organic dyes and their potential interference with biological processes demand careful consideration during experimental design. Photostability issues challenge the accuracy and duration of live-cell imaging, necessitating precise control of imaging conditions.⁴⁰ Specificity concerns emphasize the importance of validating probe selectivity to avoid misleading results. Limitations in tissue penetration and development/acquisition costs should not be underestimated. As technologies continue to evolve, addressing these limitations and making informed choices in probe selection or design will be pivotal in ensuring the accuracy and reliability of biological insights gained through organic probe-based application techniques. Researchers must adeptly navigate these challenges to harness the full potential of organic probes while minimizing their potential adverse impacts on the pursuit of scientific knowledge in the realm of bio applications.⁴¹

1.3 SERS-based molecular probes

Over the past decade, there has been growing interest in utilizing Surface-Enhanced Raman Spectroscopy (SERS) as a highly reliable platform for detecting specific molecules.⁴² SERS offers several advantages, including exceptional specificity, sensitivity, and rapid results. This technique involves exciting the analyte with photons, causing scattered photons to shift a change in energies.⁴³ By measuring these Raman-scattered photons, a spectrum related to molecular identity was generated. However, the inherent weakness of the Raman effect makes it insufficient for detecting low concentrations of analytes.⁴⁴ To address this limitation, SERS can amplify the Raman effect by orders of magnitude (ranging from 10^4 to 10^{10}) when the analyte adheres to metallic nanoparticles, a process known as SERS. This improvement occurs due to the transference of energy from the metal surface to the adsorbed analyte, resulting in an augmentation of analyte scattering. As a result, SERS can identify minute concentrations of analytes, as long as the molecules are situated in close proximity to metallic nanostructures on SERS substrate platforms.⁴⁵ Typically, a liquid sample droplet is placed onto a solid silicon or glass substrate that has been modified with a plasmonic nanoparticle surface. As the sample undergoes evaporation, analyte molecules adhere to the surface, ensuring effective detection. After its initial utilization as a spectrochemical method, SERS has been applied in a wide range of measurement approaches within the fields of analytical and biological chemistry. SERS-based analytical approaches can be classified into two categories: label-mediated and label-free methodologies.⁴⁶ In labeled methods for analyte detection, the process involves an indirect

detection approach. This entails modifying a SERS-active molecule to act as a reporter, which is then attached to the capturing moiety.



Scheme 1.5: Applications of SERS modality in the different fields. Figure adapted from reference 42

The resulting SERS signal produced by the reporter molecule is used as a measure of the analyte, thereby enhancing the specificity of detection at the interface. This technique has been effectively utilized in SERS-based immunoassays, allowing for the identification of analytes in complex environments.⁴⁷ In contrast, direct label-free detection of analytes relies on the analyte itself possessing SERS activity, and the surrounding environment must be devoid of interfering molecules to maintain a high level of specificity. Additionally, it's important to note that the optical characteristics of the SERS substrate play a critical role in determining the sensitivity of detection (**Scheme 1.5**).^{48,49}

Maiti et al., reported a novel SERS nanoprobe, known as TPE-In-PSA@Au, alongside a specialized PSA (Prostate-Specific Antigen) peptide substrate tailored for detecting the

PSA protein.⁵⁰ This nanoprobe demonstrates effective identification of PSA enzymes within a SERS-based detection system, achieving an impressive low detection limit (LOD) of 0.5 ng. This significant advancement paves the way for new possibilities in prostate cancer diagnosis. Moreover, the TPE-In-PSA@Au nanoprobe exhibits exceptional specificity for PSA-overexpressing LNCaP cells, as confirmed by SERS spectral analysis and SERS mapping. Notably, this marks the first instance of a SERS nanoprobe designed to recognize elevated PSA levels in cancer cells, utilizing an innovative TPE analogue as the Raman reporter (**Figure 1.13**).

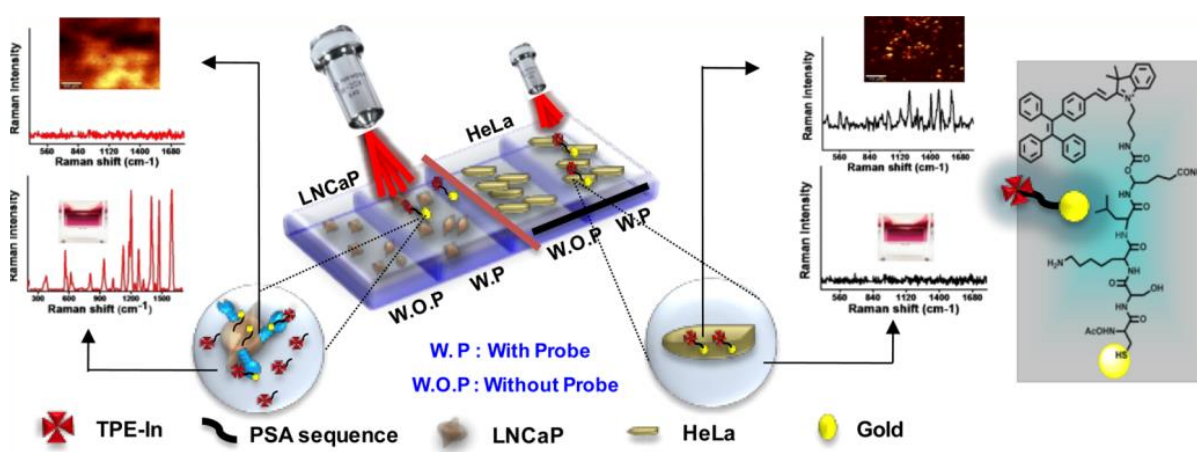


Figure 1.13: Schematic illustration of the working of PSA probe in SERS. Figure adapted from reference 50

Lee et al. have introduced an innovative method for hydrogen sulfide (H_2S) detection using paper substrates coated with silver nanoparticles (Ag NPIs) that function in both colorimetric and surface-enhanced Raman scattering (SERS) modes.⁵¹ This approach hinges on the interaction between H_2S gas and the Ag NPIs on the paper, resulting in the formation of brown-yellow Ag_2S compounds, leading to a visible colour change and a decrease in the SERS signal. This dual-mode Ag NPI-coated paper sensor demonstrates exceptional sensitivity, selectivity, reproducibility, and stability, maintaining its initial sensitivity for at least a month. Furthermore, the researchers successfully showcased the detection of endogenous H_2S in live prostate cancer cells (LNCaP) within a mere 8-hour incubation period. A crucial advantage of this method is its ability to detect H_2S immediately after cell seeding and substrate treatment, eliminating the need for additional time-consuming H_2S detection steps through simultaneous colorimetry and SERS. In another approach, Maiti et al., put forward a novel approach to revolutionizing the potential of fluorescence-SERS in developing multiplexing probes.⁵² This innovative strategy centers on creating nanoparticles capable of toggling between "on" and "off" states in both

fluorescence and SERS, creating fresh opportunities in biomarker identification. At its core, this nanosystem comprises gold nanospheres adorned with dual-responsive Raman-active fluorophores.

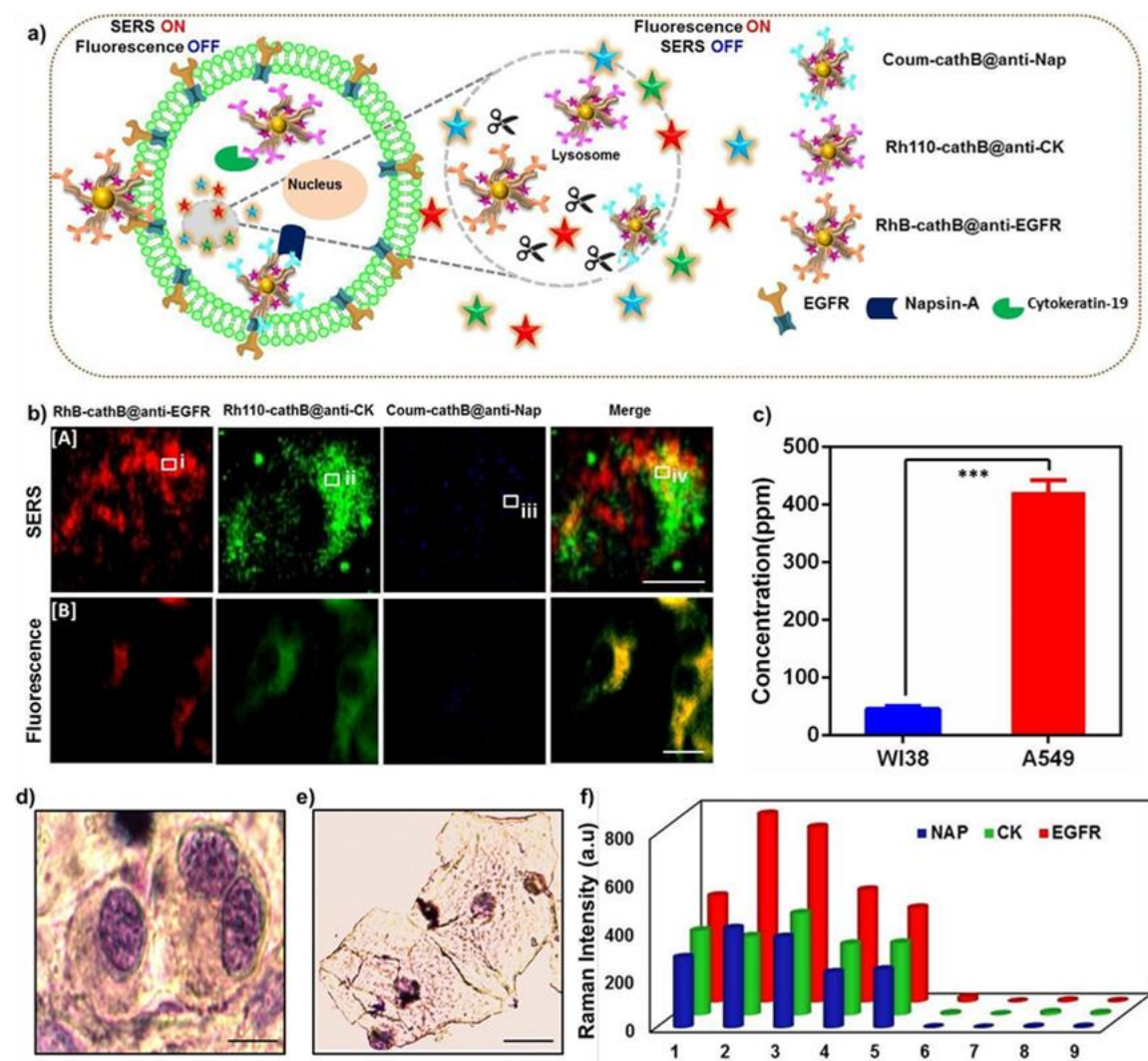


Figure 1.14: (a) The diagram illustrates how the cocktail probe is used for the multiplexed detection of biomarkers in lung cancer cells. (b) Confocal imaging was performed to analyze EGFR, CK, and Nap in A549 cells after they were treated probe. (c) ICPMS analysis measured gold content in A549 and WI38 cells. A representative microscopic image of a sputum specimen collected from (d) a cancer patient and (e) a normal healthy individual. (f) The levels of EGFR, CK, and Nap in sputum specimens were assessed using SERS analysis after treatment with the probe. Figure adapted from reference 52

These fluorophores are linked to the nanoparticle surface via a strategically placed peptide sequence, Phe-Lys-Cys (FKC). Significantly, FKC serves as a substrate for cathepsin B (cathB), a vital protease implicated in cancer progression. What distinguishes this system is the ingenious design of the tripeptide linker, which is enzymatically cleaved by cathB in the acidic pH of tumor sites. This pH-sensitive enzymatic cleavage triggers the activation of initially dormant fluorophores by disconnecting them from the nanoparticle surface,

increasing the gap between the fluorophores and the gold nanoparticle (AuNP) surface, effectively quenching SERS activity (**Figure 1.14**).

Camden and his research team have developed an innovative boronated nanoprobe that utilizes Surface-Enhanced Raman Spectroscopy (SERS).⁵³ This nanoprobe showcases remarkable quantitative, selective, and sensitive abilities when it comes to detecting H₂O₂ in a PBS environment. Importantly, it can distinguish H₂O₂ from other ROS and RNS. Moreover, this nanoprobe is highly biocompatible and has proven effective in detecting both externally introduced and naturally occurring H₂O₂ within living cells. This work represents a groundbreaking approach that offers biologists and pathologists a new method for tracking H₂O₂ involvement in cellular-level biological processes.⁵³

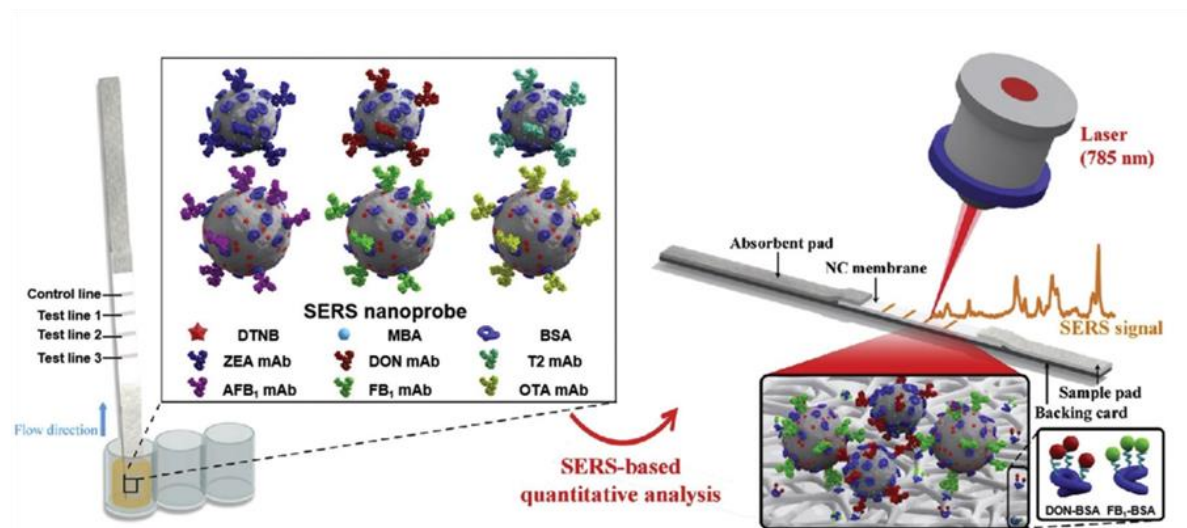


Figure 1.15: Schematic illustration of a lateral flow immunosensor for mycotoxins that utilizes multiplex SERS technology. Figure adapted from reference 54

Chen and colleagues introduced an innovative multiplex surface-enhanced Raman scattering (SERS)-based lateral flow immunosensor that effectively detects six major mycotoxins present in maize.⁵⁴ This immunosensor offers lower limits of detection (LODs) compared to instrumental analysis and most other biosensors, and all these LODs are well below the tolerable limits established by the European Union (EU), United States (USA), and China. Furthermore, this immunosensor has exhibited commendable accuracy, precision, and specificity in its assays, and it can provide results in less than 20 minutes. Consequently, it can be employed for the swift monitoring of common mycotoxins in maize samples. Moreover, the incorporation of dual Raman labels and three test lines significantly enhances the multiplexing capability of the current immunoassay format (**Figure 1.15**).

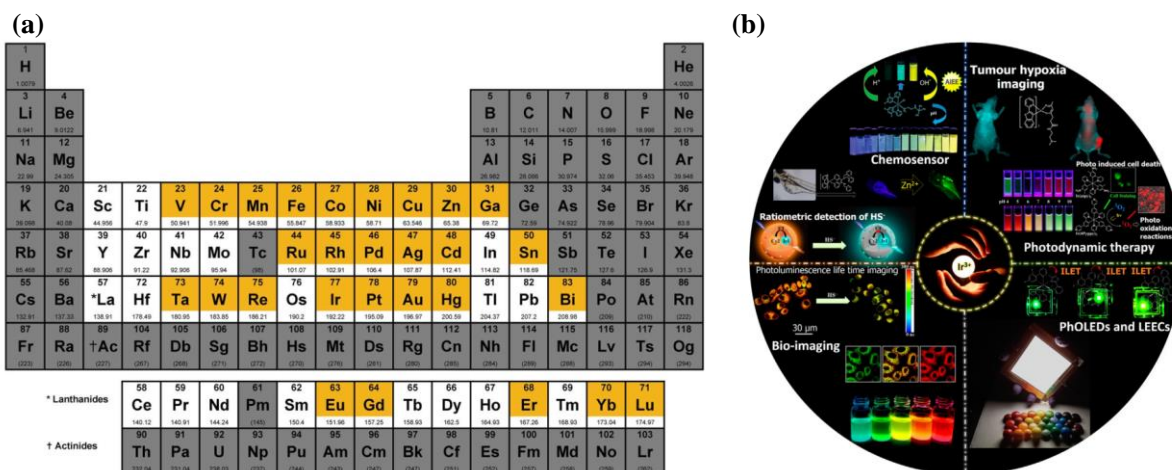
1.4 Transition Metal complexes for biological applications

The clinical success achieved with cisplatin has sparked significant research into exploring novel metal complexes as potential therapeutic agents for a diverse array of diseases. One illustrative instance involves the advancement of gold complexes, which have demonstrated promise in the treatment of rheumatoid arthritis. Similarly, silver complexes have been scrutinized for their antimicrobial properties, presenting potential solutions for combatting infectious diseases. Antimony complexes have emerged as valuable contenders for addressing conditions such as leishmaniasis, while vanadium (IV) complexes have exhibited dual roles as antiviral and antidiabetic agents. Notably, arsenic trioxide, marketed as Trisenox, has proven efficacious in the management of acute promyelocytic leukemia. Metal-activated bleomycin has been harnessed in the therapeutic strategy against Hodgkin's lymphoma and testicular cancer. Ongoing clinical trials have ushered in a new generation of transition-metal-based therapeutic agents, including liposomal cisplatin (Lipoplatin), satraplatin, and picoplatin, constituting third-generation antitumor platinum complexes. Furthermore, ruthenium complexes such as NAMI-A and KP-1019 demonstrate potent antitumor properties, while the ferrocene–quinoline conjugate ferroquine exhibits promise as an antimalarial agent. These instances underscore the extensive history and potential of therapeutic metal complexes, instilling optimism for the continued dynamic development of the field of inorganic medicine in the future.⁵⁵

Heavy-metal complexes exhibit distinctive photophysical properties that set them apart from organic fluorophores. These properties are characterized by complex excited states, often influenced by various charge-transfer reactions. The primary charge-transfer reactions involved in luminescent metal complexes include metal-to-ligand charge transfer (MLCT), ligand-to-metal charge transfer (LMCT), and intra-ligand charge transfer (ILCT). Additionally, less common electronic transitions can occur, such as ligand-to-ligand charge transfer (LLCT), metal-metal-to-ligand charge transfer (MMLCT), and metal-to-ligand-ligand charge transfer (MLLCT) (**Scheme 1.6**). The emission behavior of metal complexes is strongly dependent on factors like the central metal atom, ancillary ligands, and the local environment in which they are situated. Of particular interest are d^6 , d^8 , and d^{10} complexes, which have captured significant attention due to their unique photophysical properties.^{56,57}

These complexes are known for their strong spin–orbit coupling between singlet and triplet spin states, which results from the heavy atom effect. This strong spin–orbit coupling facilitates the intersystem crossing of excited electrons from the $^1\text{MLCT}$ state to the $^3\text{MLCT}$

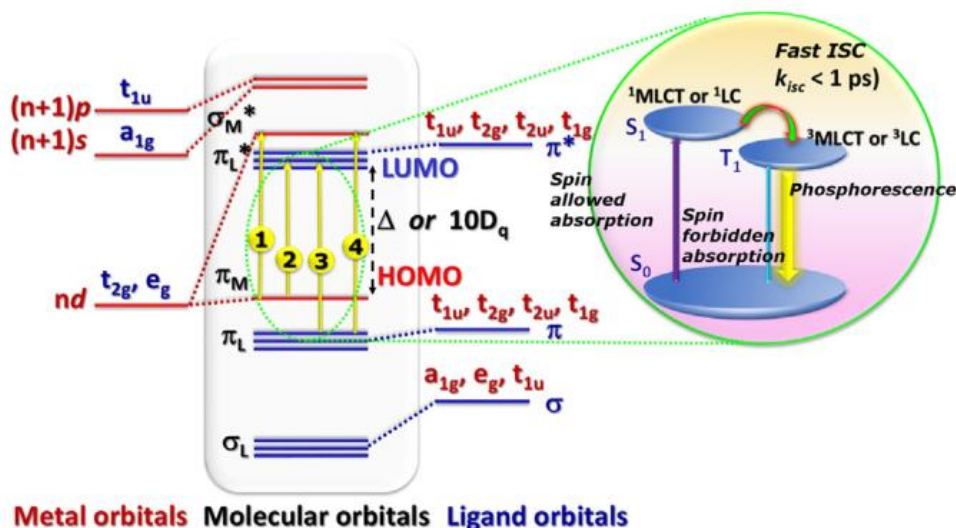
state. The relaxation of the $^3\text{MLCT}$ excited state leads to the generation of a strong and long-lived phosphorescence emission. This characteristic makes them valuable for applications in biological imaging (Scheme 1.7).^{58,59}



Scheme 1.6: Major transition metal used prepared metal complexes for bio-applications and Schematic representation of various applications of Ir complexes. Figure adapted from reference 58 and 59

However, it's important to note that the $^3\text{MLCT}$ excited state can be influenced by nonradiative processes, where the energy of the excited state is dissipated as heat rather than light due to small energy differences between energy levels. This phenomenon provides an opportunity to design metal complexes selectively tailored to interact with specific biomolecules.⁵⁸ These interactions can be detected and studied through the unique photophysical properties of these complexes. Therefore, metal complexes can serve as both selective probes and inhibitors for biological targets, offering valuable insights into various biological processes. In recent years, the realm of bio-applications has undergone a profound transformation, propelled by the remarkable strides made in harnessing the potential of iridium complexes. These complexes have emerged as frontrunners among transition metal complexes, boasting unique properties and unparalleled versatility that set them apart from their peers. This notable advancement has ushered in a new era of innovation, particularly in critical domains such as bioimaging, drug delivery, and catalysis, offering unprecedented opportunities to enhance the precision and efficacy of cutting-edge technologies and therapies. Iridium complexes have truly become the stars of the show in the world of bio-applications.⁵⁹ Their distinct attributes, which include exceptional stability and reactivity, make them stand out in a crowded field. Unlike many other transition metal complexes, iridium complexes exhibit remarkable resilience under physiological conditions, rendering them highly compatible with biological systems. This compatibility

is a game-changer in drug delivery, as these complexes can serve as efficient carriers, ensuring therapeutic molecules reach their intended targets with minimal side effects. Furthermore, the luminescent properties of iridium complexes have revolutionized bioimaging techniques.



Scheme 1.7: Diagram showing the various major transitions shown by the metal complexes. Figure adapted from reference 59

Their ability to emit light in a controlled and predictable manner has opened up exciting possibilities for real-time monitoring of biological processes. This precision is invaluable in tracking the progression of diseases and evaluating the effectiveness of treatments, ultimately leading to more tailored and effective healthcare interventions. In the field of catalysis, iridium complexes have demonstrated unparalleled catalytic activity, enabling the development of novel and efficient processes for the synthesis of pharmaceuticals and other bioactive compounds.⁵⁵ Their ability to facilitate complex chemical reactions with precision has streamlined the production of essential drugs and reduced the environmental footprint of chemical processes, aligning with the growing emphasis on sustainability in the pharmaceutical industry.⁵⁷

1.4.1 Imaging applications of Iridium complexes

Iridium(III) cyclometallates have emerged as promising and versatile phosphorescent materials in the field of bioimaging. These organometallic compounds have gained increasing preference over traditional organic molecules due to their unique ability to meet stringent criteria for bioimaging applications. One of their standout features is the exceptional quantum yield, which can reach an impressive 100%, significantly surpassing the typical maximum of 25% observed in small fluorophores (Figure 1.16).

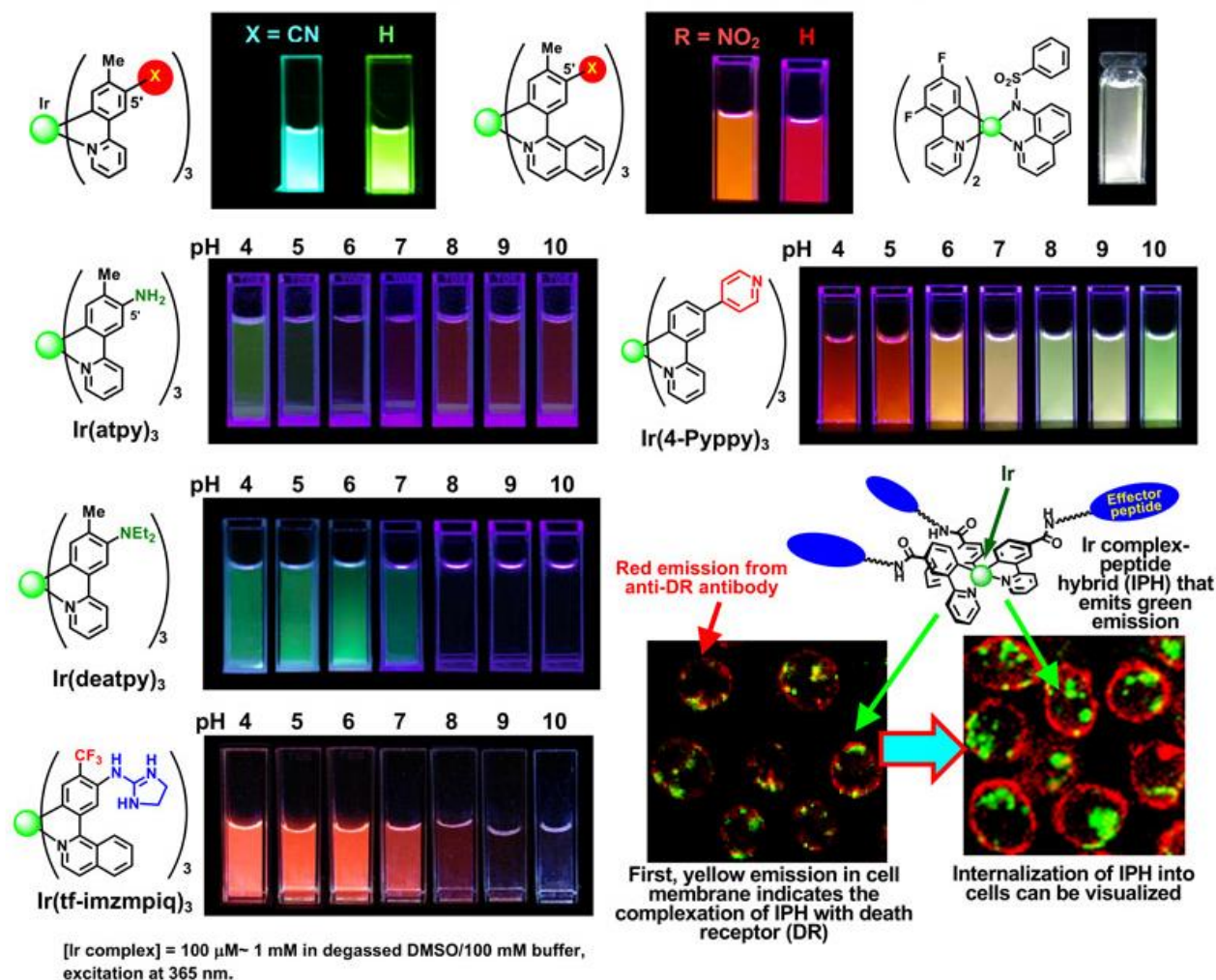


Figure 1.16: Different kinds of cyclometallated iridium complexes sensing and imaging applications. Figure adapted from reference 60

This remarkable efficiency is attributed to their distinctive properties, including spin-orbit coupling and high-triplet excitation processes. The spin-orbit coupling of Ir(III) cores plays a pivotal role in facilitating efficient transitions from singlet to triplet excited states, outperforming other metals like ruthenium(II). Thanks to its d^6 electron configuration, Ir(III) can form complexes with a wide range of ligands, leading to various excited states such as MLCT, LLCT, and LCT phenomena.⁶⁰ These complexes offer multiple excitation pathways, driven by the presence of delocalized HOMO and localized LUMO orbitals. Furthermore, the quantum efficiency of phosphorescent Ir(III) complexes can be finely tuned through ligand control strategies, while factors like size, charge, and hydrophobicity/hydrophilicity influence their cellular uptake. Enhanced cellular uptake has been observed in cationic complexes, improving their imaging efficacy.

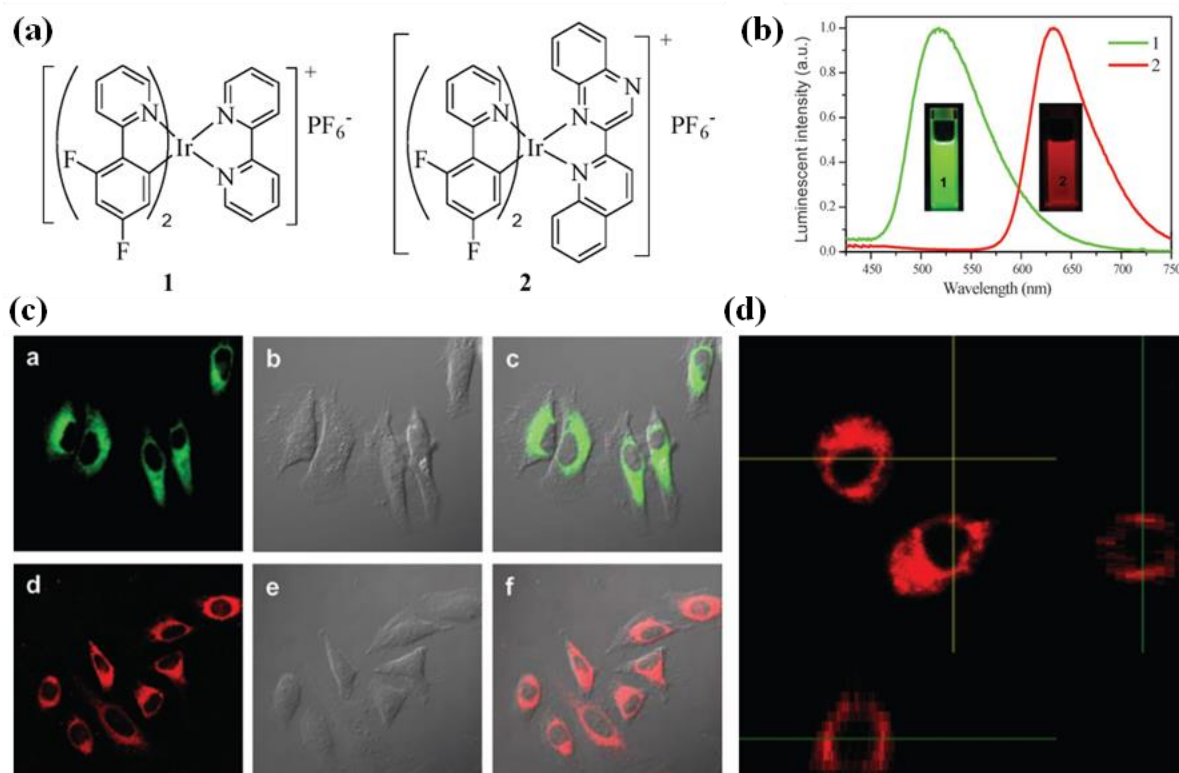


Figure 1.17: (a) The structure of probe 1 and probe 2. (b) Fluorescence spectra of probe 1 and probe 2. (c&d) The intracellular luminescence imaging with probe 1 and probe 2 along with the line diagram. Figure adapted from reference 62

Dendritic polypyridine Ir(III) complexes exhibit distinct cellular uptake patterns compared to monomeric counterparts. Adjusting the lipophilicity of Ir(III) complexes can also enhance cellular uptake without compromising efficiency. Moreover, various synthetic strategies have been developed to achieve organelle-specific staining, making Ir(III) bioimaging an exciting and promising avenue in bioscience applications.⁶¹

In 2008, Li *et al.*, introduced the initial instances of cyclometalated iridium (III) probes designed for staining the cytoplasm within living cells.⁶² These probes, denoted as complexes 1 and 2, shared a common fluorinated phenylpyridine component but differed in their diimine ligands. The positively charged nature and the incorporation of fluorine atoms into the cyclometalated ligands were identified as crucial factors influencing the ability of these probes to enter cells, impacting their lipophilicity and aqueous solubility. When live HeLa cells were exposed to complexes 1 and 2 at a concentration of 20 μ M for 10 minutes, the resulting confocal images displayed robust intracellular luminescence. This luminescence exhibited a high signal-to-noise ratio, clearly distinguishing between the cytoplasmic signal (Ic) and the background signal (Ib), with a remarkable Ic/Ib ratio exceeding 50. Furthermore, the impact of these two complexes on the proliferation of MCF-7 and HCT-8 cell lines was assessed through an MTT assay over a 24-hour incubation

period. The results indicated that cellular viability remained above 90% even at the highest tested concentration of 100 μM (Figure 1.17).

Lan *et al.*, conducted a study where they observed the imaging of nucleoli in live cells using a set of iridium(III) complexes with dipyridoquinoxaline ligand. They discovered that modifying the structural makeup of the cyclometalated ligands and adding a longer chain to the ligand component could influence the complexes ability to dissolve in fats (lipophilicity) and their toxicity to cells.⁶³

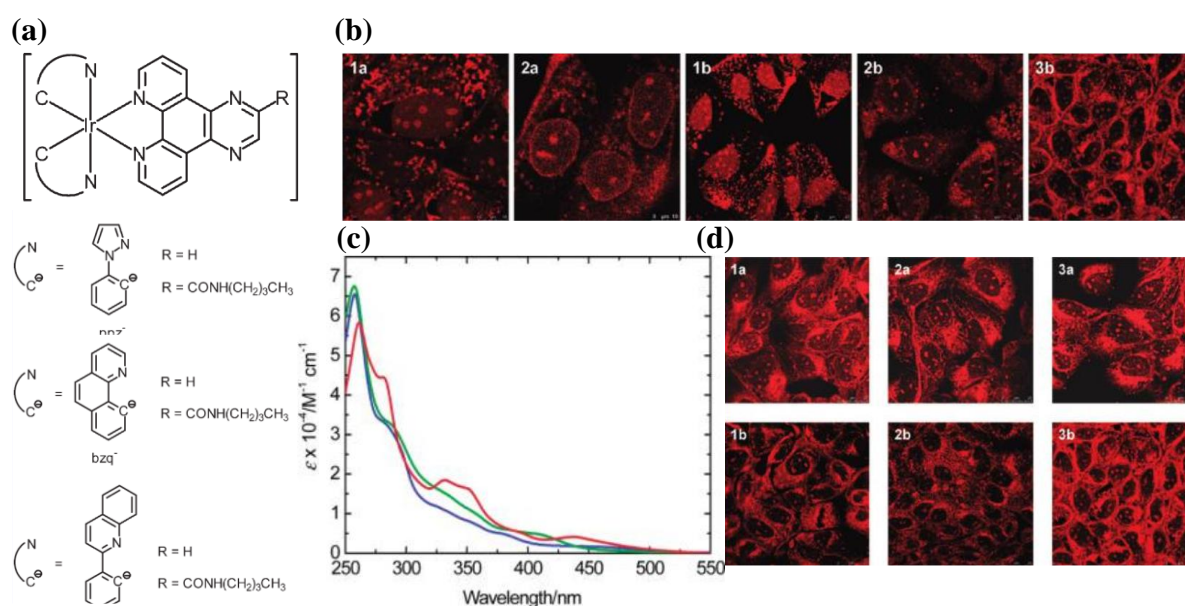


Figure 1.18: (a) The structure of the iridium molecular probe 1. (b) Fluorescence images of intracellular localization of the probe through fluorescence imaging. (c) Absorption spectra of the iridium complexes with different ligands. (d) Fluorescence laser-scanning confocal microscopy images of MDCK cells that were fixed and exposed to iridium(III) dpq and dpqa complexes. Adapted from reference 63

When the ligands had increased conjugation, they exhibited higher $\log P_{o/w}$ values, with $\text{bzq} > \text{pq} > \text{ppy}$ being the order, indicating enhanced lipophilicity. Furthermore, attaching an alkyl chain, especially a *n*-butyl one, to the two phenyl rings of the cyclometalated ligands also boosted their lipophilicity. All of these complexes demonstrated lower IC_{50} values against HeLa and MDCK cell lines compared to cisplatin, underscoring their significant cytotoxicity, especially for the more lipophilic variants. Their research in MDCK cells revealed that these complexes initially gathered in the cell nucleus after 90 minutes of incubation and then specifically accumulated in the nucleolus after 120 minutes. Importantly, they determined that these complexes bound to hydrophobic regions of proteins and intercalated with DNA (Figure 1.18).

Williams's group conducted a study involving two cyclometalated iridium(III) complexes, namely 1 and its protonated counterpart 2, both containing a 2-pyridylbenzimidazole ligand. Photophysical analysis in a dichloromethane solution revealed distinct emission profiles: 1 exhibited structured green emission, while 2 displayed an expected redshift with emission centered at 590 nm. Surprisingly, when these probes were incubated with CHO cells at a concentration of 10 mM for 5 minutes, their emission profiles were nearly indistinguishable.⁶⁴

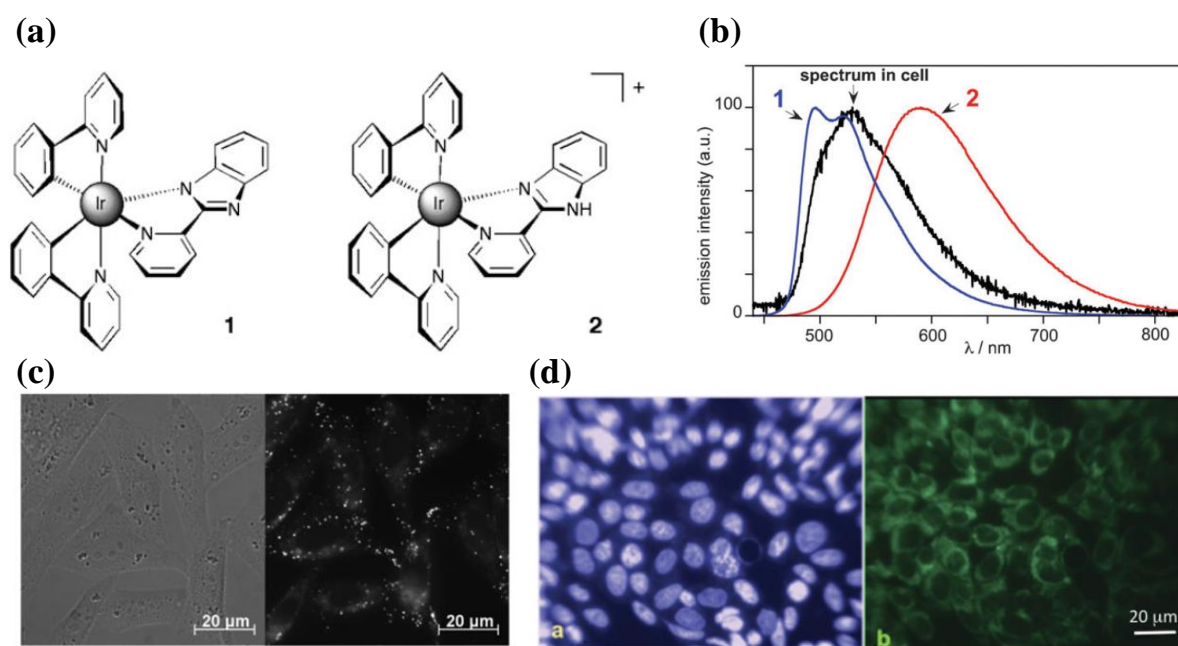


Figure 1.19: (a) The structure of the molecular complex 1 and 2. (b) Fluorescence spectra of the complex 1 and 2. (c) Bright field and fluorescence images of CHO cells incubated with complex 1. (d) Fluorescence microscopy images of live CHO cells co-stained with 1 (10 mM, 1 h incubation) and Hoechst. Figure adapted from reference 64

This phenomenon can be attributed to the protonation equilibrium between the two complexes, which is dependent on the local pH. In cellular environments typically maintained around pH 7.4, 1 predominates. However, a shift occurs in acidic lysosomes, favoring the formation of the cationic complex 2 (Figure 1.19). Importantly, these probes exhibited minimal cytotoxicity, as evidenced by IC_{50} values exceeding 200 μ M (measured after 24 hours of incubation) for both of them. Iridium complexes used for staining mitochondria often exhibit a predominantly positive charge, with only a few instances where neutral species are specifically designed for labelling mitochondria. This positive charge plays a pivotal role in promoting the localization of these complexes within mitochondria due to its strong affinity for the electrical potential of the mitochondrial

membrane. This attribute makes the positive charge an exceptionally effective factor to take into account when considering mitochondrial staining techniques.

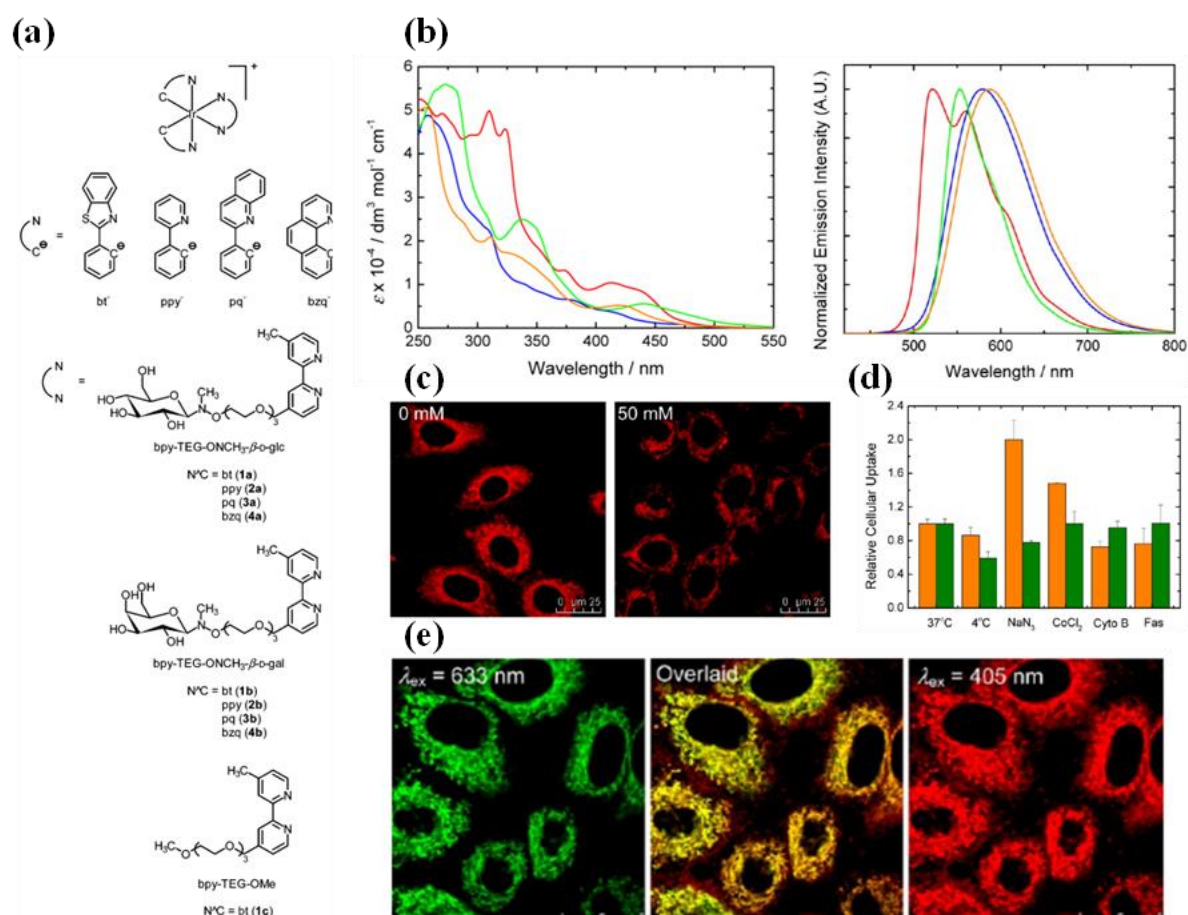


Figure 1.20: (a) The chemical structure of the reported iridium complexes. (b) Absorption and fluorescence spectra of all 4 complexes. (c) The confocal imaging of cells with and without glucose. (d) Relative cellular uptake of the complex at various conditions. (e) Colocalization of the complex with MTG dye. Figure adapted from reference 65

In another interesting study, Lo and group proposed a series of bioconjugate iridium (III) complexes, enhancing them with either a D-glucose or a D-galactose unit through a polyethylene glycol linker attached to the diimine ligand.⁶⁵ Furthermore, they altered the degree of pi conjugation on the cyclometalated ligands. The primary objective of this study was to boost the specific cellular uptake of these sugar-modified probes in cancer cells. Cancer cells often exhibit increased expression of glucose transporters (GLUTs) and hexokinases, which support their higher metabolic demands. The investigation also assessed the lipophilicity of these complexes, with a significant focus on the impact of the cyclometalated ligands nature. Remarkably, groups 1 and 2 complexes displayed comparable lipophilicity values when utilizing the same cyclometalated ligands. Overall, the lipophilic attributes of complexes 1(a-d) and 2(a-d) were slightly lower than those of

complex 3, underscoring the influence of the polar carbohydrate groups incorporated into these bioconjugates. Additionally, both complex 1a and 2a were observed to localize within the mitochondria of cells through an energy-dependent pathway. However, it's worth noting that only complex 1a demonstrated the ability to enter cells using a GLUT-mediated mechanism. This novel approach holds promise for developing more effective cancer treatments by exploiting the enhanced uptake of these bioconjugate iridium(III) complexes in cancer cells due to their sugar-appended design (**Figure 1.20**).

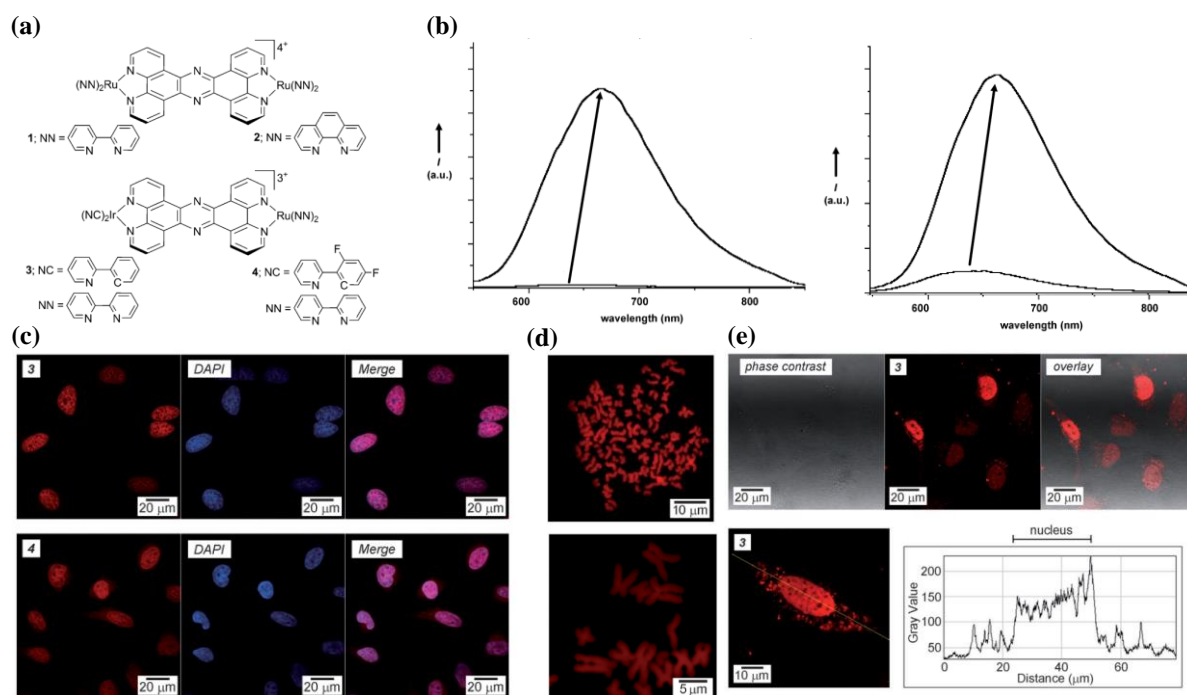


Figure 1.21: (a) The structure of the iridium and ruthenium complexes with ligands. (b) Fluorescence changes associated with the interaction of DNA with Ir and Ru complex (c) Colocalization of the molecule with DAPI. (d) The isolated chromosomes labelled with metal complex 3. (e) Live HeLa cells treated with 3. Adapted from reference 66

Thomas and Smythe introduced two novel iridium(III)–ruthenium(II) complexes, labelled as 3 and 4, which feature a tetrapyrrophenazine unit as a connecting ligand.⁶⁶ These complexes exhibit favourable water solubility, a characteristic often challenging to achieve in many cyclometalated systems. Notably, both 3 and 4 emit red light (around 640 nm) without a distinct structure and possess a low quantum yield (less than 0.02%). However, their luminescence efficiency increases significantly, approximately 10-fold for 3 and 24-fold for 4, when they come into contact with DNA. It is worth mentioning that complex 4 exhibits weaker binding to DNA compared to its non-fluorinated counterpart, 3. This reduced affinity for DNA is attributed to the higher polarity of 4. Nevertheless, the increased lipophilicity of complex 4 enhances its cellular uptake without compromising its ability to localize within the cell nucleus.

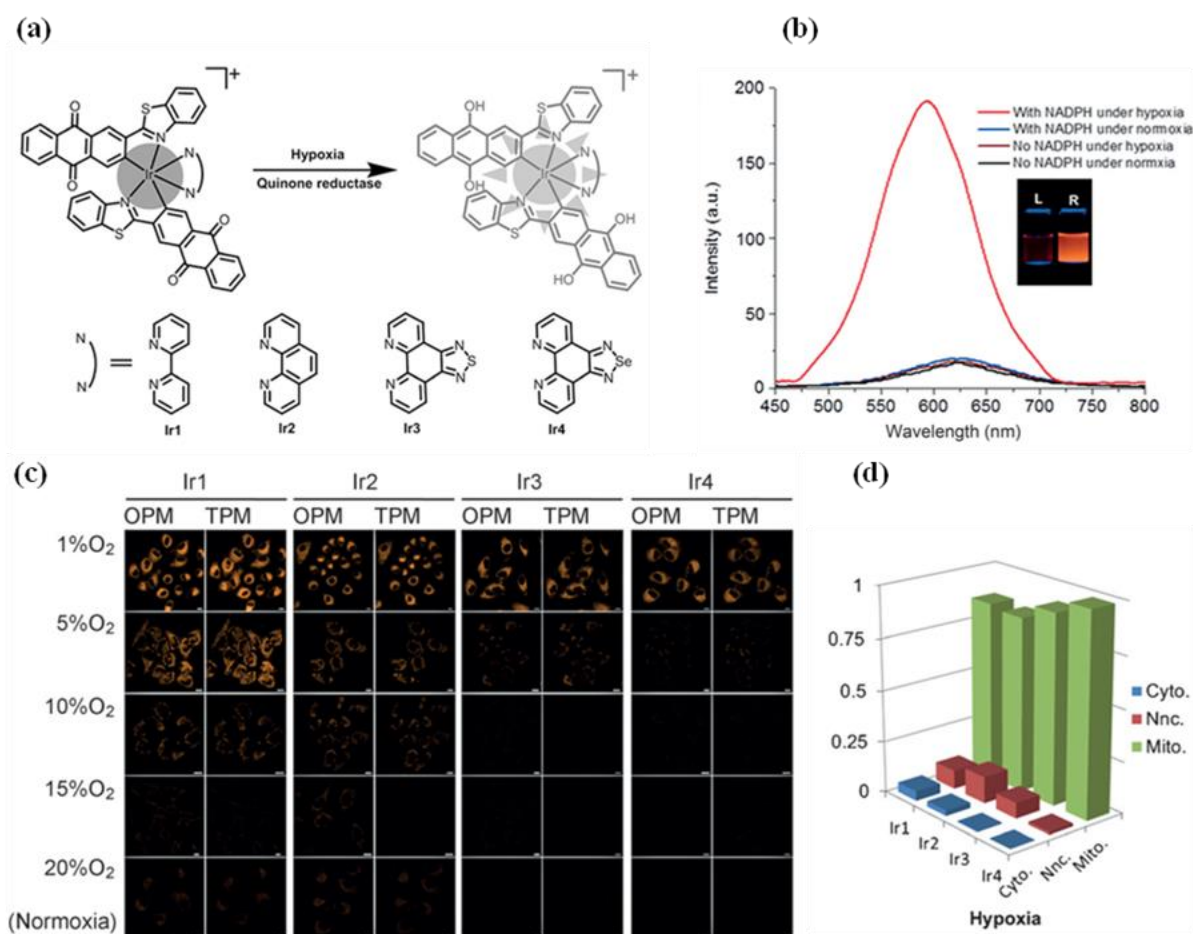


Figure 1.22: (a) The structure and hypoxia reductase sensing mechanism of the Ir-complex. (b) Fluorescence turn-on of complex under hypoxic condition in solution state. (c) The intracellular oxygen-based imaging to confirm the hypoxic activity of the complex. (d) The quantification of sub-cellular distribution of the complex. Figure adapted from reference 67

The Chao research group has developed a series of innovative iridium (III) anthraquinone complexes, designated as Ir1 through Ir4, with a primary focus on advancing hypoxia detection using a novel two-photon absorption mechanism.⁶⁷ These complexes incorporate an anthraquinone component designed to efficiently quench iridium emission (**Figure 1.21**). However, when exposed to hypoxic conditions, this component undergoes a transformation into an active hydroquinone state, leading to the generation of a detectable light signal by the probes. When introduced into A549 cells, these complexes can be reduced by the enzyme nicotinamide adenine reductase phosphate (NAD(P)H) in conjunction with cellular reductase enzymes. Under hypoxic conditions, the emission intensity of Ir1-Ir4 complexes within A549 cells increases significantly, by 11 to 19-fold, due to enzymatic reactions with NAD(P)H, and remains unaffected by other biological reducing agents. Furthermore, these probes display varying sensitivity to oxygen levels. Ir1 shows increased phosphorescence even at oxygen concentrations as high as 5%, while Ir2-Ir4 exhibits enhanced

phosphorescence at oxygen levels of 1% or lower. Importantly, these probes localize within the mitochondria of A549 cells and exhibit minimal cytotoxicity, ensuring cell viability exceeds 80% under both normal oxygen conditions and hypoxia after a 12-hour incubation period at a concentration of 10 μM . This research by the Chao group promises advancements in hypoxia detection and highlights the potential applications of these anthraquinone complexes in cellular imaging and oxygen sensing (**Figure 1.22**).

The photophysical properties of cyclometalated iridium(III) complexes have been known for a long time, but their applications in biology have gained significant attention over the last decade. These complexes have unique characteristics, such as their cationic and lipophilic nature, which facilitate cellular uptake. This has made them valuable in cellular imaging and as intracellular sensors. The formal charge of these complexes is an important factor to consider. While a higher cationic charge improves water solubility, excessively high cationic charges can limit cellular uptake efficiency. Therefore, careful consideration is required when designing these complexes for specific applications. Despite their advantages, iridium(III) complexes have limitations, including the high cost of the metal and potential toxicity. Researchers must take into account factors like organelle disruption after uptake and long-term effects when developing iridium(III) complexes for bio probes and biomedicine. However, by choosing the right ligands, functional pendants, and spacer-arms with different properties, it's possible to adjust the intracellular localization properties of these complexes to meet specific needs.^{68,69}

1.4.2 Theranostic applications of Iridium complexes

Theranostics is an exciting frontier in medicine, seamlessly merging diagnostics and therapeutics to provide a holistic approach. It goes beyond conventional disease identification, offering profound insights into a patient's molecular profile. This knowledge empowers healthcare professionals to design precise treatment strategies, optimizing outcomes while minimizing side effects.¹¹ In the era of precision medicine, theranostics holds immense potential to revolutionize disease diagnosis and treatment across various medical conditions, from cancer to neurological disorders. It signifies a shift towards personalized medicine, where interventions are customized to individual needs. Diagnostic tools in theranostics delve into a patient's molecular composition, unravelling genetic, proteomic, and metabolic intricacies. This molecular information enables tailored therapies, as seen in oncology, where specific genetic mutations can guide targeted treatments, avoiding futile and side-effect-laden approaches. Additionally, theranostics can

streamline treatment, making it more efficient and cost-effective by predicting individual responses.⁷⁰ In essence, theranostics embodies personalized medicine's essence, using advanced diagnostics to enhance efficacy, minimize side effects, and improve overall outcomes, offering hope for a future where diseases are not just treated but comprehensively understood and conquered. The convergence of diagnosis and treatment marks a significant advancement in the fight against cancer. Phototherapies, specifically Photothermal Therapy (PTT) and Photodynamic Therapy (PDT), represent a critical component of the field of cancer theranostics when integrated with diagnostic techniques. The amalgamation of these two modalities forms the basis for the development of theranostic molecular probes, epitomizing the pinnacle of personalized medicine. These probes have the remarkable ability to selectively accumulate in tumor sites, affording targeted diagnostics and treatment in one unified agent, all while sparing healthy surrounding tissues. The synergy between PTT and PDT has ushered in a new era in oncological interventions, fundamentally transforming the landscape of cancer care by providing tailored precision and renewed optimism for patients in their battle against this devastating disease.^{71,72}

1.5 Harnessing Light to Heat: Photodynamic Effect as Innovative Approaches in Cancer Treatment

In the quest for more precise and potent cancer treatments, the medical field has harnessed light's potential to combat this formidable foe. Phototherapy, encompassing Photo Thermal Therapy (PTT) and Photo Dynamic Therapy (PDT), has emerged as a groundbreaking approach, holding the promise of transforming cancer treatment. By exploiting light's unique properties, phototherapy offers targeted interventions that can eliminate cancer cells while sparing healthy tissue. In the complex world of oncology, phototherapy stands out as a beacon of hope, illuminating a path toward more effective and less invasive treatment options.^{73,74} At the core of phototherapy is its ability to utilize the interactions between light and matter, particularly cancer cells. This innovative approach bridges physics and biology, showcasing their interconnectedness in medical advancement. By utilizing specific light wavelengths, phototherapy capitalizes on cancer cells intrinsic vulnerabilities, effectively destroying them while leaving normal cells intact. One facet of phototherapy, Photo Thermal Therapy (PTT), utilizes light-induced heat to obliterate cancer cells. This method relies on nanoparticles that absorb light and convert it into heat. These nanoparticles accumulate in tumors and, when exposed to laser light, generate localized heat that eradicates cancer cells.^{75,76} Complementing Photothermal therapy is Photo Dynamic

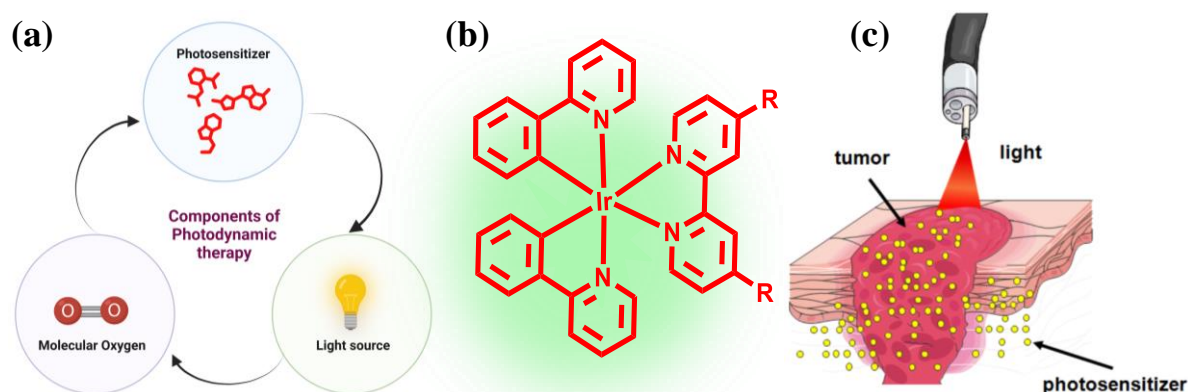
Therapy (PDT), which relies on the interaction between light, a photosensitizing agent, and oxygen. The photosensitizer is administered and accumulates in cancer cells. When exposed to specific light wavelengths, the photosensitizer activates, producing reactive oxygen species. These species cause irreversible damage to cancer cells membranes and vasculature, leading to their demise. What differentiates phototherapy from traditional cancer treatments is its precision, reducing the indiscriminate harm associated with chemotherapy and radiation. Tailoring treatment to the tumor's location minimizes side effects and enhances efficacy. By sparing healthy tissue, phototherapy reduces the debilitating consequences often linked to conventional therapies, thereby improving patients' quality of life during and after treatment. However, the rise of phototherapy presents challenges. Successful implementation requires careful selection of photosensitizers and optimal light parameters. The intricate interplay between the physical and biological aspects underscores the need for collaboration among physicists, chemists, biologists, and clinicians.^{77,78}

1.5.1 Photodynamic Therapy

Photodynamic Therapy (PDT), a groundbreaking medical technique, owes its origins to a remarkable phenomenon called the photodynamic effect. This phenomenon was first observed at the turn of the 20th century, ushering in a transformative era in healthcare. The photodynamic effect made its debut when paramecia, minuscule single-celled organisms, were exposed to acridine and then bathed in gentle light. To the astonishment of scientists, these organisms met their demise in the presence of light, whereas they thrived in darkness. In its purest form, the photodynamic effect can be described as the "harm or destruction of living tissue caused by visible light in the presence of a photosensitizer and oxygen." It is from this captivating phenomenon that the foundation of PDT was established. Photodynamic therapy, therefore, stands as a cleverly devised therapeutic approach, hinging on the utilization of this intriguing effect.^{79,80} PDT's potential knows no bounds, offering a versatile tool for eradicating a wide range of undesirable targets in the field of biology, including eukaryotic cells, prokaryotic cells, and even the troublesome culprits behind viral infections.

PDT operates at the intersection of quantum mechanics and light energy, providing a potent tool for biomedical applications. It begins with visible light in the wavelength range of 400 to 800 nm, where light energy is inversely proportional to wavelength, as described by the equation $E = hv$. This equation tells us that each unit of energy (hv) corresponds to a specific

wavelength, and when light is absorbed, it initiates a series of processes influenced by quantum mechanics. Central to PDT are the concepts of singlet and triplet states (S and T), which are determined by electron spin. Singlet excited states (S1) have short lifetimes in the nanosecond range, while triplet states (T1) have longer lifetimes ranging from microseconds to milliseconds. The critical photochemical and photo-oxidative reactions in PDT are primarily driven by these triplet states (T1) (Scheme 1.8).⁸¹



Scheme 1.8: Schematic representation (a) important requirements of PDT. (b) Structure of bipyridine conjugated Ir-complex. (c) Pictorial representation of PDT

In PDT, molecules in these excited states can trigger various processes, including photochemistry, crossing over to triplet states (T1), generating heat through non-radiative decay, or emitting fluorescence. Triplet states (T1) play a key role by directly initiating photochemical reactions, leading to the generation of reactive radicals or transferring energy to ground-state oxygen molecules ($^3\text{O}_2$), resulting in the creation of singlet oxygen molecules ($^1\text{O}_2$). It's important to note that producing singlet oxygen requires a minimum energy threshold of 20 kcal/mole, limiting the longest absorption wavelength of the photosensitizer (PS). However, other mechanisms may also be involved. Triplet states (T1) can return to the ground state (S0) through radiation-less decay or phosphorescence in specific cases. Multiphoton absorption can also populate higher excited states in certain situations, introducing complex photophysical and photochemical processes that affect phototoxicity. Within PDT, there are two primary categories: Type I and Type II PDT. Type I PDT relies on the direct interaction of the photosensitizer's excited triplet state (T1) with biomolecules, leading to the formation of reactive oxygen species (ROS) and subsequent destruction of target cells. On the other hand, Type II PDT involves transferring energy

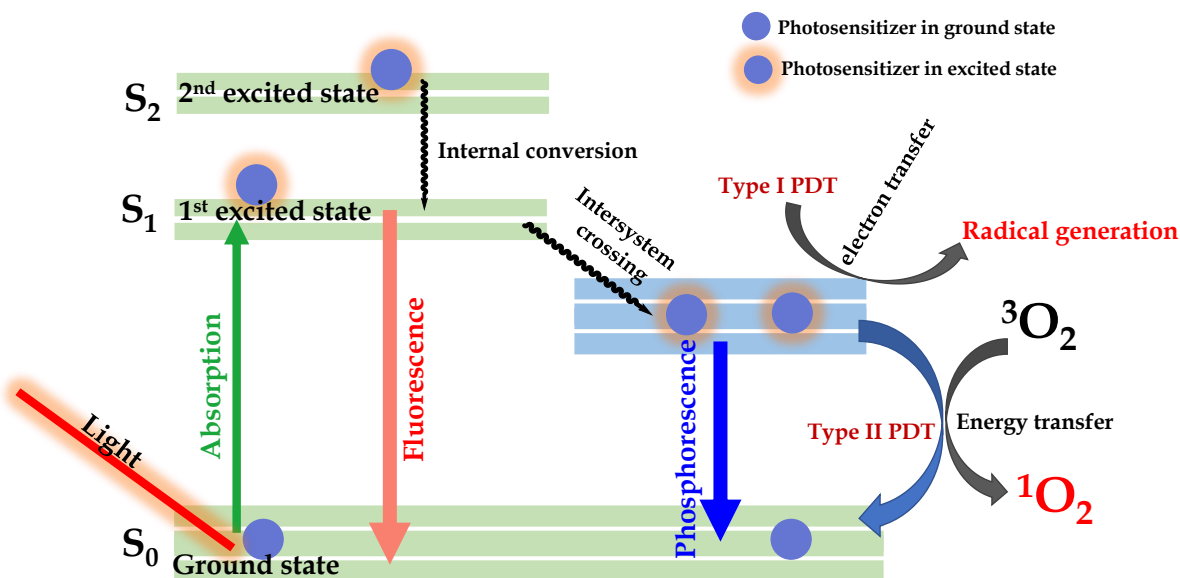
from the photosensitizer's triplet state (T1) to molecular oxygen ($^3\text{O}_2$), creating highly toxic singlet oxygen molecules ($^1\text{O}_2$) responsible for cellular damage (Scheme 1.9).⁸²

PDT primarily consists of three essential components: the Photosensitizer (PS), a light source, and molecular oxygen. At the core of PDT lies the photosensitizing agent, a critical element. This chemical compound possesses the unique ability to absorb light of a specific wavelength. When exposed to light of the appropriate wavelength, this photosensitizing agent becomes activated, leading to the generation of reactive oxygen species (ROS), including singlet oxygen. These ROS play a pivotal role in causing damage to nearby cells, ultimately leading to their destruction. Among the commonly employed photosensitizing agents in PDT are porphyrins, chlorins, and phthalocyanines. The second key component is the light source, which serves to activate the photosensitizing agent effectively. The light source emits light at a specific wavelength corresponding to the absorption peak of the photosensitizer. Common options for light sources in PDT encompass lasers, light-emitting diodes (LEDs), and specialized lamps. The selection of the appropriate light source depends on factors such as the type and location of the target tissue. Finally, molecular oxygen stands as an indispensable component in PDT. It plays a pivotal role in the production of ROS, which are responsible for the cytotoxic effects of PDT. Oxygen serves as a crucial substrate for the formation of these reactive oxygen species. Hence, maintaining adequate oxygen levels in the target tissue is of paramount importance for the successful outcome of PDT.^{83,84}

1.5.2 Shining Light on Photodynamic Therapy: The Power of Photosensitizers

Photosensitizers are remarkable substances with the unique ability to absorb specific wavelengths of light and convert them into harmful reactive species, including singlet oxygen and other radicals. These versatile compounds have found valuable applications in various biological treatments. The ideal photosensitizer possesses a combination of crucial attributes: strong light absorption, exceptional photochemical reactivity, low toxicity in the absence of light, high toxicity upon light exposure, and effective cell permeability. Among the common molecular photosensitizers, we find a diverse array, including organic dyes including porphyrins, chlorins, phthalocyanines, and transition metal complexes. Porphyrins, particularly Hematoporphyrin (Hp), stand out as promising candidates due to their ability to meet many of these essential criteria for effective photosensitization. In fact, Hp holds the distinction of being the first porphyrin employed in photodynamic therapy (PDT). Further advancements in this field have led to the development of a more potent

photosensitizer known as Photofrin II®. This modified Hp has proven effective in the treatment of various conditions, including cancer, underscoring the potential of photosensitizers in medical applications. Beyond Hp and its derivatives, the biomedical realm has witnessed the emergence of a diverse range of photosensitizers, both porphyrin-like and non-porphyrin-like. These innovative compounds continue to expand the horizons of photodynamic therapy and other biomedical treatments, offering new avenues for combating diseases and improving healthcare outcomes.^{84,85}



Scheme 1.9: Schematic representation of Jablonsky diagram of PDT showing Type I and Type II PDT

Organic photosensitizers have garnered substantial attention within the realm of photodynamic therapy, yet it is imperative to acknowledge the inherent constraints and disadvantages associated with their utilization. A prominent limitation pertains to their susceptibility to photobleaching, wherein extended exposure to light leads to the degradation of their photoactive characteristics, thereby constraining their long-term stability and therapeutic efficacy. Furthermore, the synthesis of organic photosensitizers can entail intricate and costly procedures, impeding their widespread adoption. Additionally, their absorption spectra may exhibit limitations, being confined to specific wavelengths, thereby diminishing their versatility. Moreover, in comparison to their inorganic counterparts, organic photosensitizers may manifest lower quantum yields and shorter excited-state lifetimes, consequently impacting their overall photodynamic efficiency. Finally, their biocompatibility and potential cytotoxicity necessitate meticulous consideration when employed in biomedical applications.^{86,87}

1.5.3 Iridium Complexes: A Beacon of Hope in PDT

There has been a growing interest in the development of metal-based tetrapyrrolic derivatives of Pd-II, Lu-III, and Sn-IV as photosensitizers for PDT. These compounds, such as WST11, Lutex, and Purlytin, are currently undergoing clinical trials as PDT agents. One key advantage of incorporating heavy metals into these compounds is their ability to significantly enhance the efficiency of PDT. For instance, WST11, which contains palladium (PdII), exhibits a high absorption peak at 763 nm. This wavelength allows for deeper penetration of light into tissue compared to traditional photosensitizers like Photofrin. This deeper tissue penetration is critical for effectively targeting and treating deeper-seated tumors. Moreover, when metal complexes used in PDT are luminescent, they enable precise cellular localization through techniques like confocal microscopy. This capability allows researchers and clinicians to precisely track the location of the photosensitizer within cells, aiding in the optimization of treatment protocols. Another advantage of incorporating metals into these compounds is the ability to accurately quantify the amount of the agent within cells and tissues during pre-clinical studies. Techniques like ICP-MS can be employed for this purpose.⁶⁸ However, it's important to note that organelles may need to be separated before conducting such analyses. Despite these advantages, there are challenges associated with the use of certain metal complexes, particularly those containing low-spin d^6 metals like Ru, Os, or Re. To address these issues, researchers are exploring strategies to improve the cellular uptake and bioavailability of these metal-based PSs, such as modifying their chemical structures or employing drug delivery systems. Despite the challenges, the potential benefits of using metal-based photosensitizers in PDT, including their enhanced light absorption, precise cellular localization, and accurate quantification in tissues, make them promising candidates for advancing cancer treatment strategies.^{66,69}

Cyclometalated heteroleptic Ir(III) complexes have emerged as promising candidates for photodynamic therapy (PDT). While they do exhibit reduced solubility in aqueous media and shorter absorption wavelengths compared to their Ru counterparts, their customizability in terms of photophysical and photochemical properties has garnered significant attention. Notably, Ir(III) complexes possess considerably larger Stokes shifts, minimizing interference between excitation and emission processes. Additionally, the positive charge on many Ir(III) complexes enhances their water solubility, surpassing that of organic porphyrins or phthalocyanines. One remarkable attribute of Ir(III) complexes lies in their sensitivity to molecular oxygen. In oxygenated solutions, their luminescence

quantum yields and lifetimes decrease substantially, making them efficient type II photosensitizers with near-perfect quantum yields for generating singlet oxygen ($^1\text{O}_2$). Unlike porphyrin derivatives, Ir(III) complexes exhibit exceptional chemical and photochemical stability. Crucially, these Ir(III) complexes offer the flexibility to fine-tune photophysical properties, including absorption wavelength, emission energy, and quantum yield, by modifying the cyclometalated and ancillary ligands. This adaptability makes them highly suitable for PDT requirements.⁸⁸

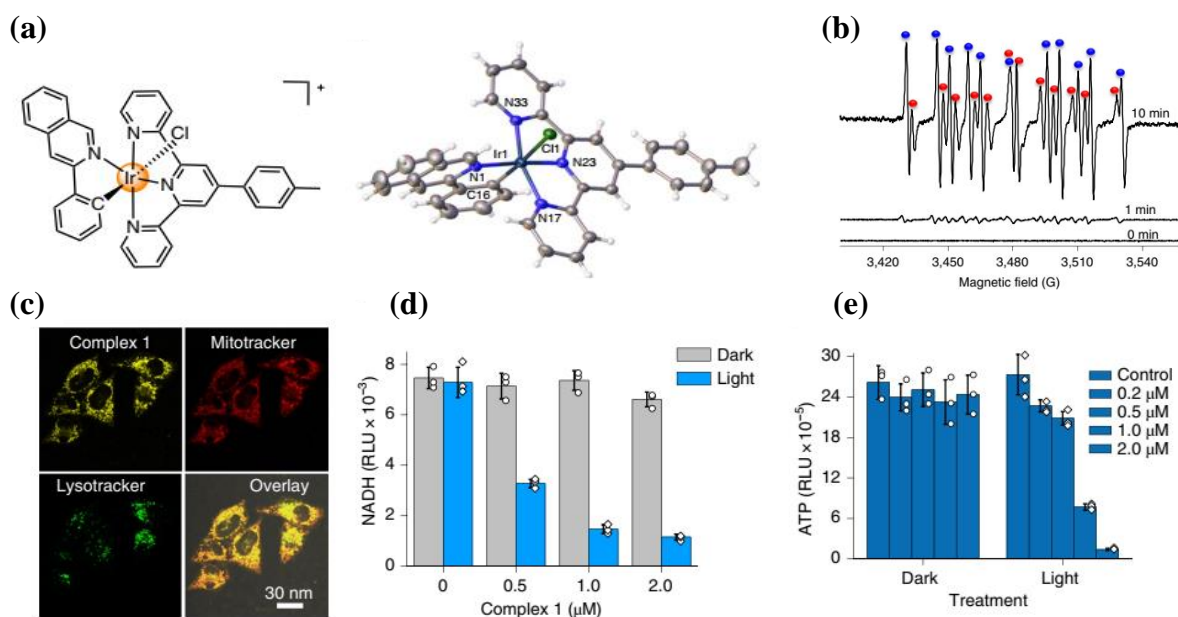


Figure 1.23: (a) The chemical and single crystal structure of the complex 1 (b) EPR spectra of the complex conforming the generation of radicals under light irradiation. (c) The intracellular localization of complex 1 through confocal imaging. (d&e) Light and dark toxicity and ATP reduction capability of complex 1. Figure adapted from reference 89

Recent breakthroughs have highlighted their high two-photon absorption cross-sections, suggesting their potential efficacy in deep tissue PDT through two-photon excitation. Furthermore, their superior luminescence quantum yields and efficient cellular uptake enable investigations into their intracellular distribution within cancer cells.

Sadler *et al.* have unveiled a groundbreaking iridium photocatalyst, complex 1, renowned for its remarkable stability and exceptionally high reduction potential, outperforming normal photosensitizers.⁸⁹ This catalyst demonstrates a staggering two-fold increase in turnover frequency for NADH oxidation in biological settings under light, surpassing organometallic half-sandwich catalysts. It also excels in photocatalyzing cytochrome c (cyt c) reduction in the presence of NADH, especially in hypoxic conditions. Through exhaustive experimental and computational investigations, the team unveiled the

mechanism, involving NAD^\bullet radical trapping. Complex 1 exhibits a unique propensity for targeting mitochondria in cancer cells, delivering nearly identical levels of photocytotoxicity in normoxic and hypoxic environments while maintaining low toxicity in unexposed normal cells. This research illuminates complex 1's potential as a potent and versatile photocatalyst for diverse biomedical applications, notably in cancer therapy, offering selective cancer cell targeting while sparing healthy ones (**Figure 1.23**).

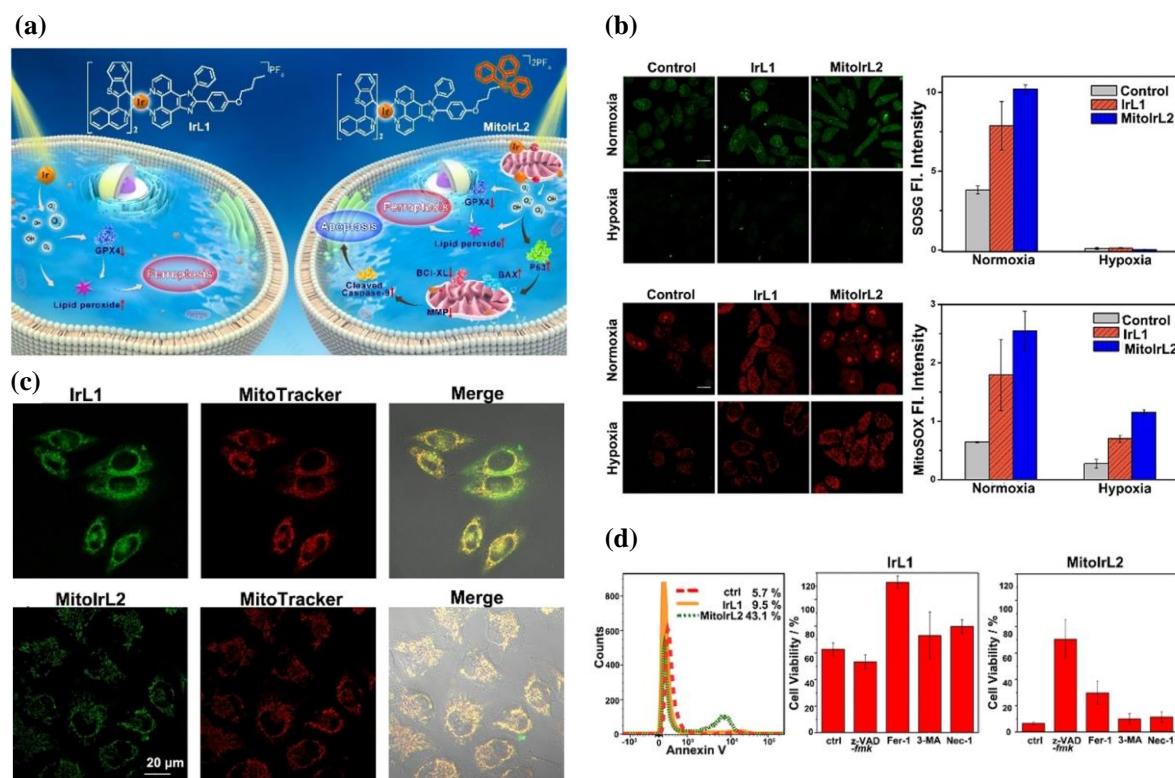


Figure 1.24: (a) Schematic illustration of the action of IrL1 and MitoIrL1 complex in cells. (b) Fluorescence images of IrL1 and MitoIrL1 in both normoxic and hypoxic situations. (c) The intracellular colocalization of both complexes. (d) Apoptotic evaluation of IrL1 and MitoIrL1 through Annexin and viability assays. Figure adapted from reference 90

In another study, He *et al.*, reported the discovery of two iridium (III)-based photosensitizers, known as IrL1 and MitoIrL2, which possess the unique capability to trigger ferroptosis.⁹⁰ The researchers devised a new cyclometalated Iridium(III) complex called IrL1, originating from benzothiophenylisoquinoline (btiq) in conjunction with imidazophenanthroline (ipt) as an additional ligand. To enhance their photodynamic impact, they introduced the mitochondria-targeting triphenylphosphonium (TPP) group into IrL1, resulting in the creation of MitoIrL2. When exposed to low oxygen conditions, IrL1 and MitoIrL2 exhibited the ability to generate superoxide ($\text{O}_2^{\bullet-}$) and hydroxyl radicals ($^{\bullet}\text{OH}$). This activity inhibited the expression of the lipid peroxidase scavenger antioxidant GPX4, leading to an accumulation of lipid peroxides and consequently inducing

ferroptosis. Furthermore, MitoIrL2 demonstrated a specific affinity for mitochondria, where it activated p53, leading to an increase in Bax expression while simultaneously inhibiting Bcl-xl expression under hypoxic conditions. This dual action resulted in the disruption of the mitochondrial membrane potential (MMP) and the suppression of adenosine triphosphate (ATP) production, ultimately triggering apoptosis (**Figure 1.24**).

In a recent analysis, Brabec *et al.* conducted a study involving octahedral Ir(III) complexes that featured a benzimidazole backbone containing NH groups. These complexes were designed to specifically target malignant cancer stem cells (CSCs) and trigger immunogenic cell death (ICD) in melanoma cells.⁹¹ To achieve this, they employed a common 1H-benzo[d]imidazole backbone with varying NH group configurations and utilized four different N, N ligands to synthesize PSs 1 through 4. In their investigation using human skin melanoma cells, the researchers found that PS 4 exhibited the highest levels of cellular uptake, photoinduced reactive oxygen species (ROS) generation, and superior phototoxicity under both normoxic and hypoxic conditions when compared to the other complexes in the series. Notably, despite the fact that most metal-based photosensitizers (PSs) known to induce ICD are typically localized in the endoplasmic reticulum (ER), compound 4 showed a preference for localization in the mitochondria. Furthermore, the authors demonstrated that PS 4 could selectively target CSCs, specifically CD20+ CSC-like A375 melanoma cells.

Chao *et al.*, recently introduced a new advancement in cancer therapy by synthesizing a novel two-photon photosensitizer, Ir-pbt-Bpa. This new compound was created by substituting the support ligand 2-phenylpyridine in the previously established Ir-Bpa compound with 2-phenylbenzo[d]-thiazole.⁹² This modification was carefully designed to improve its ability to absorb two photons, especially in the wavelength range of 740-800 nm, and it exhibits its highest absorption peak at 750 nm. Notably, Ir-pbt-Bpa exhibited remarkable efficacy in initiating Immunogenic Cell Death (ICD) upon exposure to light irradiation. The researchers went on to assess its therapeutic potential in the *In-Vivo* mice model, revealing that when combined with two-photon irradiation, Ir-pbt-Bpa effectively suppressed both primary and secondary tumors. This outcome was attributed to the synergistic effects of photodynamic therapy and immunotherapy, resulting in an improved immune microenvironment and the establishment of potent, enduring immunity. Furthermore, the study delved into the mechanisms behind Ir-pbt-Bpa's action, uncovering compelling evidence of effective endoplasmic reticulum (ER) stress induction. This was manifested through heightened CHOP and p-eIF2a expression and the highest level of

calcium ion release. These findings hold immense promise for the development of innovative cancer treatments harnessing the unique attributes of Ir-pbt-Bpa (Figure 1.25).

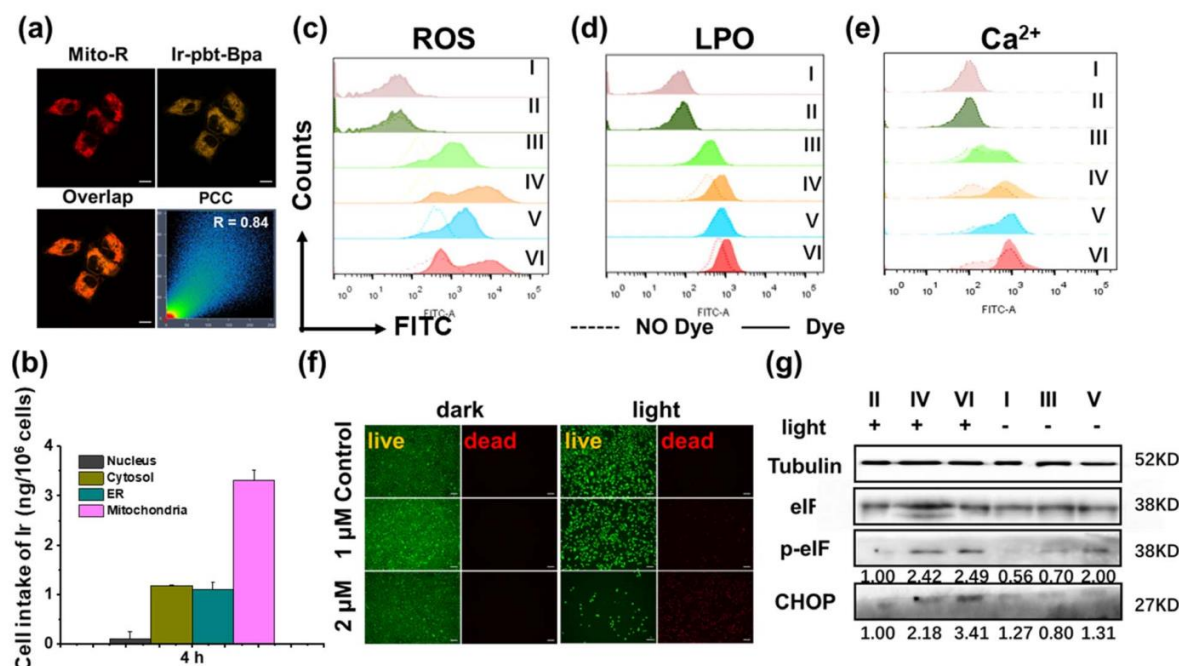


Figure 1.25: (a) Mitochondrial localization of Ir-Pbt-bpa and (b) Quantification of subcellular localization. (c,d&e) Flow cytometric analysis of cells treated with iridium complex for LPO, ROS and Ca^{2+} (f) The apoptotic evaluation to live dead assay. (g) Western blot analysis of the A375 cells after Ir-Pbt-bpa treatment. Adapted from Reference 92

In another evaluation, Yang and his team have successfully created a unique phosphorescent material by blending an Ir(III) metal complex composed of bipyridine and 2-phenylpyridine ligands with polystyrene (PS).⁹³ Complex 17, the resulting compound, exhibits impressive optical characteristics, including a strong absorption peak at approximately 450 nm, with a high molar absorption coefficient. When placed in a phosphate buffer solution, this molecule emits an orange-red phosphorescent light with a wavelength of 620 nm and a quantum yield of about 3%. To evaluate its ability to generate singlet oxygen, the researchers conducted a scavenging assay using 1,3-diphenylisobenzofuran (DPBF) and employed electron spin resonance (ESR) spectroscopy. Additionally, they investigated the potential of complex 17 for photodynamic therapy *in vivo*, utilizing a continuous wave laser with a 730 nm wavelength. This study highlights the development of a promising phosphorescent PS material based on complex 17, emphasizing its exceptional optical properties and potential applications in areas such as photodynamic therapy.

In fascinating research conducted by Mao *et al.*, they synthesized four cyclometalated iridium (III) complexes featuring bicarboline ligands. These complexes were designed to

serve as cell imaging agents and photosensitizers, specifically targeting lysosomes and becoming activated in acidic pH conditions associated with tumors.⁹⁴

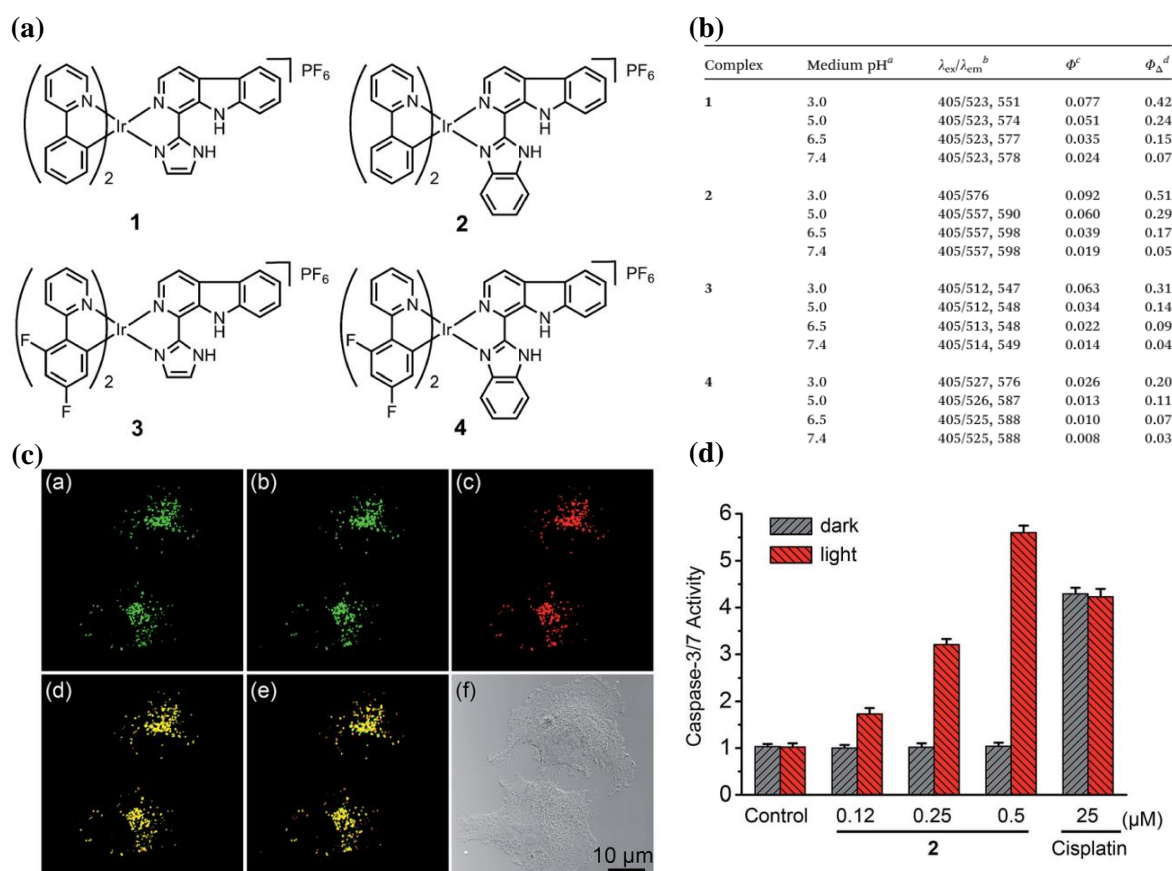


Figure 1.26: (a) The structure of the complexes under investigation. (b) Table showing the photophysical properties of the complexes. (c) The intracellular laser scanning images show the internalization. (d) Caspase activity evaluation of the molecule in light and dark conditions. Figure adapted from reference 94

These complexes exhibited heightened phosphorescent emission and the generation of singlet oxygen molecules when present in environments related to tumors and lysosomes. Further investigations into the mechanism of action revealed that PDT mediated by Complex 2 primarily triggered apoptotic cell death that relied on caspases and reactive oxygen species (ROS), primarily due to damage to lysosomes and the release of cathepsin B. An intriguing aspect of Complex 2 is its capability to be used for monitoring lysosomal integrity during PDT. This offers a convenient means of assessing the therapeutic effectiveness in real time (**Figure 1.26**).

Huang and colleagues developed two distinct Ir(III) complexes, Ir-P(ph)₃ and Ir-alkyl, with specific targeting capabilities for mitochondria and lysosomes, respectively. These complexes exhibited similar properties such as a high ¹O₂ quantum yield, long-lasting phosphorescence, and strong sensitivity to oxygen levels. When oxygen levels decreased,

both complexes displayed increased luminous intensity and extended lifetimes. In comparison to the lysosome-targeted complexes, cells treated with the mitochondrial-targeted complexes showed a slower respiration rate, leading to higher levels of oxygen within the cells under hypoxic conditions.⁹⁵

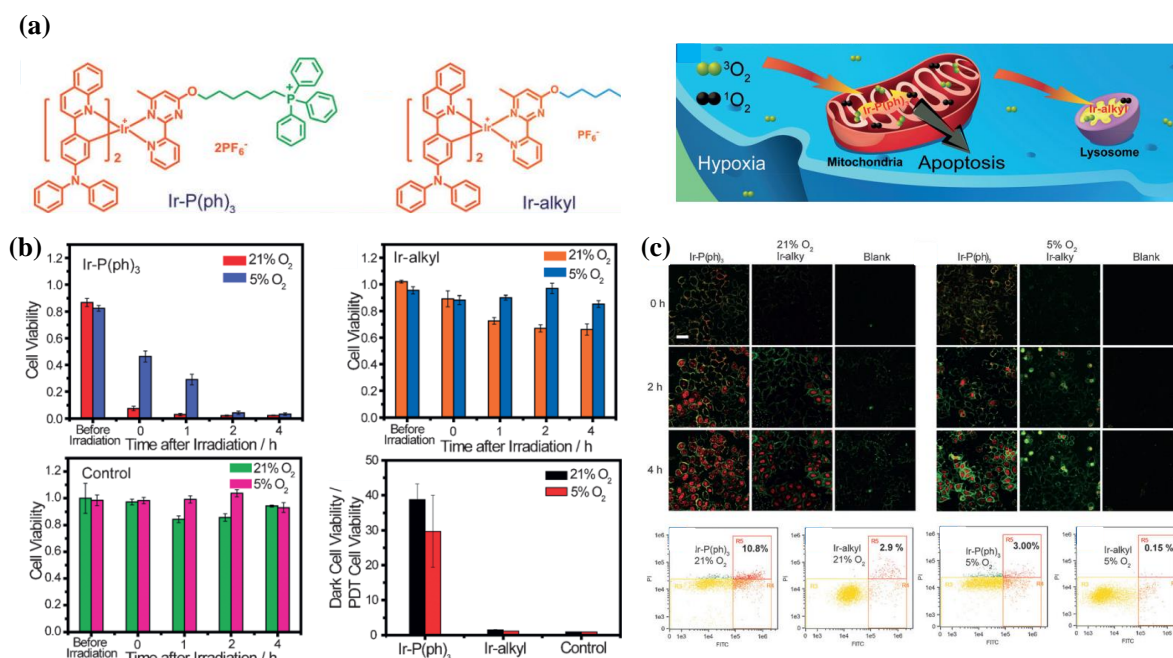


Figure 1.27: (a) The structure of the normal and Mito-targeted iridium complexes and the mechanism of action. (b) Cell viability evaluation of both the complexes in normoxic and hypoxic situations. (c) Confocal microscopy images and flow cytometry quantification of annexin V-FITC- and PI-labelled HeLa cells. Adapted from reference 95

This effect enhanced their ability to combat hypoxic tumors, as demonstrated by the MTT experiment. Ir-P(ph)₃, in particular, exhibited excellent photodynamic therapy (PDT) effectiveness under hypoxic conditions, confirming the positive impact of mitochondria-targeted PDT agents in treating hypoxic cancers (**Figure 1.27**).

Chao *et al.* recently unveiled a groundbreaking advancement in photodynamic therapy (PDT) by introducing an oxygen-independent Ir(III) complex as a photosensitizer (PS) for two-photon excitation. Their innovation incorporates an anthraquinone moiety, which efficiently activates the Ir(III) complex to generate highly cytotoxic carbon radicals while concurrently quenching its luminescence.⁹⁶ Remarkably, under hypoxic conditions, this anthraquinone-modified Ir(III) complex exhibits a unique "turn-on" behavior, wherein its emission is reactivated through enzymatic reduction by reductase, as illustrated in Figure 9E. Importantly, the reduced Ir(III) complex, when exposed to 730 nm irradiation, effectively produces carbon radicals, resulting in the disruption of mitochondrial membrane potential and subsequent induction of apoptotic cell death. This pioneering research

represents a significant stride in the development of oxygen-independent PSs for two-photon PDT, holding promise for advanced cancer therapy applications. Yuksel and colleagues developed red-wavelength-excited Ir(III) complexes featuring two BODIPY units. These complexes exhibited similar absorption bands to free BODIPY but had higher molar extinction coefficients. Their $^1\text{O}_2$ quantum yield ($\phi\Delta$) was six times greater than free BODIPY ($\phi\Delta = 0.06$ vs. 0.01). MTT experiments confirmed that under red irradiation, the Ir(III) complexes induced slight cancer cell apoptosis. However, the phototoxicity efficacy was suboptimal, attributed to the mismatched distance between the coordination center and the BODIPY unit, hindering energy or electron transfer.⁹⁷

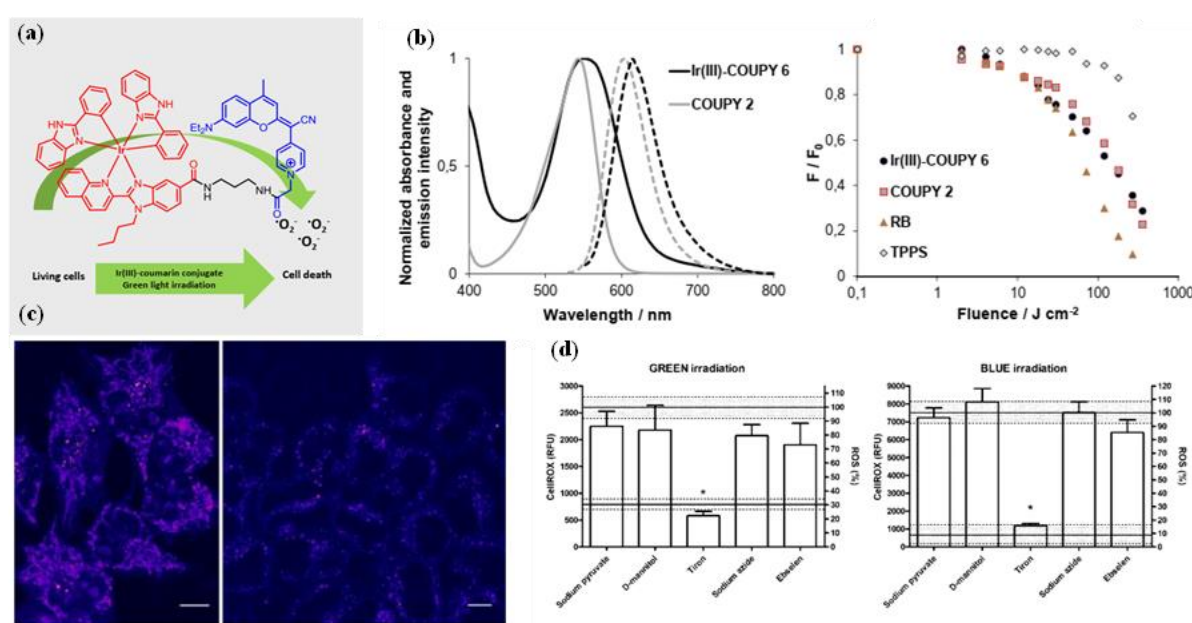


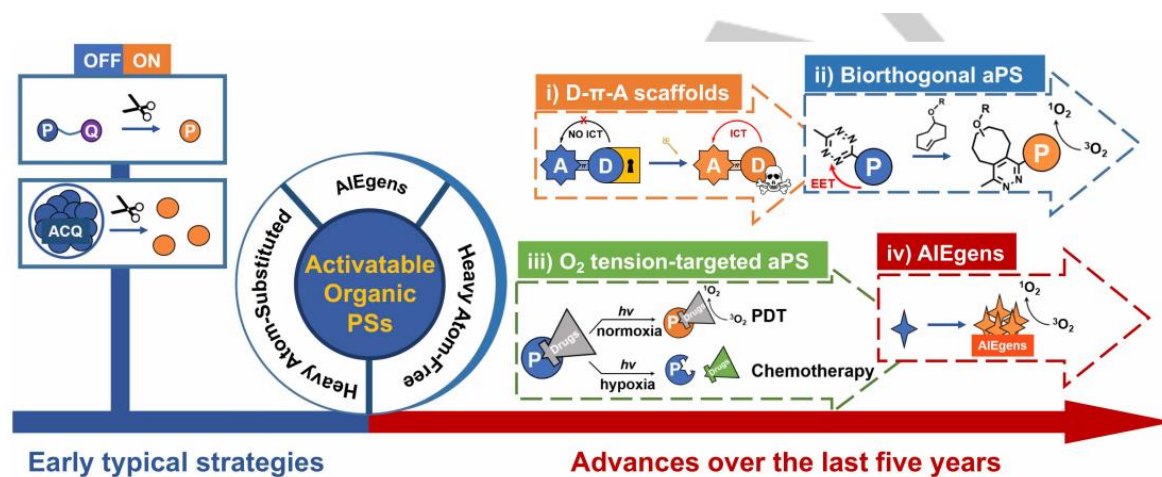
Figure 1.28: (a) The structure and sensing mechanism of the Iridium-Coumarin probe. (b) Fluorescence spectra of the synthesized complexes and their intensity profiling. (c) The intracellular localization of the probe molecule through confocal imaging. (d) The quantification of ROS production with different light irradiation. Figure adapted from reference 98

Novohradsky *et al.*, put forward an innovative approach by developing hybrid agents that combine Ir(III) cyclometallate with a suitable fluorophore for use in PDT.⁹⁸ They combined Ir(III) cyclometallate with the coumarin-appended (COUPY) fluorophore. The Ir(III)–COUPY complexes exhibit pronounced absorption peaks within the 500–600 nm range, and these peaks are a result of the $\pi-\pi^*$ transitions of coumarin. Importantly, when tuning the excitation Ir(III)–COUPY, the fluorescence of coumarin can also be observed, indicating suitable energy transfer from the Ir(III) complexes to the coumarin fluorophores. Interestingly, the cellular uptake pathway of the Ir(III)–COUPY complex differs from that of its individual components and functions through a mechanism independent of energy. When exposed to green light, Ir(III)–COUPY complexes exhibit significant phototoxicity.

These findings confirm that the inclusion of coumarin in Ir(III) complexes extends the range of wavelengths for photosensitizer excitation. In another study, Lin *et al.* pioneered the development of nano metal-organic frameworks (nMOFs) utilizing an Ir(III) complex as a photosensitizer (PS) for deep photodynamic therapy (PDT). These nMOFs, featuring crucial Hf atoms, efficiently absorbed X-rays and transferred energy to the Ir(III) complex, leading to singlet oxygen ($^1\text{O}_2$) generation.⁹⁹ With a controlled thickness of 1.2 nm, the Hf-BPY-Ir nMOFs facilitated cellular uptake and $^1\text{O}_2$ diffusion within cells (**Figure 1.28**). MTT assays on CT26 and MC38 cells revealed exceptional cytocompatibility, with cell viability above 95% even at the highest concentration. Importantly, X-ray irradiation maintained phototoxicity, suggesting nMOFs' potential for deep tissue PDT in tumors, as demonstrated by shielding tests with a 1 cm-thick beef block.

1.5.4 Activatable Photosensitizers in Photodynamic Therapy: From Bench to Bedside

Activatable Photodynamic Therapy (aPDT) represents a groundbreaking advancement in the field of medical science, ushering in a new era of precision medicine and targeted therapy. Essentially, aPDT is a treatment strategy that utilizes the complex interplay between light, photosensitizing agents, and cellular biology to selectively eliminate diseased cells while preserving healthy tissue. This innovative technique capitalizes on the high sensitivity of specific photosensitizers to particular wavelengths of light, which triggers their activation and the subsequent production of reactive oxygen species (ROS). What sets aPDT apart from traditional photodynamic therapy is its ability to precisely control when and where the photosensitizer is activated, restricting its harmful effects to predetermined cellular targets. This precision is achieved through the development and use of advanced molecular switches or intelligent nanocarriers that respond to specific cellular or environmental cues, providing exceptional control and minimizing collateral damage.¹⁰⁰ As a result, aPDT has emerged as a ray of hope in the battle against cancer, infectious diseases, and various other health conditions, holding the potential to transform clinical treatments by sparing patients from the often-debilitating side effects associated with conventional therapies (**Scheme 1.10**). As we delve deeper into the intricate mechanisms and applications of activatable PDT, we unlock the opportunity to reshape the medical landscape, offering patients not only improved treatment outcomes but also a renewed sense of optimism for a healthier future.¹⁰¹

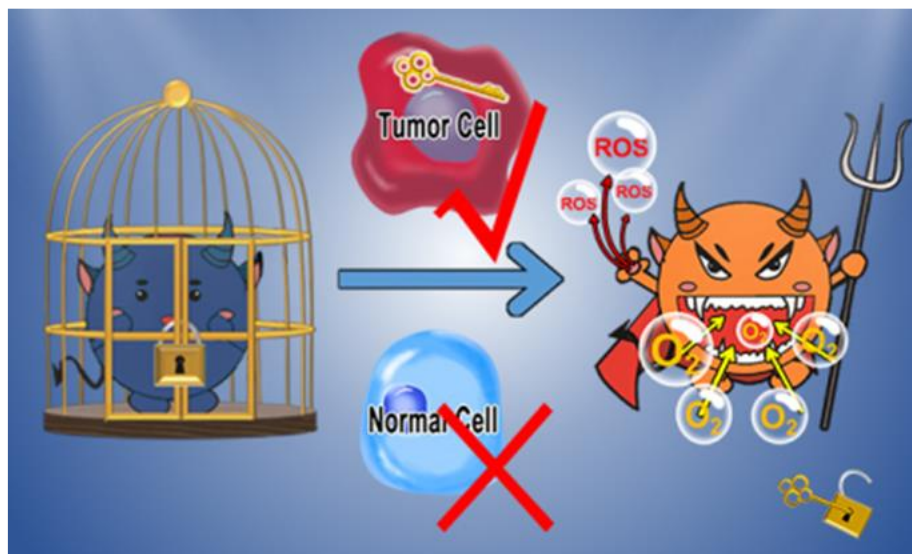


Scheme 1.10: (a) Schematic illustration of the new and old strategy used to impart activatable PDT effect. Adapted from reference 88

Activatable photosensitizers have emerged as a promising strategy in the field of photodynamic therapy (PDT) for cancer treatment. These unique compounds remain inactive until they encounter specific triggers, such as overexpressed molecules or proteins in the tumor environment. By eliminating factors that hinder the PDT effect, these stimuli-responsive activators enable precise and targeted treatment. This not only enhances the therapy's focus on cancer cells but also reduces the potential for damage to surrounding healthy tissues, making cancer treatment more effective and selective. Activatable photosensitizers, or PSs, can be activated by specific stimuli, making them highly effective at targeting diseased cells characterized by overproduced biomarkers. This targeted activation helps distinguish healthy cells from diseased ones, minimizing damage to healthy tissues during PDT. Additionally, the same pathway responsible for generating reactive oxygen species (ROS) during photoexcitation also leads to fluorescence emission, allowing confirmation of stimuli-triggered PS activation and enabling imaging-guided PDT (Scheme 1.11).¹⁰⁰

Significant efforts have been dedicated to developing activatable PSs that target disease biomarkers. One notable example is 5-aminolevulinic acid (5-ALA), which, while not photosensitive itself, is metabolized into the photoactive protoporphyrin IX (PpIX) within certain cells and tissues, allowing selective accumulation in tumor cells for PDT. Researchers have explored various activation mechanisms for activatable organic PSs. An early approach involved the aggregation-caused quenching (ACQ) effect, where high PS concentrations were enclosed within stimuli-responsive polymeric nanostructures. Self-quenching between PSs inhibited photosensitivity, which could be restored when the nanocarrier disintegrated upon encountering specific biomarkers. However, this approach

had limitations due to the unpredictable nature of polymer folding. In contrast, a newer class of fluorophores known as aggregation-induced emission (AIEgens) displayed strong fluorescence in the aggregated state but not in the monomeric state. AIEgens have been adapted to develop activatable PSs, offering innovative strategies for their design. Another early design involved the PS-quencher dyad (P-Q), where a quencher was linked to the PS through a stimuli-responsive linker, resulting in the quenching of photosensitivity due to resonance energy transfer (RET).¹⁰⁰



Scheme 1.11: Schematic representation of the mechanism of activatable PDT towards normal and cancer cells.

When specific biomarkers were present, the linker would cleave, freeing the PS and activating its photosensitivity. This approach provided a versatile platform for creating activatable PSs targeting various biomarkers by modifying the stimuli-cleavable linker. A unique activation mechanism called biomarker displacement activation (BDA) was introduced, where a PS-loaded nanocarrier complexed with a macrocyclic amphiphile inhibited the PS's photosensitivity. Excessive biomarkers in tumor tissues displaced the PS, restoring its photosensitivity. Recent research has focused on chemically modifying common fluorophores to create novel PSs, such as BODIPY, rhodamine, D- π -A dyes, and AIEgens. These derived PSs serve as frameworks to leverage established fluorescence turn-on mechanisms, offering researchers versatile tools for creating activatable photosensitizers targeting different biomarkers. In the past five years, several PS activation designs based on fluorogenic principles have emerged, including biorthogonal activatable BODIPYs, activatable Se-rhodamine with single-cell precision, silicon phthalocyanine for targeting oxygen levels, general D- π -A scaffolds, and AIEgens, among others. These innovations

hold significant promise for advancing photodynamic therapy and enhancing the precision and effectiveness of cancer treatment.¹⁰²

Akkaya *et al.*, described a unique photosensitizer called PS-Q, which can be activated by glutathione (GSH). This PS-Q was created by attaching a Br-conjugated BODIPY to a thiol-cleavable 2,4-dinitrobenzenesulfonyl (DNB) unit.

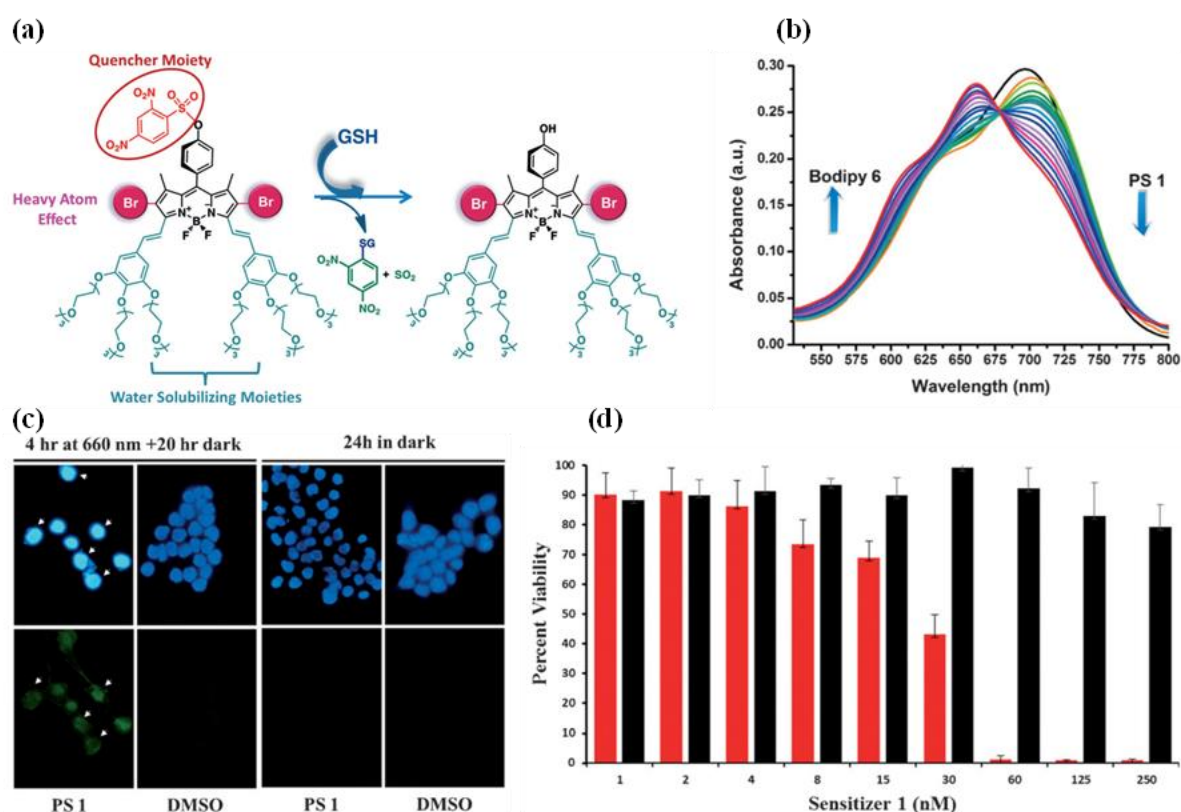


Figure 1.29: (a) Mode of action for the GSH-mediated activation of caged photosensitizers. (b) Absorption spectra of PS-1 with GSH. (c) Fluorescence microscope images of Annexin-V-stained HCT116 cells in the presence PS-1. (d) Light and dark toxicity of PS-1 in a concentration-dependent manner. Adapted from reference 103

The bromine was located at the 2,6-positions of the BODIPY dye to promote intersystem crossing (ISC), a process that enhances the generation of singlet oxygen (¹O₂) when the PS-Q is exposed to near-infrared (NIR) light at 660 nm.¹⁰³ The DNB quencher, which is attached to the BODIPY dye, plays a critical role in inhibiting the production of reactive oxygen species (ROS). It achieves this by quenching the excited state of the photosensitizer through a non-radiative deexcitation pathway, thereby preventing the unwanted generation of ROS. However, when glutathione (GSH) is present, it can interact with the DNB quencher and remove it from the PS-Q molecule. This removal process effectively "turns on" the photosensitivity of the PS-Q, restoring its ability to generate ROS upon exposure to NIR light. This unique property of GSH-mediated activation of PS-Q was demonstrated

within cells. Specifically, the researchers showed that HCT116 tumor cells, which have a high intracellular concentration of GSH, could be selectively eliminated through photoirradiation. This selective activation and removal of the DNB quencher within the cells allowed for targeted and controlled ROS generation, resulting in the destruction of the tumor cells (**Figure 1.29**).

Urano and his research team have introduced HMDESeR-bGal as an innovative photosensitizer with precise spiro cyclization control, enabling selective cell death induction exclusively in b-galactosidase-expressing cells, thereby minimizing unwanted phototoxicity as the activation occurs only upon interaction with the target enzyme.¹⁰⁴ Notably, their *Ex-Vivo* investigation using larval *Drosophila* wing discs confirmed the specific cell death induction in the b-galactosidase-expressing region, marking a significant milestone as it represents the first instance of non-localized photoirradiation achieving cell death selectivity in target cells within living tissue using a small-molecular photosensitizer. In another approach Schnermann and his team introduced the development in the field of oxygen-responsive photosensitizers, utilizing a uniquely structured SiPc molecule.¹⁰⁵ This particular SiPc derivative exhibited a dual function: it acted as a photo-uncaging agent, releasing a chemical drug in hypoxic conditions, while also serving as an active photosensitizer that generated reactive oxygen species exclusively in normoxic environments. This capability of being activated only in the presence of oxygen ensured that oxygen-consuming photodynamic therapy (PDT) treatments were administered solely under aerobic conditions, preventing further worsening of tumor hypoxia. The SiPc derivative efficiently underwent intersystem crossing to attain a long-lived triplet state, facilitating either drug delivery or ROS generation depending on the prevailing oxygen levels. Given that many solid tumors consist of diverse cellular subpopulations marked by varying levels of hypoxia, this oxygen-responsive photosensitive agent holds great promise for intelligent anti-tumor phototherapy.

To ensure the importance of AIE probes, Liu *et al.* have recently introduced a novel bioorthogonal fluorogenic AIEgen named TPETSAI for the purpose of imaging-guided cancer cell photoablation.¹⁰⁶ This AIEgen is designed with alkyne groups that are functionalized. Initially, TPETSAI exhibits dormant fluorescence, which means it does not emit light until it anchors onto the membrane of metabolic glycoengineered cancer cells. This attachment occurs through a click reaction with azide-functionalized glycans, allowing for precise targeted imaging of the cancer cells. Furthermore, TPETSAI possesses additional photosensitivity, making it suitable for efficient imaging-guided photodynamic

therapy (PDT). Importantly, the effectiveness of this approach was demonstrated intracellularly, showcasing its potential for cancer treatment without directly copying or plagiarizing prior research (Figure 1.30).

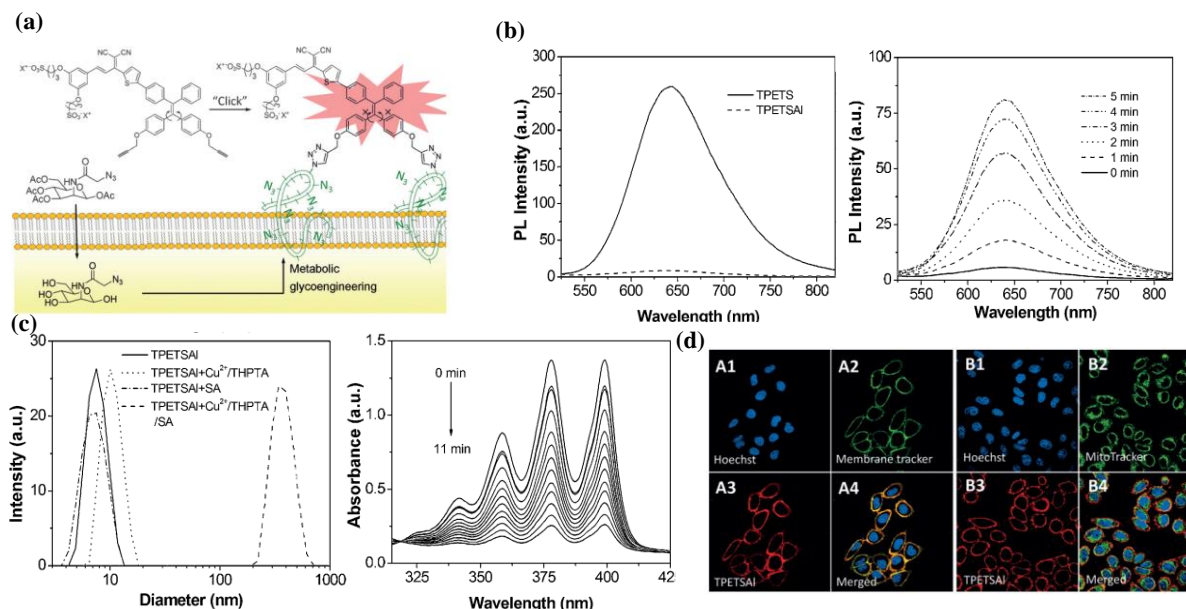


Figure 1.30: (a) The structure and activation, sensing mechanism of the probe. (b) Fluorescence spectra of the AIE probe in time-dependent manner. (c) DLS pattern showing the aggregation of the TPE probe and its singlet oxygen generation ability via ABDA assay. (d) Co-stain of TPETSAL labeled HeLa cells with A) membrane tracker Green or B) MitoTracker Green and Hoechst. Adapted from reference 106

Metal complexes exhibit excellent potential as activatable photosensitizers (PS) for photodynamic therapy (PDT). These complexes possess unique features that set them apart from their organic counterparts. One distinguishing characteristic is their inherent triplet excited state, which contributes to their high singlet oxygen quantum yield. This property makes metal complexes highly advantageous for enhancing the efficacy of activated PDT. Furthermore, metal complexes offer versatile mechanisms for quenching their PDT capability and emission characteristics. These mechanisms encompass electron transfer processes, aggregation phenomena, and Förster resonance energy transfer (FRET) interactions. These quenching mechanisms can be harnessed strategically to modulate the PDT activation, allowing precise control over the therapeutic process. In contrast to organic PS, metal complexes bring a wealth of scientific opportunities to the field of PDT. Their inherent triplet excited state and versatile quenching mechanisms make them valuable tools for tailored and efficient PDT activation, paving the way for innovative approaches in the development of advanced photodynamic therapies.

Yi *et al.*, have innovatively developed an Ir(III) complex, denoted as Ir-1, which exhibits distinctive characteristics, notably its aggregation-induced emission (AIE) property, as well as a robust phosphorescence peaking at approximately 630 nm and an impressively large Stokes shift of 227 nm.¹⁰⁷

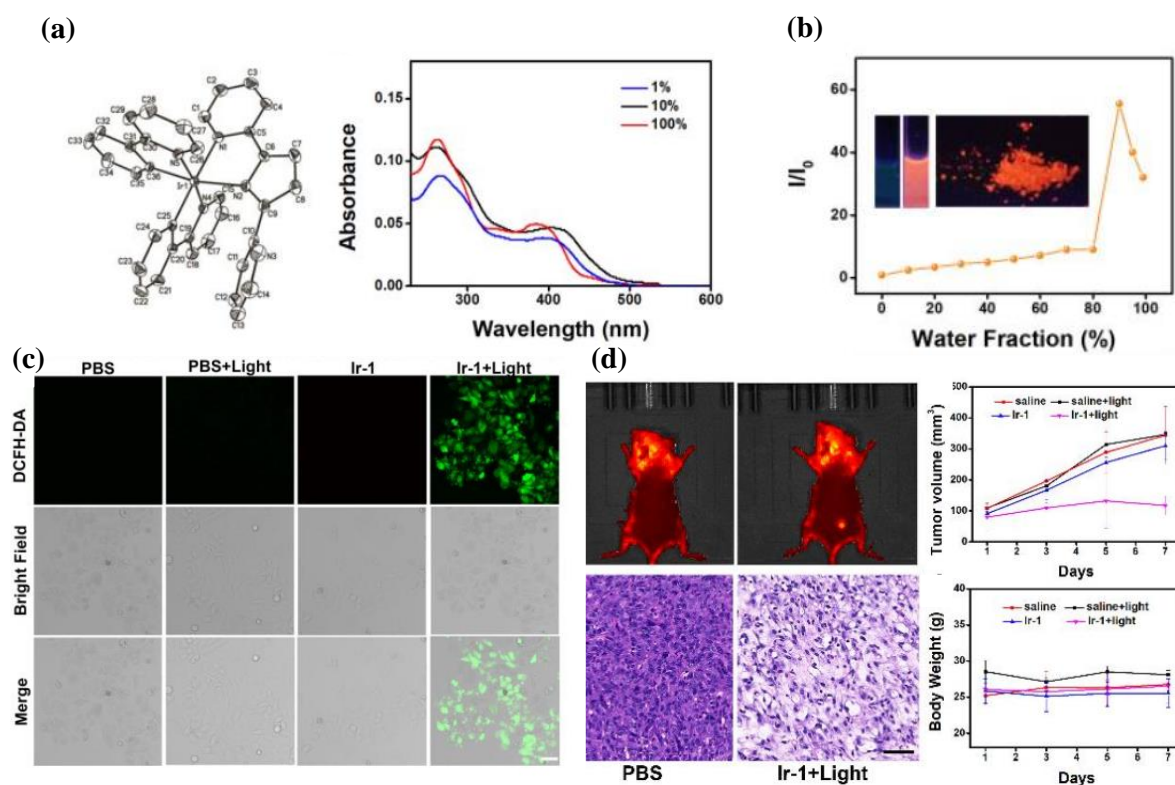


Figure 1.31: (a) The structure and absorption spectra of the probe Ir-1. (b) Aggregation induced emission property of the probe with different water fraction. (c) Intracellular ROS generation of the probe with laser irradiation through DCFDA assay. (d) *In-Vivo* animal modal studies with tumor reduction and H&E staining. Figure adapted from reference 107

In the realm of photodynamic therapy (PDT), the effectiveness of Ir-1 in generating singlet oxygen (1O_2) stands out, surpassing that of Rose Bengal by a factor of 2.3, when evaluated in an ethanol/water mixture solution with a volume ratio of 1:9. Importantly, in *In-Vitro* experiments, Ir-1 displayed superior biocompatibility and a heightened level of phototoxicity in comparison to established clinical photosensitizers. This compelling evidence underscores the potential of Ir-1 as a promising photosensitizer for image-guided PDT in the treatment of cancer, highlighting its significant contributions to advancing this therapeutic approach (Figure 1.31). In different case studies, Wong and colleagues devised a strategy to enhance the singlet oxygen generation capacity and precision of organelle targeting in the rhodamine-containing cyclometallated iridium(III) system, Ir-Rho-G2.¹⁰⁸ This strategy involved a straightforward substitution of the original cyclometallating ligand, 2-phenylpyridine (ppy), with 2,3-diphenylquinoxaline (dpqx) within the complex.

Subsequently, they further refined this design, creating a second-generation derivative, Ir-Rho-G2, by modifying the dpqx ligand to achieve a lower-lying excited state.

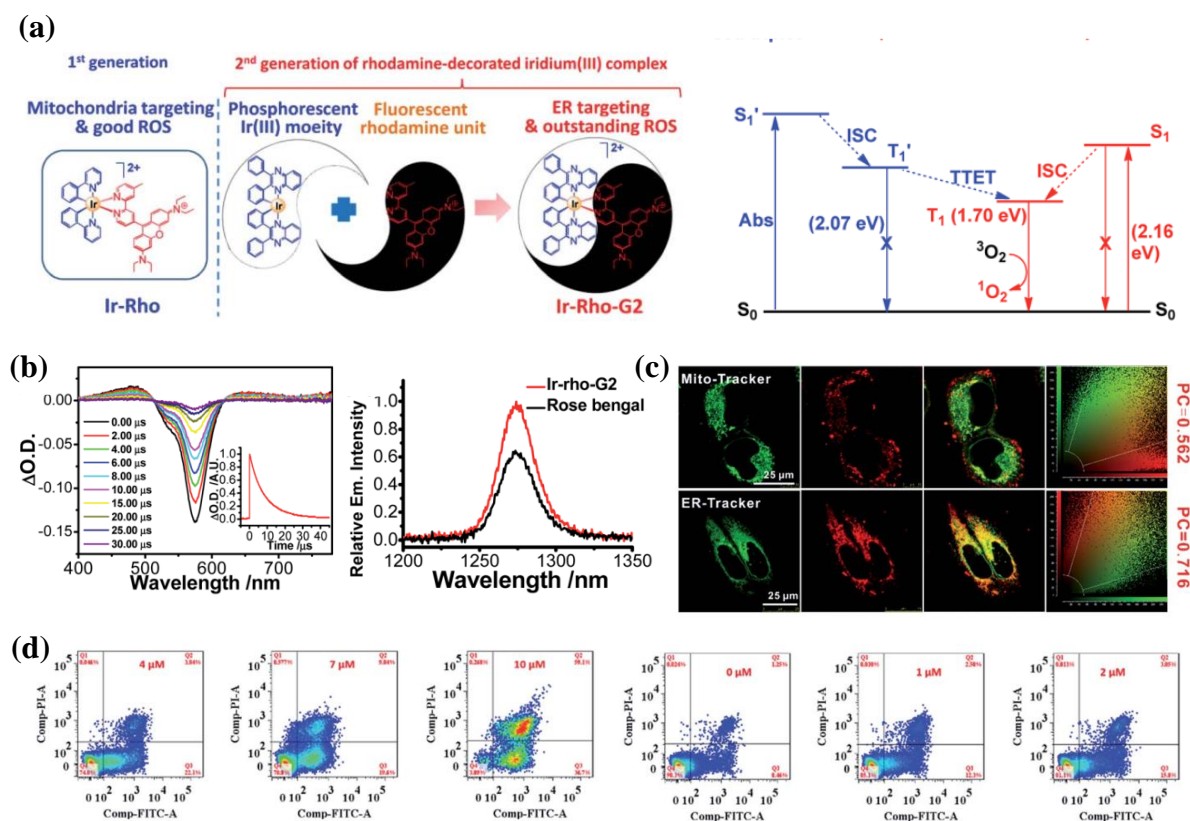


Figure 1.32: (a) The route of construction of the probe Ir-rho-G2 and its Jablonski diagram (b) Singlet oxygen generation analysis through excited state studies and oxygen phosphorescence. (c) Colocalization of the probe in the cellular milieu. (d) Extent of apoptosis by annexin studies with flowcytometry. Adapted from reference 108

The enhancements achieved in Ir-Rho-G2 were remarkable, notably in its capacity to generate singlet oxygen and precisely target the endoplasmic reticulum (ER) within cells. These advancements translated into highly effective photodynamic therapy (PDT) results, causing cancer cell death when exposed to light due to ER dysfunction. The primary goal was to extend the excited state's lifetime, leading to improved PDT outcomes. Ir-Rho-G2 exhibited exceptional efficiency in generating reactive oxygen species in both solution and cells, along with specific ER targeting, which correlated with cancer cell apoptosis upon light exposure. Importantly, it demonstrated low toxicity in the dark, high photostability, and a preference for uptake by tumor cells. *In-Vivo* experiments, including near-infrared fluorescence (NIRF) imaging and tumor PDT, confirmed its ability to accumulate at tumor sites and effectively suppress tumor growth (Figure 1.32).

Zhao and co-researchers put forward a class of photosensitizers, namely Ir1 and Ir4, designed to be triggered by the presence of glutathione (GSH), a molecule abundant in

cancer cells. These photosensitizers are constructed using iridium (III) complexes, featuring benzyl pyridinium groups that facilitate photoinduced electron-transfer (PeT) reactions.¹⁰⁹ When GSH is detected, it initiates nucleophilic substitution reactions, resulting in alterations in the photosensitizers' phosphorescence properties, including intensity, wavelength, and lifetime.

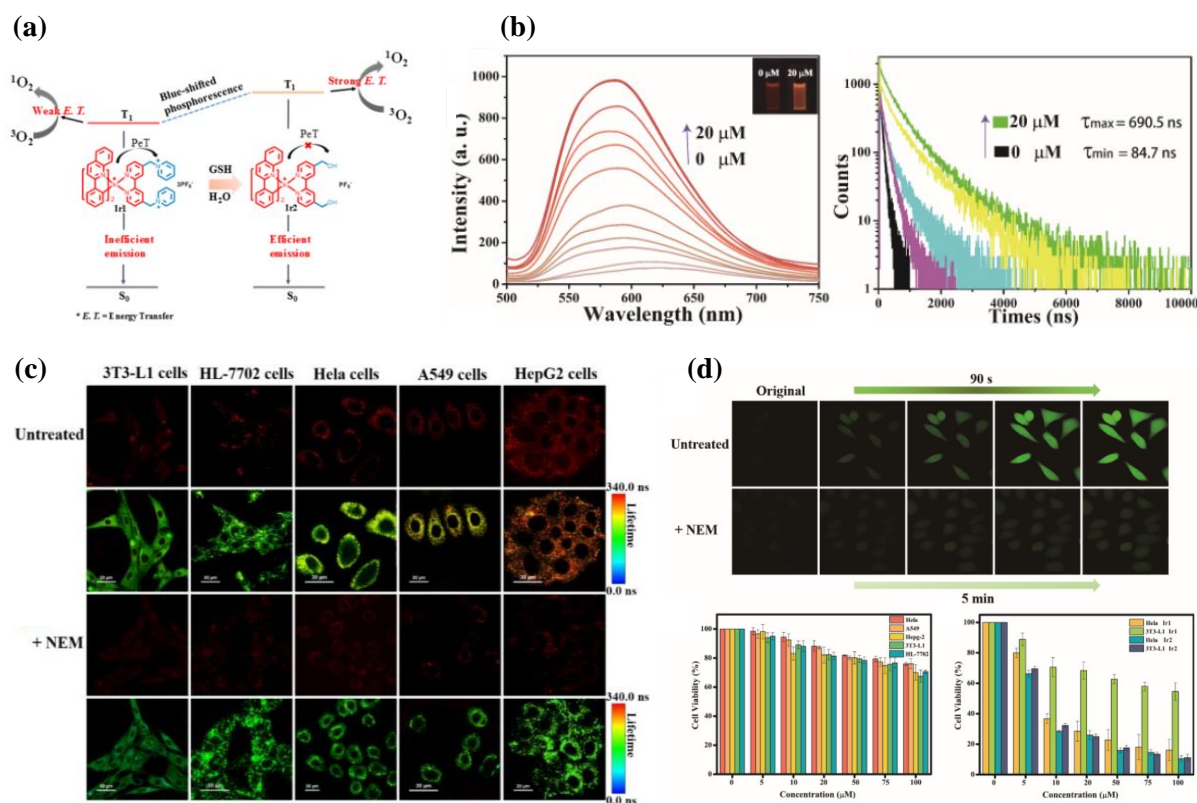


Figure 1.33: (a) The structure and the singlet oxygen activation mechanism of the GSH sensing activatable probe. (b) Emission and lifetime analysis of the probe with different concentrations of GSH. (c) Imaging of intracellular GSH level in different cells with and without GAH inhibitor. (d) Apoptotic evaluation through viability assays in presence of light. Adapted from reference 109

This heightened sensitivity to GSH is pivotal. It allows these photosensitizers to selectively pinpoint cancer cells versus healthy ones through luminescence and lifetime imaging, capitalizing on the elevated GSH levels in cancer cells. Importantly, GSH activation significantly amplifies the generation of singlet oxygen. This distinct attribute not only enables precise cancer cell targeting but also enhances PDT's efficacy in eliminating tumor cells due to the elevated GSH levels. The proof of a GSH-responsive mechanism was demonstrated by substituting the pyridinium group in Ir1 with hydroxyl, yielding a new complex, Ir2, which exhibited blue-shifted, intensified emission, extended lifetime, and increased singlet oxygen production (Figure 1.33).

Yuan et al., presents a novel iridium (III) complex probe, $[\text{Ir}(\text{ppy})_2(\text{NTY-bpy})](\text{PF}_6)$, designed for the detection of cysteine (Cys) both in laboratory settings and in living organisms. The development of this probe involves the incorporation of a strong electron-withdrawing group, nitroolefin, into the bipyridine ligand of the Ir(III) complex. The luminescent properties of the probe are initially quenched due to an intramolecular charge transfer (ICT) process but are subsequently activated by a specific recognition reaction with Cys. This compound, $[\text{Ir}(\text{ppy})_2(\text{NTY-bpy})](\text{PF}_6)$, demonstrates high sensitivity and selectivity in detecting Cys and is biocompatible. Furthermore, its long-lasting emission enables time-gated luminescence analysis of Cys in both cellular and human serum samples, making it a practical choice for phosphorescence and time-gated luminescence imaging, as well as flow cytometry analysis of Cys in live samples.¹¹⁰

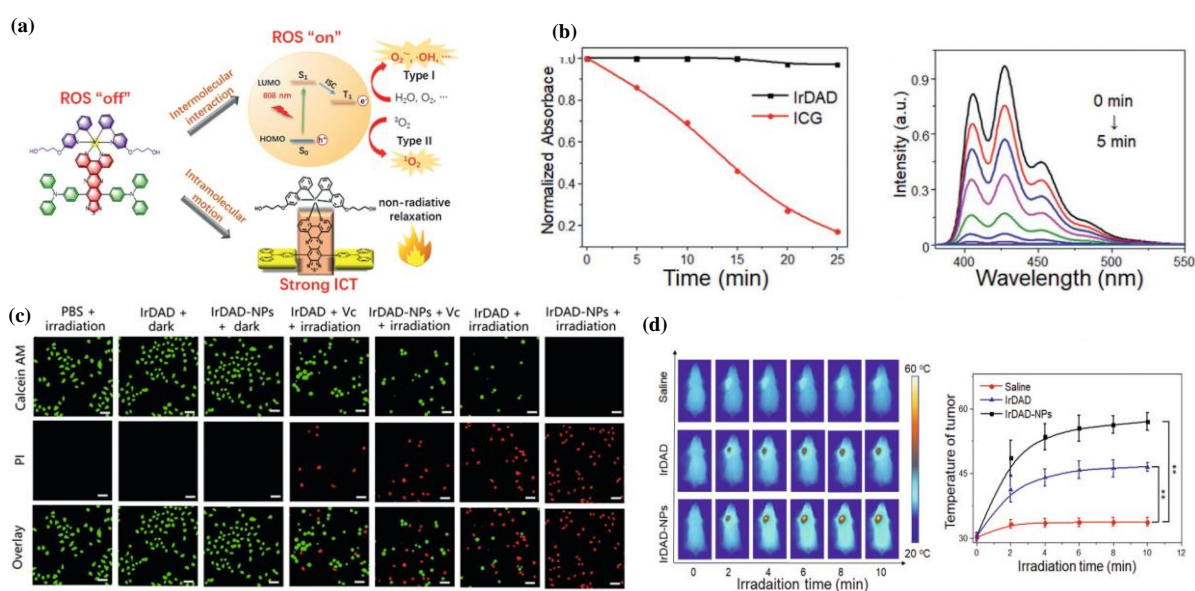


Figure 1.34: (a) The structure and the mechanism of action of the activatable probe. (b) Absorbance studies to confirm singlet oxygen generation with ABDA assay. (c) Live-dead assay with different combinations of the probe with and without laser. (d) In-Vivo analysis showing the imaging and tumour reduction studies. Adapted from reference 78

In their study, Gou and colleagues developed an iridium(III) complex, IrDAD, featuring a unique D–A–D type ligand with strong near-infrared absorption and efficient Intramolecular Charge Transfer (ICT). IrDAD displayed a remarkable contrast in its behaviour between monomeric and aggregated states, as it generated no Reactive Oxygen Species (ROS) in the former but exhibited significant ROS production in the latter, a departure from typical aggregation-caused quenching (ACQ) dyes. This property, combined with the advantageous intermolecular interactions and intramolecular motion, resulted in IrDAD's ultralow radiative transition, allowing for maximized conversion of photo energy into ROS and heat for both Photodynamic Therapy (PDT) and Photothermal

Therapy (PTT). To enhance its therapeutic potential, IrDAD was further developed into nanoparticles (IrDAD-NPs) by conjugating it with polyethylene glycol (PEG). *In-Vivo* experiments demonstrated that IrDAD-NPs exhibited preferential tumor accumulation and led to significant tumor regression, showcasing their potential for advanced cancer phototherapy (Figure 1.34).⁷⁸

1.6 Objectives and methodologies for the present investigation

In the field of cancer diagnostics and therapy, one of the most challenging tasks is to comprehensively understand the cellular-level changes that occur within biological systems in their natural environment. To overcome these challenges, scientists are actively exploring the development of new functional materials with enhanced sensing capabilities with therapeutic potential. This thesis focuses on a systematic exploration of the design, synthesis, and evaluation of cationic cyclometalated iridium (III) complexes with biosensing properties, specifically for the applications in activatable photodynamic therapy in cancer treatment. The key innovation lies in the precise activation of these complexes at the target site, thereby enhancing the treatment's effectiveness while minimizing systemic toxicity. The synthesis of several cationic metal complexes based on iridium metal is presented, followed by an investigation of their optical properties, which are harnessed for various sensing, imaging, and photodynamic therapy-based treatments in combination with other strategies. These functional materials have the potential to create therapeutically relevant probes for applications like point-of-care diagnosis and personalized treatment.

The thesis comprises four chapters, each delving into different aspects of this research. The first chapter provides an overview of recent advancements in photodynamic therapy, emphasizing the use of metal complexes as photosensitizing agents and their potential in cancer diagnostic and theranostic applications for effective therapeutic outcomes. It also includes a review of existing literature on functional small molecule-based optical probes, photosensitizers, and their biological applications.

Chapter 2 details the design and synthesis of a cationic cyclometalated Ir(III) complex using a quinoline-appended bipyridine as the auxiliary ligand. This complex is designed for targeted activation through nicotinamide adenine dinucleotide-reduced (NADH), a crucial molecule in cellular homeostasis. The complex serves as a molecular probe for assessing the state of endogenous NADH using surface-enhanced Raman spectroscopy (SERS) and fluorescence techniques. The activation of this probe upon interaction with NADH enables the switching of SERS and luminescence, achieving remarkable detection

limits. Furthermore, the activated complex is explored for its potential as a photosensitizer in producing singlet oxygen for cancer treatment.

Chapter 3 focuses on the creation of a multifunctional photosensitizer complex with theranostic applications. This complex, called Ir-Nap, is designed to enable efficient photodynamic therapy in hypoxic tumors by generating singlet oxygen through heat-triggered cycloreversion of endoperoxides. The complex is integrated into a magnetic nanoparticle (MNP) platform with photothermal capabilities, allowing for a combination of oxidative and photothermal damage in tumor cells. To protect the therapy from circulation-related issues, a responsive MnO₂ coating is applied to the MNP surface, and a cancer-targeting peptide is incorporated for active cell targeting. This approach results in a potent triple therapeutic combination effect on cancer cells.

Chapter 4 introduces a novel H₂S activatable photodynamic agent for cancer treatment. The cyclometallated iridium compound initially exhibits weak photoluminescence but becomes highly active in the presence of H₂S. This activation is achieved by blocking the photo-induced electron transfer process, leading to the regeneration of emission and the activation of photodynamic therapy. The complex demonstrates exceptional selectivity for H₂S and effectively transforms it into a potent PDT agent while reducing ATP levels in cells, making cancer cells more susceptible to apoptosis during treatment. This innovative approach has the potential to revolutionize cancer treatment through depletion-assisted activatable PDT with highly photoactive iridium complexes.

References

- (1) Li, X.; Gao, X.; Shi, W.; Ma, H. Design Strategies for Water-Soluble Small Molecular Chromogenic and Fluorogenic Probes. *Chemical Reviews*. January 8, 2014, pp 590–659. <https://doi.org/10.1021/cr300508p>.
- (2) Sameiro, M.; Gonçalves, T. Fluorescent Labeling of Biomolecules with Organic Probes. *Chem Rev* **2009**, *109* (1), 190–212. <https://doi.org/10.1021/cr0783840>.
- (3) Fam, T. K.; Klymchenko, A. S.; Collot, M. Recent Advances in Fluorescent Probes for Lipid Droplets. *Materials*. MDPI AG September 18, 2018. <https://doi.org/10.3390/ma11091768>.
- (4) Zhou, J.; Ma, H. Design Principles of Spectroscopic Probes for Biological Applications. *Chemical Science*. Royal Society of Chemistry 2016, pp 6309–6315. <https://doi.org/10.1039/c6sc02500e>.
- (5) De Silva, A. P.; Moody, T. S.; Wright, G. D. Fluorescent PET (Photoinduced Electron Transfer) Sensors as Potent Analytical Tools. *Analyst* **2009**, *134* (12), 2385–2393. <https://doi.org/10.1039/b912527m>.

- (6) Wu, D.; Sedgwick, A. C.; Gunnlaugsson, T.; Akkaya, E. U.; Yoon, J.; James, T. D. Fluorescent Chemosensors: The Past, Present and Future. *Chemical Society Reviews*. Royal Society of Chemistry December 7, 2017, pp 7105–7123. <https://doi.org/10.1039/c7cs00240h>.
- (7) Hira, J.; Uddin, M. J.; Haugland, M. M.; Lentz, C. S. From Differential Stains to Next Generation Physiology: Chemical Probes to Visualize Bacterial Cell Structure And Physiology. *Molecules (Basel, Switzerland)*. NLM (Medline) October 26, 2020. <https://doi.org/10.3390/molecules25214949>.
- (8) Jung, K. H.; Lee, K. H. Molecular Imaging in the Era of Personalized Medicine. *Journal of Pathology and Translational Medicine*. Seoul National University 2015, pp 5–12. <https://doi.org/10.4132/jptm.2014.10.24>.
- (9) Salih, S.; Elliyanti, A.; Alkatheeri, A.; AlYafei, F.; Almarri, B.; Khan, H. The Role of Molecular Imaging in Personalized Medicine. *Journal of Personalized Medicine*. MDPI February 1, 2023. <https://doi.org/10.3390/jpm13020369>.
- (10) Zhao, P.; Deng, Y.; Xiang, G.; Liu, Y. Nanoparticle-Assisted Sonosensitizers and Their Biomedical Applications. *International Journal of Nanomedicine*. Dove Medical Press Ltd 2021, pp 4615–4630. <https://doi.org/10.2147/IJN.S307885>.
- (11) Ramya, B. A. *Development of Molecular Probes and Nano-Carrier Delivery System for Intracellular Sensing and Theranostic Applications*.
- (12) Gao, F. P.; Lin, Y. X.; Li, L. L.; Liu, Y.; Mayerhöffer, U.; Spent, P.; Su, J. G.; Li, J. Y.; Würthner, F.; Wang, H. Supramolecular Adducts of Squaraine and Protein for Noninvasive Tumor Imaging and Photothermal Therapy *In Vivo*. *Biomaterials* **2014**, 35 (3), 1004–1014. <https://doi.org/10.1016/j.biomaterials.2013.10.039>.
- (13) Sempionatto, J. R.; Lasalde-Ramírez, J. A.; Mahato, K.; Wang, J.; Gao, W. Wearable Chemical Sensors for Biomarker Discovery in the Omics Era. *Nature Reviews Chemistry*. Nature Research December 1, 2022, pp 899–915. <https://doi.org/10.1038/s41570-022-00439-w>.
- (14) Broza, Y. Y.; Zhou, X.; Yuan, M.; Qu, D.; Zheng, Y.; Vishinkin, R.; Khatib, M.; Wu, W.; Haick, H. Disease Detection with Molecular Biomarkers: From Chemistry of Body Fluids to Nature-Inspired Chemical Sensors. *Chemical Reviews*. American Chemical Society November 27, 2019, pp 11761–11817. <https://doi.org/10.1021/acs.chemrev.9b00437>.
- (15) Dou, W. T.; Han, H. H.; Sedgwick, A. C.; Zhu, G. B.; Zang, Y.; Yang, X. R.; Yoon, J.; James, T. D.; Li, J.; He, X. P. Fluorescent Probes for the Detection of Disease-Associated Biomarkers. *Science Bulletin*. Elsevier B.V. April 30, 2022, pp 853–878. <https://doi.org/10.1016/j.scib.2022.01.014>.
- (16) Wu, D.; Sedgwick, A. C.; Gunnlaugsson, T.; Akkaya, E. U.; Yoon, J.; James, T. D. Fluorescent Chemosensors: The Past, Present and Future. *Chemical Society Reviews*. Royal Society of Chemistry December 7, 2017, pp 7105–7123. <https://doi.org/10.1039/c7cs00240h>.

-
- (17) Jiao, Y.; Zhu, B.; Chen, J.; Duan, X. Fluorescent Sensing of Fluoride in Cellular System. *Theranostics*. Ivyspring International Publisher 2015, pp 173–187. <https://doi.org/10.7150/thno.9860>.
- (18) Yuan, L.; Lin, W.; Zheng, K.; He, L.; Huang, W. Far-Red to near Infrared Analyte-Responsive Fluorescent Probes Based on Organic Fluorophore Platforms for Fluorescence Imaging. *Chem. Soc. Rev.* **2013**, *42* (2), 622–661. <https://doi.org/10.1039/C2CS35313J>.
- (19) Eun Jun, M.; Roy, B.; Han Ahn, K. “Turn-on” Fluorescent Sensing with “Reactive” Probes. *Chemical Communications* **2011**, *47* (27), 7583–7601. <https://doi.org/10.1039/c1cc00014d>.
- (20) Tian, X.; Murfin, L. C.; Wu, L.; Lewis, S. E.; James, T. D. Fluorescent Small Organic Probes for Biosensing. *Chemical Science*. Royal Society of Chemistry March 14, 2021, pp 3406–3426. <https://doi.org/10.1039/d0sc06928k>.
- (21) Sahoo, S. K.; Sharma, D.; Ber, R. K.; Crisponi, G.; Callan, J. F. Iron(III) Selective Molecular and Supramolecular Fluorescent Probes. *Chem Soc Rev* **2012**, *41* (21), 7195–7227. <https://doi.org/10.1039/c2cs35152h>.
- (22) Wang, L.; Zhang, J.; Kim, B.; Peng, J.; Berry, S. N.; Ni, Y.; Su, D.; Lee, J.; Yuan, L.; Chang, Y. T. Boronic Acid: A Bio-Inspired Strategy to Increase the Sensitivity and Selectivity of Fluorescent NADH Probe. *J Am Chem Soc* **2016**, *138* (33), 10394–10397. <https://doi.org/10.1021/jacs.6b05810>.
- (23) Joo, J. H.; Youn, D.; Park, S. Y.; Shin, D. S.; Lee, M. H. Mitochondria-Targetable Red-Emitting Probe for Real-Time Fluorescence Monitoring of NAD(P)H in Live Cells. *Dyes and Pigments* **2019**, *170*. <https://doi.org/10.1016/j.dyepig.2019.107561>.
- (24) Xiao, P.; Liu, J.; Wang, Z.; Tao, F.; Yang, L.; Yuan, G.; Sun, W.; Zhang, X. A Color Turn-on Fluorescent Probe for Real-Time Detection of Hydrogen Sulfide and Identification of Food Spoilage. *Chemical Communications* **2021**, *57* (41), 5012–5015. <https://doi.org/10.1039/d1cc01369f>.
- (25) Wang, T.; Douglass, E. F.; Fitzgerald, K. J.; Spiegel, D. A. A “Turn-On” Fluorescent Sensor for Methylglyoxal. *J Am Chem Soc* **2013**, *135* (33), 12429–12433. <https://doi.org/10.1021/ja406077j>.
- (26) Cheng, T.; Xu, Y.; Zhang, S.; Zhu, W.; Qian, X.; Duan, L. A Highly Sensitive and Selective OFF-ON Fluorescent Sensor for Cadmium in Aqueous Solution and Living Cell. *J Am Chem Soc* **2008**, *130* (48), 16160–16161. <https://doi.org/10.1021/ja806928n>.
- (27) The Huy, B.; Thangadurai, D. T.; Sharipov, M.; Ngoc Nghia, N.; Van Cuong, N.; Lee, Y. I. Recent Advances in Turn Off-on Fluorescence Sensing Strategies for Sensitive Biochemical Analysis - A Mechanistic Approach. *Microchemical Journal*. Elsevier Inc. August 1, 2022. <https://doi.org/10.1016/j.microc.2022.107511>.
- (28) Cao, J.; Zhang, H.; Liang, S.; Xu, Q. Rapid and Sensitive Fluorescence Sensing Detection of Nitroaromatic Compounds in Water Samples Based on Pyrene Functionalized Nanofibers Mat Prepared via Green Approach. *Microchemical Journal* **2021**, *165*. <https://doi.org/10.1016/j.microc.2021.106175>.
-

- (29) Demas, J. N.; DeGraff, B. A.; Coleman, P. B. Peer Reviewed: Oxygen Sensors Based on Luminescence Quenching. *Anal Chem* **1999**, *71* (23), 793A-800A. <https://doi.org/10.1021/ac9908546>.
- (30) Ngoc Nghia, N.; The Huy, B.; Thanh Phong, P.; Han, J. S.; Kwon, D. H.; Lee, Y. I. Simple Fluorescence Optosensing Probe for Spermine Based on Ciprofloxacin-Tb³⁺ Complexation. *PLoS One* **2021**, *16* (5), e0251306. <https://doi.org/10.1371/journal.pone.0251306>.
- (31) Roy, S.; Bobde, Y.; Ghosh, B.; Chakraborty, C. Targeted Bioimaging of Cancer Cells Using Free Folic Acid-Sensitive Molybdenum Disulfide Quantum Dots through Fluorescence “Turn-Off.” *ACS Appl Bio Mater* **2021**, *4* (3), 2839–2849. <https://doi.org/10.1021/acsabm.1c00090>.
- (32) Koteeswari, R.; Ashokkumar, P.; Malar, E. J. P.; Ramakrishnan, V. T.; Ramamurthy, P. Highly Selective, Sensitive and Quantitative Detection of Hg²⁺ in Aqueous Medium under Broad PH Range. *Chemical Communications* **2011**, *47* (27), 7695–7697. <https://doi.org/10.1039/c1cc12018b>.
- (33) Gupta, N.; Reja, S. I.; Bhalla, V.; Gupta, M.; Kaur, G.; Kumar, M. A Bodipy Based Dual Functional Probe for the Detection of Hydrogen Sulfide and H₂S Induced Apoptosis in Cellular System. *Journal Name RSCPublishing COMMUNICATION This journal is J. Name* **2012**, *00*, 1–3. <https://doi.org/10.1039/x0xx00000xReceived>.
- (34) Shi, L.; Yan, C.; Guo, Z.; Chi, W.; Wei, J.; Liu, W.; Liu, X.; Tian, H.; Zhu, W. H. De Novo Strategy with Engineering Anti-Kasha/Kasha Fluorophores Enables Reliable Ratiometric Quantification of Biomolecules. *Nat Commun* **2020**, *11* (1). <https://doi.org/10.1038/s41467-020-14615-3>.
- (35) Saranya, G.; Anees, P.; Joseph, M. M.; Maiti, K. K.; Ajayaghosh, A. A Ratiometric Near-Infrared Fluorogen for the Real Time Visualization of Intracellular Redox Status during Apoptosis. *Chemistry - A European Journal* **2017**, *23* (30), 7191–7195. <https://doi.org/10.1002/chem.201700839>.
- (36) Lim, C. S.; Masanta, G.; Kim, H. J.; Han, J. H.; Kim, H. M.; Cho, B. R. Ratiometric Detection of Mitochondrial Thiols with a Two-Photon Fluorescent Probe. *J Am Chem Soc* **2011**, *133* (29), 11132–11135. <https://doi.org/10.1021/ja205081s>.
- (37) Niu, L.-Y.; Guan, Y.-S.; Chen, Y.-Z.; Wu, L.-Z.; Tung, C.-H.; Yang, Q.-Z. *BODIPY Based Ratiometric Fluorescent Sensor for Highly Selective Detection of Glutathione over Cysteine and Homocysteine*; 2012. <http://pubs.acs.org>.
- (38) Cheng, D.; Pan, Y.; Wang, L.; Zeng, Z.; Yuan, L.; Zhang, X.; Chang, Y.-T. Selective Visualization of the Endogenous Peroxynitrite in an Inflamed Mouse Model by a Mitochondria-Targetable Two-Photon Ratiometric Fluorescent Probe. *J Am Chem Soc* **2017**, *139* (1), 285–292. <https://doi.org/10.1021/jacs.6b10508>.
- (39) Jensen, E. C. Use of Fluorescent Probes: Their Effect on Cell Biology and Limitations. *Anatomical Record*. Blackwell Publishing Inc. 2012, pp 2031–2036. <https://doi.org/10.1002/ar.22602>.

-
- (40) Xiao, D.; Qi, H.; Teng, Y.; Pierre, D.; Kutoka, P. T.; Liu, D. Advances and Challenges of Fluorescent Nanomaterials for Synthesis and Biomedical Applications. *Nanoscale Research Letters*. Springer 2021. <https://doi.org/10.1186/s11671-021-03613-z>.
- (41) Berezin, M. Y.; Achilefu, S. Fluorescence Lifetime Measurements and Biological Imaging. *Chem Rev* **2010**, *110* (5), 2641–2684. <https://doi.org/10.1021/cr900343z>.
- (42) Perumal, J.; Wang, Y.; Attia, A. B. E.; Dinish, U. S.; Olivo, M. Towards a Point-of-Care SERS Sensor for Biomedical and Agri-Food Analysis Applications: A Review of Recent Advancements. *Nanoscale*. Royal Society of Chemistry January 14, 2021, pp 553–580. <https://doi.org/10.1039/d0nr06832b>.
- (43) Spring, H.; Cem, M. S. U. SERS Surface Enhanced Raman Spectroscopy. *J. of Physical chemistry* **2001**, *27*, 113–186.
- (44) Ramya, A. N.; Arya, J. S.; Madhukrishnan, M.; Shamjith, S.; Vidyalekshmi, M. S.; Maiti, K. K. Raman Imaging: An Impending Approach Towards Cancer Diagnosis. *Chemistry - An Asian Journal*. John Wiley and Sons Ltd March 1, 2021, pp 409–422. <https://doi.org/10.1002/asia.202001340>.
- (45) Joseph, M. M.; Narayanan, N.; Nair, J. B.; Karunakaran, V.; Ramya, A. N.; Sujai, P. T.; Saranya, G.; Arya, J. S.; Vijayan, V. M.; Maiti, K. K. Exploring the Margins of SERS in Practical Domain: An Emerging Diagnostic Modality for Modern Biomedical Applications. *Biomaterials* **2018**, *181*, 140–181. <https://doi.org/10.1016/j.biomaterials.2018.07.045>.
- (46) Lee, S.; Chon, H.; Yoon, S.-Y.; Lee, E. K.; Chang, S.-I.; Lim, D. W.; Choo, J. Fabrication of SERS-Fluorescence Dual Modal Nanoprobes and Application to Multiplex Cancer Cell Imaging. *Nanoscale* **2012**, *4* (1), 124. <https://doi.org/10.1039/c1nr11243k>.
- (47) Ramya, A. N.; Samanta, A.; Nisha, N.; Chang, Y. T.; Maiti, K. K. New Insight of Squaraine-Based Biocompatible Surface-Enhanced Raman Scattering Nanotag for Cancer-Cell Imaging. *Nanomedicine* **2015**, *10* (4), 561–571. <https://doi.org/10.2217/nmm.14.125>.
- (48) Karunakaran, V.; Saritha, V. N.; Joseph, M. M.; Nair, J. B.; Saranya, G.; Raghu, K. G.; Sujathan, K.; Kumar, K. S.; Maiti, K. K. Diagnostic Spectro-Cytology Revealing Differential Recognition of Cervical Cancer Lesions by Label-Free Surface Enhanced Raman Fingerprints and Chemometrics. *Nanomedicine* **2020**, *29*. <https://doi.org/10.1016/j.nano.2020.102276>.
- (49) Karunakaran, V.; Saritha, V. N.; Ramya, A. N.; Murali, V. P.; Raghu, K. G.; Sujathan, K.; Maiti, K. K. Elucidating Raman Image-Guided Differential Recognition of Clinically Confirmed Grades of Cervical Exfoliated Cells by Dual Biomarker-Appended SERS-Tag. *Anal Chem* **2021**, *93* (32), 11140–11150. <https://doi.org/10.1021/acs.analchem.1c01607>.
- (50) Ramya, A. N.; Joseph, M. M.; Nair, J. B.; Karunakaran, V.; Narayanan, N.; Maiti, K. K. New Insight of Tetraphenylethylene-Based Raman Signatures for Targeted SERS Nanoprobe Construction Toward Prostate Cancer Cell Detection. *ACS Appl Mater Interfaces* **2016**, *8* (16). <https://doi.org/10.1021/acsami.6b01908>.
-

- (51) Ahn, Y. J.; Gil, Y. G.; Lee, Y. J.; Jang, H.; Lee, G. J. A Dual-Mode Colorimetric and SERS Detection of Hydrogen Sulfide in Live Prostate Cancer Cells Using a Silver Nanoplate-Coated Paper Assay. *Microchemical Journal* **2020**, *155*. <https://doi.org/10.1016/j.microc.2020.104724>.
- (52) Saranya, G.; Joseph, M. M.; Karunakaran, V.; Nair, J. B.; Saritha, V. N.; Veena, V. S.; Sujathan, K.; Ajayaghosh, A.; Maiti, K. K. Enzyme-Driven Switchable Fluorescence-SERS Diagnostic Nanococktail for the Multiplex Detection of Lung Cancer Biomarkers. *ACS Appl Mater Interfaces* **2018**. <https://doi.org/10.1021/acsami.8b15583>.
- (53) Gu, X.; Wang, H.; Schultz, Z. D.; Camden, J. P. Sensing Glucose in Urine and Serum and Hydrogen Peroxide in Living Cells by Use of a Novel Boronate Nanoprobe Based on Surface-Enhanced Raman Spectroscopy. *Anal Chem* **2016**, *88* (14), 7191–7197. <https://doi.org/10.1021/acs.analchem.6b01378>.
- (54) Zhang, W.; Tang, S.; Jin, Y.; Yang, C.; He, L.; Wang, J.; Chen, Y. Multiplex SERS-Based Lateral Flow Immunosensor for the Detection of Major Mycotoxins in Maize Utilizing Dual Raman Labels and Triple Test Lines. *J Hazard Mater* **2020**, *393*. <https://doi.org/10.1016/j.jhazmat.2020.122348>.
- (55) Ning, Y.; Jin, G. Q.; Wang, M. X.; Gao, S.; Zhang, J. L. Recent Progress in Metal-Based Molecular Probes for Optical Bioimaging and Biosensing. *Current Opinion in Chemical Biology*. Elsevier Ltd February 1, 2022. <https://doi.org/10.1016/j.cbpa.2021.102097>.
- (56) Liu, Z.; He, W.; Guo, Z. Metal Coordination in Photoluminescent Sensing. *Chem Soc Rev* **2013**, *42* (4), 1568–1600. <https://doi.org/10.1039/c2cs35363f>.
- (57) Li, G.; Zhu, Z. Q.; Chen, Q.; Li, J. Metal Complex Based Delayed Fluorescence Materials. *Organic Electronics*. Elsevier B.V. June 1, 2019, pp 135–152. <https://doi.org/10.1016/j.orgel.2019.02.022>.
- (58) Reddy, M. L. P.; Bejoymohandas, K. S. JPhCPhB C Photochemistry Review Evolution of 2, 3-Bipyridine Class of Cyclometalating Ligands as Efficient Phosphorescent Iridium(III) Emitters for Applications in Organic Light Emitting Diodes. “*Journal of Photochemistry & Photobiology, C: Photochemistry Reviews*” **2016**, *29*, 29–47. <https://doi.org/10.13140/RG.2.2.33202.50885>.
- (59) Frei, A.; Zuegg, J.; Elliott, A. G.; Baker, M.; Braese, S.; Brown, C.; Chen, F.; G. Dowson, C.; Dujardin, G.; Jung, N.; King, A. P.; Mansour, A. M.; Massi, M.; Moat, J.; Mohamed, H. A.; Renfrew, A. K.; Rutledge, P. J.; Sadler, P. J.; Todd, M. H.; Willans, C. E.; Wilson, J. J.; Cooper, M. A.; Blaskovich, M. A. T. Metal Complexes as a Promising Source for New Antibiotics. *Chem Sci* **2020**, *11* (10), 2627–2639. <https://doi.org/10.1039/c9sc06460e>.
- (60) Aoki, S.; Matsuo, Y.; Ogura, S.; Ohwada, H.; Hisamatsu, Y.; Moromizato, S.; Shiro, M.; Kitamura, M. Regioselective Aromatic Substitution Reactions of Cyclometalated Ir(III) Complexes: Synthesis and Photochemical Properties of Substituted Ir(III) Complexes That Exhibit Blue, Green, and Red Color Luminescence Emission. *Inorg Chem* **2011**, *50* (3), 806–818. <https://doi.org/10.1021/ic101164g>.

-
- (61) Lo, K. K. W.; Tso, K. K. S. Functionalization of Cyclometalated Iridium(III) Polypyridine Complexes for the Design of Intracellular Sensors, Organelle-Targeting Imaging Reagents, and Metallodrugs. *Inorg Chem Front* **2015**, *2* (6), 510–524. <https://doi.org/10.1039/c5qi00002e>.
- (62) Yu, M.; Zhao, Q.; Shi, L.; Li, F.; Zhou, Z.; Yang, H.; Yi, T.; Huang, C. Cationic Iridium(III) Complexes for Phosphorescence Staining in the Cytoplasm of Living Cells. *Chemical Communications* **2008**, No. 18, 2115–2117. <https://doi.org/10.1039/b800939b>.
- (63) Zhang, K. Y.; Li, S. P. Y.; Zhu, N.; Or, L. W. S.; Cheung, M. S. H.; Lam, Y. W.; Lo, K. K. W. Structure, Photophysical and Electrochemical Properties, Biomolecular Interactions, and Intracellular Uptake of Luminescent Cyclometalated Iridium(III) Dipyridoquinoxaline Complexes. *Inorg Chem* **2010**, *49* (5), 2530–2540. <https://doi.org/10.1021/ic902465b>.
- (64) Murphy, L.; Congreve, A.; Pålsson, L. O.; Williams, J. A. G. The Time Domain in Co-Stained Cell Imaging: Time-Resolved Emission Imaging Microscopy Using a Protonatable Luminescent Iridium Complex. *Chemical Communications* **2010**, *46* (46), 8743–8745. <https://doi.org/10.1039/c0cc03705b>.
- (65) Law, W. H. T.; Lee, L. C. C.; Louie, M. W.; Liu, H. W.; Ang, T. W. H.; Lo, K. K. W. Phosphorescent Cellular Probes and Uptake Indicators Derived from Cyclometalated Iridium(III) Bipyridine Complexes Appended with a Glucose or Galactose Entity. *Inorg Chem* **2013**, *52* (22), 13029–13041. <https://doi.org/10.1021/ic401714p>.
- (66) Wragg, A.; Gill, M. R.; Turton, D.; Adams, H.; Roseveare, T. M.; Smythe, C.; Su, X.; Thomas, J. A. Tuning the Cellular Uptake Properties of Luminescent Heterobimetallic Iridium(III)-Ruthenium(II) DNA Imaging Probes. *Chemistry - A European Journal* **2014**, *20* (43), 14004–14011. <https://doi.org/10.1002/chem.201403693>.
- (67) Sun, L.; Chen, Y.; Kuang, S.; Li, G.; Guan, R.; Liu, J.; Ji, L.; Chao, H. Iridium(III) Anthraquinone Complexes as Two-Photon Phosphorescence Probes for Mitochondria Imaging and Tracking under Hypoxia. *Chemistry - A European Journal* **2016**, *22* (26), 8955–8965. <https://doi.org/10.1002/chem.201600310>.
- (68) Cho, Y. J.; Kim, S. Y.; Choi, C. M.; Kim, N. J.; Kim, C. H.; Cho, D. W.; Son, H. J.; Pac, C.; Kang, S. O. Photophysics and Excited-State Properties of Cyclometalated Iridium(III)-Platinum(II) and Iridium(III)-Iridium(III) Bimetallic Complexes Bridged by Dipyridylpyrazine. *Inorg Chem* **2017**, *56* (9), 5305–5315. <https://doi.org/10.1021/acs.inorgchem.7b00384>.
- (69) Cho, Y.; Kim, S.; Choi, C. M.; Kim, N. J.; Kim, C. H.; Cho, D. W. Photophysics and Properties of Cyclometalated Iridium (III) – Platinum (II) and Iridium (III) – Iridium (III) Bimetallic Complexes Bridged by Dipyridylpyrazine Experimental Section C NMR Spectra for Compound 1 Was Recorded on a Varian Mercury 300 . 1–40.
- (70) He, T.; Qin, X.; Jiang, C.; Jiang, D.; Lei, S.; Lin, J.; Zhu, W. G.; Qu, J.; Huang, P. Tumor PH-Responsive Metastable-Phase Manganese Sulfide Nanotheranostics for
-

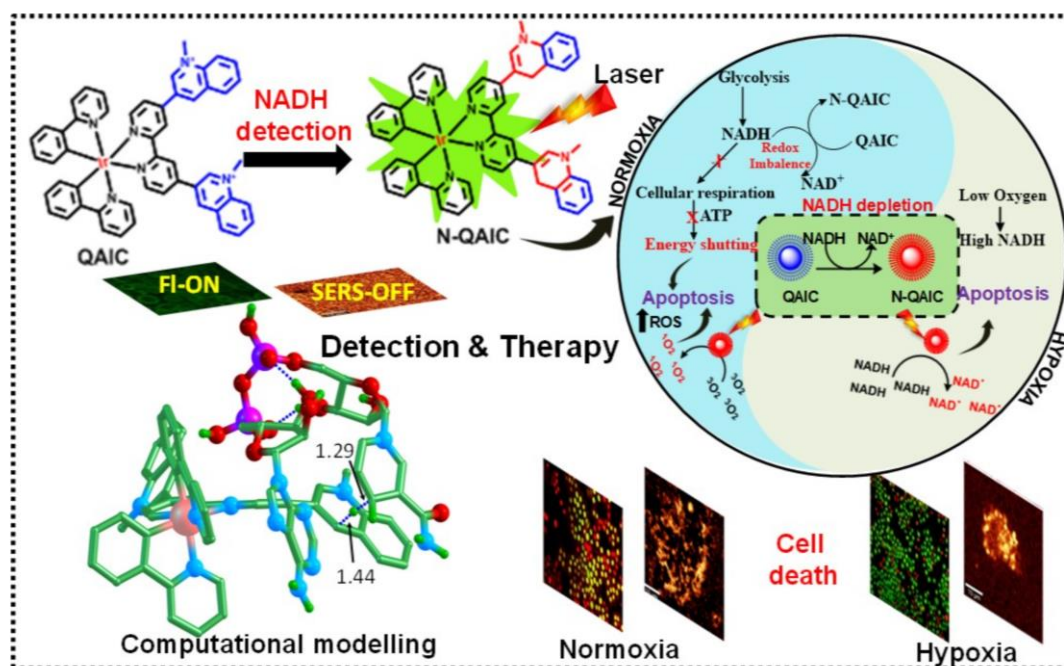
- Traceable Hydrogen Sulfide Gas Therapy Primed Chemodynamic Therapy. *Theranostics* **2020**, *10* (6), 2453–2462. <https://doi.org/10.7150/thno.42981>.
- (71) Cheng, L.; Wang, C.; Liu, Z. Functional Nanomaterials for Phototherapies of Cancer. *Chinese Journal of Clinical Oncology* **2014**, *41* (1), 18–26. <https://doi.org/10.3969/j.issn.1000-8179.20131829>.
- (72) Imberti, C.; Zhang, P.; Huang, H.; Sadler, P. J. New Designs for Phototherapeutic Transition Metal Complexes. *Angewandte Chemie* **2020**, *132* (1), 61–73. <https://doi.org/10.1002/ange.201905171>.
- (73) Tang, W.; Xu, H.; Kopelman, R.; Philbert, M. A. Photodynamic Characterization And. *J. Photochem. Photobiol.* **2005**, *81*, 242–249.
- (74) Dolmans, D. E. J. G. J.; Fukumura, D.; Jain, R. K. Photodynamic Therapy for Cancer. *Nature Reviews Cancer*. 2003. <https://doi.org/10.1038/nrc1071>.
- (75) Cheng, L.; Wang, C.; Feng, L.; Yang, K.; Liu, Z. Functional Nanomaterials for Phototherapies of Cancer. *Chemical Reviews*. American Chemical Society November 12, 2014, pp 10869–10939. <https://doi.org/10.1021/cr400532z>.
- (76) Tian, B.; Wang, C.; Zhang, S.; Feng, L.; Liu, Z. Photothermally Enhanced Photodynamic Therapy Delivered by Nano-Graphene Oxide. *ACS Nano* **2011**, *5* (9), 7000–7009. <https://doi.org/10.1021/nn201560b>.
- (77) Kwon, Y. M. I. N.; Je, J. A. E. Y.; Cha, S. H.; Oh, Y.; Cho, W. O. N. H. O. Synergistic Combination of Chemo - Phototherapy Based on Temozolomide / ICG - Loaded Iron Oxide Nanoparticles for Brain Cancer Treatment. **2019**, 1709–1724. <https://doi.org/10.3892/or.2019.7289>.
- (78) Zhao, J.; Yan, K.; Xu, G.; Liu, X.; Zhao, Q.; Xu, C.; Gou, S. An Iridium (III) Complex Bearing a Donor–Acceptor–Donor Type Ligand for NIR-Triggered Dual Phototherapy. *Adv Funct Mater* **2021**, *31* (11). <https://doi.org/10.1002/adfm.202008325>.
- (79) Mroz, P.; Yaroslavsky, A.; Kharkwal, G. B.; Hamblin, M. R. Cell Death Pathways in Photodynamic Therapy of Cancer. *Cancers*. June 2011, pp 2516–2539. <https://doi.org/10.3390/cancers3022516>.
- (80) Celli, J. P.; Spring, B. Q.; Rizvi, I.; Evans, C. L.; Samkoe, K. S.; Verma, S.; Pogue, B. W.; Hasan, T. Imaging and Photodynamic Therapy: Mechanisms, Monitoring, and Optimization. *Chem Rev* **2010**, *110* (5), 2795–2838. <https://doi.org/10.1021/cr900300p>.
- (81) Tardivo, J. P.; Del Giglio, A.; De Oliveira, C. S.; Gabrielli, D. S.; Junqueira, H. C.; Tada, D. B.; Severino, D.; De Fátima Turchiello, R.; Baptista, M. S. Methylene Blue in Photodynamic Therapy: From Basic Mechanisms to Clinical Applications. *Photodiagnosis Photodyn Ther* **2005**, *2* (3), 175–191. [https://doi.org/10.1016/S1572-1000\(05\)00097-9](https://doi.org/10.1016/S1572-1000(05)00097-9).
- (82) Correia, J. H.; Rodrigues, J. A.; Pimenta, S.; Dong, T.; Yang, Z. Photodynamic Therapy Review: Principles, Photosensitizers, Applications, and Future Directions. *Pharmaceutics* **2021**, *13* (9). <https://doi.org/10.3390/pharmaceutics13091332>.

-
- (83) Wu, Y.; Li, S.; Chen, Y.; He, W.; Guo, Z. Recent Advances in Noble Metal Complex Based Photodynamic Therapy. *Chem Sci* **2022**. <https://doi.org/10.1039/d1sc05478c>.
- (84) Dos Santos, A. F.; De Almeida, D. R. Q.; Terra, L. F.; Baptista, M. S.; Labriola, L. Photodynamic Therapy in Cancer Treatment - an Update Review. *J Cancer Metastasis Treat* **2019**, *2019*. <https://doi.org/10.20517/2394-4722.2018.83>.
- (85) Awuah, S. G.; You, Y. Boron Dipyrromethene (BODIPY)-Based Photosensitizers for Photodynamic Therapy. *RSC Adv* **2012**, *2* (30), 11169. <https://doi.org/10.1039/c2ra21404k>.
- (86) Wu, W.; Shao, X.; Zhao, J.; Wu, M. Controllable Photodynamic Therapy Implemented by Regulating Singlet Oxygen Efficiency. **2017**, *1700113*. <https://doi.org/10.1002/advs.201700113>.
- (87) Zheng, Y.; He, L.; Zhang, D. Y.; Tan, C. P.; Ji, L. N.; Mao, Z. W. Mixed-Ligand Iridium(III) Complexes as Photodynamic Anticancer Agents. *Dalton Transactions* **2017**, *46* (34), 11395–11407. <https://doi.org/10.1039/c7dt02273e>.
- (88) Abbas, S.; Din, I. ud D.; Raheel, A.; Tameez ud Din, A. Cyclometalated Iridium (III) Complexes: Recent Advances in Phosphorescence Bioimaging and Sensing Applications. *Applied Organometallic Chemistry*. John Wiley and Sons Ltd March 1, 2020. <https://doi.org/10.1002/aoc.5413>.
- (89) Huang, H.; Banerjee, S.; Qiu, K.; Zhang, P.; Blacque, O.; Malcomson, T.; Paterson, M. J.; Clarkson, G. J.; Staniforth, M.; Stavros, V. G.; Gasser, G.; Chao, H.; Sadler, P. J. Targeted Photoredox Catalysis in Cancer Cells. *Nat Chem* **2019**, *11* (11), 1041–1048. <https://doi.org/10.1038/s41557-019-0328-4>.
- (90) Yuan, H.; Han, Z.; Chen, Y.; Qi, F.; Fang, H.; Guo, Z.; Zhang, S.; He, W. Ferroptosis Photoinduced by New Cyclometalated Iridium(III) Complexes and Its Synergism with Apoptosis in Tumor Cell Inhibition. *Angewandte Chemie - International Edition* **2021**, *60* (15), 8174–8181. <https://doi.org/10.1002/anie.202014959>.
- (91) Viguera, G.; Markova, L.; Novohradsky, V.; Marco, A.; Cutillas, N.; Kosthrunova, H.; Kasparkova, J.; Ruiz, J.; Brabec, V. A Photoactivated Ir(III) Complex Targets Cancer Stem Cells and Induces Secretion of Damage-Associated Molecular Patterns in Melanoma Cells Characteristic of Immunogenic Cell Death. *Inorg Chem Front* **2021**, *8* (21), 4696–4711. <https://doi.org/10.1039/d1qi00856k>.
- (92) Wang, L.; Karges, J.; Wei, F.; Xie, L.; Chen, Z.; Gasser, G.; Ji, L.; Chao, H. A Mitochondria-Localized Iridium(III) Photosensitizer for Two-Photon Photodynamic Immunotherapy against Melanoma. *Chem Sci* **2023**, *14* (6), 1461–1471. <https://doi.org/10.1039/d2sc06675k>.
- (93) Xue, F.; Shi, M.; Yan, Y.; Yang, H.; Zhou, Z.; Yang, S. Iridium Complex Loaded Polypyrrole Nanoparticles for NIR Laser Induced Photothermal Effect and Generation of Singlet Oxygen. *RSC Adv* **2016**, *6* (19), 15509–15512. <https://doi.org/10.1039/c5ra22092k>.
- (94) He, L.; Li, Y.; Tan, C. P.; Ye, R. R.; Chen, M. H.; Cao, J. J.; Ji, L. N.; Mao, Z. W. Cyclometalated Iridium(III) Complexes as Lysosome-Targeted Photodynamic
-

- Anticancer and Real-Time Tracking Agents. *Chem Sci* **2015**, *6* (10), 5409–5418. <https://doi.org/10.1039/c5sc01955a>.
- (95) Lv, W.; Zhang, Z.; Zhang, K. Y.; Yang, H.; Liu, S.; Xu, A.; Guo, S.; Zhao, Q.; Huang, W. A Mitochondria-Targeted Photosensitizer Showing Improved Photodynamic Therapy Effects Under Hypoxia. *Angewandte Chemie* **2016**, *128* (34), 10101–10105. <https://doi.org/10.1002/ange.201604130>.
- (96) Kuang, S.; Sun, L.; Zhang, X.; Liao, X.; Rees, T. W.; Zeng, L.; Chen, Y.; Zhang, X.; Ji, L.; Chao, H. A Mitochondrion-Localized Two-Photon Photosensitizer Generating Carbon Radicals Against Hypoxic Tumors. *Angewandte Chemie - International Edition* **2020**, *59* (46), 20697–20703. <https://doi.org/10.1002/anie.202009888>.
- (97) Aksakal, N. E.; Eçik, E. T.; Kazan, H. H.; Yenilmez Çiftçi, G.; Yuksel, F. Novel Ruthenium(Ii) and Iridium(Iii) BODIPY Dyes: Insights into Their Application in Photodynamic Therapy: *In-Vitro*. *Photochemical and Photobiological Sciences* **2019**, *18* (8), 2012–2022. <https://doi.org/10.1039/c9pp00201d>.
- (98) Novohradsky, V.; Rovira, A.; Hally, C.; Galindo, A.; Vigueras, G.; Gandioso, A.; Svitelova, M.; Bresolí-Obach, R.; Kostrhunova, H.; Markova, L.; Kasparikova, J.; Nonell, S.; Ruiz, J.; Brabec, V.; Marchán, V. Towards Novel Photodynamic Anticancer Agents Generating Superoxide Anion Radicals: A Cyclometalated IrIII Complex Conjugated to a Far-Red Emitting Coumarin. *Angewandte Chemie - International Edition* **2019**, *58* (19), 6311–6315. <https://doi.org/10.1002/anie.201901268>.
- (99) Lan, G.; Ni, K.; Xu, R.; Lu, K.; Lin, Z.; Chan, C.; Lin, W. Nanoscale Metal–Organic Layers for Deeply Penetrating X-Ray-Induced Photodynamic Therapy. *Angewandte Chemie - International Edition* **2017**, *56* (40), 12102–12106. <https://doi.org/10.1002/anie.201704828>.
- (100) Lovell, J. F.; Liu, T. W. B.; Chen, J.; Zheng, G. Activatable Photosensitizers for Imaging and Therapy. *Chem Rev* **2010**, *110* (5), 2839–2857. <https://doi.org/10.1021/cr900236h>.
- (101) Wang, W.; Jin, Y.; Xu, Z.; Liu, X.; Bajwa, S. Z.; Khan, W. S.; Yu, H. Stimuli-Activatable Nanomedicines for Chemodynamic Therapy of Cancer. *Wiley Interdisciplinary Reviews: Nanomedicine and Nanobiotechnology*. Wiley-Blackwell July 1, 2020. <https://doi.org/10.1002/wnan.1614>.
- (102) Anees, P.; Sreejith, S.; Ajayaghosh, A. Self-Assembled near-Infrared Dye Nanoparticles as a Selective Protein Sensor by Activation of a Dormant Fluorophore. *J Am Chem Soc* **2014**, *136* (38), 13233–13239. <https://doi.org/10.1021/ja503850b>.
- (103) Turan, I. S.; Cakmak, F. P.; Yildirim, D. C.; Cetin-Atalay, R.; Akkaya, E. U. Near-IR Absorbing BODIPY Derivatives as Glutathione-Activated Photosensitizers for Selective Photodynamic Action. *Chemistry - A European Journal* **2014**, *20* (49), 16088–16092. <https://doi.org/10.1002/chem.201405450>.
- (104) Ichikawa, Y.; Kamiya, M.; Obata, F.; Miura, M.; Terai, T.; Komatsu, T.; Ueno, T.; Hanaoka, K.; Nagano, T.; Urano, Y. Selective Ablation of β -Galactosidase-Expressing Cells with a Rationally Designed Activatable Photosensitizer.

-
- Angewandte Chemie* **2014**, *126* (26), 6890–6893.
<https://doi.org/10.1002/ange.201403221>.
- (105) Anderson, E. D.; Gorke, A. P.; Schnermann, M. J. Near-Infrared Uncaging or Photosensitizing Dictated by Oxygen Tension. *Nat Commun* **2016**, *7*.
<https://doi.org/10.1038/ncomms13378>.
- (106) Yuan, Y.; Xu, S.; Cheng, X.; Cai, X.; Liu, B. Bioorthogonal Turn-On Probe Based on Aggregation-Induced Emission Characteristics for Cancer Cell Imaging and Ablation. *Angewandte Chemie* **2016**, *128* (22), 6567–6571.
<https://doi.org/10.1002/ange.201601744>.
- (107) Yang, K.; Zhou, Y.; Wang, Y.; Zhao, S.; Wu, X.; Peng, X.; Huang, L.; Jiang, L.; Lan, M.; Yi, X. Y. An Iridium Complex as an AIE-Active Photosensitizer for Image-Guided Photodynamic Therapy. *Chem Asian J* **2021**, *16* (13), 1780–1785.
<https://doi.org/10.1002/asia.202100291>.
- (108) Zhou, L.; Wei, F.; Xiang, J.; Li, H.; Li, C.; Zhang, P.; Liu, C.; Gong, P.; Cai, L.; Wong, K. M. C. Enhancing the ROS Generation Ability of a Rhodamine-Decorated Iridium(III) Complex by Ligand Regulation for Endoplasmic Reticulum-Targeted Photodynamic Therapy. *Chem Sci* **2020**, *11* (44), 12212–12220.
<https://doi.org/10.1039/d0sc04751a>.
- (109) Huang, T.; Yu, Q.; Liu, S.; Zhang, K. Y.; Huang, W.; Zhao, Q. Rational Design of Phosphorescent Iridium(III) Complexes for Selective Glutathione Sensing and Amplified Photodynamic Therapy. *ChemBioChem* **2019**, *20* (4), 576–586.
<https://doi.org/10.1002/cbic.201800507>.
- (110) Du, Z.; Zhang, R.; Song, B.; Zhang, W.; Wang, Y. L.; Liu, J.; Liu, C.; Xu, Z. P.; Yuan, J. Iridium(III) Complex-Based Activatable Probe for Phosphorescent/Time-Gated Luminescent Sensing and Imaging of Cysteine in Mitochondria of Live Cells and Animals. *Chemistry - A European Journal* **2019**, *25* (6), 1498–1506.
<https://doi.org/10.1002/chem.201805079>.
-

NADH-Depletion Triggered Energy Shutting with Cyclometalated Iridium (III) Complex Enables Bimodal Luminescence-SERS Sensing and Photodynamic Therapy



Abstract

The nicotinamide adenine dinucleotide-reduced (NADH) maintains intracellular redox status by functioning as a hydride (H) carrier in cellular homeostasis and its imbalance is reflected in many diseases including cancer. Here we report a quinoline appended iridium complex (QAIC) as a bimodal molecular probe with respect to fluorescence and surface-enhanced Raman spectroscopy (SERS), to assess the endogenous NADH in cancerous cells. NADH-triggered activation of QAIC enabled complementary luminescence turn-ON and SERS turn-OFF switching patterns and furnished a detection limit of 25.6 nM in luminescence and 15 pM in SERS w.r.t. NADH. Transition state modeling using density functional theory calculations proved that a facile migration of H—from NADH to QAIC transformed the activated QAIC (denoted as NAD---QAICH i.e., N-QAIC) with an energy span of 19.7 kcal/mol. Furthermore, N-QAIC is probed as a photosensitizer which subsequently generates singlet oxygen upon laser irradiation to source the photodynamic therapy (PDT) by blocking the photo-induced electron transfer (PeT) during the hydride

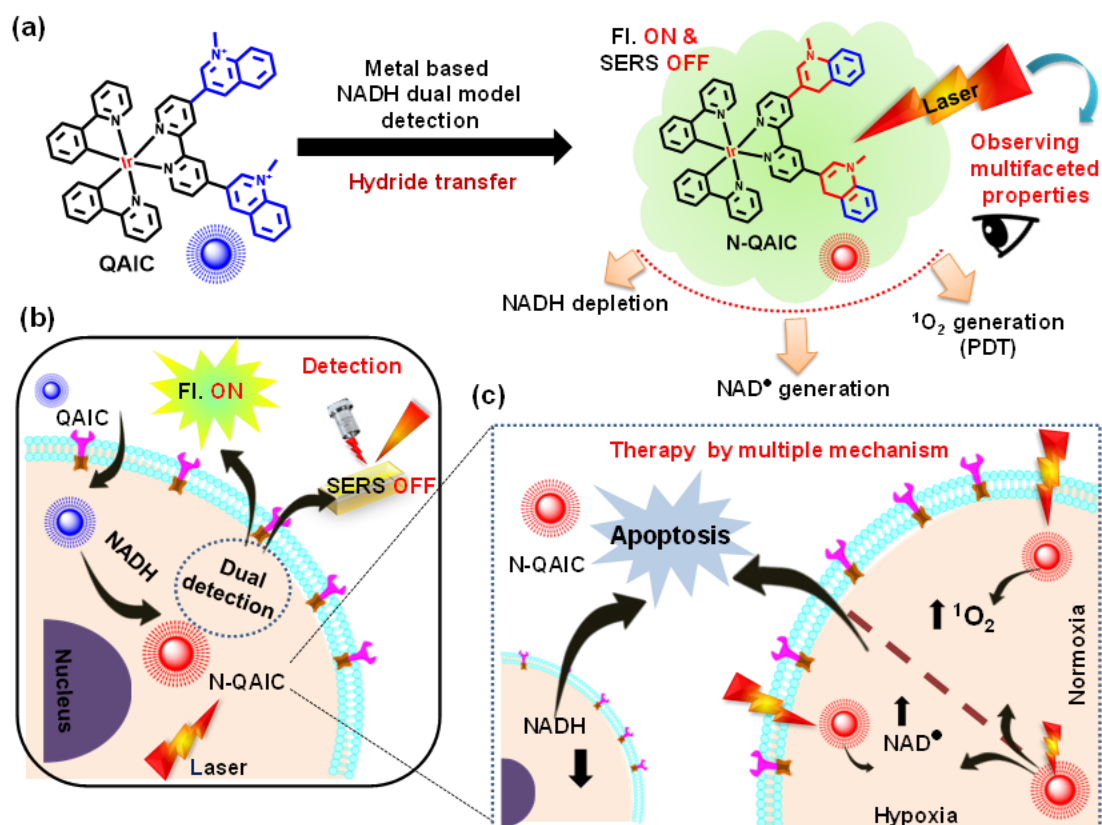
transfer process. Interestingly, N-QAIC-triggered NAD radicals were observed during the intracellular reduction of cytochrome c in hepatocellular carcinoma cells (HepG2) as identified by the signature Raman fingerprint at 750 cm⁻¹. Therefore, light-triggered radical generation of iridium complex propelled the toxic NAD radical without the requirement of molecular oxygen, illustrating a new way of oxygen-independent PDT. The current approach with the active shutting of energy production via NADH depletion followed by image-guided PDT by the cyclometalated iridium complex unveiled a futuristic candidate for cancer theranostics.

2.1 Introduction

Altered cellular metabolism is a hallmark of cancer¹ where, the excess energy required for various anaplerotic reactions is managed by the intracellular levels of nicotinamide adenine dinucleotide in reduced form (NADH).² As a cofactor, NADH performs vital roles in the metabolic activities of cells including energy production, response to stimuli, redox balancing, electron transport and regulates the redox homeostasis.³ The classical Warburg theory and the modern symbiotic theory of cancer metastasis eventually spotlight the significance of NADH in cancer progression.⁴ Since cancer cells intuitively prefer to transform pyruvate to lactate, elevated NADH levels can be considered as a marker for tumorigenesis. Therefore, selective depletion of NADH can shut down the energy production, forcing the cells into a redox uncertainty.⁵ Tumor develop a hypoxic core and create a barrier to most of the therapies. Screening of metabolites related to low oxygen conditions figure out the elevated level of NADH, making it as a key targeting modality towards tumor hypoxia.⁶ In this regard, it is worth to explore NADH detection using new generation molecular probes which enable to direct both sensing and therapy.⁷ Molecular probes built upon metal complexes with the capacity for the simultaneous detection of NADH and exerting therapeutic effect will hold certain merits.⁸ The fascinating photophysical features, high quantum yield, ease of synthesis and tunable emission characteristics of iridium based cyclometalated complexes satisfies the requirements of a molecular sensor. Moreover, the activated singlet oxygen conversion efficiency and elevated aqueous solubility are added advantages of iridium complexes over other organic sensor moieties.^{9,10} So far, there is no report on the selective detection of intracellular NADH using cyclometalated iridium complexes. Recent studies established that iridium metal complex can act as photo redox agents to produce carbon-centered free radical from specific metabolites including NADH.¹¹

Photodynamic therapy (PDT) has received attention in precision medicine due to its localized therapeutic possibilities over the conventional cancer treatment modalities. The practical application of PDT depends on the availability of efficient photosensitizers (PS) capable of producing reactive oxygen species (ROS) in type-I and other free radicals in type-II upon light trigger.^{12,13} Free radical scavenging activity of antioxidants in the cellular environment reduces the efficiency of PS and hence a molecule which selectively activated in tumor micro environment could be useful in clinical settings. Hypoxic nature of most tumours hampers the production of ROS and thereby restrains the PDT process. Moreover, PDT itself, by utilizing the intracellular oxygen reserves, leads to severe hypoxia, thereby making the situation more complex. Therapeutic approaches for handling hypoxia and enhance the efficiency of PDT is the hallmark of antitumor treatment.¹⁴ Since reduced oxygen concentration is the major bottleneck of PDT, researchers are focusing on approaches that work without the need of oxygen i.e. oxygen independent PDT.

Herein, an oxygen independent PDT approach has been demonstrated using an in-house iridium-based metal complex wherein 1-methylquinolium moiety appended by pyridine was positioned as the ancillary ligand. The newly designed complex named as '1-methylquinolium Appended Iridium Complex' (QAIC); can selectively monitor the dynamics in the cytosolic NAD⁺ and NADH redox states *via* performing a redox reaction between NADH and QAIC. The ancillary ligand in the QAIC was introduced to promote a redox reaction with NADH, with high specificity and fidelity. As a new insight, the unique Raman signature peak of iridium at around 1042 cm⁻¹ facilitates real-time monitoring of the complex through surface enhanced Raman spectroscopy (SERS). A fine-tuned turn-ON luminescence and turn-OFF SERS signals was observed when QAIC gets reduced by NADH. It was hypothesized that, the reaction of QAIC with NADH could stop the process of photo induced electron transfer (PeT) and concomitant activation of both luminescence and PDT with a charge reversal promotes a decline in the SERS signals. Our molecular probe expected to exhibit the following processes, (i) real-time detection of endogenous NADH in cancer cells, (ii) turn-ON luminescence and turn-OFF SERS switching bimodal detection, (iii) tracking the molecular events *via* SERS fingerprint analysis, (iv) possibility of NADH depletion triggered cancer therapy, (v) NAD radical generation capability and (vi) inducing enhanced PDT towards both normoxic and hypoxic conditions. So far, this is the first demonstration where the NADH triggered "ON-OFF" sensing approach synchronizing the detection as well as phototherapy with iridium-based metal complex by SERS and fluorescence-based bimodal strategies (**Scheme 2.1**).



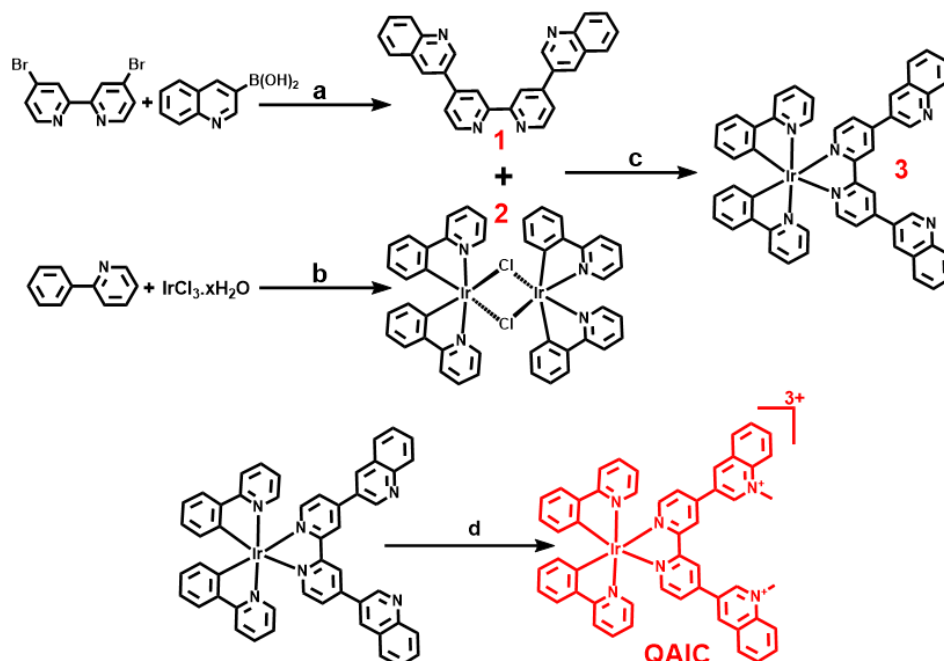
Scheme 2.1: Schematic illustration of NADH sensing and light assisted therapeutic action by QAIC. (a) The mechanism of NADH detection with QAIC, and light triggered additional events monitored after the sensing process. (b) QAIC internalisation followed by sensing of NADH in HepG2 cells by dual model imaging and (c) corresponding NADH depletion mediated therapy and laser triggered therapeutic mechanism of NADH activated QAIC in normoxic (with singlet oxygen) and hypoxic (with NAD radical) situations

2.2 Results and discussion

2.2.1 Design and synthesis of quinolone appended iridium complex (QAIC).

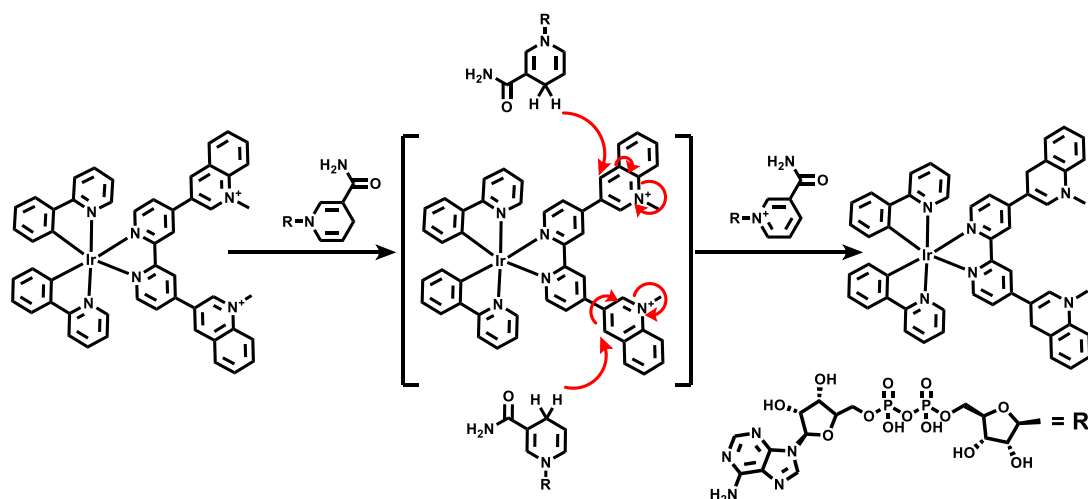
The cyclometalated iridium (III) complex QAIC is synthesized through a three-step process. The constitution of Ir (III) complex is furnished by two 4-(2-pyridyl) benzene (ppy) ligands and one bipyridine ligand which is appended with 1-methylquinolium unit at 4 and 4' positions. The quarternized N-centers of the quinoline moiety provide two positive charges to this ligand. The ligand is abbreviated as (Nq^+Nq^+) where the N stand for the N-donor ligands of the bipyridine and q^+ 's stands for the 1-methylquinolium substituents at 4 and 4' positions. Thus, QAIC can be written as $[Ir(ppy)_2(Nq^+Nq^+)]^+$ with a total charge on the complex is +3. The detailed description of the synthetic procedures adopted and all the characterization steps are described in the supporting information (Scheme 2.1). The hypothesis is based on NADH mediated activation of QAIC effectively turn-ON the luminescence with the simultaneous induction of localized PDT by blocking the PeT via

selective shutting of electron transfer between iridium metal center (PeT donor) and the electron deficient nitrogen of quinoline moiety (PeT acceptor)¹⁵ (Scheme 2.3).



Scheme 2.2: Reagents and conditions: (a) Aq-K₂CO₃-Toluene, Pd(PPh₃)₄ TBAB-24 h, 90°C. (b) 2-ethoxyethanol/water (1:2), reflux(90°C) 24 h. (c) DCM-MeOH (1:1) -reflex (40°C) 12 h. (d) AcCN-MeI- reflux(110°C) 24 h

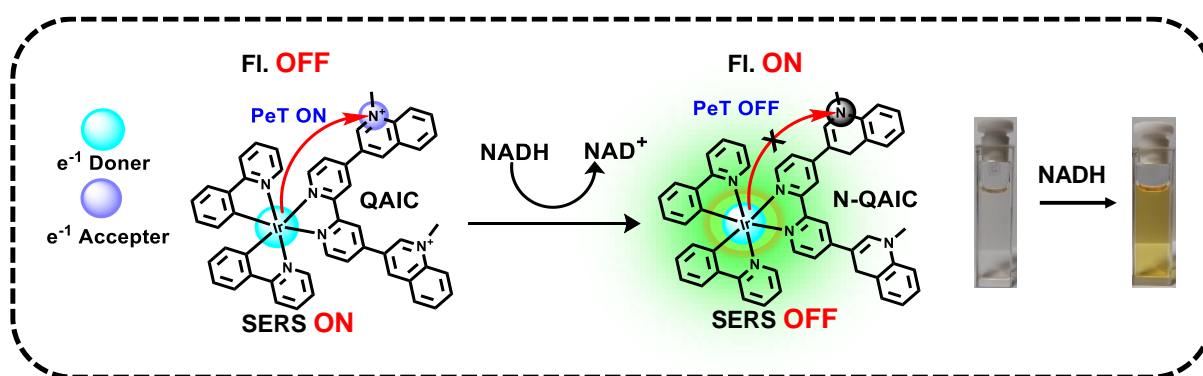
Compared to the available NADH sensing organic probes¹⁶, the enhanced water solubility due the tri-cationic structure, synthetic easiness and the targeted activation of PDT up on NADH trigger through image guided manner along with NADH depletion effect resembles QAIC as a potential NADH probe.



Scheme 2.3: Mechanism of reaction between NADH and QAIC to form N-QAIC

2.2.2 Photophysical assessment and activation of QAIC by NADH.

UV-Vis absorption spectrum of the complex (10 μM in HEPES buffer, pH 7.4) showed energy absorption bands at 316 - 350 nm which corresponds to spin-allowed ligand-centered $\pi\text{-}\pi^*$ transitions for cyclometalated (ppy) and ancillary (Nq^+Nq^+) ligands. The mixed singlet and triplet metal-to-ligand charge-transfer ($^1\text{MLCT}$ and $^3\text{MLCT}$) and ligand-to-ligand charge-transfer (LLCT) transitions are responsible for the weak and low-energy bands between 400 to 510 nm.^{17,18}



Scheme 2.4: Schematic illustration of NADH-triggered targeted activation of QAIC and its dual model sensing capability

A change in colour from pale yellow to orange is observed due to a new band at 475 nm in the UV spectra upon incubation of QAIC with 2 equivalents of NADH (20 μM , 1 h at 37 $^{\circ}\text{C}$) (**Figure 2.1 a**). QAIC displayed negligible luminescence at 565 nm (excitation 475 nm, slit width 4 nm) after incubation with 2 equivalents of NADH about 20 minutes, exhibited a 12-fold enhanced blue shifted emission from 565 nm to 555 nm (**Figure 2.1 b**). Also, the emission turn-ON response at 555 nm was observed with increasing the NADH concentration with a linear response R^2 value of 0.9969 (**Figure 2.1c**).

The observed luminescence turn-ON behavior of QAIC can be attributed to the quenching of PeT due to the reduction of QAIC by NADH. The Ir(III) centre in cyclometalated complex is known for its PeT behavior when positively charged nitrogen centre is incorporated in the aromatic ligands.¹⁹ Here PeT switch-OFF occurs due to the hydride transfer from NADH to QAIC. The reduction would eliminate the net charge on the nitrogen and convert QAIC to the activated N-QAIC (**Scheme 2.4**). The diminished electron acceptance capacity of N-QAIC causes a decrease in PeT and also facilitates the inter system crossing (ISC) to improve the luminescent properties of the complex.¹⁹ The NADH-QAIC redox reaction in the sensing process was further confirmed by mass spectrometric analysis. HRMS analysis for the peak at 315.157 (calcd for $\text{C}_{52}\text{H}_{40}\text{IrN}_6^{3+}$ with

m/z 313.164, where $z = 3$) for QAIC is changed to 943.312 (calcd for $C_{52}H_{42}IrN_6^+$ with m/z 943.310) upon NADH addition which confirms the hydride transfer from NADH to QAIC.

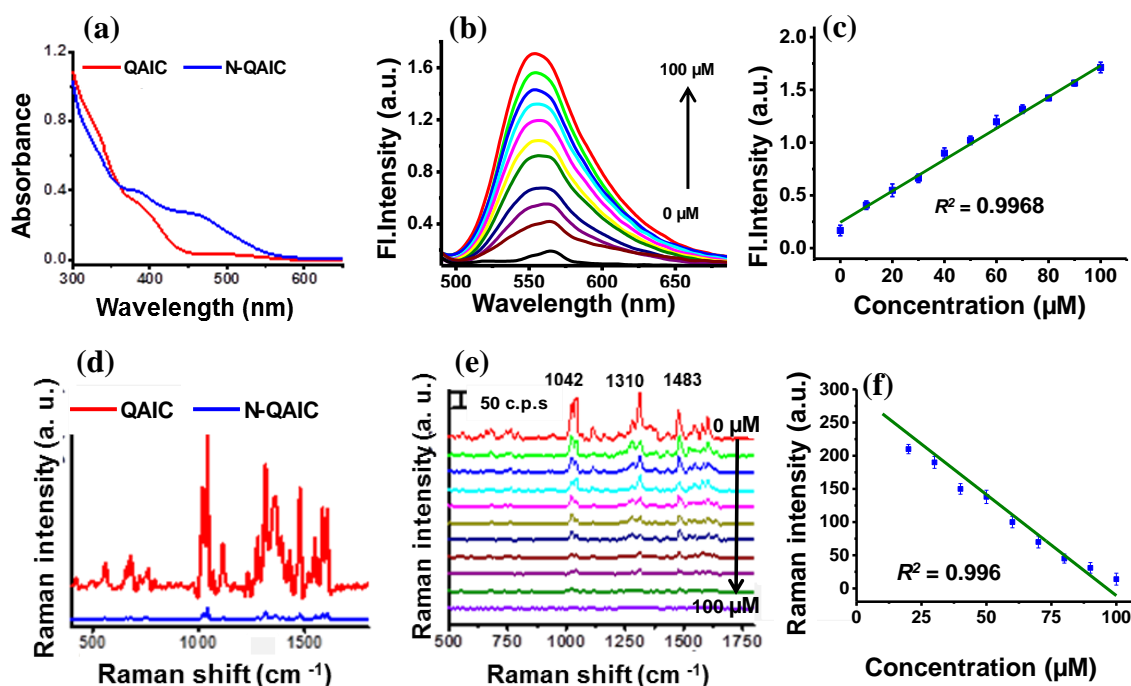


Figure 2.1: (a) UV-Visible changes associated with NADH mediated activation of QAIC (red) and QAIC with NADH (blue) after incubation (10 μM). (b) Emission characteristics of QAIC with increasing concentration of NADH (0–100 μM) followed by 1 h incubation in HEPES (pH 7.4, , excitation 475 nm, emission 555 nm, slit width: 4 nm/4 nm) and (c) Linear correlation graph between emission intensities and concentrations of NADH (with $r^2=0.996$) (d) Study of QAIC (10 μM) from SERS-ON state (red) to SERS-OFF state (blue) upon incubation with NADH for 1 h. (e) The SERS switching OFF process with 60 nm AuNP as SERS substrate (excitation wavelength 633 nm).(f) The linear correlation of SERS intensities and concentrations of NADH (with $r^2=0.9660$).

Additionally, SERS analysis using negatively charged citrate-stabilized spherical gold nanoparticles (AuNP) as substrate was performed to trace the Raman fingerprints of QAIC. An intense Raman peak at 1042 cm^{-1} is observed due to the aromatic ring chain vibrations while peaks corresponding to 1228 , 1277 and 1310 cm^{-1} are assigned to the ring breathing C-H bending of the phenyl moieties. Upon treatment with 2 equivalents of NADH, a sharp quenching in the characteristic Raman peaks of QAIC occurred indicating a clear SERS turn-OFF response towards NADH detection (**Figure 2.1d**). Further, a linear response of hydride transfer between QAIC and NADH in the Raman channel is observed by recording the SERS spectra with increasing NADH concentration. The well resolved spectra can be attributed to the strong electrostatic interaction between the positively charged (Nq^+Nq^+) ligand in QAIC with the negatively charged citrate stabilized AuNPs. The reduction of QAIC by NADH converts the charged (Nq^+Nq^+) to the neutral ($NqNq$) which weakens the interaction with AuNPs, rendering a SERS turn-OFF phenomenon (**Figure 2.1e**) with a

unit of QAIC with an energy span of 19.7 kcal/mol. The product complex NAD...QAICH is more stable than the reactant complex by 10.0 kcal/mol indicating that stronger electrostatic interaction exists between the cationic NAD and di positively charged QAICH.

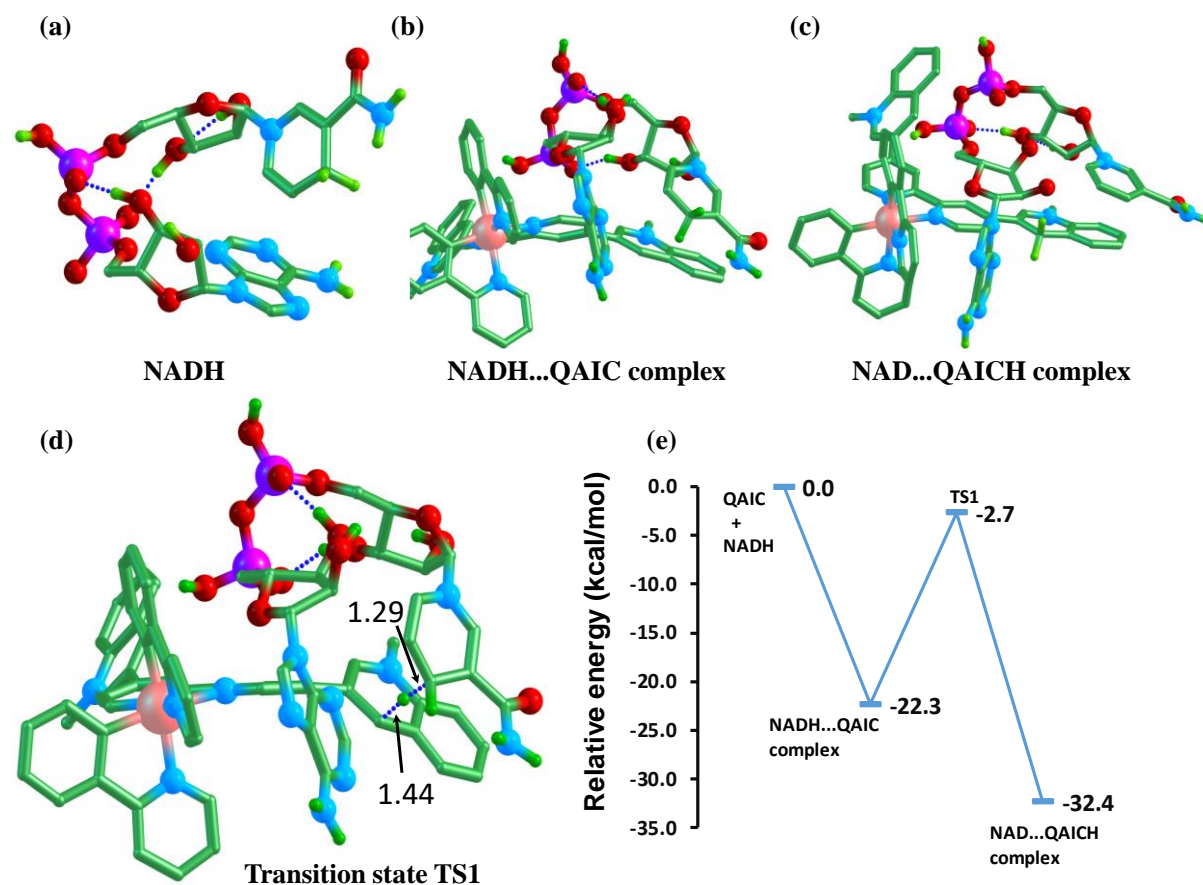


Figure 2.3: The optimized chemical structure of (a) NADH (charge = 0), (b) NADH...QAIC complex, (c) NAD...QAICH complex and (d) transition state TS1. (e) The hydride transfer from nicotinamide ring to quinolone ring is happening through TS1 wherein the activated C-H distances are given in Å. Many H atoms are omitted for clarity.

The high exothermic character of this reaction suggests the spontaneous conversion NADH to NAD due to the strong ability of QAIC to abstract a hydride from the C-H bond of NADH (the reaction is exergonic by 10.9 kcal/mol). The hydride transfer from NADH to QAIC, followed by the PeT Turn-OFF behaviour suggests a novel sensing mechanism for NADH by QAIC. The Ir(III) centre in cyclometalated complexes were reported to possess PeT effect with positively charged nitrogen in an aromatic ring.¹⁹ The observed luminescence turn-ON phenomena can be attributed to the blockage of PeT by NADH. The hydride transfer from NADH will cause a reduction of the 4th position in the quinoline ring. This reaction would eliminate the net charge on the nitrogen and convert the complex to an NADH activated iridium complex (NAD--QAICH: N-QAIC).

2.2.3 NADH homeostasis by QAIC under cellular physiology.

The intracellular concentration of NADH varies between cancer cells of different origin.²⁰ Therefore, the NADH level was evaluated in different human cancer cell lines, *viz.* cervical (HeLa), breast (MCF-7) and hepatocellular carcinoma (HepG2) and normal fibroblast cells (WI-38) with the aid of a commercially available NADH quantification kit. Among all, HepG2 cells maintained the highest levels of NADH (**Figure 2.4a**). Hence, further studies were conducted with HepG2 cells. Most of the molecular probes failed to assess the intracellular NADH due to the poor water solubility and aggregation caused in cellular medium.

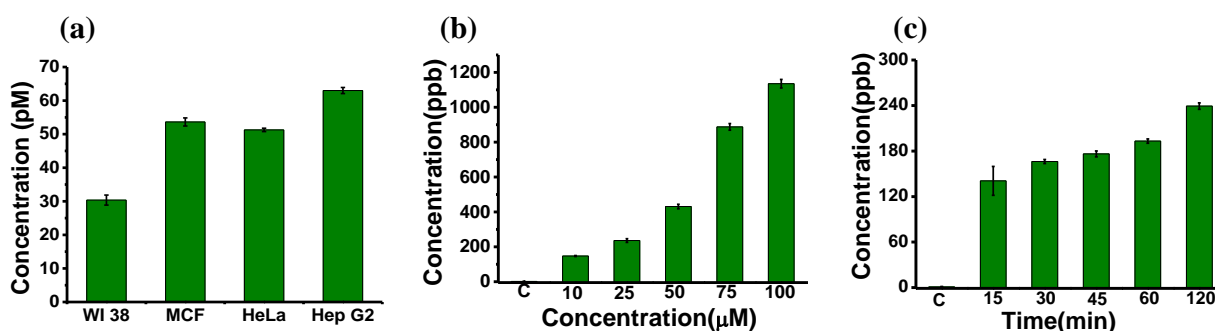


Figure 2.4: (a) Quantification of intracellular NADH from different cancer and normal cell lines. Quantification of extent of internalization by analyzing the iridium metal content in treated HepG-2 cells via ICP-MS analysis in a (b) concentration and (c) time dependent manner.

In the case of QAIC, the (Nq^+Nq^+) ligand environment improves its hydrophilicity and also reduces the aggregation behavior. Cytotoxicity evaluation confirmed the biocompatible nature of the QAIC. Moreover, QAIC was observed to be resistant against photo bleaching in cells (475 nm laser with 0.5 W/cm² power) as well as in solution state (475 nm laser with 0.5 W/cm² power). To study the cellular uptake efficiency of QAIC, ICPMS analysis was performed which displayed a time and concentration-dependent uptake in HepG2 cells with more than 50 % of internalization based on iridium metal under ambient conditions (**Figure 2.4b&c**).

QAIC exhibited a measurable, time-dependent luminescence turn-ON response towards endogenous NADH in HepG2 cells, gradually from 15 min onwards and indicated most prominent at around 60 min (**Figure 2.5a**). Complementing to the luminescence analysis, intense Raman signals was observed at the beginning (within 0 to 15 min) upon incubation of QAIC, which gradually decreases and eventually SERS turn OFF occurred at around 60

min (**Figure 2.5a**). The most intense peak around 1042 cm^{-1} , the C-H bending mode of QAIC was utilized for SERS mapping in HepG2 cells.

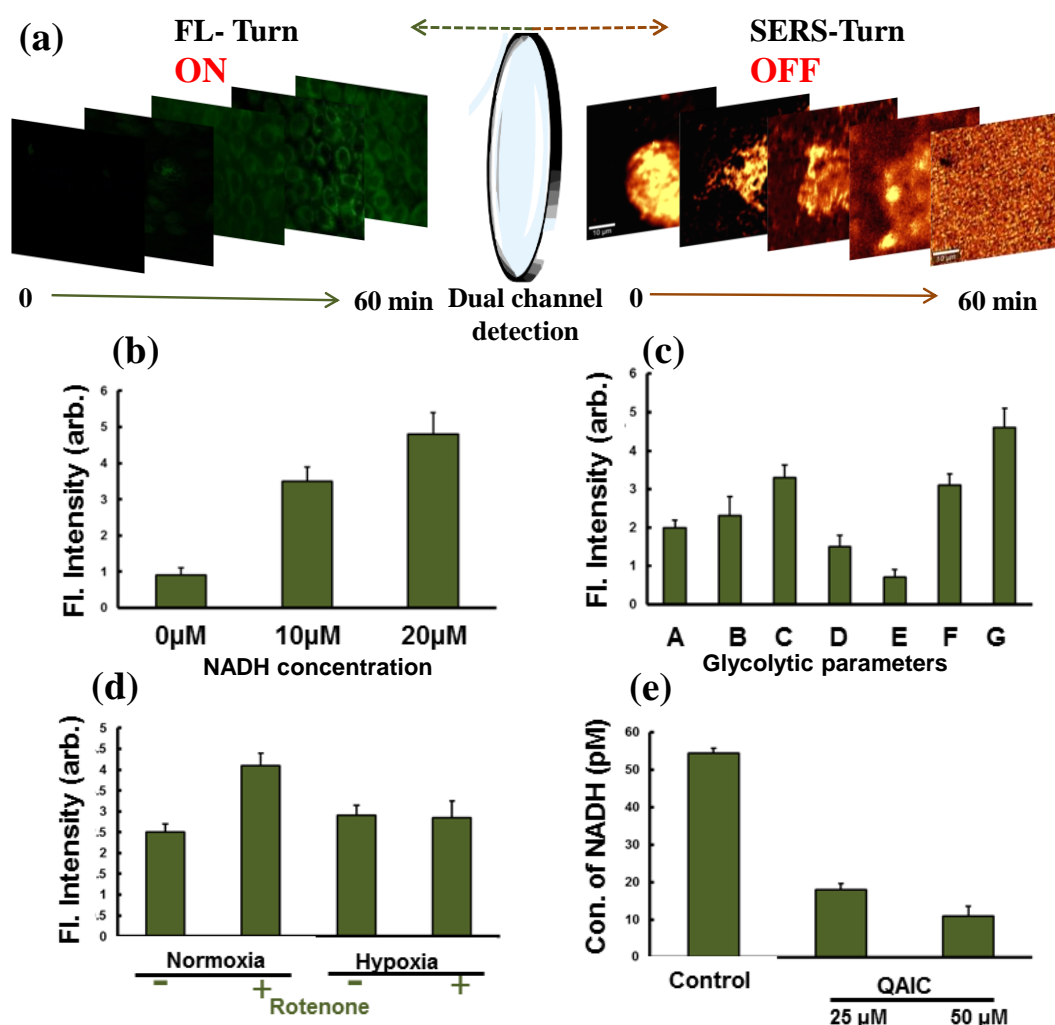


Figure 2.5: (a) Time dependent fluorescence imaging of HepG2 cells showing the fluorescence-ON process via activation of QAIC by NADH shown in the left panel. Corresponding Time dependent SERS imaging of HepG2 cells showing the Raman-OFF process via activation of QAIC by NADH shown in the right panel. (b) Fluorescence enhancement of QAIC from cells incubated with exogenous NADH. (c) Effect of pre-incubation of various glycolytic intermediates on the NADH sensing by QAIC (A-control, B-10 mM glucose, C-20 mM glucose, D-5 mM pyruvate, E-10 mM pyruvate, F-5 mM lactate, G-10 mM lactate). (d) The activation of QAIC in the presence of Rotenone in Normoxic and Hypoxic situation (e) Quantification of intracellular NADH from HepG2 cells incubated with QAIC using commercially available kit

To further confirm NADH-mediated selective activation of QAIC, HepG2 cells were treated with different metabolic precursors, *viz.* glucose, pyruvate and lactate that either promotes or reduces intracellular NADH level. A concentration-dependent increase was noticed in the luminescence signals when HepG2 cells were pre-treated with NADH (**Figure 2.5b**). It is well known that the glycolytic pathway uses glucose as a precursor molecule for energy production leading to the formation of NADH.²¹ The increase in the

luminescence intensity from HepG2 cells pre-incubated with glucose suggests the redox reaction between NADH and QAIC. Also, intense luminescence signals are observed when the cells are treated with pyruvate due to the utilization of intracellular NADH by the enzyme lactate dehydrogenase. This enzyme elevates the NADH levels significantly when exogenous lactate is supplied (**Figure 2.5c**). Intracellular glutathione (GSH) plays a central role in maintaining the redox balance and homeostasis of cells.²² Cells pre-treated with GSH displayed a reduction in the luminescence intensity, while the administration of GSH inhibitor helps to regain the fluorescence. Recently our group reported that clinically used chemotherapeutic paclitaxel causes a reduction in the cellular GSH level.²² An amplified luminescence with the paclitaxel treatment not only confirmed this drug mediated GSH reduction, but also displayed the efficiency of QAIC to precisely monitor NADH kinetics. To further illustrate the cross talk between GSH and NADH, cells were treated with a GSH inducer α -Lipoic acid, which bring about a noticeable reduction in the luminescence intensity. An increased luminescence from the HepG2 cells maintained under hypoxic conditions upon comparison with the cells maintained under normal oxygen concentrations evidently proved the inflated NADH level in low oxygen conditions. The increased luminescence with low oxygen status is assumed to be due to the interruption of partially preserved mitochondrial respiration which caused an accumulation of intracellular NADH. In order to validate this hypothesis, an electron transport chain blocking agent rotenone was employed, which will elevate NADH concentration.²³ Under normoxia, rotenone enhanced the luminescence of QAIC whereas in hypoxia, no notable changes were observed. This is due to the partially preserved mitochondrial respiration, which itself reduce the activity of respiratory Complex-I in hypoxia (**Figure 2.5d**). Elevated antioxidant levels in hypoxia make PDT a challenging treatment option. Treatment of cells with resveratrol, a potent antioxidant enhances the fluorescence in hypoxia whereas, no changes can be observed in normoxia.²⁴ QAIC is capable of sensing tiny fluctuations in the cellular levels of NADH associated with various events. It is worth to mention that NADH depletion can interrupt redox homeostasis to initiate a cascade of physiological process including apoptosis. As an interesting observation, a reduction in the intracellular NADH level upon treatment of QAIC was monitored using NADH quantification kit. Beside NADH sensing, QAIC played the role of NADH scavenger which will ultimately trigger a redox imbalance with an energy shutting process²⁵ (**Figure 2.5e**).

2.2.4 Evaluation of photo-oxidation of NADH by QAIC.

The unique performance of iridium metal complexes towards light contributes miscellaneous photo-activities like radical generation from co-enzymes including NADH.¹¹ Upon treatment with QAIC, there was a decline in the intensity with the absorption and emission band of NADH with an increasing time of laser irradiation, irrespective of temperature change (**Figure 2.6a**). It is obvious that the 1-methylquinolium part on the ancillary ligand of QAIC is selectively reduced in presence of NADH. However, this localized reduction does not impart any change in the chemical behavior of the metal complex. In this context, it is envisaged that in the presence of light, NADH activated QAIC (N-QAIC) is capable to generate NAD radicals. To confirm the generation of NAD radicals, a semi-quantitative analysis was performed using 2,7-dichlorifluorescein diacetate (DCF-DA) with Fenton system (H₂O₂/Fe³⁺) as the positive control. A sharp increase in the emission intensity for DCF was monitored at 545 nm upon laser (475 nm with 0.5 W/cm² power) irradiation, which indicated the production of NAD radicals as it converts the DCFH to DCF (**Figure 2.6b**).

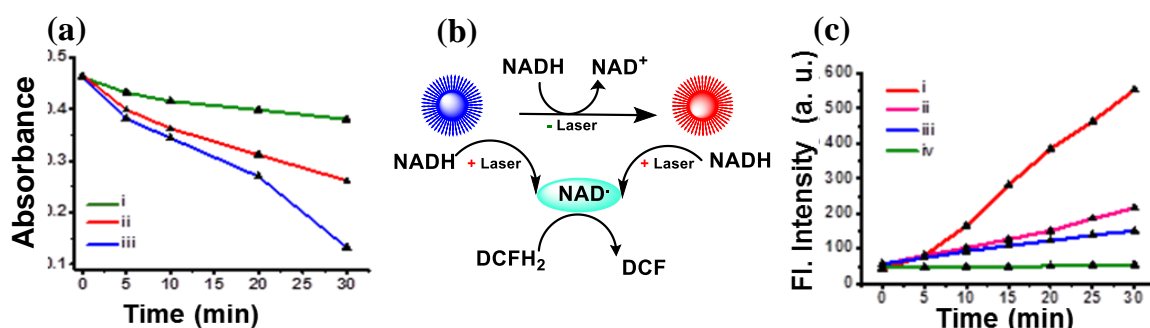


Figure 2.6: (a) NADH degradation by QAIC under different external stimuli, i- without external stimulus, ii-Under temperature incubation at 37°C, iii- light mediated degradation (475 nm laser) (b) Schematic representation of radical generation process followed by DCF activation of QAIC. (c) Activation of DCFH by NAD radical generated by QAIC with 475 nm laser (475 nm, 0.5W/cm²) i-Positive control OH radical, ii-QAIC+DCFH₂+L (Normoxia), iii-QAIC+DCFH₂+L (Hypoxia), iv-DCFH₂+LASER).

This experiment was performed to investigate the effect of radical generation in the absence of oxygen (purged the solution with argon) which again displayed an enhanced fluorescence via DCF formation resembling the capability of QAIC to act as a radical generator under hypoxic condition (**Figure 2.6c**). Therefore, it is worth to mention that the NAD radical generation occurs in the presence of excess NADH after hydride transfer reaction in QAIC.

2.2.5 Photo-reduction of cytochrome c by QAIC and NADH.

The NAD radicals play a critical role in the Fe^{3+} -cytochrome c (cyt *c*) reduction in the intracellular milieu.¹¹ In the absence of oxygen, the Fe^{3+} -cyt *c* act as a terminal electron acceptor in the mitochondrial electron transport chain and can be converted to Fe^{2+} -cyt *c* with the help of single electron donors like NAD radicals. The UV-absorption band of cyt *c* showed an enhancement of β (520 nm) and α (550 nm) bands corresponding to the Fe^{2+} -cyt *c*, upon treatment with QAIC and NADH in argon pugged solutions by laser irradiation (Figure 2.7a). A liner enhancement of these bands with a R^2 value of 0.9939 from 0 to 30 minutes of laser (475 nm) irradiation confirmed the Fe^{3+} -cyt *c* reduction.

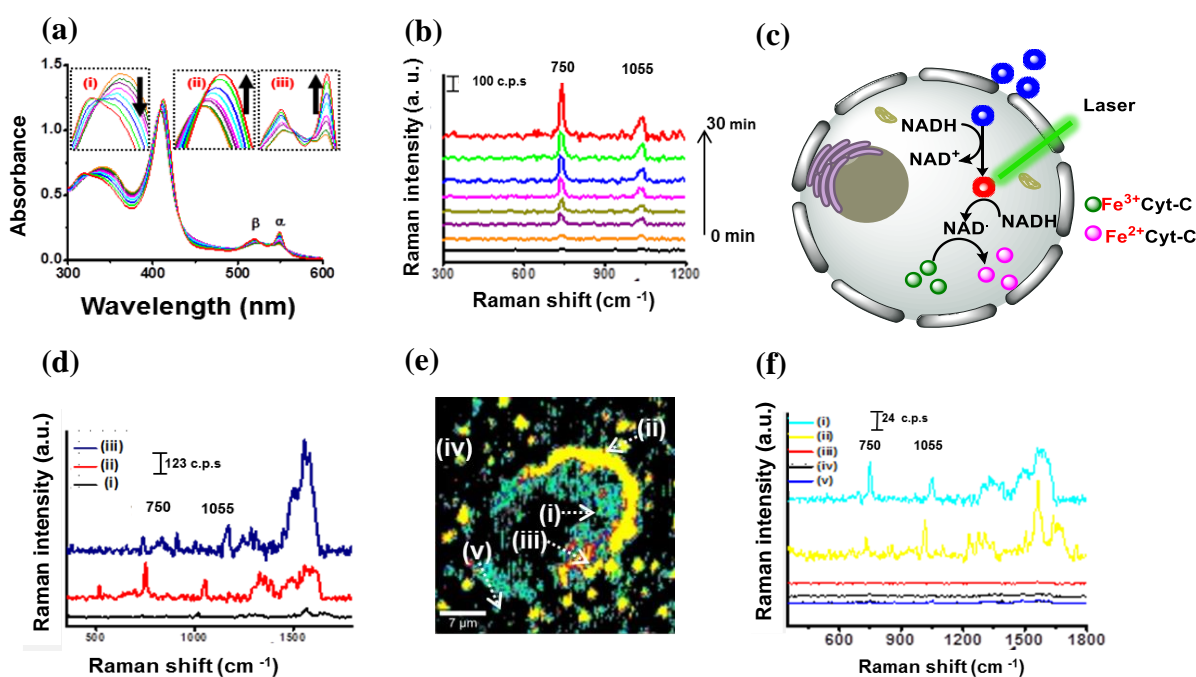


Figure 2.7: (a) Conformation of Fe^{3+} -cyt-*c* reduction by QAIC and NADH with laser via UV-Visible spectroscopy inset shows the enlarged portion of absorption changes occurred in α , β (iii) and other bands. (b) SERS titration of reduction of Fe^{3+} -cyt-*c* to and Fe^{2+} -cyt-*c* by QAIC and NADH with 475 nm laser irradiation. (c) Schematic representation of Fe^{3+} -cyt-*c* reduction of QAIC with NADH in the intracellular milieu. (d) Tracking of cytochrome c reduction via SERS mapping of HepG2 cells incubated with QAIC and NADH after laser irradiation: i-Control HepG2, ii-QAIC+NADH+ L, iii-QAIC+NADH. (e) Cluster mapping of HepG2 cells using the 750 cm^{-1} peak and (f) Corresponding SERS spectra from the selected parts.

The Raman bands were evaluated for oxidized and reduced forms of cyt *c* which showed a remarkable variation in the SERS signal intensity²⁷ confirming the photo reduction process. An intense Raman peak at 750 cm^{-1} corresponding to the pyrrole breathing vibrations was explicitly marked upon treatment of QAIC in the presence of NADH and laser irradiation when compared with isolated pure Fe^{3+} -cyt *c*. Similarly, time dependent

SERS titration of oxidized Fe³⁺-cyt *c* treated with QAIC and NADH under laser spark displayed fingerprint Raman peak at 750 cm⁻¹ associated with the reduced cyt *c*. with an increasing order of peak intensity but neither Fe³⁺-cyt *c* alone or other combinations imparted this effect (**Figure 2.7b**). Later, the cyt *c* dynamics in the cells was investigated based on SERS spectral assessment (**Figure 2.7c**). The ultra-sensitive SERS modality enables to track metabolites.²⁸ Appearance of unique Raman peak at 750 cm⁻¹ was traceable (**Figure 2.7d**) selectively in the treated cells. Intense Raman signal from the HepG2 cells clearly confirms the QAIC mediated generation of NAD radicals followed by cyt *c* reduction (**Figure 2.7e&f**).²⁷

2.2.6 Switching-off PeT to PDT during NADH sensing by QAIC.

Cyclometalated iridium complexes are considered as PDT agents due to their tunable photophysical features.²⁹ Here, QAIC is not expected to have PDT efficiency due to the inherent PeT effect between the metal center and ligand.

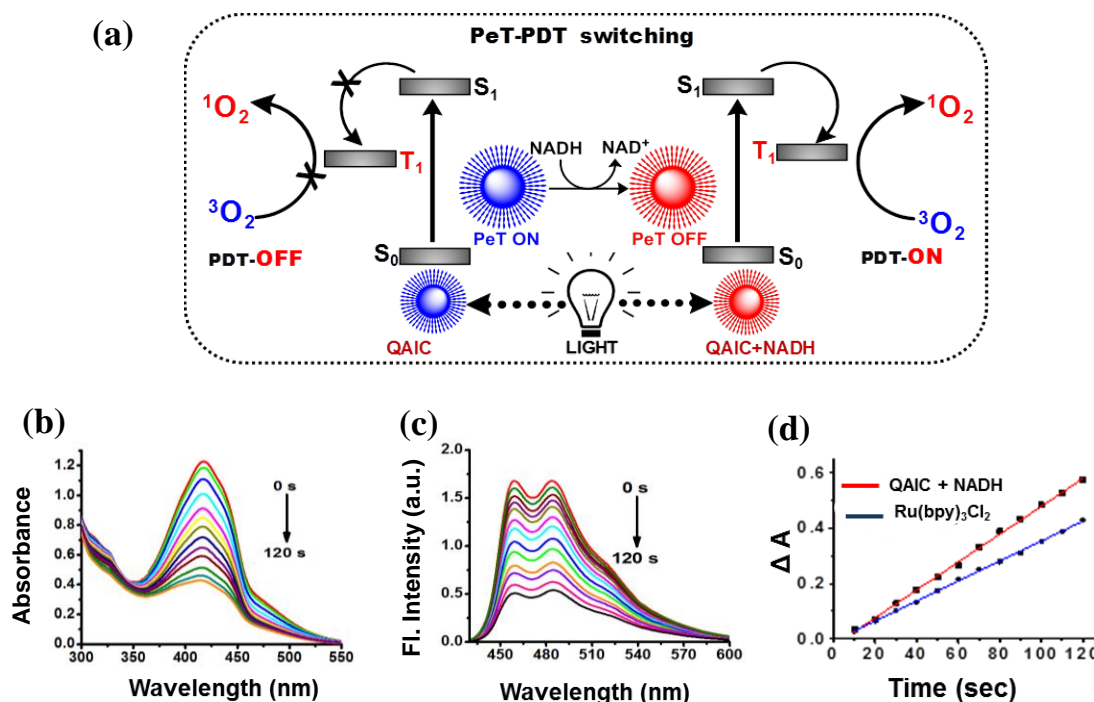


Figure 2.8: (a) Schematic illustration of PeT-PDT switching process of QAIC. (b) Singlet oxygen generation capability of QAIC via NADH mediated PeT switching using the absorbance change of DPBF at 410 nm from 0 to 120 seconds and the (c) corresponding emission spectrum. (d) Liner plot for singlet oxygen quantum yield of QAIC+NADH with [Ru(bpy)₃]Cl₂.

In the current scenario, NADH mediated reduction transform the QAIC emissive and subsequently PeT off state modulate the production of singlet oxygen (¹O₂) in presence of laser irradiation.³⁰ Since ¹O₂ generation is directly related to the efficiency of ISC (S₁ to

T_1), the PeT would facilitate a new route to the deactivation of excited electron. Therefore, PeT can be used as a switching phenomenon to impart controllable PDT (**Figure 2.8a**) caused by 1O_2 .³¹ In order to establish the 1O_2 generation capability, a crucial experiment was carried out wherein NADH pre-treated QAIC was monitored along with singlet oxygen scavenger 1,3-diphenylisobenzofuran (DPBF) by employing $[Ru(bpy)_3]Cl_2$ as a standard reference material. In the solution state irradiation with 475 nm laser caused a reduction in the absorption and emission intensity of DPBF within 120 seconds confirming the 1O_2 generation capability of N-QAIC (**Figure 2.8b, c**). A control experiment performed with QAIC alone, NADH alone and other combinations failed to impart any change in the absorption and emission intensity (**Figure 2.8d**).

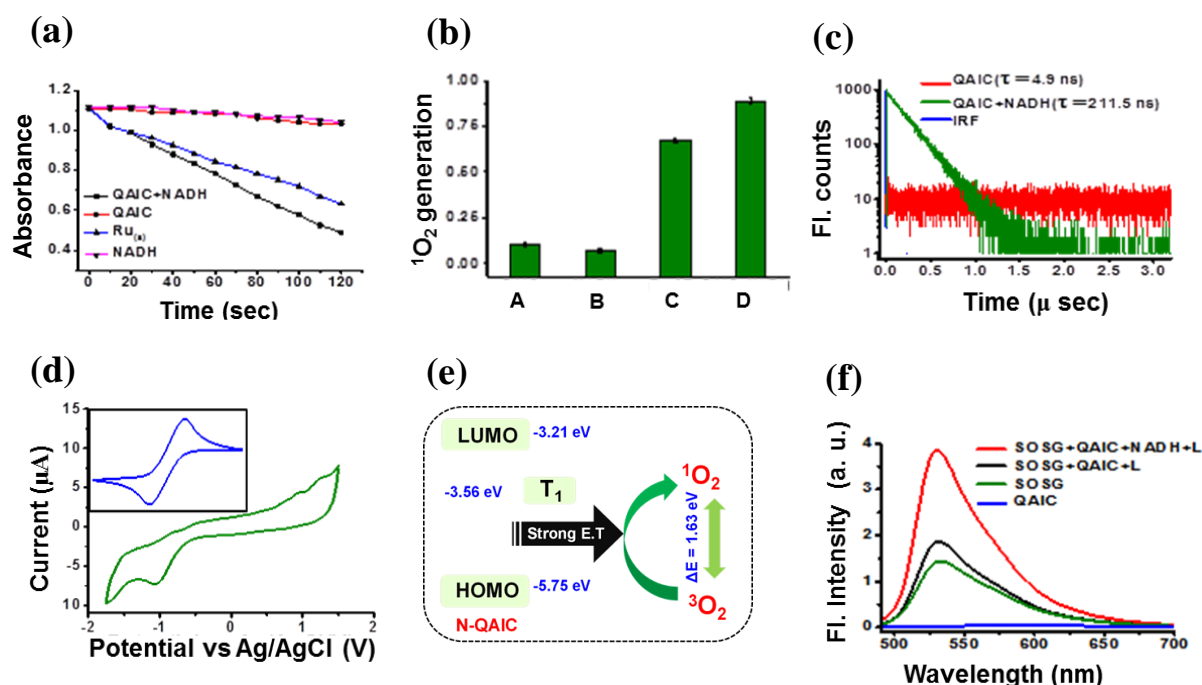


Figure 2.9: (a) Relative absorption changes of DPBF at 410 nm caused by QAIC+ NADH, QAIC alone, NADH alone and standard $[Ru(bpy)_3]Cl_2$. (b) Relative singlet oxygen generation capacity of the molecules under investigation (A-QAIC, B-NADH, C- $[Ru(bpy)_3]Cl_2$, D-N-QAIC). (c) Calculation of phosphorescent life time of QAIC and QAIC+NADH using TCSPC analysis with argon purging. (d) Cyclic voltammetry analysis of QAIC+NADH using ferrocene as standard (inset shows the voltammogram of ferrocene) and (e) HOMO-LUMO and triplet energy state diagram showing the conversion efficiency of triplet oxygen to singlet via triplet-to-triplet energy transfer. (f) Conformation of singlet oxygen generation using well known singlet oxygen sensor SOSG in acetonitrile.

The singlet oxygen quantum yield (Φ) of N-QAIC was found to be 0.86 when compared against the reference ($[Ru(bpy)_3]Cl_2$) with Φ value of 0.57.³² In addition, a liner plot with the change in absorbance of DPBF (ΔA) induced by N-QAIC with respect to time confirmed the higher quantum yield (**Figure 2.9a**). The above experiments illustrated the NADH

mediated generation of $^1\text{O}_2$ by QAIC through switching-off mechanism of PeT. The relative $^1\text{O}_2$ generation of N-QAIC was assessed in comparison with QAIC (**Figure 2.9b**). Further, an amplified excited state lifetime of N-QAIC (211 ns) upon comparison with bare QAIC (4.9 ns) via time-correlated single-photon counting (TCSPC) indicated highly populated triplet state of the activated molecule, confirming the NADH mediated PeT-PDT switching mechanism (**Figure 2.9c**). The populated triplet state transfer energy to triplet molecular oxygen via triplet to triplet energy transfer (TTET) process which eventually generates singlet oxygen for PDT.^{33,34} Cyclic voltammetry experiment was performed to evaluate the oxidation and reduction potential of N-QAIC by employing ferrocene as a standard. The HOMO and LUMO calculations were made by utilizing the equation HOMO or LUMO = $-(E_{\text{onset of IrIII}} \text{ vs. } E_{\text{onset of ferrocene}}) - 4.8 \text{ eV}$.⁹ The obtained energy difference indicated the close proximity between the energy levels of triplet state and with the molecular oxygen. This close proximity facilitates the efficient transfer of energy from triplet state of N-QAIC to triplet of molecular oxygen to generate singlet oxygen (**Figure 2.9d&e**). Finally, the singlet oxygen generation capacity was verified with help of singlet oxygen sensor green (SOSG)²³ that accounts for the singlet oxygen generation potential of a molecule by producing a green emission. The emission profile of SOSG treated with QAIC followed by 475 nm laser irradiation does not impart any characteristic change, while N-QAIC treatment instantly gives an enhanced emission maximum at 540 nm with 60 seconds of laser irradiation (**Figure 2.9f**). The activation of SOSG fluorescence revealed the capacity of N-QAIC to produce singlet oxygen.

2.2.7 PDT evaluation by the activated N-QAIC in cells.

In addition to the sensing of NADH, the efficiency to produce NAD radicals and singlet oxygen extends the application of the cyclometalated iridium complex QAIC as a photosensitizer for PDT (**Figure 2.10a**). The *in vitro* phototherapeutic potential has been investigated in hepatocellular carcinoma cell lines. Initially, the cytotoxicity of QAIC was evaluated by MTT assay confirming non-toxic nature even at higher concentrations (100 μM). Next the phototoxicity of N-QAIC was evaluated where an eight-fold enhanced cytotoxicity in normoxia (**Figure 2.10b**) upon comparison with the dark (without laser irradiation) proved the enhanced photodynamic effect induced *via* PeT-PDT switching mechanism.

Again, administration of a singlet oxygen scavenger sodium azide caused a reduction (Figure 2.10b) in the laser-assisted cytotoxicity. This observation confirmed that the cytotoxicity imparted by NAD radicals alone without the aid of molecular oxygen. In the presence of excess of NADH, QAIC generates toxic NAD radical which acted as an apoptotic initiator in hypoxia (Figure 2.10c). The laser-triggered production of ROS by N-QAIC could proceed through mitochondria-mediated cell death which indicated by the reduction of mitochondrial membrane potential ($\Delta\Psi_m$) in both normoxic and hypoxic situations (Figure 2.10 d & e).

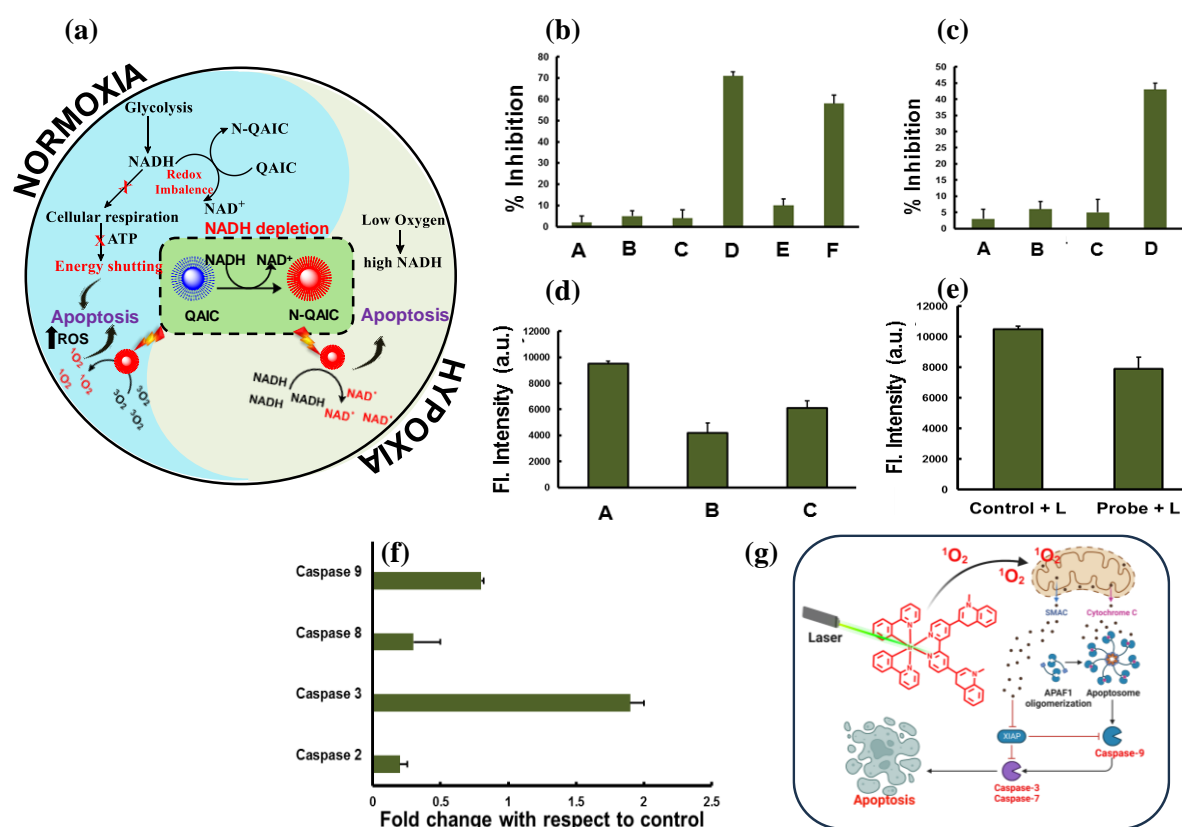


Figure 2.10: (a) Schematic illustration of apoptosis induced by the molecule via PeT-PDT switching in normoxic and hypoxic conditions. Photo toxicity of activated QAIC with and without laser in (b) normoxic (A-Control, B- Control + L, C-QAIC, D-QAIC + L, E-QAIC + NaN₃, F-QAIC + NaN₃ + L) and (c) hypoxic (A-Control, B- Control + L, C- QAIC, D-QAIC+L) conditions. Evaluation of mitochondrial membrane potential associated with PDT in (d) normoxic (A-Control + L, B-QAIC + L, C- QAIC+NaN₃+L) and (e) hypoxic situations. (f & g) Activation of caspase and mechanism of activation of caspase through PDT

Since mitochondria-mediated cell death often proceeds through the cascade activation of caspases, we have evaluated the change in the caspase expression upon exposure of PDT. The elevated expression of caspase 3 and 9 confirmed the execution of mitochondria mediated intrinsic apoptotic pathway (Figure 2.10 f & g). In order to confirm the programmed execution of cell death mechanism, various apoptosis assays were carried out

in both normoxic and hypoxic conditions^{35,36}. The extent of phototoxicity caused by activated QAIC in presence of 532 nm laser spark was evident with the orange-red fluorescence from the cells (**Figure 2.11 a**) in comparison with the green coloured control cells when acridine orange/ethidium bromide dual staining assay was performed.

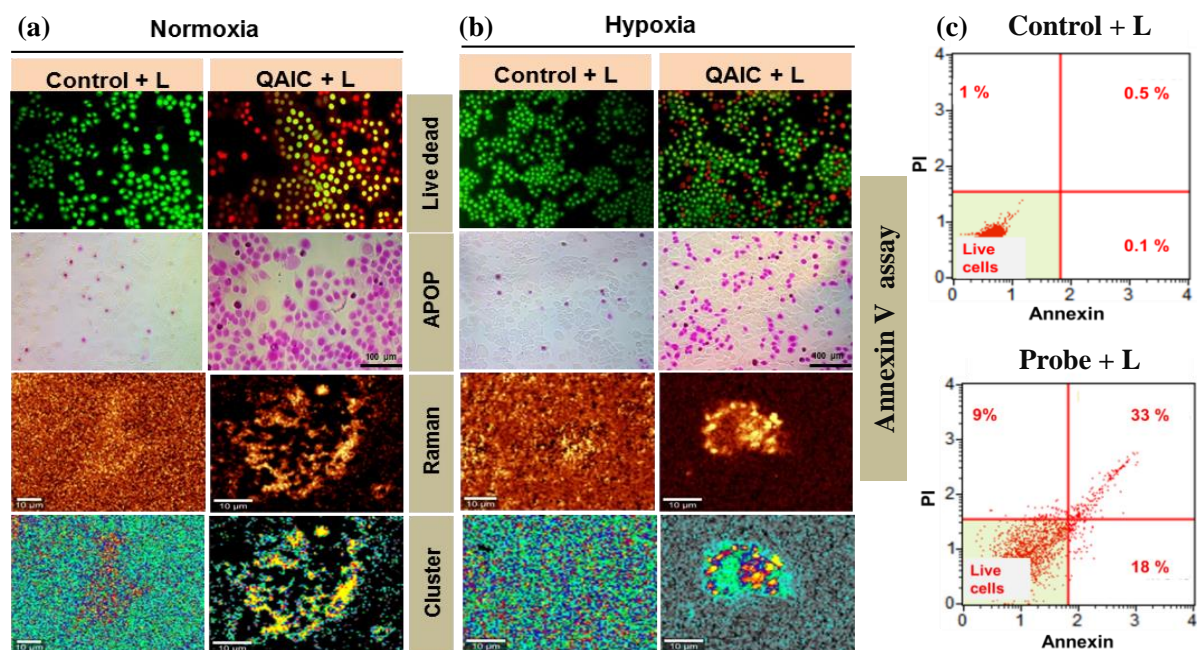


Figure 2.11: Evaluation of apoptotic inductions through PDT by the complex QAIC in HepG2 cells via acridine orange-ethidium bromide dual staining, APOP assay and SERS imaging with cluster mapping (using 1042 cm^{-1} band of QAIC) under (a) normoxic and (b) in hypoxic condition. (c) quantification of extent of apoptosis by Annexin V assay via flowcytometric analysis

A similar pattern of apoptotic evaluation was performed with APO Percentage assay, in which QAIC with laser treatment turned out the purple dye-stained dead cells whereas other combinations remained unstained (**Figure 2.11a**). There was a marginal reduction in the extent of apoptosis when cells were pre-treated with sodium azide due to the singlet oxygen scavenging property of sodium azide. Even in the absence of molecular oxygen, induction of apoptosis was evident which illustrated the fact that NAD radical alone can execute the orchestration of cell death (**Figure 2.11b**). Finally, to quantify the extent of apoptosis *via* flow cytometry, annexin V-FITC assay was employed. The annexin V positivity was notably increased in cells treated with QAIC followed by laser irradiation (**Figure 2.11c**). Outstanding multiplexing capacity, superior sensitivity and the precise evaluation of molecular fingerprints in complex biological compositions augmented the application of SERS to track biomolecular changes during cellular events.³⁵ Distinct Raman peaks corresponding to protein degradation and nuclear damage authenticates the orchestration of apoptosis. SERS spectra from N-QAIC upon laser trigger resolved the unique Raman

peak patterns due to apoptotic events which includes the variation in 838 cm^{-1} of phosphate backbone, 503 , 648 and 1128 cm^{-1} associated with lipids, protein degradation, 1585 cm^{-1} during double strand breakage.³⁶ In the conditions prevailing normal oxygen concentration, more fingerprint changes were observed due to the active involvement of singlet oxygen and NAD radicals in the process of PDT (**Figure 2.11a**). Although to a lesser extent, appreciable signs of apoptosis was evident in hypoxic conditions (**Figure 2.11b**) which validated the programmed cell death induced *via* NAD radical in an oxygen independent pathway. Synergistically, QAIC recognize the dynamic fluctuations of NADH and impart NADH depletion assisted enhanced phototherapeutic effect in both in hypoxic and normoxic conditions.

2.3. Conclusion

A insightful cyclometalated iridium complex $[\text{Ir}(\text{ppy})_2(\text{Nq}^+\text{Nq}^+)]^+$, QAIC have been synthesized which resembled as a theranostic molecular probe for cancer phototherapy. The QAIC can sense the dynamics associated with intracellular NADH *via* PeT switching process through bimodal luminescence and Raman imaging by SERS modality and simultaneously transformed into an activated photo theranostics motif N-QAIC. The depletion of cellular NADH by QAIC exerted an imbalance in the redox status and the same has been utilized for targeted PDT that is demonstrated in hepatocellular carcinoma cells. The QAIC generated NAD radical upon laser trigger endowed an additional therapeutic option in tumour hypoxia. The toxic NAD radical generated by QAIC in low oxygen conditions induced oxygen independent photodynamic effect. Considering the fact that oxygen deficiency and antioxidants are the major impediment of hypoxic PDT, our design strategy may produce a paradigm change in hypoxic cancer treatment for future therapeutic benefit towards diverse medical conditions.

2.4 Experimental section

2.4.1 Materials and Methods

The chemicals including 4,4'-Dibromo-2,2'-bipyridine, 3-Quinolineboronic acid, Potassium carbonate, TBAB, $\text{Pd}(\text{PPh}_3)_4$, $\text{IrCl}_3 \cdot x\text{H}_2\text{O}$, 2-phenyl pyridine, 2-methoxyethanol, methyl iodide, diphenylisobenzofuran were purchased from TCI Chemicals. All solvents were of reagent grade and were purchased from local companies. All solvents were dried and distilled prior to use by following standard procedures. ^1H NMR spectra were recorded on a Bruker 500 MHz FT-NMR (model) spectrometer at 25°C . The chemical shift (δ) data and coupling constant (J) values were given in parts per

million (ppm) and Hertz (Hz), respectively. High-resolution mass spectra (HRMS) were recorded on a Thermo Scientific Exactive ESI-MS spectrophotometer. UV/vis spectra were obtained by using a Shimadzu UV-2600 UV-Vis spectrophotometer and emission spectra were recorded on a Fluoromax-4 Spectrofluorometer with a 1 cm quartz cuvette. All experiments were carried out at 298 K unless otherwise specified. SERS experiments were carried out using a WITec Raman microscope (WITec, Inc., Germany) containing 600 g/mm grating and Peltier cooled charge-coupled device detector unit. The samples were excited using a 633 nm laser with 10 mW power, and the Stoke-shifted Raman spectra were collected in the region of 300 –2000 cm^{-1} with a resolution of 1 cm^{-1} and an integration time of 1 s and 10 accumulations. Prior to each measurement, calibration was done with a silicon standard (Raman peak at 520 cm^{-1}). Data processing was carried out using WITec Project Plus (v5.2) software package. Excited state decays were measured using a picosecond single-photon counting system (TCSPC) (Horiba, DeltaFlex).

2.4.2 Synthesis and characterization

2.4.2.1 Synthesis of Quinoline appended bipyridine ligand (compound 1)

4,4'-Dibromo-2,2'-bipyridine (3.139 g, 10 mmol) and 3-Quinolineboronic acid (3.45 g, 20 mmol) were dissolved in a mixture of 60 mL toluene and 10 mL 2 M aqueous potassium carbonate. To this TBAB (1.66 g, 5 mmol) in water (10 mL) was added. The mixture was stirred at room temperature for 30 minutes under Argon followed by adding $\text{Pd}(\text{PPh}_3)_4$ (0.020 g, 1.74×10^{-3} mmol) and then heated to 90 °C for 24 h. After the completion of the reaction indicated by TLC, the mixture was poured into water and extracted three times with ethyl acetate. The organic layer was dried over anhydrous sodium sulphate. After removing the solvent under reduced pressure, the residue was chromatographed on a silica gel column with $\text{CHCl}_3:\text{CH}_3\text{OH}$ as eluent giving the compound as a pale-yellow solid. Yield: 74%. **^1H NMR (500 MHz, MeOD):** δ 9.32 (d, $J = 1.5$ Hz, 2H), 8.89 (s, 4H), 8.70 (s, 2H), 8.18 (d, $J = 8.5$ Hz, 2H), 8.04 (d, $J = 8$ Hz, 2H), 7.85 – 7.81 (m, 4H), 7.70 (t, $J = 7.5$ Hz, 2H). **MS (ESI-MS):** Calcd for $\text{C}_{28}\text{H}_{18}\text{N}_4 \text{M}^+$: 410.1531; Found $\text{M}+\text{H}^+$: 492.1630.

2.4.2.2 Synthesis of Precursor molecule for Quinoline Appended Iridium complex (compound 3)

The synthesis was started with the preparation of Ir dimer complex (Nonoyama, 1974), a solution of $\text{IrCl}_3 \cdot x\text{H}_2\text{O}$ (224.36 mg, 0.75 mmol) and 2-phenyl pyridine (350 mg, 1.58 mmol) in 2-methoxyethanol/ H_2O (3:1, v/v%) was refluxed at 90°C for 24 h, under argon

atmosphere. After the reaction, the solution was cooled down to room temperature and poured into 50 mL of water. The precipitated yellow solid (compound 2), was filtered and washed with n-hexane (5 mL x 3) and cold diethyl ether (5 mL x 3). The next step was preceded without any further purification of the obtained crude product. A mixture of compound 2 (200 mg, 0.1866 mmol) and compound 1 (197 mg, 0.48 mmol) in CH₂Cl₂/CH₃OH (1:1, v/v%) was refluxed under an argon atmosphere for 12 h. Upon completion of the reaction, the solution was cooled down to room temperature and the solvent was removed under reduced pressure. The residue obtained was subjected to column chromatography in silica gel (100-200 mesh) column with chloroform/Methanol system, giving the intermediate compound as an orange solid. Yield 68 %, **¹H NMR (500 MHz, MeOD)**: δ 9.40 (s, 2H), 9.35 (d, J = 2.5 Hz, 2H), 8.96 (d, J = 2 Hz, 2H), 8.10 (d, J = 6 Hz, 3H), 8.07 (s, 1H), 8.04 (d, J = 9 Hz, 4H), 7.98 (d, J = 5.5 Hz, 2H), 7.79 (t, J = 8 Hz, 6H), 7.74 (d, J = 6 Hz, 2H), 7.63 (t, J = 7.5 Hz, 2H), 7.02 (t, J = 6.5 Hz, 2H), 6.98 (t, J = 7.5 Hz, 2H), 6.84 (t, J = 7.5 Hz, 2H), 6.27 (d, J = 7.5 Hz, 2H). **MS (ESI-MS)**: Calcd for C₅₀H₃₄IrN₆⁺ M⁺: 911.2474; Found M⁺: 911.2495

2.4.2.3 Synthesis of Quinoline Appended Iridium Complex (QAIC)

A mixture of orange solid, compound 3 (100 mg, 0.109 mmol) and methyl iodide (78 mg, 0.549 mmol) were dissolved in acetonitrile in a sealed tube and refluxed at 110^o C overnight. The solid precipitated was filtered through Büchner funnel and washed with n-hexane, cold diethyl ether followed by dichloromethane affords the QAIC as a brick red solid. Yield: 62%, **¹H NMR (500 MHz, DMSO-d₆)**: δ 10.27 (s, 2H), 10.13 (s, 2H), 9.81 (s, 2H), 8.64 (t, J = 8 Hz, 4H), 8.41 (t, J = 8.5 Hz, 2H), 8.35 – 8.34 (m, 4H), 8.19 (t, J = 7.5 Hz, 2H), 8.10 (d, J = 6 Hz, 2H), 8.01 (d, J = 8 Hz, 2H), 7.98 (d, J = 15 Hz, 2H), 7.85 (d, J = 5.5 Hz, 2H), 7.23 (t, J = 7 Hz, 2H), 7.11 (t, J = 7.5 Hz, 2H), 7.00 (t, J = 7.5 Hz, 2H), 6.29 (d, J = 7.5 Hz, 2H), 4.78 (s, 6H). **¹³C NMR (125 MHz, DMSO-d₆)** δ 167.3, 156.5, 151.0, 150.4, 150.0, 149.5, 145.7, 144.6, 144.3, 139.6, 138.6, 137.3, 131.6, 131.5, 131.3, 130.9, 129.2, 127.4, 125.7, 124.5, 123.9, 123.1, 120.7, 119.8, 46.4.; **MS (MALDI-TOF)**: Calcd for C₅₂H₄₀IrN₆³⁺ M⁺: 941.290; Found M⁺: 941.273

2.4.3 Photophysical Evaluation

2.4.3.1 Measurement of preliminary photophysical properties.

In general, the UV-Vis absorption and emission spectra were obtained on a Shimadzu UV-2600 UV-Vis spectrophotometer and Fluoromax-4 Spectrofluorometer respectively. The

excitation/emission slit width was set to 4 nm with medium scan speed. Stock solutions of the complex QAIC were made in spectroscopic grade acetonitrile (1 mM) were used to prepare the working solutions in buffer (HEPES, pH 7.4). Absorbance spectra were recorded from 300-700 nm while the emission spectra were from 490-750 nm. All the experiments were repeated three times to confirm the reproducibility of the results.

2.4.3.2 Detection of NADH and Limit of Detection

To investigate the linear response of QAIC towards NADH, a 10 μM solution of QAIC in HEPES buffer was incubated for 2 hs at 37⁰C with different concentrations of NADH (0 to 100 μM) and measure the corresponding photoluminescence at 565 nm. (Excitation wavelength 475 nm and slit width 4 nm). The Limit of detection (LOD) of the complex in the fluorescent channel is calculated using the equation $\text{LOD} = 3\sigma/S$ Where S is the slope of the linear plot and σ is the standard deviation of the blank.(Smith et al., 2018)

2.4.3.3 Mass spectroscopic proof of NADH reaction

The complex QAIC and an equimolar mixture of QAIC and NADH in acetonitrile were incubated for 2 h and subjected to HRMS analysis and examined for the peak corresponding to 943.30 of the product of QAIC with NADH(N-QAIC).

2.4.3.4 Stability and selectivity

Stability studies of the QAIC and N-QAIC were monitored by UV/Vis spectroscopy. The freshly prepared 10 μM solutions of QAIC and N-QAIC in HEPES buffer was checked or the absorption from zero to 24 h. The photostability of freshly prepared 10 μM solutions of QAIC and N-QAIC in HEPES buffer will be irradiated with 475 nm long pass LASER at 37⁰C and the UV/Vis absorption from zero to 1 h was checked for confirming the Photostability. The selectivity of the iridium complex QAIC towards other reactive analytes was investigated by treating 100 μM of different species (for GSH concentration taken is 1mM) with 10 μM of QAIC and incubated for 2 h at 37⁰C to measure the corresponding photoluminescence at 565 nm. (Excitation wavelength 475 nm and slit width 4 nm).

2.4.3.5 pH dependent emission of QAIC with NADH

The emission profile of QAIC with NADH at different pH was investigated by incubating the freshly prepared 100 μM NADH with 10 μM QAIC at different pH (37⁰C for 2 h) and measure the corresponding photoluminescence at 555 nm (excitation wavelength 475 nm and slit width 4 nm).

2.4.3.6 SERS analysis of QAIC

To investigate the linear response of QAIC towards NADH via Raman platform, a 10 μM solutions of QAIC in Milli-Q water was incubated for 2 h at 37 $^{\circ}\text{C}$ with different concentrations of NADH (0 to 100 μM). After the incubation, 2 μL of the samples were mixed with 18 μL of 40 nm gold nanoparticles (Herizchi et al., 2016) (AuNP) and measured the corresponding SERS signals (Excitation wavelength 633 nm, LASER power 10 mW and integration time 1s, 10 accumulations).

2.4.3.7 LASER triggered degradation of NADH

To establish the light triggered conversion of NADH, a 5 μM solution of the complex mixed with freshly prepared 140 μM solution of NADH was irradiated with 475 nm LASER at 25 $^{\circ}\text{C}$ and time dependent absorption and emission spectra corresponds to NADH were measured.

2.4.3.8 Conformation of NAD radical generation

a. DCF-DA method

To confirm the radical generating ability of QAIC, a ROS probe 2,7-dichlorofluorescein diacetate (DCFH-DA) was used. After conversion of DCFH-DA into 2,7-dichlorofluorescein- H_2 (DCFH $_2$), DCFH $_2$ can be further transformed into highly fluorescent 2,7-dichlorofluorescein (DCF) in the presence of NAD radical and monitored at 530 nm. Briefly, a 25 mM solution of DCF-DA was activated to DCFH $_2$ according to the literature procedure. (Reiniers et al., 2017) The activated DCFH $_2$ (10 μM in DMSO) was treated with N-QAIC (5 μM) and NADH (48 μM) were analyzed in the presence and absence of oxygen with 475 nm laser irradiation. The corresponding spectral changes at 530 nm was analyzed through fluorescence spectrometer. The hydroxyl radical generated via Fenton reaction is used as the positive control(Lv et al., 2018) and DCFH $_2$ with laser used as control experiment to validate the result.

b. Reduction of Fe^{3+} - Cyt-C to Fe^{2+} - Cyt-C

To check the reduction of cytochrome C by QAIC and N-QAIC absorption spectroscopic analysis and SERS titration were conducted according to the literature report(Huang et al., 2019). Briefly, QAIC/N-QAIC (2.5 μM), NADH (48 μM) and cyt c (11 μM) in argon purged (PBS solution in a cuvette (3 mL) was degassed by bubbling Ar for 15 min) were monitored by UV-vis and Raman spectrometer in the dark or on irradiation with 475 nm light from 0 to 30 minutes. Aliquots of stock solutions of cyt c (1 mM), NADH (10 mM)

and QAIC (1 mM) were added to the cuvette while continuously bubbling nitrogen into the PBS.

2.4.4 photodynamic efficiency

2.4.4.1 Singlet oxygen generation studies

Solutions of QAIC and N-QAIC (QAIC incubated with NADH for 10 minutes) in acetonitrile were checked for the singlet oxygen generation studies by using 1,3-diphenylisobenzofuran (DPBF) as the singlet oxygen scavenger. The total concentration ratio of Ir(III) complexes and DPBF was made to 1:10 and irradiated using 475 nm long pass LASER. The generated singlet oxygen will induce photo-oxidation of the furanose ring of DPBF leading to breaking of its conjugation, which imparts a decrease in absorbance of DPBF at 410 nm without affecting absorption of the complex. These changes in absorbance were recorded every 10 s. The quantum yields for $^1\text{O}_2$ production of the complexes QAIC and N-QAIC under irradiation in acetonitrile were evaluated using a steady-state method with absorption change of DPBF as the $^1\text{O}_2$ indicator and $[\text{Ru}(\text{bpy})_3]\text{Cl}_2$ as the standard ($\phi_s=0.57$ in acetonitrile) using the equation

$$\phi_c = \phi_s (S_c \times F_s / S_s \times F_c)$$

where subscripts ϕ_c and ϕ_s designate the singlet oxygen quantum yield of complex and $[\text{Ru}(\text{bpy})_3]\text{Cl}_2$ respectively; S stands for the slope of plots of the absorbance of DPBF (at 410 nm) against irradiation time of complex and standard; F stands for the absorption correction factor of complex and standard, which is given by $F = 1 - 10^{-\text{OD}}$ (OD represents the optical density of complex and $[\text{Ru}(\text{bpy})_3]\text{Cl}_2$ at 475 nm).

2.4.4.2 Singlet oxygen generation studies of NADH

To confirm the inefficiency of NADH alone to generate singlet oxygen up on 475 nm LASER trigger was examined by irradiating a 10 μM solution of NADH with DPBF and checked for the spectral parameters from 0 to 180 s.

2.4.4.3 Photostability study of DPBF up on LASER

The photo inertness of DPBF up on 475 nm LASER trigger was screened by checking the spectral parameters (absorption and emission) of the compound under light illumination from 0 to 5 minutes.

2.4.4.4 Singlet oxygen generation study using SOSG

To evaluate the Singlet oxygen generation of N-QAIC and QAIC in solution state 5 μM solution of N-QAIC and QAIC in acetonitrile were mixed with 10 μM singlet oxygen sensor green and irradiated with 475 nm long pass LASER. The photoluminescence of SOSG at 525 nm were measured.

2.4.4.5 Time Correlated Single Photon Counting (TCSPC) analysis for excited state lifetime.

The excited state lifetime of QAIC before and after the reaction with NADH in the presence and absence of oxygen was measured. Briefly, a solution of QAIC and QAIC incubated with NADH in acetonitrile was analyzed using TCSPC with IRF as the standard (excitation wavelength 510 nm, time range 3.2 μs , energy 250 KHz)

2.4.4.6 Cyclic Voltammetric analysis

Cyclic voltammetric analysis of QAIC and N-QAIC were measured with a computer-controlled BAS CV-50W potentiostat under an argon atmosphere in dry and oxygen-free acetonitrile with 0.1 M tetrabutylammonium hexafluorophosphate (TBAH) as supporting electrolyte (Dumur et al., 2011). A regular three electrode set-up consisting of an Ag/AgCl electrode and a platinum wire counter electrode was used. The redox potentials were referenced against the ferrocene/ferrocenium redox couple as an internal standard.

2.4.5 In vitro evaluation

2.4.5.1 Cell culture methods

The human hepatocarcinoma cancer cell line Hep-G2 was obtained from American Type Culture Collection (ATCC, Manassas, VA, USA). Cells were maintained in Dulbecco's modified Eagle medium (DMEM) with 10% fetal bovine serum and 5% CO_2 at 37 $^\circ\text{C}$. Cells were cultured in glass-bottom, 96-well black plates, T-25 flasks, T-75 flasks, and 4-well chamber slides for various experiments 2 days prior to the conduction of experiments. All the experiments were performed in triplicate for accurate results.

2.4.5.2 ICP-MS Analysis of iridium content

The cellular uptake capacity of the complexes was measured by determination of intracellular iridium contents through ICP-MS, Briefly, Hep-G2 cells were seeded into 6 well plate for 24 h. The medium was removed and replaced with medium/DMSO (v/v, 99:1) containing QAIC (10,25,50,75 and 100 μM). After 2 h incubation, the cells were trypsinized, collected in PBS (3 mL) and counted. The cells were pelletized and lysed in

radio immunoprecipitation assay (RIPA) Buffer. HNO₃ (65%, 1 mL) was added to the lysates of the whole cell and the mixture was incubated at room temperature for 24 h to digest entirely. The solution was then diluted to a final volume of 10 mL with Milli-Q water. The same experiment was repeated in time dependent manner by varying the incubation time from 15 minutes to 2 h. Finally, the concentration of iridium was measured using the ICP-MS

2.4.5.3 Quantification of NADH from different cancer cell lines

MCF-7 (human breast cancer), HeLa (human cervical cancer cells), HepG2 (human hepatocellular carcinoma) and WI-38 (human lung fibroblast) cells were cultured in Dulbecco's Modified Eagle Medium (DMEM) containing 10% FBS, penicillin (100 U/mL), and streptomycin (100 U/mL) at 37°C under 5% CO₂ atmosphere. Cell samples were prepared for NADH quantification, 2 x 10⁵ cells were plated in 6 well plates and incubated for 24 h. Cells were scraped out in ice cold PBS and pelleted by centrifugation which were then extracted using NADH extraction buffer. Further quantification was performed using NADH quantification kit (MAK037, Sigma Aldrich, USA) as per the manufacture's protocol.

2.4.6 Live cell imaging

2.4.6.1 Endogenous NADH stimulated live cell imaging via fluorescence

HepG2 cells were seeded into 96 well plate and treated with 25 µM concentration of QAIC incubated at 37°C with different time period. After required incubation time the cells were washed with PBS and time dependent fluorescence images were taken from 0 to 60 minutes.

2.4.6.2 Endogenous NADH stimulated live cell imaging via SERS

Cells were cultured in 16 well chamber slide made of glass at a seeding density of 7 x 10³ cells /well. Cells were incubated with QAIC followed by AuNP and time dependent SERS spectral mapping was carried out using confocal Raman microscope (alpha300R, WITec Inc. Germany) with a laser beam directed to the sample through 20X objective and a Peltier cooled CCD detector. For this, scan range was given as 50 µm X 50µm with 100 X 100 pixel. The sample was excited by a power of 10 mW from 633 nm laser and mapping was done based on 1042 cm⁻¹ peak using 600 g/mm grating. Integration time was fixed as 0.05 s and the intensity-modulated images were prepared by image processing option in control 5.2 software. A minimum of three independent measurements were made for each sample.

2.4.6.3 Action of exogenous NADH

HepG2 cells were seeded into 96 well plate and treated with 25 μ M concentration of QAIC and incubated at 37⁰C for 45 minutes. After the incubation cells were washed with PBS and added fresh media followed by different concentrations of NADH (10 and 20 μ M) and incubated for 40 minutes. Washed with PBS and fluorescence images were taken using green filter.

2.4.6.4 Glucose dependent study

HepG2 cells were incubated with different concentrations of glucose (10 and 20 mM) for 60 minutes followed by 25 μ M of QAIC at 37⁰C for 45 minutes, washed with PBS and fluorescence images were taken.

2.4.6.5 Pyruvate and lactate dependent study

HepG2 cells were seeded into 96 well plate and incubated with varying concentrations of pyruvate (5 and 10 mM) for 60 minutes followed by treating with 25 μ M of QAIC and incubated at 37⁰C for 45 minutes. After the incubation cells were washed with PBS and images were taken. The same procedure was repeated in case of lactate also (incubation time 30 minutes). The combined effect of pyruvate and lactate were also examined by adopting the same procedure with the addition of 10 mM lactate followed by 5 mM pyruvate.

2.4.6.6 GSH and Paclitaxel dependent study

HepG2 cells were treated with GSH (5 and 10 mM) and GSH inhibitor BSO (5 mM) for 60 minutes, prior to the addition of QAIC. After the required incubation images were taken. For paclitaxel mediated GSH depletion study cells were incubated with 10 μ M paclitaxel for 4 h followed by treating with 25 μ M of QAIC and incubated at 37⁰C for 45 minutes.

2.4.6.7 Effect of hypoxia

HepG2 cells were pre-treated with cobalt chloride (100 μ M) to establish the hypoxic condition (1% oxygen). Images were taken after incubating 25 μ M of QAIC at 37⁰C for 45 minutes. The experiments were repeated for normoxic conditions.

2.4.6.8 Effect of Rotenone

HepG2 cells were incubated with Rotenone (5 μM) and then treated with QAIC in both normoxic and hypoxic conditions to study the effect of oxidative phosphorylation inhibitors on NADH levels. Fluorescence images were taken after 2 h incubation.

2.4.6.9 Phototoxicity of QAIC via MTT assay

Hep G2 human liver cancer cells were seeded into 96 well plates and incubated for 24 h (at 37 °C 5% CO_2). After the incubation cells were treated with varying concentrations of QAIC (0.1-100 μM) for 12 h., MTT (0.5 mg /ml) was added to each well and kept at 37°C for 4 h, and finally the so formed formazan crystals were dissolved in DMSO and the OD was measured at 570 nm using a microplate reader. To validate the photodynamic effect Hep G2 human liver cancer cells were seeded into 96 well plates and incubated for 24 h (at 37 °C 5% CO_2) at normoxic (20% O_2) and hypoxic (1% O_2) conditions. After the incubation cells were treated with 25 μM of QAIC followed by irradiation of 532nm LASER for 5 minutes. After 12 h incubation, MTT (0.5 mg /ml) was added to each well and kept at 37°C for 4 h and finally, the so formed formazan crystals were dissolved in DMSO and the OD was measured at 570 nm using a microplate reader. (Sujai et al., 2019)

2.4.6.10 Mitochondrial Membrane Potential Assay

The mitochondrial membrane depolarization was analyzed using TMRE mitochondrial membrane potential assay in which a lipophilic, cationic dye that accumulates in the negatively charged mitochondrial matrix is utilized. The HepG-2 cells were plated onto 12-well plates (1×10^5 cells/well) on a 5% CO_2 incubator at 37 °C. When the cells attained almost 70% confluency, they were subjected to 25 μM QAIC treatment followed by laser irradiation for 5 minutes. Then the cells were treated with TMRE reagent and incubated for 30 minutes, cells were trypsinized, washed with ice cold phosphate buffered saline (PBS, pH 7.4) thrice, lysed, and mitochondrial membrane potential estimation was performed as per the kit protocol (TMRE-Mitochondrial Membrane Potential Assay Kit, ab113852, Abcam, Cambridge, UK). Further, measurements were made with a fluorimeter (FLx800, Bio-Tek, Winooski, VT, USA) at an excitation wavelength of 490 nm and an emission wavelength of 510 nm.

2.4.6.11 Evaluation apoptotic potential

Evaluation of the mode of cytotoxicity exhibited by QAIC was performed on cancer cells with various apoptotic assays after administration of 25 μM of QAIC with and without laser

via dual staining acridine orange –ethidium bromide assay, APO Percentage assay (Biocolor, Belfast, Northern Ireland) and finally by FITC-Annexin V staining (BD Pharmingen no. 556547, BD Biosciences, San Jose, CA). Assessment of apoptosis using the acridine orange-ethidium bromide dual staining procedure was performed as described in literature (Liu et al., 2015). The cells were observed under an inverted fluorescent microscope, using a FITC filter (Olympus 1X51, Singapore) to view the apoptotic or non-apoptotic cells. The apoptosis was further confirmed using APO Percentage dye (Biocolor, Belfast, Northern Ireland) as per manufacturer’s instructions. Light microscopic images of APO Percentage dye-labelled cells, which stained pink under a light microscope, were used to quantify the extent of apoptosis. The dye uptake was further quantified using colorimetric method according to the manufacturer’s instruction. The cells were lysed and the absorbance was measured at 550nm using a microplate reader (Biotech, USA).

2.4.7 Computational studies

2.4.7.1 Density functional theory calculations

For optimization of all the geometries, the density functional theory (DFT) method wB97xD proposed by Head-Gordon and co-workers (Chai and Head-Gordon, 2008) is used which involves dispersion and features excellent geometry optimization performance. (Minenkov et al., 2012) Since the molecular complexes are large, the moderate size double zeta split-valence basis set with polarization function, 6-31G(d) is selected all main block elements while the LanL2DZ basis set is selected for Ir wherein the inner core electrons were replaced with the relativistic effective core potential (ECP) of Hay and Wadts (total 1596 basis functions for the NADH...QAIC complex). (Hay and Wadt, 1985; Krishnan et al., 1980) This method is abbreviated as wB97xD/BS1. Vibrational frequency analysis at wB97xD/BS1 is also done to confirm the nature of the optimized structures. The transition state was characterized by a single imaginary frequency along the reaction coordinate, whereas all the reactants and intermediates were confirmed to be minima by locating zero imaginary frequency. Further, the optimized geometries were subjected to single point calculation with the incorporation of solvation effect (solvent = acetonitrile) using the implicit self-consistent reaction field model (SCRF), SMD as implemented in Gaussian16. (M. J. Frisch, Marenich et al., 2016) To improve the energy parameters, this single point calculation is done using the higher basis set 6-311++G (d, p) for main block elements and LanL2DZ for Ir (total 2765 basis functions for NADH...QAIC). The single point method is abbreviated as wB97xD+SMD/BS.

2.5 References

- (1) Hanahan, D.; Weinberg, R. A. Hallmarks of Cancer: The next Generation. *Cell* **2011**. <https://doi.org/10.1016/j.cell.2011.02.013>.
- (2) Yaku, K.; Okabe, K.; Hikosaka, K.; Nakagawa, T. NAD Metabolism in Cancer Therapeutics. *Front Oncol* **2018**, *8* (DEC), 1–9. <https://doi.org/10.3389/fonc.2018.00622>.
- (3) Chiarugi, A.; Dölle, C.; Felici, R.; Ziegler, M. The NAD Metabolome - A Key Determinant of Cancer Cell Biology. *Nat Rev Cancer* **2012**, *12* (11), 741–752. <https://doi.org/10.1038/nrc3340>.
- (4) Kim, S. Y. Cancer Energy Metabolism: Shutting Power off Cancer Factory. *Biomol Ther (Seoul)* **2018**, *26* (1), 39–44. <https://doi.org/10.4062/biomolther.2017.184>.
- (5) Xiao, W.; Wang, R. S.; Handy, D. E.; Loscalzo, J. NAD(H) and NADP(H) Redox Couples and Cellular Energy Metabolism. *Antioxid Redox Signal* **2018**, *28* (3), 251–272. <https://doi.org/10.1089/ars.2017.7216>.
- (6) Eales, K. L.; Hollinshead, K. E. R.; Tennant, D. A. Hypoxia and Metabolic Adaptation of Cancer Cells. *Oncogenesis* **2016**, *5* (1), e190–e190. <https://doi.org/10.1038/oncsis.2015.50>.
- (7) Wang, L.; Zhang, J.; Kim, B.; Peng, J.; Berry, S. N.; Ni, Y.; Su, D.; Lee, J.; Yuan, L.; Chang, Y. T. Boronic Acid: A Bio-Inspired Strategy to Increase the Sensitivity and Selectivity of Fluorescent NADH Probe. *J Am Chem Soc* **2016**, *138* (33), 10394–10397. <https://doi.org/10.1021/jacs.6b05810>.
- (8) Reddy, M. L. P.; Bejoymohandas, K. S. Evolution of 2, 3'-Bipyridine Class of Cyclometalating Ligands as Efficient Phosphorescent Iridium (III) Emitters for Applications in Organic Light Emitting Diodes. *Journal of Photochemistry and Photobiology C: Photochemistry Reviews* **2016**, *29*, 29–47. <https://doi.org/10.1016/j.jphotochemrev.2016.10.001>.
- (9) Nam, J. S.; Kang, M. G.; Kang, J.; Park, S. Y.; Lee, S. J. C.; Kim, H. T.; Seo, J. K.; Kwon, O. H.; Lim, M. H.; Rhee, H. W.; Kwon, T. H. Endoplasmic Reticulum-Localized Iridium (III) Complexes as Efficient Photodynamic Therapy Agents via Protein Modifications. *J Am Chem Soc* **2016**, *138* (34), 10968–10977. <https://doi.org/10.1021/jacs.6b05302>.
- (10) He, L.; Li, Y.; Tan, C. P.; Ye, R. R.; Chen, M. H.; Cao, J. J.; Ji, L. N.; Mao, Z. W. Cyclometalated Iridium (III) Complexes as Lysosome-Targeted Photodynamic Anticancer and Real-Time Tracking Agents. *Chem Sci* **2015**, *6* (10), 5409–5418. <https://doi.org/10.1039/c5sc01955a>.
- (11) Huang, H.; Banerjee, S.; Qiu, K.; Zhang, P.; Blacque, O.; Malcomson, T.; Paterson, M. J.; Clarkson, G. J.; Staniforth, M.; Stavros, V. G.; Gasser, G.; Chao, H.; Sadler, P. J. Targeted Photoredox Catalysis in Cancer Cells. *Nat Chem* **2019**, *11* (11), 1041–1048. <https://doi.org/10.1038/s41557-019-0328-4>.

-
- (12) Dolmans, D. E. J. G. J.; Fukumura, D.; Jain, R. K. Photodynamic Therapy for Cancer. *Nature Reviews Cancer*. 2003. <https://doi.org/10.1038/nrc1071>.
- (13) Brown, S. B.; Brown, E. A.; Walker, I. The Present and Future Role of Photodynamic Therapy in Cancer Treatment. *Lancet Oncology*. 2004. [https://doi.org/10.1016/S1470-2045\(04\)01529-3](https://doi.org/10.1016/S1470-2045(04)01529-3).
- (14) Li, X.; Kwon, N.; Guo, T.; Liu, Z.; Yoon, J. Innovative Strategies for Hypoxic-Tumor Photodynamic Therapy. *Angewandte Chemie - International Edition*. 2018. <https://doi.org/10.1002/anie.201805138>.
- (15) You, Y.; Cho, S.; Nam, W. Cyclometalated Iridium (III) Complexes for Phosphorescence Sensing of Biological Metal Ions. *Inorganic Chemistry*. 2014. <https://doi.org/10.1021/ic4013872>.
- (16) Sun, P.; Zhang, H.; Sun, Y.; Liu, J. The Recent Development of Fluorescent Probes for the Detection of NADH and NADPH in Living Cells and in Vivo. *Spectrochimica Acta - Part A: Molecular and Biomolecular Spectroscopy* **2021**. <https://doi.org/10.1016/j.saa.2020.118919>.
- (17) Sudheesh, K. V.; Jayaram, P. S.; Samanta, A.; Bejzymohandas, K. S.; Jayasree, R. S.; Ajayaghosh, A. A Cyclometalated IrIII Complex as a Lysosome-Targeted Photodynamic Therapeutic Agent for Integrated Imaging and Therapy in Cancer Cells. *Chemistry - A European Journal* **2018**, *24* (43), 10999–11007. <https://doi.org/10.1002/chem.201801918>.
- (18) Cao; Cai-Ping Tan; Mu-He Chen; Na Wu; De-Yang Yao; Xing-Guo Liu; Liang-Nian Ji; Zong-Wan Mao. Targeting Cancer Cell Metabolism with Mitochondria-Immobilized Phosphorescent Cyclometalated Iridium (III) Complexes. *Chem Sci* **2017**, *8*, 631, 631–640. <https://doi.org/10.1039/c6sc02901a>.
- (19) Huang, T.; Yu, Q.; Liu, S.; Zhang, K. Y.; Huang, W.; Zhao, Q. Rational Design of Phosphorescent Iridium (III) Complexes for Selective Glutathione Sensing and Amplified Photodynamic Therapy. *ChemBioChem* **2019**, *20* (4), 576–586. <https://doi.org/10.1002/cbic.201800507>.
- (20) Da Veiga Moreira, J.; Hamraz, M.; Abolhassani, M.; Bigan, E.; Pérès, S.; Paulevé, L.; Nogueira, M. L.; Steyaert, J. M.; Schwartz, L. The Redox Status of Cancer Cells Supports Mechanisms behind the Warburg Effect. *Metabolites* **2016**, *6* (4), 1–12. <https://doi.org/10.3390/metabo6040033>.
- (21) Parry, E. Influence on NADH of Glycolysis Content in Human Erythrocytes. **2019**, *216* (3).
- (22) Saranya, G.; Anees, P.; Joseph, M. M.; Maiti, K. K.; Ajayaghosh, A. A Ratiometric Near-Infrared Fluorogen for the Real Time Visualization of Intracellular Redox Status during Apoptosis. *Chemistry - A European Journal* **2017**, *23* (30), 7191–7195. <https://doi.org/10.1002/chem.201700839>.
-

- (23) Kim, S.; Fujitsuka, M.; Majima, T. Photochemistry of Singlet Oxygen Sensor Green. *Journal of Physical Chemistry B* **2013**, *117* (45), 13985–13992. <https://doi.org/10.1021/jp406638g>.
- (24) Pan, X.; Zhao, Y.; Cheng, T.; Zheng, A.; Ge, A.; Zang, L.; Xu, K.; Tang, B. Monitoring NAD(P)H by an Ultrasensitive Fluorescent Probe to Reveal Reductive Stress Induced by Natural Antioxidants in HepG2 Cells under Hypoxia. *Chemical Science* **2019**, *10* (35), 8179–8186. <https://doi.org/10.1039/c9sc02020a>.
- (25) Purohit, V.; Simeone, D. M.; Lyssiotis, C. A. Metabolic Regulation of Redox Balance in Cancer. *Cancers*. 2019. <https://doi.org/10.3390/cancers11070955>.
- (26) Okada, M.; Smith, N. I.; Palonpon, A. F.; Endo, H.; Kawata, S.; Sodeoka, M.; Fujita, K. Label-Free Raman Observation of Cytochrome c Dynamics during Apoptosis. *Proc Natl Acad Sci U S A* **2012**. <https://doi.org/10.1073/pnas.1107524108>.
- (27) Joseph, M. M.; Narayanan, N.; Nair, J. B.; Karunakaran, V.; Ramya, A. N.; Sujai, P. T.; Saranya, G.; Arya, J. S.; Vijayan, V. M.; Maiti, K. K. Exploring the Margins of SERS in Practical Domain: An Emerging Diagnostic Modality for Modern Biomedical Applications. *Biomaterials* **2018**, *181*, 140–181. <https://doi.org/10.1016/j.biomaterials.2018.07.045>.
- (28) Lv, W.; Zhang, Z.; Zhang, K. Y.; Yang, H.; Liu, S.; Xu, A.; Guo, S.; Zhao, Q.; Huang, W. A Mitochondria-Targeted Photosensitizer Showing Improved Photodynamic Therapy Effects Under Hypoxia. *Angewandte Chemie - International Edition* **2016**. <https://doi.org/10.1002/anie.201604130>.
- (29) Yogo, T.; Urano, Y.; Mizushima, A.; Sunahara, H.; Inoue, T.; Hirose, K.; Iino, M.; Kikuchi, K.; Nagano, T. Selective Photoinactivation of Protein Function through Environment-Sensitive Switching of Singlet Oxygen Generation by Photosensitizer. *Proc Natl Acad Sci U S A* **2008**, *105* (1), 28–32. <https://doi.org/10.1073/pnas.0611717105>.
- (30) Escudero, D. Revising Intramolecular Photoinduced Electron Transfer (PET) from First-Principles. *Acc Chem Res* **2016**, *49* (9), 1816–1824. <https://doi.org/10.1021/acs.accounts.6b00299>.
- (31) Wu, W.; Yang, P.; Ma, L.; Lalevée, J.; Zhao, J. Visible-Light Harvesting Pt II Complexes as Singlet Oxygen Photosensitizers for Photooxidation of 1, 5-Dihydroxynaphthalene. **2013**, No. coumarin 6, 228–231. <https://doi.org/10.1002/ejic.201200665>.
- (32) Mehraban, N.; Freeman, H. S. Developments in PDT Sensitizers for Increased Selectivity and Singlet Oxygen Production. *Materials*. 2015. <https://doi.org/10.3390/ma8074421>.
- (33) Wang, Z.; Ivanov, M.; Gao, Y.; Bussotti, L.; Foggi, P.; Zhang, H.; Russo, N.; Dick, B.; Zhao, J.; Di Donato, M.; Mazzone, G.; Luo, L.; Fedin, M. Spin–Orbit Charge-Transfer Intersystem Crossing (ISC) in Compact Electron Donor–Acceptor Dyads: ISC Mechanism and Application as Novel and Potent Photodynamic Therapy Reagents. *Chemistry - A European Journal* **2020**. <https://doi.org/10.1002/chem.201904306>.
-

- (34) Nam, J. S.; Kang, M. G.; Kang, J.; Park, S. Y.; Lee, S. J. C.; Kim, H. T.; Seo, J. K.; Kwon, O. H.; Lim, M. H.; Rhee, H. W.; Kwon, T. H. Endoplasmic Reticulum-Localized Iridium(III) Complexes as Efficient Photodynamic Therapy Agents via Protein Modifications. *J Am Chem Soc* **2016**, *138* (34), 10968–10977. <https://doi.org/10.1021/jacs.6b05302>.
- (35) Liu, K.; Liu, P. cheng; Liu, R.; Wu, X. Dual AO/EB Staining to Detect Apoptosis in Osteosarcoma Cells Compared with Flow Cytometry. *Med Sci Monit Basic Res* **2015**, *21*, 15–20. <https://doi.org/10.12659/MSMBR.893327>.
- (36) Arya, J. S.; Joseph, M. M.; Sherin, D. R.; Nair, J. B.; Manojkumar, T. K.; Maiti, K. K. Exploring Mitochondria-Mediated Intrinsic Apoptosis by New Phytochemical Entities: An Explicit Observation of Cytochrome c Dynamics on Lung and Melanoma Cancer Cells. *J Med Chem* **2019**, *62* (17), 8311–8329. <https://doi.org/10.1021/acs.jmedchem.9b01098>.
- (37) Nair, J. B.; Joseph, M. M.; Arya, J. S.; Sreedevi, P.; Sujai, P. T.; Maiti, K. K. Elucidating a Thermoresponsive Multimodal Photo- Chemotherapeutic Nanodelivery Vehicle to Overcome the Barriers of Doxorubicin Therapy. **2020**. <https://doi.org/10.1021/acsami.0c08762>.
- (38) Joseph, M. M.; Ramya, A. N.; Vijayan, V. M.; Nair, J. B.; Bastian, B. T.; Pillai, R. K.; Therakathinal, S. T.; Maiti, K. K. Targeted Theranostic Nano Vehicle Endorsed with Self-Destruction and Immunostimulatory Features to Circumvent Drug Resistance and Wipe-Out Tumor Reinitiating Cancer Stem Cells. *Small* **2020**, *16* (38), 1–17. <https://doi.org/10.1002/sml.202003309>.

GSH-depletion Assisted Chemo dynamic Therapy Followed by NIR-laser Induced Combined Phototherapy Towards Triple-negative breast cancer



Abstract

Hypoxia, characterized by reduced oxygen levels, hinders the effectiveness of photodynamic therapy (PDT), limiting its clinical use. PDT further exacerbates this problem by depleting intracellular oxygen reserves, restricting its application for various conditions. To address this challenge, a novel triple therapy approach has been developed, incorporating a singlet oxygen delivery system. This innovative system revolves around Ir-Nap (Naphthalene appended Iridium complex), a compound capable of autonomously generating singlet oxygen through the participation of cycloaddition reactions. This unique property leads to stable endoperoxide formation at lower temperatures, releasing singlet oxygen at higher temperatures, enabling PDT effects. To optimize Ir-Nap-endo delivery and therapeutic potential, it was ingeniously integrated into a polydopamine (PDA) nano system, serving dual roles in controlled release and mild photothermal therapy (PTT). This multifunctional platform utilizes a single laser source for both oxygen delivery and PTT effects. Enhancing specificity and efficacy, the construct was encapsulated in glutathione (GSH)-responsive

manganese dioxide (MnO₂) nanoparticles, acting as chemodynamic agents. Gradual MnO₂ degradation depletes intracellular GSH and promotes cellular oxygenation, boosting radical generation for chemodynamic therapy. For targeted therapy against triple-negative breast cancer (TNBC) cells, the entire construct was conjugated with a GRP78 recognizing small peptide substrate as a -targeting motif, facilitating preferential recognition and uptake by TNBC cells. This integrated approach, combining GSH depletion, singlet oxygen generation, PTT, chemodynamic therapy, and tumor-specific targeting, offers a promising avenue for advanced cancer treatment. The probe exhibited exceptional therapeutic efficacy in both in vitro and in vivo settings, overcoming challenges in combination therapy and paving the way for next-generation cancer nanomedicine.

3.1 Introduction

Tumor hypoxia, characterized by low oxygen levels, is a critical aspect of solid cancer development that significantly impacts disease progression and treatment outcomes. In tumor tissues, oxygen levels often plummet below 10 mmHg, in stark contrast to the 40-60 mmHg range seen in normal tissues. This severe oxygen deprivation exerts a multitude of effects on cancer biology, fostering aggressive behaviour in cancer cells.¹ Those cells or tissues located near blood vessels are better oxygenated and tend to grow rapidly, while cells in more oxygen-deprived regions may appear dormant, oscillating between growth and self-destruction. The cyclic pattern of hypoxia followed by reoxygenation can further exacerbate tumor aggressiveness.² The tumor microenvironment, composed of diverse cell types and surrounding tissue, plays a pivotal role in cancer growth and resistance to treatment. Hypoxia is closely intertwined with angiogenesis, as it triggers a cascade involving hypoxia-inducible factor 1 (HIF-1), leading to the production of vascular endothelial growth factor (VEGF) and the formation of aberrant, leaky blood vessels. This worsens the local oxygen shortage, amplifying the tumor's aggressiveness.³ Moreover, hypoxia profoundly affects how tumor cells generate energy. They switch from utilizing oxygen for energy (oxidative phosphorylation) to a process called glycolysis in response to low oxygen levels. This metabolic adaptation, regulated by HIF-1 α and the mTOR pathway, allows tumor cells to survive in the oxygen-depleted environment.⁴ Intriguingly, even in the absence of hypoxia, the activation of cancer-causing genes can promote glycolysis, emphasizing the intricate interplay between genetic factors and the tumor's surroundings in metabolic reprogramming.⁵ Hypoxia-inducible factors (HIFs) govern genes associated with tumor immunity under low-oxygen conditions, often resulting in the infiltration of immune-

suppressing cells such as myeloid-derived suppressor cells (MDSCs), tumor-associated macrophages (TAMs), and T-regulatory (Treg) cells.³

In this relentless pursuit of improved cancer treatment, combination therapy has emerged as a promising strategy in oncology, offering newfound hope and the potential for enhanced treatment outcomes. This innovative approach combines photothermal therapy (PTT), chemodynamic therapy (CDT), and photodynamic therapy (PDT), each with its unique mechanisms of action, to create a multifaceted assault on cancer cells and their microenvironment.⁶ In the following sections, we will delve into the significance of combination therapy in cancer treatment, highlighting its potential benefits, mechanisms, and the imperative need for ongoing research and clinical trials.^{7,8} One of the key pillars of combination therapy for cancer is photothermal therapy (PTT). PTT utilizes near-infrared (NIR) radiation to selectively generate localized heat which is induced by nanoparticles or photosensitizers within cancer cells leading to the cell death process. What makes PTT remarkable is its precision in targeting cancer cells while sparing healthy surrounding tissues. This precision is achieved by exploiting the differential absorption of NIR radiation by cancerous versus normal cells. Consequently, PTT offers a promising avenue for localized treatment with reduced systemic side effects.⁹ In PTT, nanoparticles such as gold nanoparticles or carbon nanotubes are commonly employed as agents to efficiently absorb NIR radiation. Once these nanoparticles accumulate within cancer cells, they absorb NIR light, resulting in a localized temperature increase through the photothermal effect. This temperature rise triggers a cascade of events within the cancer cells, including protein denaturation, membrane damage, and DNA disruption, culminating in cell death. The precision and minimal invasiveness of PTT makes it a valuable addition to combination therapy.¹⁰

Chemodynamic therapy (CDT), a relatively newer entrant in the field of cancer therapy, operates on a different principle. Instead of relying on light-based approaches like PTT and PDT, CDT induces cytotoxicity within the tumor microenvironment through chemical reactions.^{11,12} This innovative approach capitalizes on the unique conditions present within cancerous tissues, including the abundance of hydrogen peroxide (H_2O_2).¹² In CDT, catalysts, often transition metal-based nanoparticles, are introduced into the tumor microenvironment.^{13,14} These catalysts facilitate the conversion of H_2O_2 into highly reactive oxygen species (ROS) through Fenton or Fenton-like reactions.¹⁵ ROS, such as hydroxyl radicals ($\cdot OH$), are notorious for their destructive potential. When generated in

high concentrations, ROS initiates a cascade of damaging events within the tumor, including lipid peroxidation, protein oxidation, and DNA fragmentation, ultimately leading to cell death. CDT's ability to target the tumor microenvironment rather than just cancer cells themselves offers a complementary approach to traditional cancer treatments.^{16,17} By disrupting the supportive milieu surrounding cancer cells, CDT weakens their defences and makes them more susceptible to other therapeutic modalities, such as PTT and PDT.¹⁸

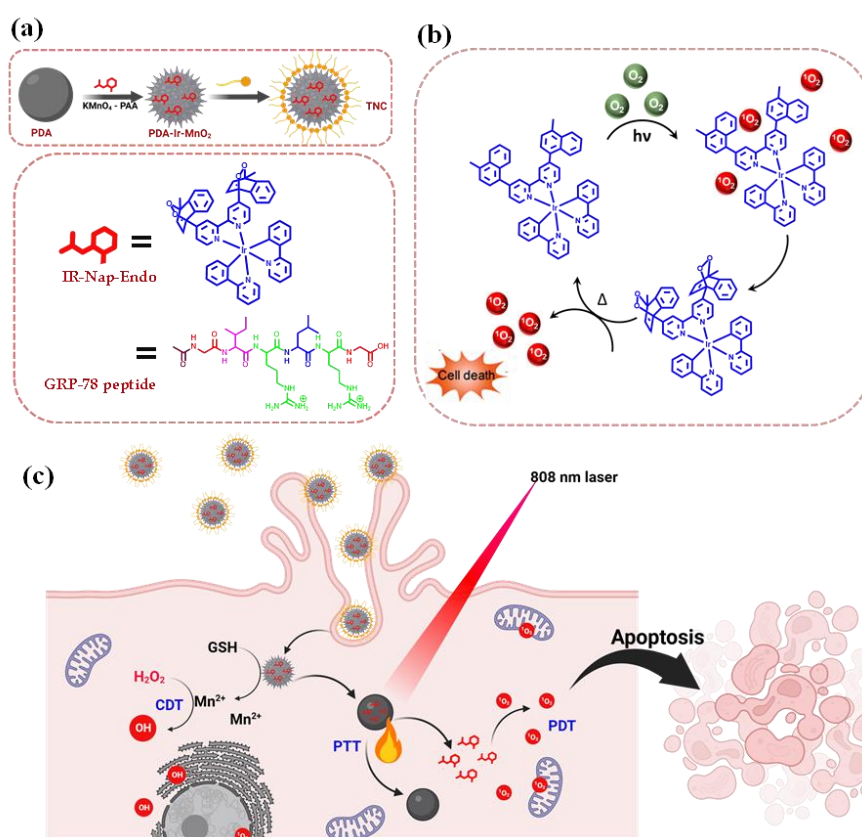
Photodynamic therapy (PDT) has emerged as a promising paradigm in precision medicine, offering a minimally invasive treatment approach with notable advantages over conventional therapies like chemotherapy, radiotherapy, and surgery. Its potential lies in the precise targeting of cancer cells through the activation of photosensitizing agents, which generate reactive oxygen species (ROS) upon exposure to light.^{19,20} This selective mechanism minimizes damage to healthy tissue, making PDT an attractive option for various malignancies. However, despite its therapeutic promise, PDT has not yet attained widespread adoption as a frontline treatment. Its limited applicability does not stem from a shortage of efficient photosensitizers or delivery mechanisms but rather from a fundamental hurdle ingrained in the photodynamic process itself. Central to the challenge is the phenomenon of hypoxia, a condition characterized by low oxygen levels within tumors.⁵ This oxygen-deficient environment poses a significant obstacle to the generation of ROS, crucial for the PDT process. Paradoxically, PDT compounds this issue by depleting intracellular oxygen reserves, exacerbating the already existing hypoxia. This intricate interplay between PDT and tumor oxygenation profoundly impacts therapeutic outcomes, particularly in solid tumors marked by inadequate oxygen availability.²¹ In response to these challenges, researchers have shifted their focus toward devising strategies for oxygen-independent PDT. Aromatic endoperoxides, derived from polycyclic aromatic hydrocarbons like naphthalene and anthracene, offer a solution. These compounds can serve as chemical sources of singlet oxygen when thermally triggered.^{22,23}

The true power of combination therapy in cancer treatment emerges when these three modalities—PTT, CDT, and PDT—are harnessed together. Each modality brings its unique strengths to the table, and their combination results in synergistic effects that have the potential to significantly enhance cancer treatment efficacy.¹⁶ Firstly, the combination of PTT, CDT, and PDT targets cancer cells from multiple angles, overwhelming their defences and reducing the likelihood of treatment resistance. PTT's precise cellular targeting is complemented by CDT's disruption of the tumor microenvironment, making it more susceptible to the damaging effects of PDT.

Secondly, the ability to customize the treatment regimen, including the sequence and timing of these therapies, allows for optimal therapeutic outcomes. For example, initiating CDT before PTT and PDT may weaken the tumor microenvironment, making cancer cells more susceptible to subsequent phototherapy.⁹ Thirdly, combination therapy has the potential to reduce the therapeutic doses required for each individual modality. Lower doses are often associated with reduced side effects, a critical consideration in cancer treatment to improve the patient's quality of life. The promise of combination therapy in cancer treatment is undeniably exciting. It offers the potential for improved treatment outcomes, reduced side effects, and increased versatility in addressing a wide range of cancer types.^{6,8} However, it is crucial to emphasize that the field of combination therapy is still in its nascent stages, and rigorous research and clinical trials are essential to validate its efficacy and safety. As researchers continue to unravel the complexities of tumor hypoxia and refine the techniques of PTT, CDT, and PDT, the future holds great promise for combination therapy as a formidable weapon in the battle against cancer. Collaborative efforts between scientists, clinicians, and medicinal companies will be instrumental in translating these innovative approaches into effective treatments that can benefit patients worldwide. With perseverance and dedication, combination therapy may well emerge as a transformative force in the fight against cancer, providing new hope and improved outcomes for those facing this formidable adversary.^{24,25}

In this study, an impactful strategy was proposed that involves the integration of a sophisticated singlet oxygen delivery system comprising an iridium complex denoted as Ir-Nap. This complex possesses the unique ability to autonomously generate singlet oxygen through its iridium centre and subsequently engage in a cycloaddition reaction with the self-produced singlet oxygen, facilitated by the naphthalene appendage, resulting in the formation of an endoperoxide species.²³ It is noteworthy that this endoperoxide exhibits stability at lower temperatures; however, at elevated temperatures exceeding 45°C, it undergoes a cycloreversion process, liberating singlet oxygen and thereby inducing photodynamic therapy (PDT) effects. To optimize the delivery and therapeutic potential of Ir-Nap-endo, we judiciously incorporated it into a polydopamine (PDA) nanoparticle. This multifunctional nanoplatform not only facilitates the controlled release of the compound but also serves as a mild photothermal therapy (PTT) agent, generating heat upon laser irradiation.²⁶ Consequently, this dual-action system enables both oxygen delivery and PTT effects, all achievable through a single laser source. To enhance the specificity and efficacy of this construct, we further encapsulated it within glutathione (GSH)--responsive

manganese dioxide (MnO_2) nanoparticles. These MnO_2 nanoparticles possess the ability to reduce intracellular protective GSH levels, thereby enhancing their potential as chemodynamic agents. The gradual degradation of the MnO_2 layer not only reduces GSH but also promotes cellular oxygenation, augmenting the generation of radicals for chemodynamic therapy.²⁷ To achieve selective targeting of triple-negative breast cancer (TNBC) cells, the surface of nano-construct was functionalized with a GRP78-targeting peptide sequence. This peptide acts as a targeting ligand, enabling the preferential recognition and uptake of the construct by TNBC cells. This comprehensive approach combines GSH depletion followed by singlet oxygen generation, PTT, Chemodynamic therapy, and tumor-specific targeting, making it a promising avenue for advanced cancer treatment (**Scheme 3.1**).



Scheme 3.1: Pictorial representation of sequential events induced by TNC in TNBC cells. (a) The construction and the components of the nano construct. (b) The mechanism of generation and cycloreversion of the singlet oxygen delivery system. (c) The step wise sequential events induced by TNC in TNBC cells after internalization

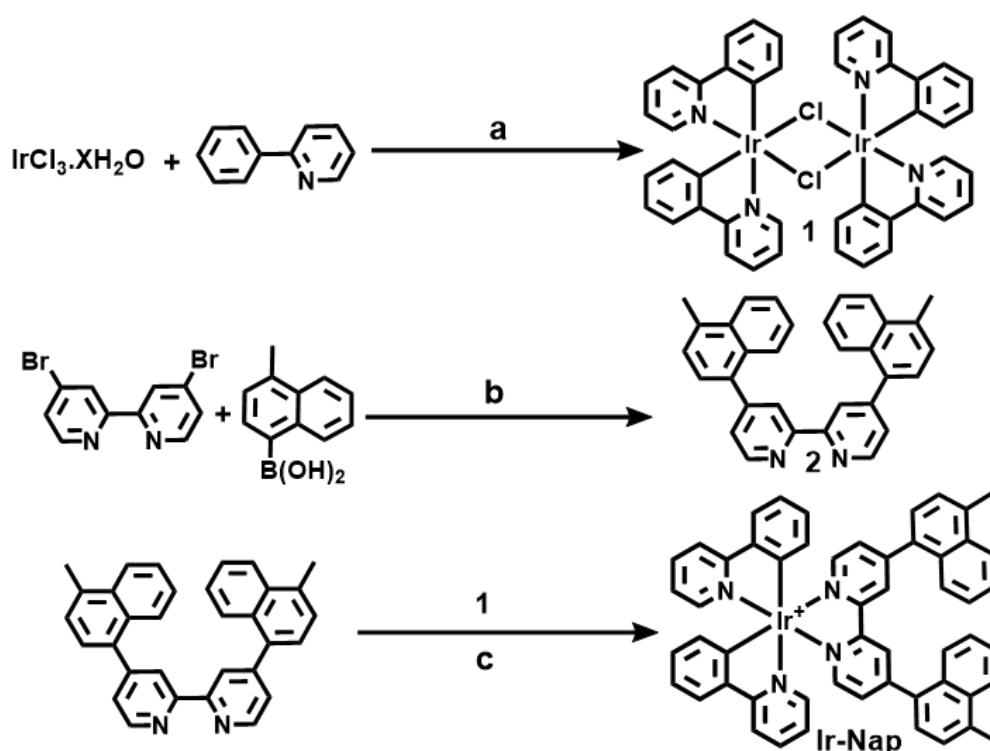
3.2 Results and discussion

The theranostic nano construct (TNC), designed for combination therapy, consists of four distinct components, each with unique attributes to optimize treatment outcomes. These

components were meticulously synthesized and effectively linked together to create the ultimate theranostic nanoprobe, TNC. This innovative nanoprobe offers a multifaceted approach to therapy, capitalizing on the specialized properties of its constituent parts, ensuring a synergistic and potent therapeutic effect. Through careful preparation and successful conjugation, TNC emerges as a promising tool for both treatment and diagnosis, paving the way for more effective and personalized healthcare interventions

3.2.1 Synthesis and characterization of singlet oxygen delivery system

The chemical synthesis process commenced with the creation of the cyclometalating ligand 2-phenyl pyridine, achieved through a palladium-catalyzed Suzuki cross-coupling reaction. The as-synthesized cyclometalated ligand was then combined with Iridium chloride using the Nonoyama reaction, resulting in the formation of a chlorine-bridged Iridium dimeric complex. The target complex, Ir-Nap, was subsequently obtained by replacing the bridging chlorine with an ancillary bipyridine ligand containing naphthalene appendages. This ligand was synthesized from 4,4'-dibromo-2,2'-bipyridine and 4-methylnaphthalene-1-boronic acid through a Suzuki coupling reaction (Scheme 3.2).



Scheme 3.2: Schematic illustration of the synthesis of Ir-Nap. Reagent and conditions: (a) [i] 2-ethoxyethanol/water (8:2), reflux, 24 h. (b) Aq- K_2CO_3 -Toluene, $\text{Pd(PPh}_3)_4$, TBAB-24 h, 90°C. (c) DCM/ethanol (1:3), Argon, 60°C, 12 h and NH_4PF_6 .

Finally, the chlorine counterion in the complexes was substituted with PF₆ through an anion exchange reaction involving ammonium hexafluorophosphate. The synthesized complexes underwent thorough characterization using HRMS and NMR spectroscopic techniques. A thorough examination was conducted to acquire a comprehensive grasp of the molecule, encompassing detailed investigations into its structural, photophysical, and electrochemical characteristics. These assessments encompassed the use of UV-visible and Fluorescence spectroscopy, as well as cyclic voltammetry techniques, with the findings presented in the accompanying material and methods.

3.2.2 Photophysical evaluation of singlet oxygen delivery system

Ir-Nap (10 μ M), has been the subject of extensive investigation to elucidate its intriguing photophysical properties and its potential utility in various scientific and practical applications. The characterization of this compound began with a comprehensive analysis using UV-Vis absorption and emission spectroscopy (Figure 3.1a).

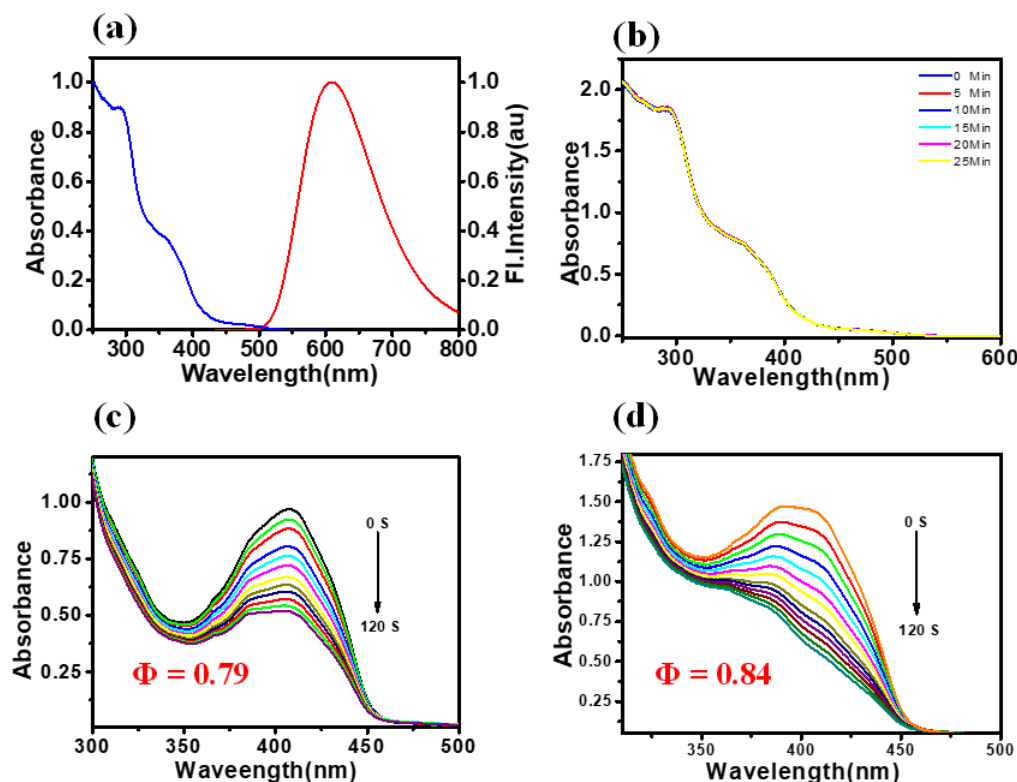


Figure 3.1: (a) UV-visible absorption spectra and emission spectra of the complex Ir-Nap (10 μ M in acetonitrile) and (b) Photostability studies of the complex with 475 laser irradiations from 0 to 25 min. (c) and (d) Singlet oxygen generation study with DPBF both Ir-Nap and Ir-Nap-endo respectively.

These techniques unveiled a metal-to-ligand charge transfer (MLCT) band within the spectral range of 475-510 nm, coupled with an emission peak centered at 610 nm. This

initial characterization hinted at the compound's ability to undergo electronic transitions, a crucial feature for understanding its behavior as a photosensitizer (**Figure 3.1 b&c**). To delve deeper into its functionality, the singlet oxygen generation capacity of Ir-Nap was rigorously examined. The use of 1,3-diphenylisobenzofuran (DPBF), a known singlet oxygen scavenger, allowed for the evaluation of Ir-Nap's photosensitization potential. As anticipated, Ir-Nap demonstrated its prowess in inducing the photo-sensitization of ground-state molecular oxygen, leading to the formation of singlet oxygen. The interaction between Ir-Nap and DPBF resulted in a discernible decrease in both absorption and emission profiles, a clear indication of singlet oxygen generation. This observation underscores the compound's capacity to harness light energy for the production of a highly reactive oxygen species, a feature that holds great promise for applications in photodynamic therapy and photochemical synthesis. The singlet oxygen quantum yield (Φ) provides a quantitative measure of a compound's ability to generate singlet oxygen. In the case of Ir-Nap, its Φ value was determined to be 0.79, which was notably higher than that of the reference compound, Ru(bpy)₃Cl₂,²⁸ which exhibited a Φ value of 0.57. This result underlines Ir-Nap's superior photosensitizing capacity, making it an attractive candidate for applications demanding high singlet oxygen production. However, to provide a more accurate assessment of Ir-Nap's singlet oxygen generation potential, it was imperative to account for its singlet oxygen trapping capabilities. This was achieved by preparing the endoperoxide form of Ir-Nap (Ir-Nap-endo) before conducting the Φ measurement (**Figure 3.1c**).

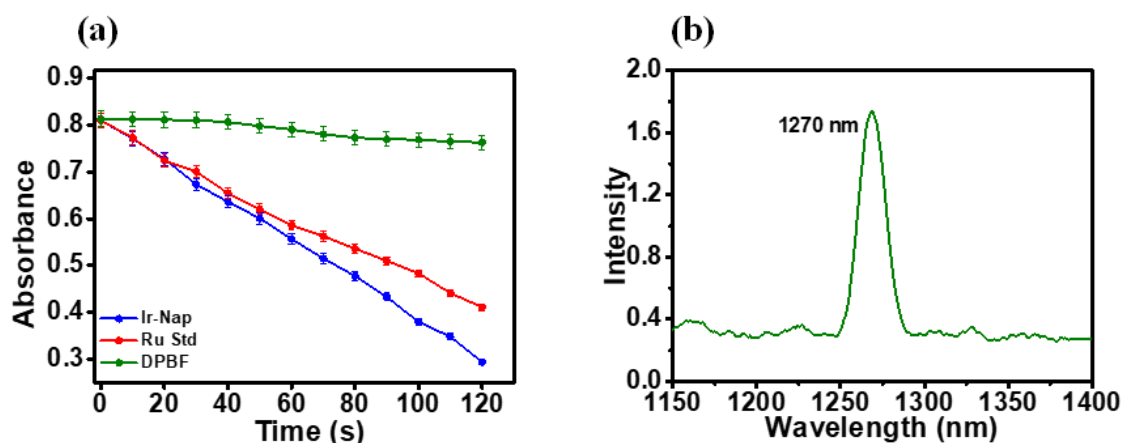


Figure 3.2: (a) Depletion of DPBF absorption profile upon interaction with Ir-Nap, Ru based standard complex [RuBpy₃]Cl₂ and the DPBF alone after irradiation with 475 nm laser for 2 min (b) Singlet oxygen phosphorescence spectra at 1270 nm of Ir-Nap sample irradiated with laser in acetonitrile

The Φ value determined with the endoperoxide was notably higher at 0.84, further highlighting Ir-Nap's exceptional ability to both generate and trap singlet oxygen

effectively (**Figure 3.1d**). Moreover, the study delved into the direct monitoring of singlet oxygen by recording its emission at 1275 nm. Ir-Nap exhibited strong oxygen phosphorescence at this wavelength, providing concrete evidence of its singlet oxygen generation capabilities. This direct measurement reinforces the compound's potential for applications where the real-time detection of singlet oxygen is crucial, such as in photodynamic therapy and environmental monitoring (**Figure 3.2a&b**).

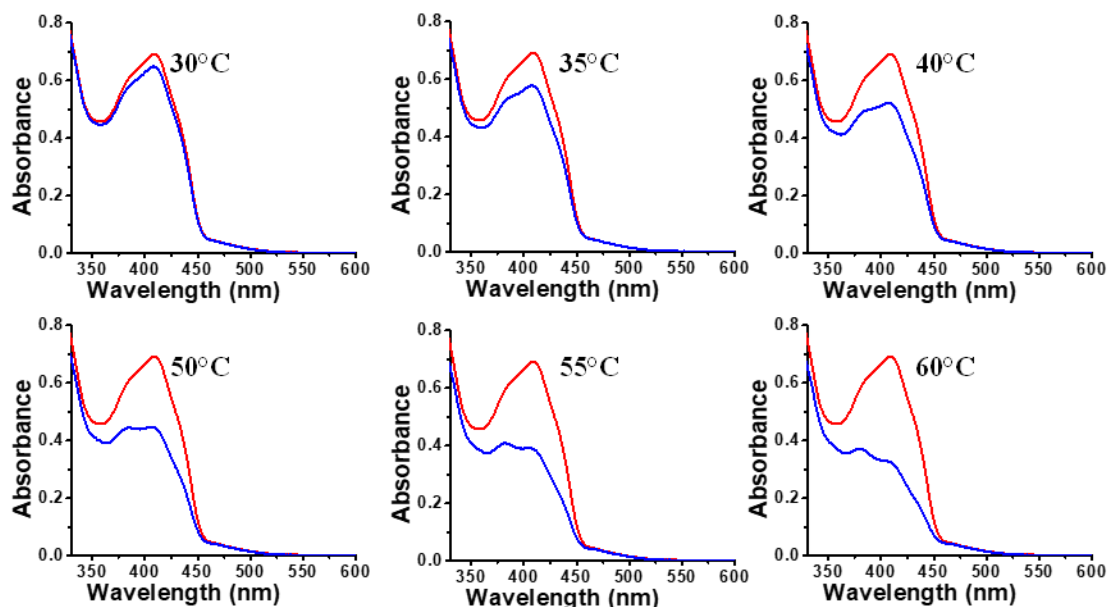


Figure 3.3: Depletion of DPBF absorption profile upon heating with Ir-Nap endo from 30 to 60°C. Each graph was a separate experiment with the same concentration of Ir-Nap-endo and DPBF.

One of the distinctive attributes of Ir-Nap is its ability to trap singlet oxygen, effectively acting as a reservoir for the controlled release of this valuable species. To investigate this intriguing property, a series of experiments were conducted. A solution containing Ir-Nap was exposed to 380 nm light irradiation within a photoreactor, while DPBF was introduced into the solution. The temperature of the solution was systematically elevated from 30 to 60°C, allowing for the monitoring of absorbance changes. Remarkably, the results revealed the release of trapped singlet oxygen through a temperature-assisted cycloreversion of endoperoxide. This unique mechanism was unmistakably indicated by the decline in the absorbance of the DPBF peak (**Figure 3.3**). Notably, control experiments performed with DPBF alone under identical conditions exhibited no significant changes, conclusively ruling out the possibility of experimental error arising from DPBF photoirradiation. Ir-Nap's ability to effectively store and release singlet oxygen holds great promise for applications where the controlled release of singlet oxygen is of paramount importance, such as in the development of targeted drug delivery systems (**Figure 3.4a&b**).

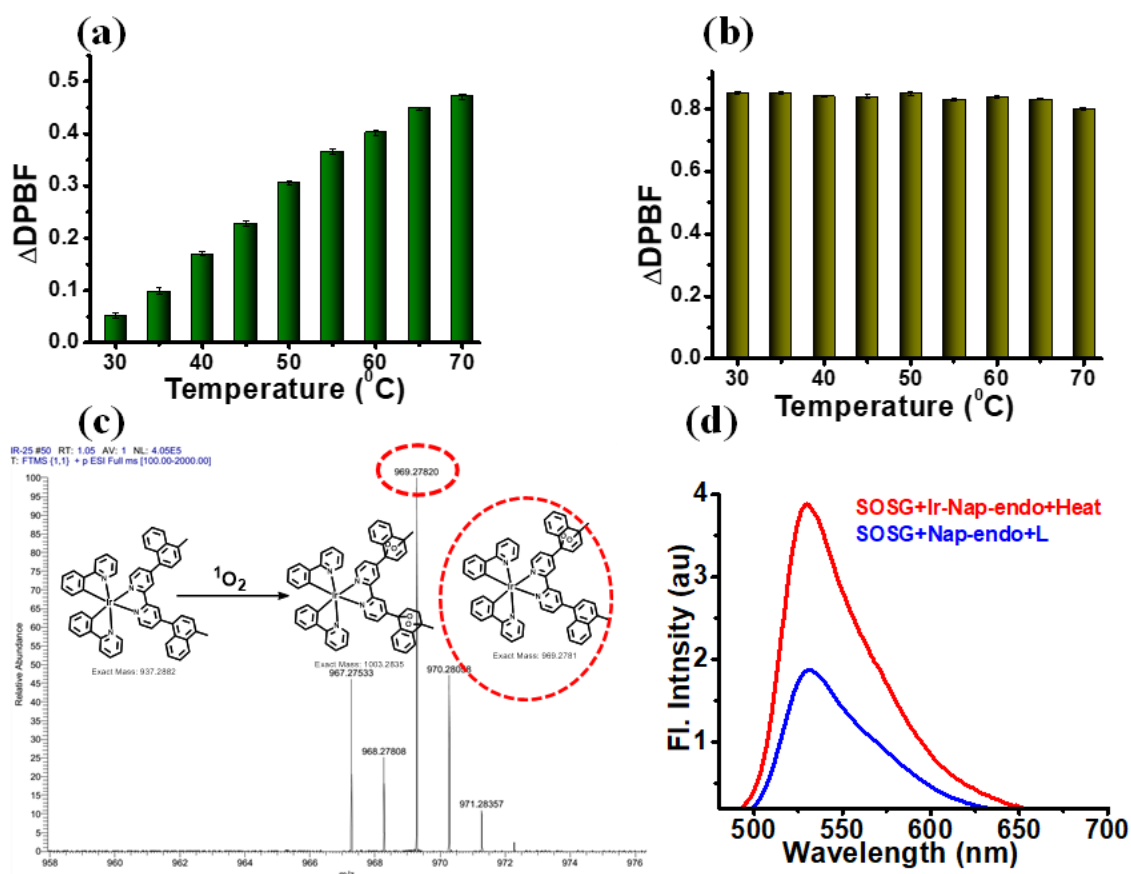


Figure 3.4: (a) UV-visible absorption spectral change of DPBF with Ir-Nap-endo upon heating from 30 to 70°C. (b) UV-visible absorption spectral change of alone upon heating from 30 to 70°C. (c) HRMS conformation of Ir-Nap-endo formation showing the existence of mono adduct. (d) Singlet oxygen generation study with SOSG both Ir-Nap and Ir-Nap-endo in heat and laser assisted method.

In order to further substantiate the effective trapping and subsequent storage of singlet oxygen within the naphthalene moiety of the molecule HRMS analysis was carried out. The molecular ion peak of the Ir-Nap molecule, at 937.290 m/z, exhibited a noteworthy transition, displaying a significant shift to 969.278 m/z. This alteration in mass spectrometry data aligns convincingly with the introduction of an oxygen atom into the Ir-Nap molecule, indicative of the formation of Ir-Nap-endo through a mono-oxygenation process. This observation provides compelling scientific evidence supporting the singlet oxygen trapping and incorporation within the molecular structure of Ir-Nap-endo (Figure 3.4c). Quantifying the efficiency of singlet oxygen generation is essential for assessing the practical utility of Ir-Nap as a photosensitizer. This dual functionality positions Ir-Nap as a versatile tool for applications requiring precise control over singlet oxygen release kinetics. The confirmation of singlet oxygen release kinetics was reinforced by using the widely recognized singlet oxygen probe SOSG. When Ir-Nap-endo was exposed to laser irradiation, a noticeable increase in SOSG fluorescence was observed (Figure 3.4d).

Moreover, when the sample was heated to 50°C, the fluorescence intensity was further raised beyond the levels achieved with laser assistance. This unequivocally validates both the ability of the system to generate singlet oxygen with laser assistance and its potential for releasing singlet oxygen when subjected to heat.

3.2.3 Synthesis of the Photothermal Agent

The subsequent phase of the research aimed at the development and synthesis of a photothermal agent capable of initiating controlled thermal reactions, leading to the precise decomposition of Ir-Nap-endo, thereby facilitating the targeted generation of singlet oxygen.

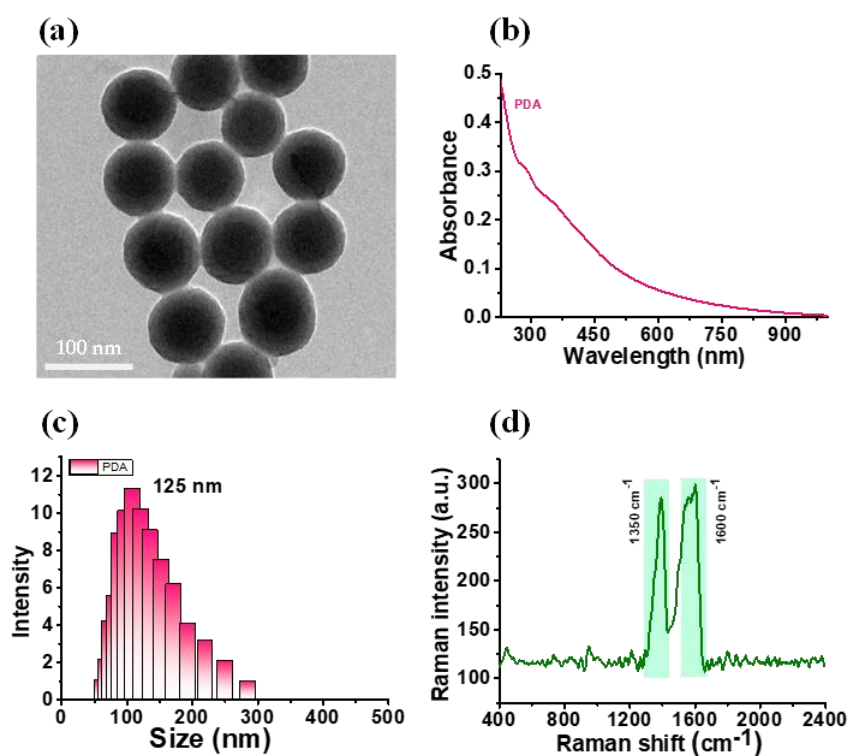


Figure 3.5: (a) TEM image of the prepared PDA nanoparticle. (b) UV-visible absorption spectra of the PDA nanoparticle with NIR absorbance. (c) DLS analysis of the PDA nanoparticle. (d) Raman spectra of the of the PDA nanoparticle with G and D bands.

Additionally, it was imperative to identify an efficient carrier particle for loading Ir-Nap-endo. To address these objectives, we initiated the synthesis of Polydopamine nanoparticles within a size range of 80-120 nm via a polymerization process involving dopamine hydrochloride and a mild base, ammonium hydroxide.

Polydopamine exhibited inherent characteristics such as robust negative zeta potential and substantial adsorption capacity, offering significant advantages for the electrostatic binding of positively charged iridium complexes, ensuring high loading efficiency. The morphology

of the resulting Polydopamine nanoparticles was meticulously examined using Transmission Electron Microscopy (TEM), revealing a spherical structure with an average size of 80 nm (**Figure 3.5a**). Dynamic Light Scattering (DLS) analysis corroborated this, confirming an average size of 100 nm (**Figure 3.5c**). Furthermore, UV-visible absorption spectral analysis unveiled a broad absorption profile spanning from the ultraviolet (200 nm) to near-infrared (1000 nm) regions, rendering Polydopamine well-suited for near-infrared (NIR) laser-activatable photothermal applications (**Figure 3.5b**). This property is crucial for both the subsequent photothermal activation of Ir-Nap-endo and photothermal therapy. Further characterization included Raman spectral analysis, which affirmed the presence of characteristic G band at 1300 cm^{-1} and D bands at 1600 cm^{-1} associated with Polydopamine nanoparticles, reinforcing their identity and structural properties (**Figure 3.5d**).

To assess the photothermal capabilities of the synthesized nanoparticles, a temperature generation analysis was conducted. Water served as a negative control, while natural melanin nanoparticles isolated from squid ink were the positive control. Evaluation under irradiation with an 808 nm laser, chosen for its enhanced tissue penetration capabilities within the biological window, demonstrated that both PDA and bare SNP (natural melanin nanoparticles) reached a temperature of $70\text{ }^{\circ}\text{C}$ within 15 minutes, whereas water could only generate a temperature of $30\text{ }^{\circ}\text{C}$ (**Figure 3.6a**). This temperature increase validated the efficacy of the 808 nm laser for Photothermal Therapy (PTT), with no consideration given to alternative lasers with lower wavelengths due to their inferior tissue penetration capabilities. The exponential temperature rises of up to $60\text{ }^{\circ}\text{C}$ within 8 minutes of laser irradiation over five consecutive cycles, totalling 90 minutes, underscoring the exceptional photothermal efficiency and stability of the PDA nanoparticles. The calculated photothermal conversion efficiency of the probe was an impressive 49.8%, signifying a remarkably high value for a theranostic nanoprobe (**Figure 3.6b&c**). The generated heat was deemed sufficient for inducing hyperthermia and promoting the cycloreversion of endoperoxide from Ir-Nap-endo, facilitating PDT. The Polydopamine nanoparticles prepared here displayed a zeta potential of -36.5 mV , providing a highly negatively charged surface conducive to the electrostatic attachment of these nanoparticles to the positively charged Ir-Nap-endo, ultimately forming the desired PDA-Ir-Nap-endo composite called PIR. The formation of PIR was confirmed through UV spectroscopic studies, where a clear merging of the peaks of the Iridium complex with PDA spectra was observed. Further confirmation of the electrostatic interaction with Ir-Nap-endo was obtained through zeta potential analysis, revealing a gradual reduction in the highly negative zeta potential of

PDA to -14.9 upon conjugation with Ir-Nap-endo, indicating a clear confirmation of their association (Figure 3.6d).

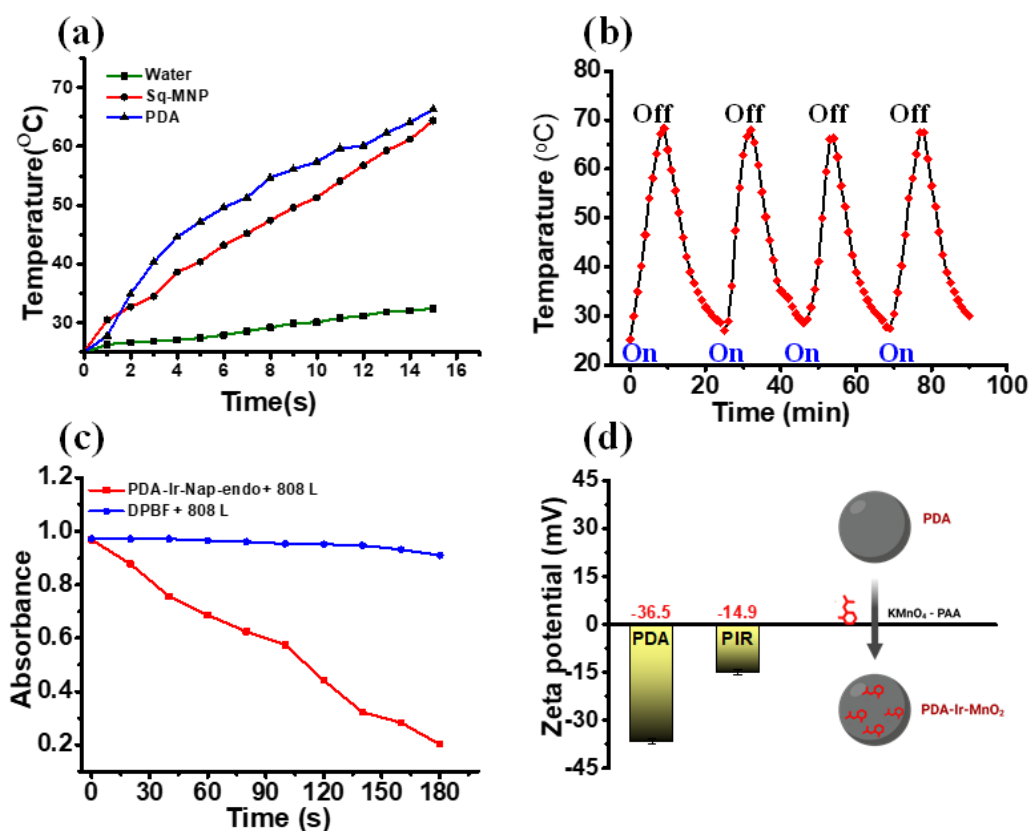


Figure 3.6: (a) Temperature generation studies on PDA nanoparticles along with control samples. (b) Regenerative PTT ability of the PDA system with continuous on-off cycles. (c) Change in absorbance of DPBF alone and DPBF incubated with PDA-Ir-Nap-endo followed by 808 nm laser treatment. (d) Zeta potential change associated with the electrostatic conjugation of PS to the PDA nanoparticle.

In the investigation of the prepared PIR, an essential step was to assess its ability to release singlet oxygen upon laser activation, thereby confirming the efficacy of laser-assisted heat-triggered singlet oxygen release. To conduct this evaluation, PIR was combined with the singlet oxygen scavenger molecule DPBF, and a series of laser irradiation experiments were conducted. As anticipated, when subjected to 808 nm laser irradiation, the PIR exhibited its remarkable photothermal therapy (PTT) capability, leading to the generation of heat within the Polydopamine (PDA) nanoparticles. This rise in temperature induced the cycloreversion of the endoperoxide moiety within the PIR, consequently liberating singlet oxygen. Importantly, this singlet oxygen was found to efficiently react with and neutralize DPBF molecules. The outcome of these experiments was readily observable through spectroscopic analysis. Specifically, the presence of singlet oxygen, as generated by the PIR under laser irradiation, was evident in the substantial attenuation of the DPBF

absorption peak. This clear reduction in DPBF absorption highlighted the success of the combined approach, where heat-assisted photodynamic therapy (PDT) was effectively achieved. It is noteworthy that when PDA nanoparticles were employed in isolation, devoid of the PIR, there was no discernible impact on the DPBF absorption. This result underscores the specific contribution of the PIR in facilitating singlet oxygen release and its subsequent interaction with DPBF (Figure 3.6c).

3.2.4 MnO₂ coating of the nano construct for tumor microenvironment responsive activation

The designed PIR was further enhanced through the strategic incorporation of tumor microenvironment-responsive biocompatible MnO₂ nanoparticles. These MnO₂ nanoparticle layers exhibit distinctive attributes that render them highly suitable for targeted therapeutic interventions.

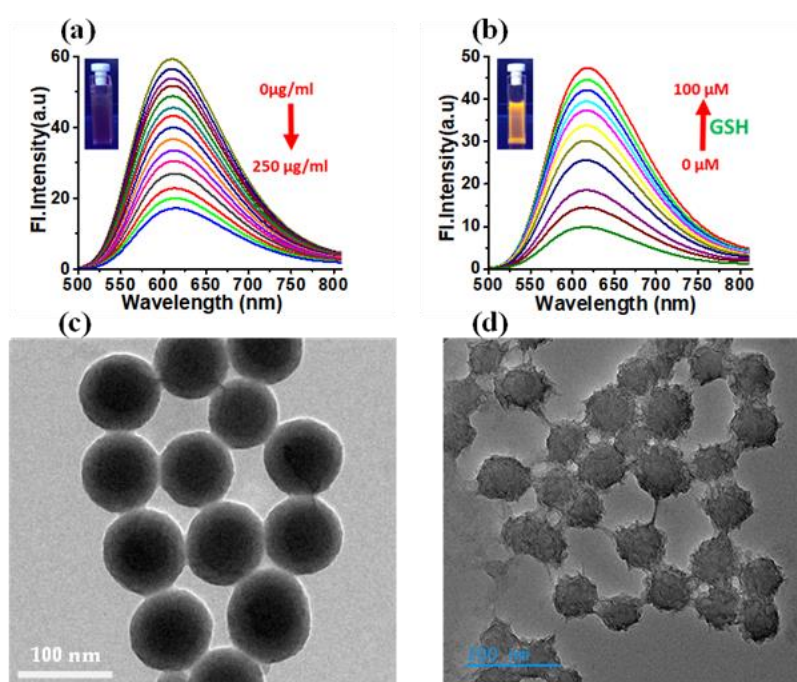


Figure 3.7: (a) Emission quenching of Ir-Nap-endo with the addition of PDA-MnO₂. (b) Regeneration of emission by treating with varying concentrations of GSH. (c & d) TEM images of the PDA nanoparticle and PDA coated with MnO₂ layered archine type nanoparticle.

Notably, the MnO₂ layer exhibits specific susceptibility to degradation within the tumor microenvironment, facilitated by the presence of glutathione (GSH), thereby not only reducing cellular resistance but also affording additional therapeutic benefits. The orchestrated degradation process, mediated by GSH, results in the generation of a substantial quantity of oxygen and Mn²⁺ ions. Oxygen, generated through this process,

serves to alleviate the hypoxic conditions commonly observed within tumors, thus creating a favorable milieu for the implementation of radical and ROS-mediated therapeutic strategies. Concurrently, the formed Mn^{2+} ions swiftly engage with the overexpressed hydrogen peroxide within cancer cells, instigating a Fenton-type reaction that generates highly reactive hydroxyl radicals (OH^{\bullet}). This Chemodynamic therapy component complements the oxygen-induced effects, collectively constituting the initial stage of a multifaceted combination therapy regimen. The Ir-Nap-endo conjugated PDA (PIR) was subjected to a reaction with KMnO_4 in the presence of polyallyl amine, leading to the formation of a thin layer of MnO_2 -coated PIR known as the “Untargeted Theranostic Nano Construct” (UTNC). The successful confirmation of MnO_2 coverage was evident by the quenching of the red fluorescence initially emitted by the PIR sample. To validate this, we introduced varying concentrations of MnO_2 nanoparticles to the highly fluorescent Ir-Nap-endo solution. The significant decrease in luminescence from the iridium complex at 615 nm as we increased the MnO_2 concentration provided a clear explanation for the change in PIR emission upon conjugation with MnO_2 (Figure 3.7a). The addition of different concentrations of GSH to this quenched solution effectively restored the emission of the initially quenched fluorophore, further confirming the degradation of the MnO_2 layer on the PIR surface (Figure 3.7b). This change in behaviour was supported by a noticeable shift in zeta potential from -14 to +22 after coating with MnO_2 , providing additional evidence of successful coverage. To corroborate the MnO_2 coating using microscopic analysis, HR-TEM was employed on the samples (Figure 3.7c&d).

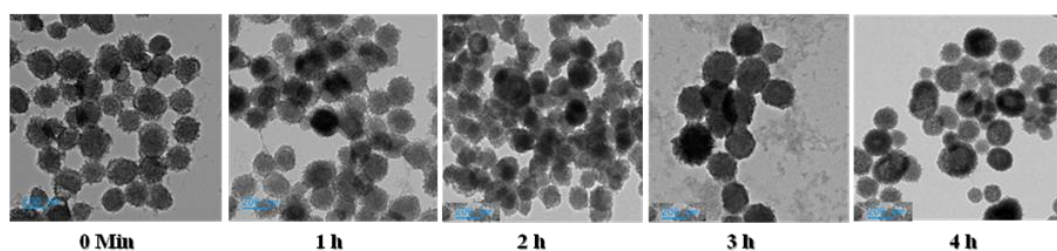


Figure 3.8: TEM result showing the degradation of archine type MnO_2 layer from PDA by treating with 3 mM GSH in a time-dependent manner

The distinct spherical PDA nanoparticle transformed into an arch-like structure upon MnO_2 coating. Elemental analysis conducted through TEM revealed peaks corresponding to Mn in the spectra, providing further validation of the coating. To determine the precise time for complete degradation, we conducted a time-dependent degradation study based on GSH and analysed the samples through TEM. The TEM images clearly indicated complete degradation within 5 hours, with shattered small aggregates of residual Mn visible in the

figures. Due to the reducing properties of GSH, the surface of the PDA nanoparticle also exhibited some degradation. These time-dependent GSH-based degradation studies are valuable for calculating the irradiation time needed for the PTT-triggered PDT effect from the construct (Figure 3.8). As previously elucidated, the deterioration of MnO₂ nanoparticles facilitated by GSH leads to the production of oxygen and Mn²⁺ ions (Figure 3.9a).

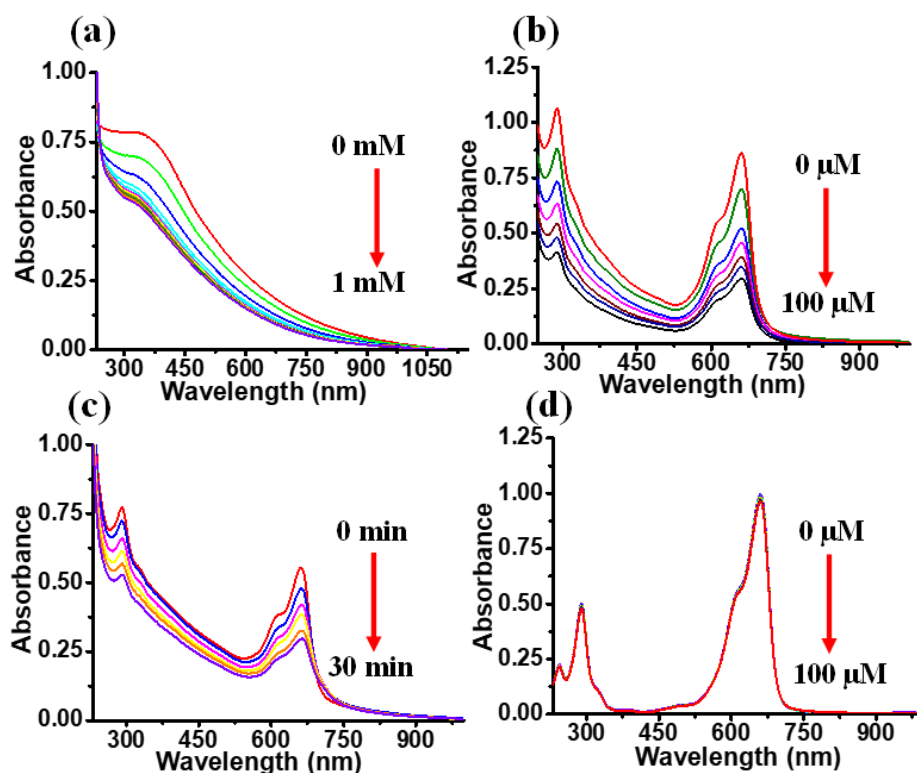


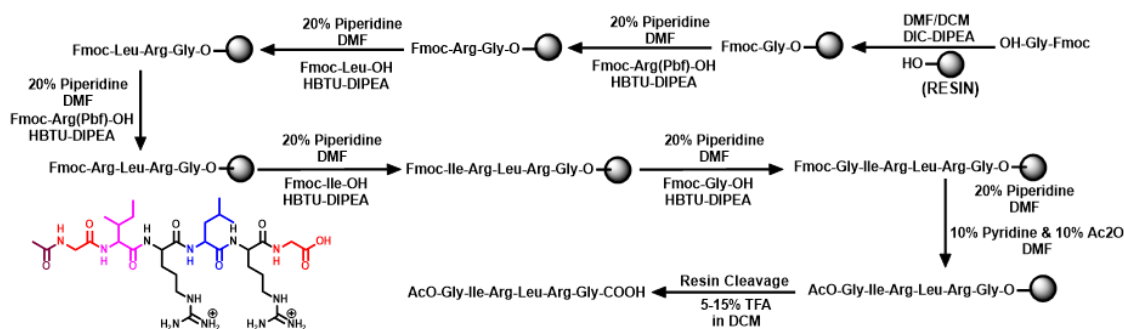
Figure 3.9: (a) Absorption spectra showing the degradation of MnO₂ layer of PDA-MnO₂ upon reaction with GSH. The degradation of MB dye upon pre-treating with PDA-MnO₂ followed GSH and H₂O₂ (b) concentration and (c) time dependent manner. (d) MB treated with only GSH and H₂O₂.

These Mn²⁺ ions subsequently engage with hydrogen peroxide, instigating a chemodynamic process that generates deleterious hydroxyl ([•]OH) radicals. The presence of GSH from a unique, unidentified triggering nanocomposite (UTNC) was evaluated for its capacity to induce OH radical formation, employing a well-established methylene blue (MB) degradation assay. Methylene blue molecules exhibit distinct degradation patterns in the presence of radical species, resulting in a discernible reduction in their structural integrity, most notably indicated by the attenuation of the characteristic 660 nm spectral peak. Notably, when MB dye was administered in isolation or in combination with varying concentrations of H₂O₂ and GSH, no discernible alterations in the dye's spectral characteristics were observed. Conversely, when the UTNC was introduced into the MB

solution, followed by the addition of GSH and varying concentrations of H₂O₂, a marked reduction in the 660 nm peak of MB was observed, displaying a clear correlation with both concentration and time (Figure 3.9). This pronounced degradation of the MB dye, precipitated by the introduction of GSH, serves as compelling evidence of GSH-facilitated degradation and subsequent radical generation through the chemodynamic effect. This pivotal experiment unequivocally underscores the system's potential to induce GSH depletion and initiate the chemodynamic effect, thereby showcasing its promising scientific significance.

3.2.5 Synthesis of targeting peptide to target GRP-78

The efficacy of utilizing nanostructures hinges on their precise delivery to the intended target site while sparing unaffected areas of the body. To achieve this goal, the scientific community has primarily employed targeting motifs. Depending on the specific requirements, various functionalities have been employed to target the tumor microenvironment. Among these strategies, small peptides that specifically home in on overexpressed surface proteins have emerged as exceptionally promising candidates. Their exceptional specificity, precise targeting capabilities toward surface proteins, and effective conjugation strategies with different constructs render them remarkably versatile for targeting purposes.



Scheme 3.3: Synthesis of S-GRP-78 targeted hexapeptide GIRLRG with N-acetylation

One such surface protein, GRP-78 (S-GRP-78), exhibits pronounced overexpression in cancer cells, notably in Triple-Negative Breast Cancer (TNBC) cells, while relatively scarce in normal cell counterparts. A peptide selectively directed at S-GRP-78 can guide the nano construct exclusively to TNBC cells, leaving other cells unimpacted. Additionally, it facilitates the internalization of the nano construct through receptor-mediated endocytosis. A hexapeptide substrate, GIRLRG, with a heightened affinity for S-GRP-78 targeting, was synthesized through solid-phase peptide synthesis (SPPS) employing

HMPB-MBHA as the polymer-supported resin and utilizing Fmoc chemistry (Scheme 3.3). The SPPS process is initiated with the initial amino acid coupling to the resin, followed by a series of deprotection and coupling steps in succession. Ultimately, the N-acetylated peptide was liberated from the resin using trifluoroacetic acid (TFA) and thoroughly characterized via proton, carbon, and high-resolution mass spectrometry (HRMS) techniques.

3.2.6 Formulation of the Theranostic nano construct (TNC)

In the process of fabricating the Theranostic nano construct (TNC), a crucial step involved the conjugation of the GRP-78 targeting peptide to the UTNC (Figure 3.10a).

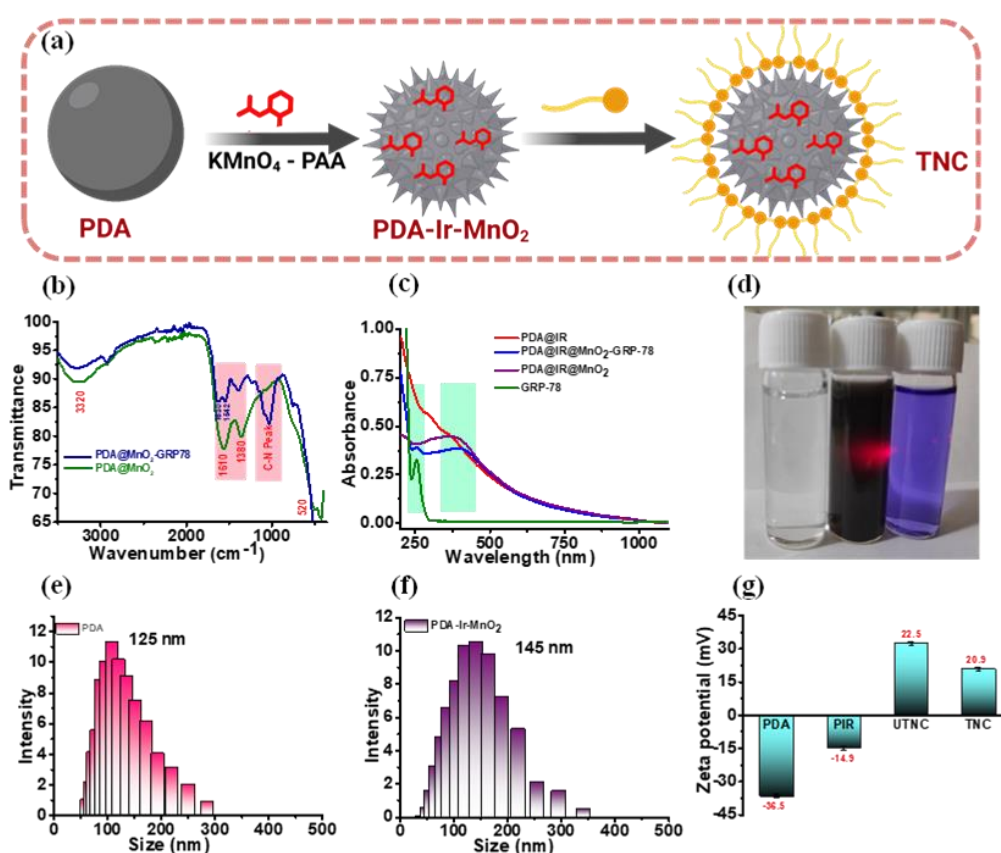


Figure 3.10: (a) Schematic illustration of PDA to TNC. (b) IR spectra showing the successful conjugation of GRP-78 peptide to the PDA-MnO₂. (c) Absorption spectra showing sequential changes associated with each modification from PDA-IR to TNC. (d) Tyndall effect shown by the TNC compare with crystal violet dye and the dopamine monomer. (e) The changes associated with DLS size of PDA and (f) after the MnO₂ coating of PDA. (g) Zeta potential changes associated with each modification from PDA-IR to TNC.

This peptide serves as a vital driver, facilitating the precise localization of the construct to the intended target area. To enable this coupling, the surface of the UTNC was endowed with NH₂ functional groups through the utilization of polyallylamine during its synthesis.

The linkage of the GRP-78 targeted peptide to the UTNC was accomplished through an amide coupling reaction, employing EDC/NHS reagents. This chemical reaction yielded the desired TNC, representing the culmination of the conjugation process. Notably, the success of this conjugation was corroborated through infrared (IR) spectroscopic analysis.

This analytical technique revealed the presence of characteristic peaks arising from the peptide component, aligning seamlessly with the spectral features of the UTNC (**Figure 3.10b**). Further validation of the conjugation was undertaken via UV-Vis analysis. This analysis unveiled distinctive peaks in the spectrum of the TNC, attributable to its constituent elements. Notably, an additional minor peak at approximately 280 nm was observed, corresponding to the presence of the peptide moiety within the construct (**Figure 3.10c & d**). The size analysis through DLS clearly indicates a change in DLS size from 125nm to 145 nm (**Figure 3.10 e&f**). Lastly, the alteration in the zeta potential was assessed as a result of incorporating amine functionalities. The zeta potential, which was initially measured at 22.5 mV, was reduced to 20.9 following the utilization of these amine groups (**Figure 3.10g**). This reduction in zeta potential is indicative of the modification occurring on the UTNC surface during the conjugation process. This advancement holds promise for targeted theranostic applications, where the TNC can navigate and act upon specific areas of interest within biological systems.

2.2.7 *In vitro* Imaging Studies

The successful achievement of targeted delivery of the nano construct hinged on the critical overexpression of GRP78. The entire construct's ability to selectively target its destination relied upon the targeting unit's capacity to reach the intended site of action to validate the heightened expression of GRP-78 protein in triple-negative breast cancer (TNBC) cells, we conducted a Western blot analysis.

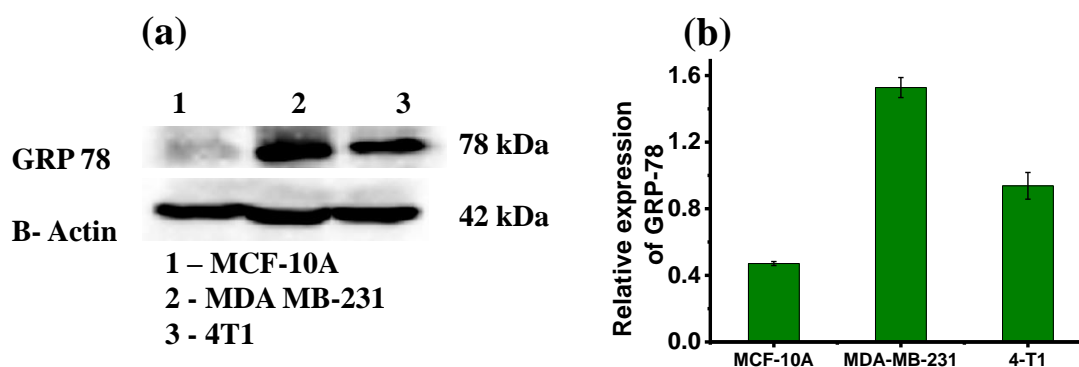


Figure 3.11: (a) Western blot analysis to confirm the over-expression of GRP-78 in MDMB-231, MCF-10-A, and 4-T1. (b) Relative expression of S-GRP-78 normalized with beta-actin.

Both TNBC cell lines, MDA-MB-231 and 4T1, as well as the normal MCF-10 cells, underwent protein isolation and subsequent blotting to assess the extent of S-GRP-78 overexpression. The results unequivocally demonstrated significant overexpression of GRP-78 protein in both TNBC cell lines, as evidenced by distinct and intense bands corresponding to 78 kDa, the molecular weight of GRP-78. In contrast, only faint bands were observed in the normal cell counterpart. These findings conclusively affirm the upregulation of this protein, which serves as the target for precise and selective delivery (Figure 3.11). Before delving into the rigorous in vitro investigations, an essential preliminary step involved the evaluation of the biocompatibility, time of internalization, and toxicity of the TNC construct, as well as its constituent components. To validate the temporal internalization process through fluorescence imaging investigations, the experimental design underwent a modification. The inclusion of an MnO₂ layer on the construct's surface effectively quenched the fluorophores' emission, rendering them inadequate for monitoring the internalization time point when the MnO₂ layer was present. To address this limitation, a novel construct devoid of the MnO₂ layer was synthesized to affirm the internalization process.

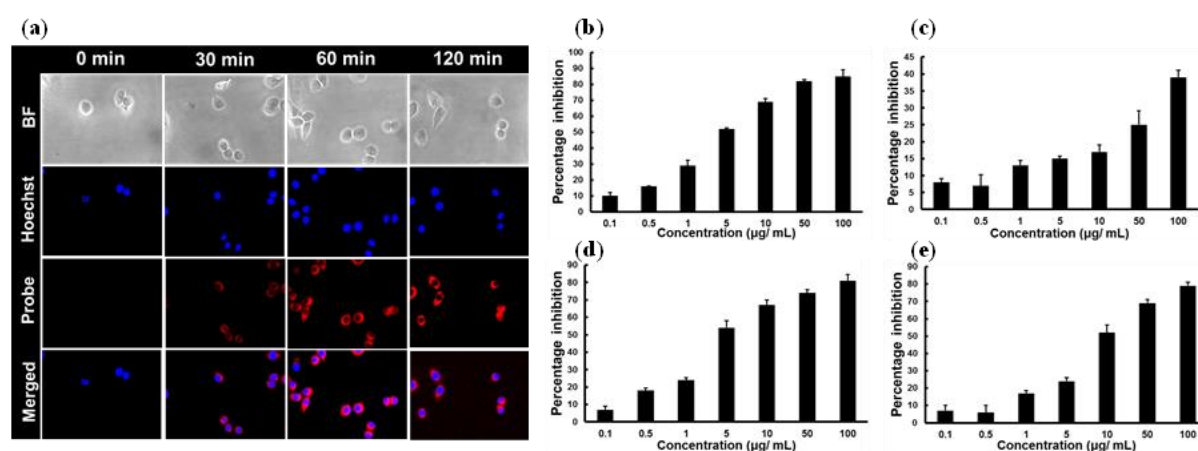


Figure 3.12: (a) The internalization of the PDA-Ir-Nap-peptide in MDA-MB-231 cells in time time-dependent manner co-incubated with Hoechst. (b-e) MTT assay of the construct in MDA-MB-231,4-T1, MCF-10-A, and MDA-MB-231 tumor spheroids at 24 h with 808 laser irradiations.

In this scheme, Ir-Nap was electrostatically affixed to polydopamine (PDA), followed by the conjugation of the GRP-78 peptide. Subsequently, this construct was introduced into MDA-MB-231 cells, and time-dependent fluorescence imaging was conducted in conjunction with the utilization of the standard nuclear tracker dye Hoechst. Remarkably, within a mere 30-minute incubation period, discernible red fluorescence emanated from the Ir-Nap-endo in intercellular milieu. The peak fluorescence intensity was observed at the 1-

hour time period. Subsequent to this hour-long interval, the fluorescence intensity exhibited minimal changes, leading us to establish the initial internalization time as 1 hour (Figure 3.12a). Further, we aim to assess the toxicity induced by the construct. This critical assessment was conducted through the widely recognized MTT assay, utilizing both triple-negative breast cancer (TNBC) MDAMB-231, 4T1 cells, and normal mammary epithelial MCF-10A cells. This initial inquiry forms the cornerstone of our study, as it helps establish the safety and viability of the TNC construct for potential therapeutic applications, shedding light on its potential impact on both cancerous and healthy cellular environments. Understanding the compatibility and safety profiles of the TNC construct is crucial for advancing our understanding of its potential as a promising tool in the field of cancer research and therapy. Upon evaluating the range of concentrations from 0.1 $\mu\text{g/ml}$ to 100 $\mu\text{g/ml}$ in TNBC cells (both MDA-MB-231 and 4T1), it is evident that there is a clear correlation between increasing concentration and the toxic effects observed. This anticipated outcome can be attributed to the initial phase of the therapy, known as the Chemodynamic effect and GSH depletion. The presence of GSH plays a crucial role in facilitating the release of Mn^{2+} ions, which subsequently react with the overexpressed H_2O_2 in the TNBC cells. This reaction leads to the formation of highly toxic hydroxyl radicals, which are responsible for the observed toxicity in the TNBC cells. In contrast, when the same construct was tested on the normal counterpart cells, MCF-10A, it exhibited significantly lower toxicity. This reduced toxicity can be attributed to the limited internalization of the construct and the lower levels of GSH and H_2O_2 in these cells (Figure 3.12b).

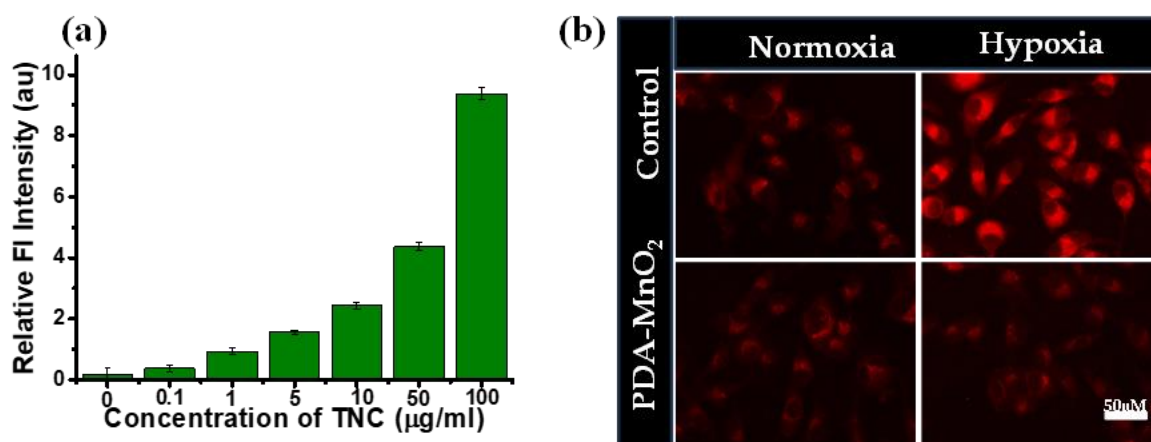


Figure 3.13: (a) The quantification of DCF fluorescence after treatment with varying concentrations of PDA-MnO₂. (b) Oxygen sensing with aid of in both normoxic and hypoxic conditions after treatment with PDA-MnO₂.

To substantiate our findings, we executed a DCFDA-based assay in which DCFDA, initially devoid of fluorescence, reacts with reactive oxygen species (ROS) to undergo a transformation into the highly fluorescent DCF molecule, distinguished by its characteristic green luminescence. We exposed cells to varying concentrations of TNC, ranging from 0 to 100 $\mu\text{g/ml}$, followed by the introduction of DCFDA. This led to an observable rise in green fluorescence directly proportional to the concentration of TNC applied. The results convincingly illustrated a concentration-dependent reactivity of hydroxyl (OH) radicals generated through a Fenton-type reaction involving Mn^{2+} and peroxide within the cellular milieu with DCFDA, corroborating our hypothesis concerning their involvement. In contrast, the control group, consisting of untreated cells, exhibited no noteworthy increase in green fluorescence, even after a 2-hour incubation period. This compelling outcome underscores the pivotal role of Mn^{2+} ions and H_2O_2 in facilitating radical generation, firmly establishing them as significant contributors to the observed fluorescence patterns (**Figure 3.13a**). To evaluate the oxygenation process during the degradation of MnO_2 layers on the surface of PDA nanoparticles using a well-established oxygen probe, $[\text{RuBpy}_3]\text{Cl}_2$, it was noted a pronounced quenching effect in the red fluorescence signal in the presence of molecular oxygen. It's worth noting that the presence of red-emitting PS Ir-Nap-endo could potentially confound the results of this fluorescence-based assay. To address this issue, a PDA nanostructure it devised which was devoid of Ir-Nap-endo, covered with MnO_2 , and subjected it to MDA-MB cells under both normoxic and hypoxic conditions. In the normoxic environment, where oxygen levels are abundant, a minimal change in of fluorescence intensity was observed even after exposing the cells to PDA- MnO_2 . This can be attributed to the surplus of oxygen, effectively quenching the fluorescence, even without additional exogenous oxygen supplementation (**Figure 3.13b**).

Transitioning to the hypoxic condition, it was observed a notable initial enhancement in red fluorescence within the hypoxic cells, which subsequently diminished significantly upon treatment with PDA- MnO_2 . This marked reduction in fluorescence intensity can be unequivocally attributed to the oxygen molecules generated during the degradation of MnO_2 , facilitated by glutathione (GSH). Importantly, the experiment clearly demonstrated the conversion of hypoxic regions to normoxic states through the provision of oxygen from the nano construct. These inner hypoxic cores, upon interaction with the TNC, effectively transformed into normoxic regions. This transformation not only contributed to the generation of radicals but also coincided with a sharp reduction in GSH levels during degradation, thereby enhancing therapeutic efficacy by reducing cellular resistance. The

decline in glutathione (GSH) levels played a crucial role in the deterioration of MnO₂ layer, marking a significant turning point in the efficacy of phototherapies. GSH, acting as a vigilant scavenger of radicals, served as a guardian for cells, shielding them from potential harm during treatment. Its inherent ability to resist depletion consistently protected cells, ultimately diminishing the overall treatment's effectiveness. The nano construct introduced a transformative element by significantly reducing GSH levels, ultimately contributing to an enhanced therapeutic effect. This reduction in GSH, facilitated by the nano construct, resulted in a more favorable treatment outcome due to the absence of GSH interference.

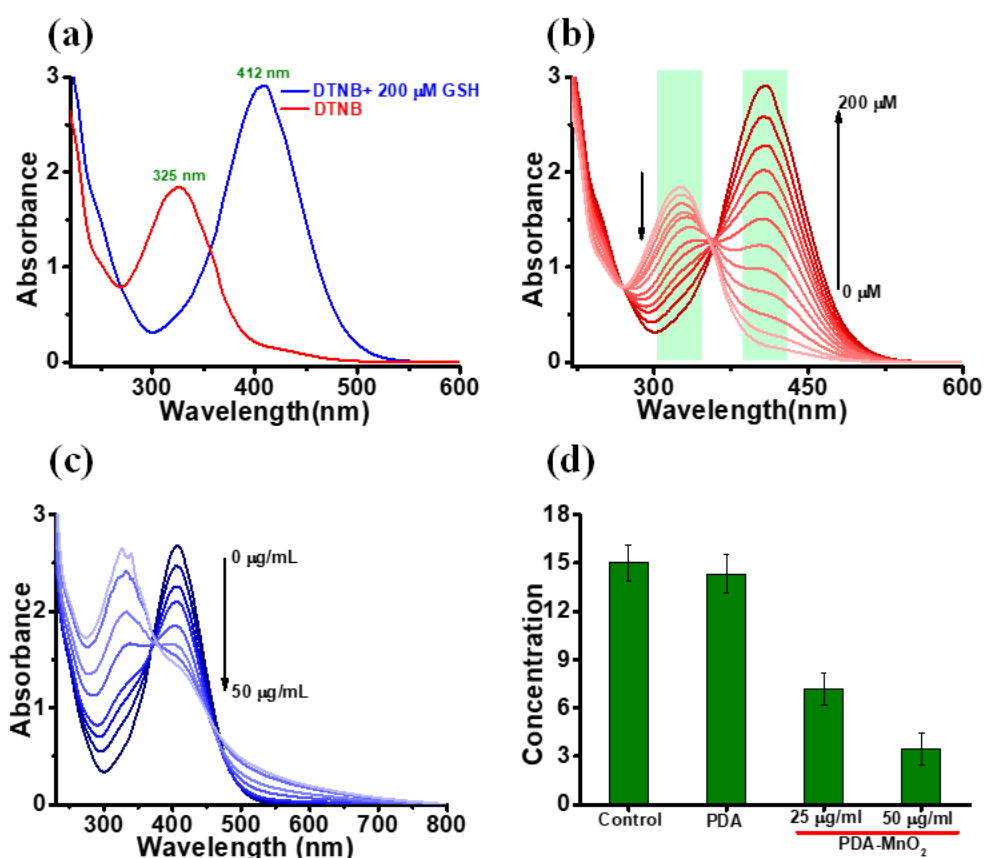


Figure 3.14: (a) The absorption spectra of DTNB and DTNB treated with GSH. (b) Titration showed the changes of DTNB upon incubation with different concentrations of GSH. (c) The depletion of GSH when incubated with PDA-MnO₂ was proved by the DTND assay. (d) The quantification of GSH from cells after treatment with PDA-MnO₂ asses by GSH kit.

To validate the occurrence of an event in the solution state, a widely recognized GSH probe known as DTNB (5,5'-dithiobis-(2-nitrobenzoic acid)). The alteration in the absorbance spectra of DTNB was scrutinized. Notably, the 325 nm peak of DTNB exhibited a discernible shift to 412 nm upon its interaction with glutathione (GSH) (Figure 3.14a). This spectral shift can be attributed to the formation of nitro thiophenol molecules resulting from the interaction between DTNB and GSH. Importantly, the augmentation in the

intensity of the 412 nm peak was found to be directly proportional to the concentration of GSH present in the solution. To quantify this relationship, a standard calibration curve was constructed over a GSH concentration range of up to 200 μM (Figure 3.14b). Subsequently, separate vials containing a fixed concentration of 200 μM GSH were treated individually with varying concentrations of PDA-MnO₂ ranging from 0 to 50 $\mu\text{g/ml}$. Following the requisite incubation period, each solution was subjected to treatment with 100 μM DTNB, and their absorption spectra were meticulously analyzed. Remarkably, a conspicuous reduction in the peak intensities was observed as the concentration of the PDA-MnO₂ construct increased. This marked decline in peak intensity, correlating with escalating concentrations of the construct, unequivocally signifies the consumption of GSH in the degradation process (Figure 3.14c). Consequently, this decrease substantiates the notion that the MnO₂ layer effectively utilizes GSH, resulting in a diminished GSH concentration within the experimental solution when titrated with DTNB. This phenomenon serves as a definitive indicator of GSH utilization by the MnO₂ layer, thereby substantiating the event under investigation. To confirm the GSH depletion, a GSH assay kit (Sigma Aldrich) was employed, providing concrete evidence of this crucial change. In experiments where cells were subjected to varying concentrations of the nano construct (TNC), a marked decrease in GSH levels was observed compared to the control group (Figure 3.14d).

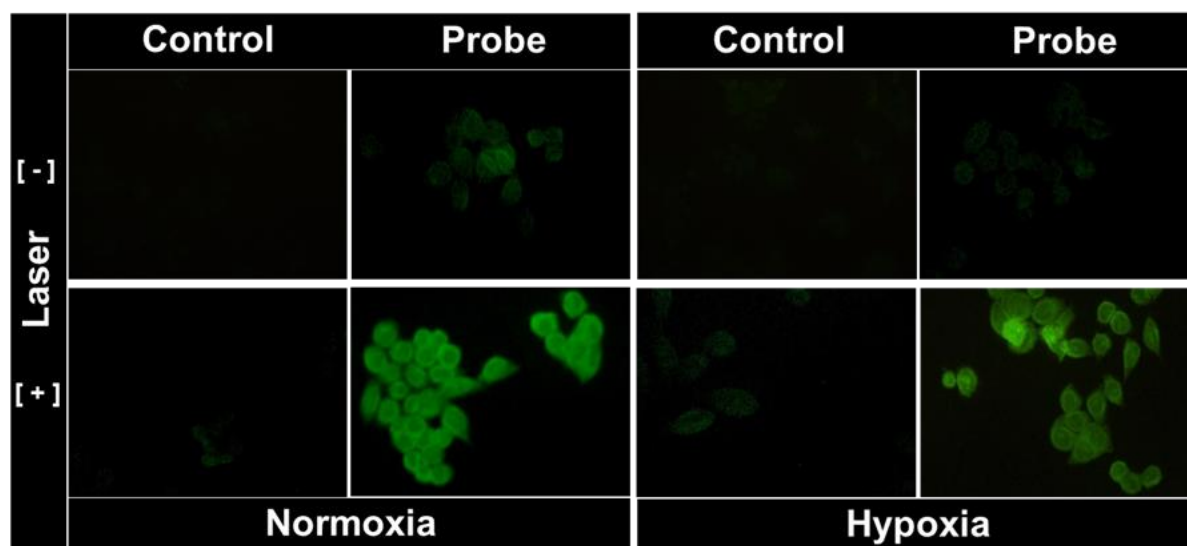


Figure 3.15: The singlet oxygen generation from cells treated with PDA-Ir-Nap-endo conjugated with the peptide in normoxic and hypoxic conditions with and without 808 nm laser.

In contrast, treatments involving solely PDA or other combinations failed to produce any discernible alterations in the outcomes. This striking observation strongly emphasizes the nano construct's potential to effectively deplete GSH levels, thus leading to improved

therapeutic results. The experiment initially demonstrated the temperature-assisted release of trapped singlet oxygen in a liquid solution using the DPBF assay. To validate this phenomenon in a cellular environment, an essential experiment involved the use of an 808 nm laser. The well-known singlet oxygen probe molecule SOSG was employed, which transforms from being nonfluorescent to highly emitting green fluorescence upon interaction with singlet oxygen. To achieve this, the PDA-Ir-Nap-endo conjugated with the peptide was assessed and deliberately avoided using the MnO₂-coated final construct TNC because it would reintroduce oxygen in hypoxic areas during degradation, preventing effective delivery of singlet oxygen to the hypoxic core through laser activation. The distinct green fluorescence of SOSG was clearly observed in cells incubated with PDA-Ir-Nap-endo followed by irradiating with 808 nm laser in both normoxic and hypoxic conditions. The emergence of green fluorescence in the SOSG probe clearly validates the release of trapped singlet oxygen due to the photothermal effect induced by PDA when irradiated with an 808 nm laser. Conversely, cells that were not subjected to laser irradiation in both normoxic and hypoxic conditions did not exhibit any fluorescence, further supporting the conclusion that the cycloreversion was triggered by heat generated during the laser irradiation. This clearly visualizes the ability of the singlet oxygen delivery system even in the hypoxic area (**Figure 3.15**).

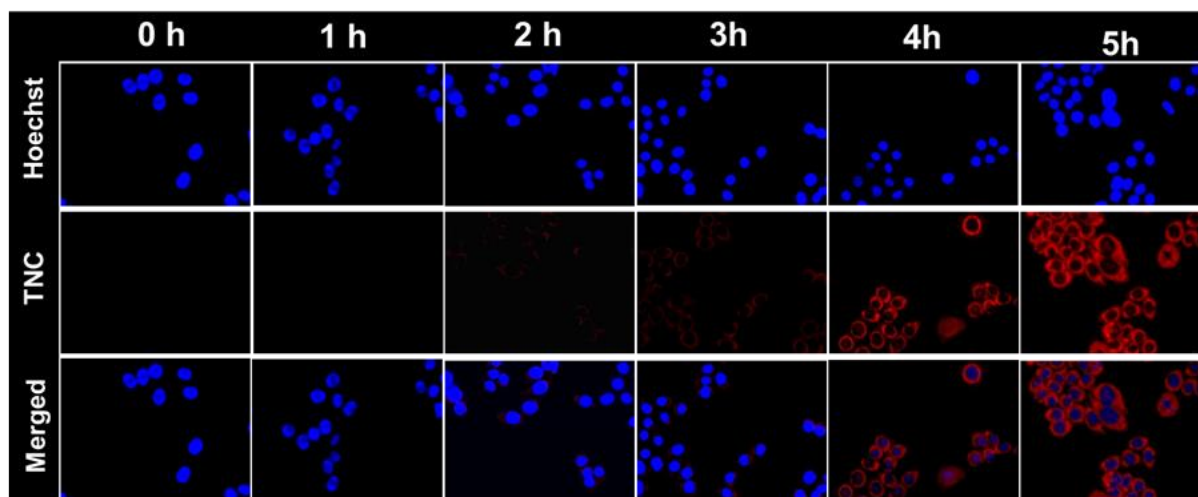


Figure 3.16: The degradation of the MnO₂ layer on the surface of PDA-Ir-Nap-MnO₂ confirmed by the recovery of fluorescence from the PS.

The precise timing of the degradation of the MnO₂ layer on the PIR surface held significant importance for both Photothermal Therapy (PTT) and Photodynamic Therapy (PDT) processes. The ability to induce hyperthermia and trigger the cycloreversion reaction through heat depended on the liberation of PDA nanoparticles, which were crucial for

effective interaction with the laser. Thus, it was vital to establish the specific timeframe during which the PDA, working in tandem with the delivery system, became available to perform its intended function. To pinpoint this exact moment, a time-dependent degradation experiment was conducted within cellular environments. Notably, the complete recovery of the quenched fluorescence of the photosensitizer (PS) molecule only occurred after the degradation of the MnO₂ layer. The research utilized time-dependent fluorescence imaging studies to gain a comprehensive understanding of when the complete degradation and subsequent emission recovery occurred. The observations during the experiment revealed that the degradation process commenced as early as 2 hours and reached its conclusion around the 4-hour mark (**Figure 3.16**). Following this timeframe, there was minimal change in fluorescence intensity. These findings provided precise insight into the ideal moment for laser irradiation, enabling the simultaneous execution of PTT and PDT.

3.2.8 *In vitro* Therapeutic Assessment

All essential parameters were fine-tuned through various cell-based assays and photophysical assessments. With these optimized parameters in hand, our next objective is to enhance the therapeutic efficacy of TNC. To initiate this process, it was evaluated the quantification of laser-assisted cell death using the MTT assay.

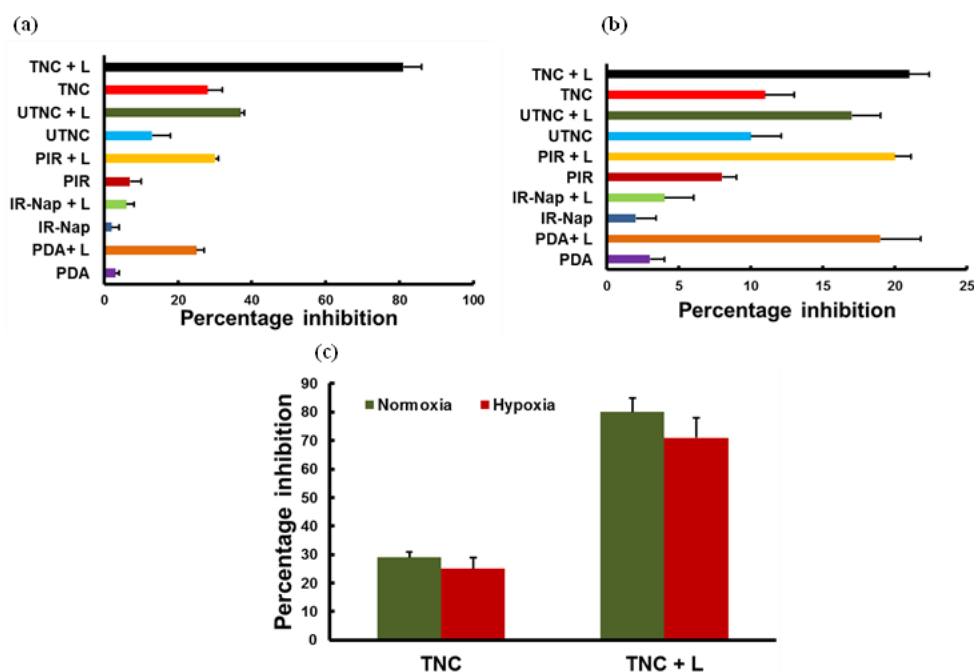


Figure 3.17: (a) *In vitro* cytotoxicity assay of various constructs with and without laser irradiation MDA-MB-231 and (b) MCF-10A cells. (c) The comparison of cytotoxicity induces by TNC in both hypoxic and normoxic situations with and without laser.

Cells were exposed to TNC treatment and then incubated for approximately 4 hours to allow for the complete degradation of the MnO₂ layer. Subsequently, the cells were subjected to laser irradiation, and cytotoxic assessments were conducted. Notably, a substantial reduction in the viability of MDA-MB 231 cells was observed in the TNC with laser group, indicating a pronounced photothermal therapy (PTT) triggered photodynamic therapy (PDT) effect. In contrast, other constructs exhibited less inhibition of proliferation compared to the TNC with laser treatment. In the case of MCF-10A cells, the same treatment groups displayed minimal cytotoxic effects in comparison to the heightened impact observed in triple-negative breast cancer (TNBC) cells. This discrepancy can be attributed to the targeted internalization occurring specifically in TNBC cells (**Figure 3.17 a&b**). The presence of a targeting peptide motif in the nano construct enables it to selectively accumulate within TNBC cells through receptor-mediated endocytosis, which is lacking in normal MCF-10A cells due to the absence of GRP-78 overexpression. This analysis underscores the synergistic and targeted effects of the TNC specifically within TNBC cells. To further substantiate the impact of hypoxic conditions, the TNC construct was subjected to cell treatment both in hypoxic and normoxic environments. Remarkably, when TNC was activated by laser, it exhibited a nearly equivalent percentage (72%) of inhibition in cellular proliferation under both normoxic and hypoxic conditions. This observation underscores the potential of TNC as an efficient PDT agent capable of delivering singlet oxygen even in oxygen-depleted hypoxic environments (**Figure 3.17c**).

To validate the programmed cell death process known as apoptosis, a comprehensive apoptotic assessment was conducted. To ascertain the potential of the theranostic nano system, apoptotic evaluations in both 2D and 3D culture models using MDA-MB spheroids was performed. These experiments were conducted in parallel with conventional 2D cell cultures. The therapeutic efficacy of the nano construct was further substantiated through a series of apoptotic assays. In comparison to the control group, cells treated with TNC followed by laser irradiation exhibited prominent signs of apoptosis. This was evident through a significantly larger population of cells displaying orange/red staining, as observed in the live/dead assay, both in the 2D cell culture and multicellular spheroids. To visualize apoptotic induction without relying on fluorescent markers, the APO Percentage assay was carried out. This assay reinforced the superior therapeutic performance of the probe, as indicated by a notably higher proportion of apoptotic cells stained with a pink colour (**Figure 3.18**). To precisely discern the mechanism of the apoptotic pathway, whether it involved the intrinsic mitochondria-mediated pathway or the extrinsic pathway,

we conducted a caspase assay. The elevated levels of caspase 3 clearly indicated the involvement of the mitochondrial pathway, confirming its intrinsic nature (**Figure 3.19a**). To further corroborate these findings, changes in mitochondrial membrane potential using the TMRE assay was conducted. This dye preferentially accumulates in healthy, unpolarized mitochondria compared to depolarized ones due to changes in membrane potential. The TNC group subjected to laser treatment exhibited a sharp decline in TMRE fluorescence intensity, signifying a reduction in mitochondrial membrane potential and thereby providing additional evidence for the intrinsic pathway (**Figure 3.19b**).

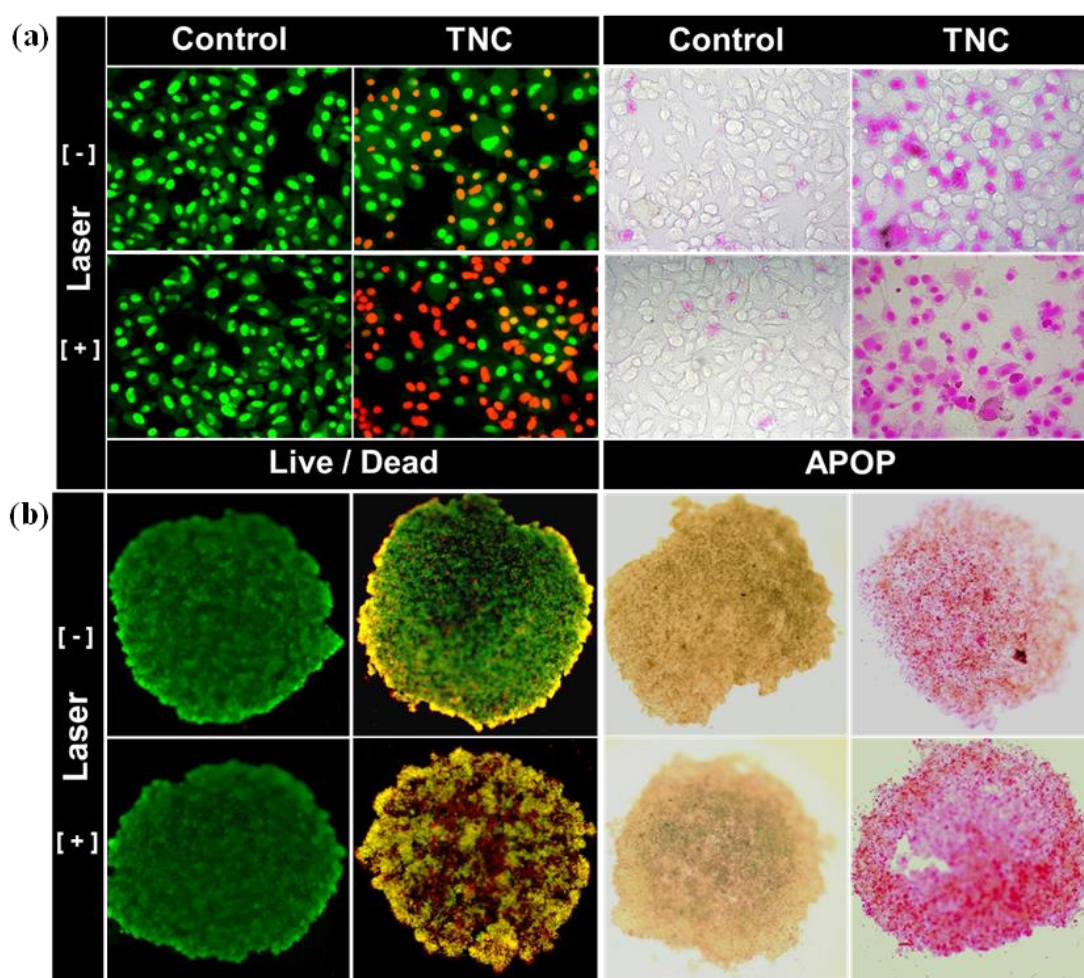


Figure 3.18: (a&b) Apoptotic evaluation of TNC on MDA-MB-231 and multicellular spheroids using acridine orange-ethidium bromide dual staining and APO Percentage staining with and without the aid of 808 nm laser.

In the final investigation, a comprehensive examination was conducted into the intricate process of cell death triggered by the nanoprobe known as TNC. The primary focus of this study centered on the analysis of the cell cycle, employing MDA-MB cells as the experimental model. Various laser conditions were applied to expose these cells to TNC.

Subsequently, a dual staining method involving propidium iodide and FITC was employed to gain valuable insights into the underlying mechanisms. The research findings provided compelling evidence of a notable increase in the sub-G0 population among cells subjected to the combined TNC and laser treatment. This significant observation strongly suggests that apoptosis, a tightly regulated form of programmed cell death, is the predominant mode of cell demise in this experimental context. The sub-G0 population, typically indicating cells with DNA content lower than that of the G0/G1 phase, is widely recognized as a hallmark of apoptosis. This intriguing discovery underscores the effectiveness of TNC in inducing programmed cell death when combined with laser irradiation.

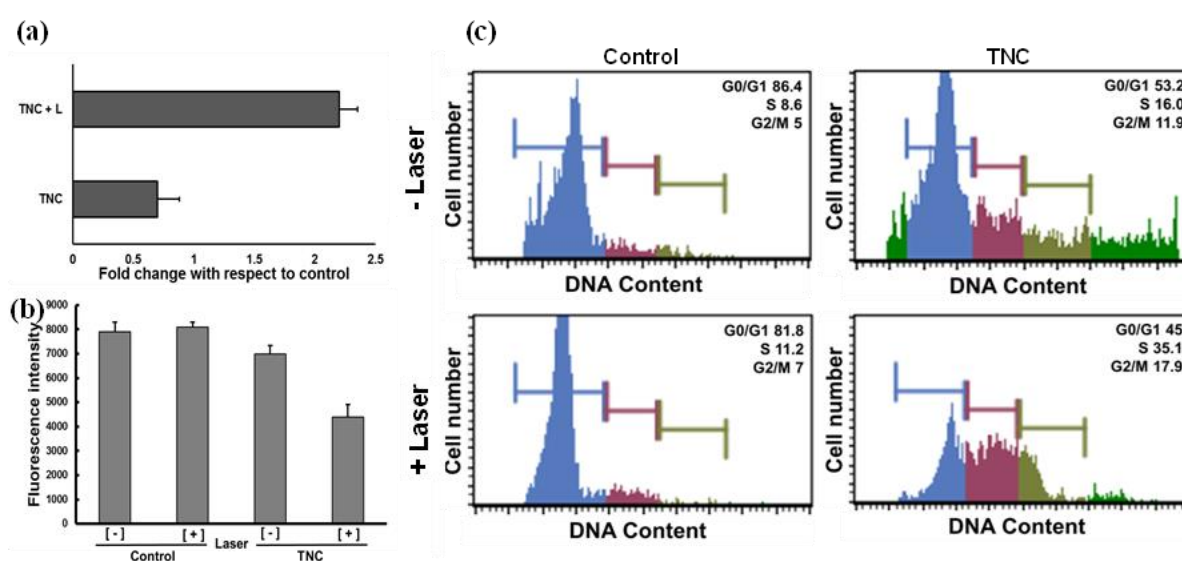


Figure 3.19: (a) Activation of caspase 3 upon treatment with TNC followed by 808 nm laser irradiation. (b) Mitochondrial membrane depolarisation confirmed with the aid of TMRM assay. (c) The analysis of sub G0 population and DNA content through cell cycle analysis.

A meticulous examination of the cell cycle dynamics following TNC and laser treatment has provided valuable insights into the underlying molecular mechanisms that contribute to the therapeutic potential of this nanoprobe (**Figure 3.19c**). The ability to selectively induce apoptosis in cancer cells, such as MDA-MB cells, holds paramount importance in cancer therapy. This approach not only presents a promising avenue for targeted cancer treatment but also minimizes harm to healthy tissues.

3.2.9 *In-Vivo* studies

The research has shifted focus towards exploring the potential of theranostic nano constructs (TNCs) for advanced applications. TNCs exhibit remarkable stability and the ability to induce apoptosis in hypoxic conditions, making them promising for *In-Vivo* use. Their biocompatibility is confirmed through rigorous hemolytic assays. TNCs' structural

integrity and efficacy endure over extended periods, instilling confidence in their long-term therapeutic potential. Their unique ability to induce apoptosis in hypoxic environments holds promise for addressing low-oxygen conditions. This shift underscores our commitment to harnessing TNCs' full benefits in cutting-edge applications. With this highlighted characteristic the work further moves on to the *In-Vivo* studies of the construct.

3.2.9.1 *In-vivo* – toxicity profiling of TNC

The primary advantage of employing a targeted nano construct (TNC) lies in its precise cargo delivery to the tumor site while minimizing adverse effects on healthy organs. To validate the TNC's suitability as a targeted nano delivery system, an acute toxicity assessment was conducted in female Balb/c mice aged 6-8 weeks (3 animals per group). In this study, a single intraperitoneal administration of TNC at a dose of 2000 g/Kg body weight was administered, and the mice were closely monitored for 14 days to observe changes in body weight, physiological parameters, and behaviour.

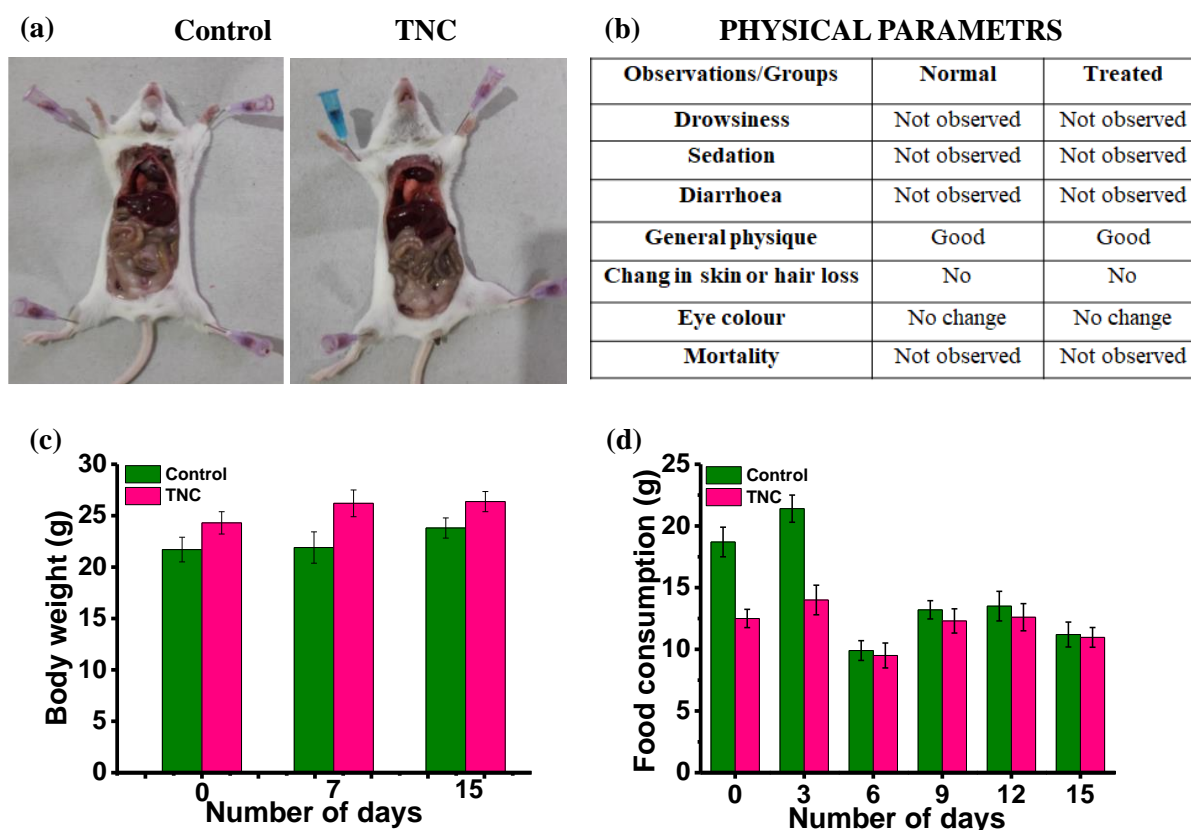


Figure 3.20: (a) Necropsy of control and TNC treated mice. (b) Physical parameters of both control and treated mice. (c&d) Body weight and food consumption rate of control and treated mice.

On the 15th day, the animals were euthanized to assess their internal organs (**Figure 3.20**). The findings revealed that there were no fatalities, and there were no statistically significant alterations in body weight, physiological indicators, behavioral patterns, or food consumption following TNC administration (**Figure 3.20b-d**). Consequently, it was established that the LD₅₀ (lethal dose 50) value would exceed 2000g/Kg body weight, and a sub-acute toxicity evaluation would employ a 1/10th dose, which is below the acute dose threshold (200 mg/kg body weight).

3.2.9.2 Sub-acute toxicity

Detailed toxicity analysis of TNC was performed in male and female Balb/c mice (6-8 weeks old, 5 animals/group) by giving 28 consecutive doses of TNC.

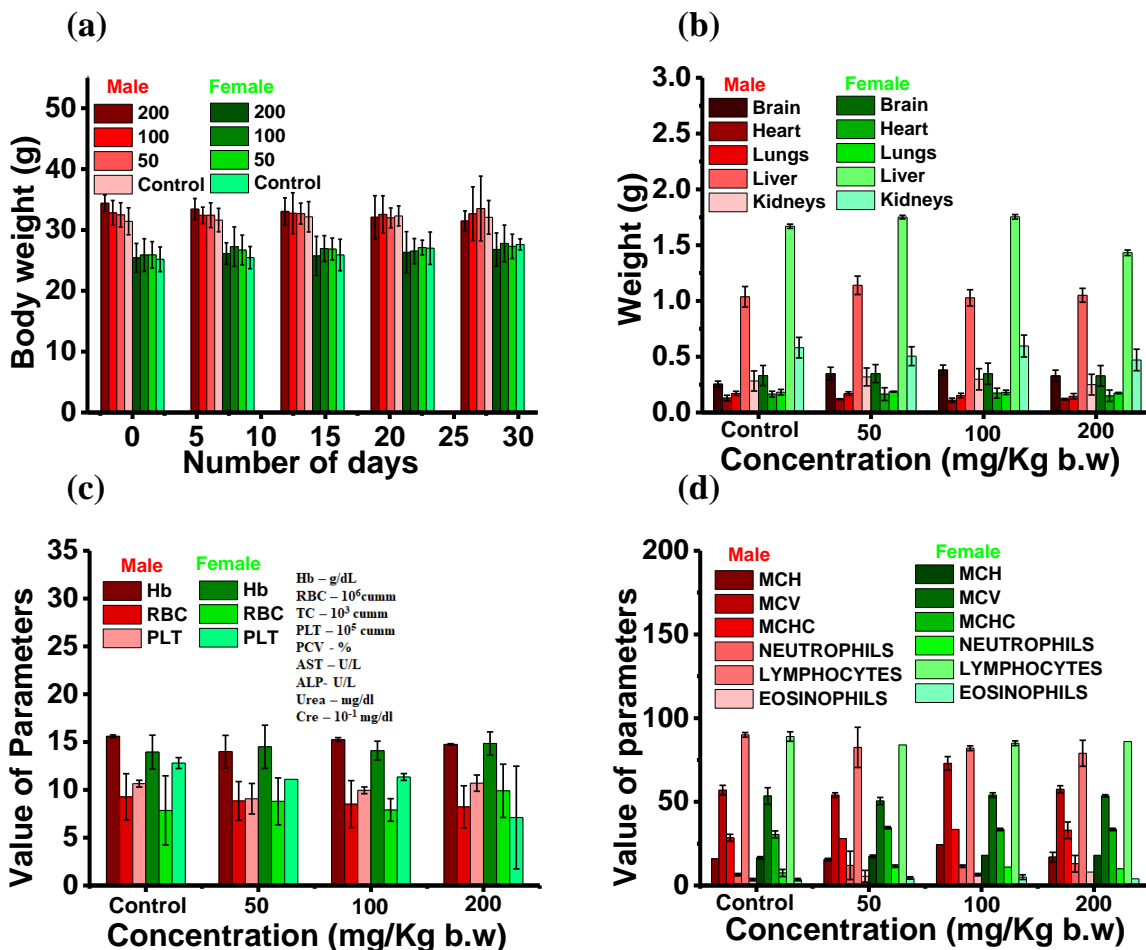


Figure 3.21: (a) Body weight of control and treated mice after 28 days continuous administration of TNC compared with control. (b) Dissected organ parameters of mice after 28 days continuous administration of TNC compared with control. (c&d) Blood parameters of the mice after administration of TNC (neutrophil, lymphocyte and eosinophil were expressed in percentage, MCH-pg, MCHC-g/dL, MCV-fl)

Intraperitoneal injection of 50, 100 and 200 mg/Kg. body weight doses of TNC were administered to different groups of animals. The mice were monitored during the period of TNC administration for adverse reactions to the TNC (through changes in behaviour and mortality). Animals were weighed periodically and monitored their food and water consumption (**Figure 3.21a**). At the end of the experimental period, the animals were sacrificed and blood and serum collected for hematological and biochemical analyses. Organs were collected, weighed, and observed for any abnormalities. No significant weight loss and organ abnormalities were observed in both male and female mice with continuous administration of TNC (**Figure 3.21b**).

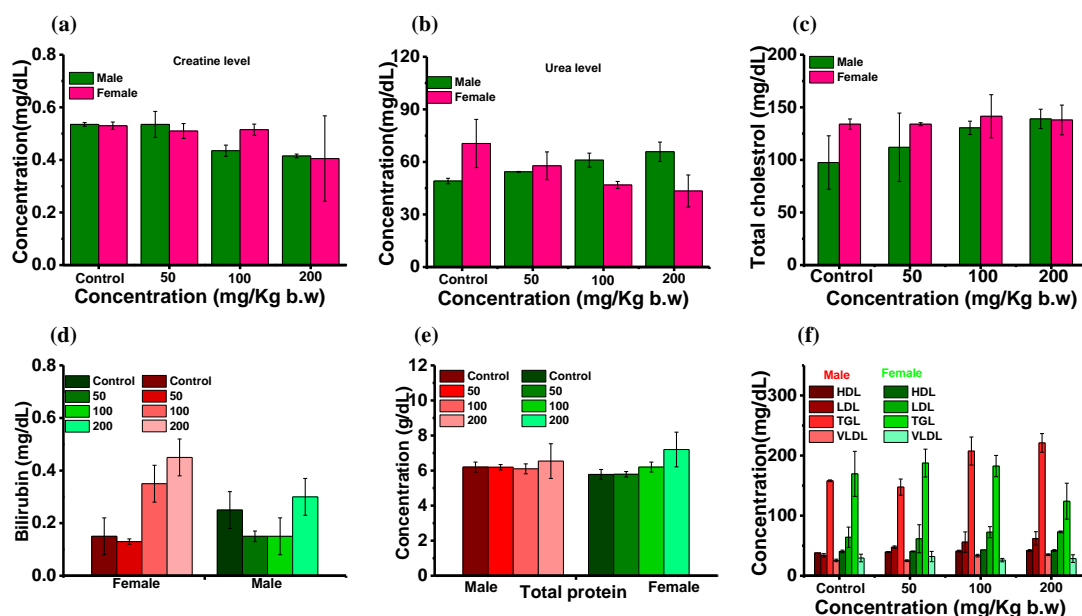


Figure 3.22: Liver parameters of the control and treated mice after 28 days continuous administration of TNC compared with control. **(a)** Creatine level of the male and female mice compare with control after 28 days administration. **(b)** Changes in the urea level of the male and female mice compare with control after 28 days administration. **(c)** Total cholesterol level of the animal after administration of TNC. **(d)** Bilirubin level of the male and female mice compare with control after TNC administration. **(e)** Lipoproteins level of the treated and control mice after the 28-day administration.

Even though, changes in Hb count and total WBC count were observed (**Figure 3.21 c&d**) for higher doses (100 and 200 mg/Kg body weight) along with elevated AST, Urea, and Creatinine levels (**Figure 3.22 a & b**), a lower dose of 50 mg/kg body weight was found to be safe to administer to the animals. The protein and cholesterol levels in the animals also indicated the safety of the TNC (Figure 22c-d). The parameters related to the kidney function are normal

compared to the control (Figure 3.23). Thus, a dose of 50 mg/kg body weight was selected for further antitumor studies that are in progress with 4T1 TNBC mouse model.

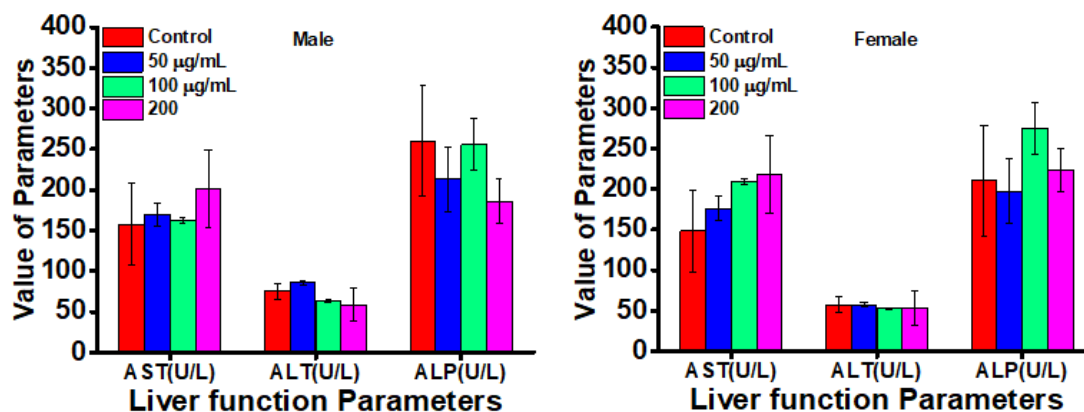


Figure 3.23: Liver function parameters of male and female mice after administration of TNC compared with control

3.3. Conclusion

In summary, an insightful multimodal theranostic nano construct has been successfully developed, enabling the implementation of combination therapy specifically targeted towards TNBC (Triple-Negative Breast Cancer) cells, effective in both normoxic and hypoxic conditions. This nano construct comprises four major components, each with distinct functions that collectively synergize to create an impactful combinational therapy. The nano construct is composed of a singlet oxygen self-generating and self-loading delivery system, Ir-Nap-endo, electrostatically conjugated with a photothermal agent, PDA nanoparticle. This assembly is further enveloped by a GSH-responsive MnO_2 layer, featuring a TNBC-targeting hexapeptide. This specific peptide guides the entire construct to the TNBC site, where the MnO_2 layer undergoes degradation due to the overexpressed GSH, resulting not only in GSH depletion but also in initiating the first phase of combination therapy through a Chemodynamic effect. Subsequent laser irradiation with an 808 nm laser activates both photothermal therapy (PTT) and photodynamic therapy (PDT) simultaneously through the thermal cycloreversion process using the PDA nanoparticle. *In vitro* and *in vivo* results have demonstrated the execution of GSH-associated Chemodynamic effects, followed by laser-induced PTT-triggered PDT. This approach addresses the challenges of hypoxia and PDT-mediated hypoxia, which have historically limited the broader application of PDT, through a combination therapeutic strategy. The

findings presented in this study represent a paradigm shift in cancer treatment and hold significant promise for future clinical translations, offering substantial benefits in the field of oncology.

3.4. Experimental Section

3.4.1 Materials and Methods

The reagents, such as 4,4'-dibromo-2,2'-bipyridine, methylnaphthaleneboronic acid, Potassium carbonate, TBAB, Pd(PPh₃)₄, IrCl₃·xH₂O, 2-phenyl pyridine, 2-methoxyethanol, methyl iodide, and diphenylisobenzofuran, were purchased from TCI Chemicals. Reagent-grade solvents were obtained from local suppliers and were dried and distilled prior to use following standard procedures. ¹H NMR spectra were recorded at 25°C on a Bruker 500 MHz FT-NMR spectrometer, with chemical shifts (δ) and coupling constant (J) values reported in ppm and Hz, respectively. High-resolution mass spectra (HRMS) were obtained using a Thermo Scientific Exactive ESI-MS spectrophotometer. UV/vis spectra were acquired using a Shimadzu UV-2600 UV-Vis spectrophotometer, and emission spectra were recorded with a Fluoromax-4 Spectrofluorometer using a 1 cm quartz cuvette. All experiments were conducted at 298 K unless specified otherwise. Surface-enhanced Raman spectroscopy (SERS) experiments were performed using a WITec Raman microscope (WITec, Inc., Germany) equipped with a 600 g/mm grating and a Peltier-cooled charge-coupled device detector. Samples were excited using a 633 nm laser with a power of 10 mW, and the Raman spectra were collected in the range of 300 to 2000 cm⁻¹ with a resolution of 1 cm⁻¹ and an integration time of 1 s, averaging over 10 accumulations. Prior to each measurement, calibration was performed using a silicon standard with a Raman peak at 520 cm⁻¹. Data analysis was carried out using the WITec Project Plus (v5.2) software package. Excited state lifetimes were measured using a picosecond single-photon counting system (TCSPC) from Horiba, DeltaFlex.

3.4.2 Synthesis of Naphthalene appended Bipyridine

4,4'-dibromo-2,2'-bipyridine (500 mg, 1.6 mmol) and 1-methylnaphthaleneboronic acid (595 mg, 3.2 mmol) were dissolved in a mixture of 60 mL toluene and 10 mL 2 M aqueous potassium carbonate. To this TBAB (1.56 g, 5 mmol) in water (10 mL) was added. The mixture was stirred at room temperature for 30 minutes under Argon followed by adding Pd(PPh₃)₄ (0.020 g, 1.74×10⁻³ mmol) and then heated to 90°C for 24 h. After the completion of the reaction indicated by TLC, the mixture was poured into water and extracted three

times with ethyl acetate. The organic layer was dried over anhydrous sodium sulphate. After removing the solvent under reduced pressure, the residue was chromatographed on a silica gel column with $\text{CHCl}_3:\text{CH}_3\text{OH}$ as eluent giving the compound as a off-white solid. Yield: 82%

^1H NMR (500 MHz, CDCl_3): δ 8.80 (d, $J = 1.5$ Hz, 2H), 8.73 (s, 1H), 8.71 (s, 1H), 7.79 (dd, $J_1 = 8$ Hz, $J_2 = 2$ Hz, 2H), 7.72 (s, 1H), 7.71 (s, 1H), 7.52-7.51 (m, 2H), 7.49 (d, $J = 1.5$ Hz, 1H), 7.48 (t, $J = 2$ Hz, 1H), 7.46 (t, $J = 1.5$ Hz, 2H), 7.45 (d, $J = 1$ Hz, 1H), 7.39 (s, 1H), 7.37 (s, 1H), 2.25 (s, 6H) ppm. **^{13}C NMR (125 MHz, CDCl_3):** δ 155.4, 147.6, 145.2, 136.1, 135.2, 134.6, 131.5, 127.5, 126.1, 125.9, 125.7, 125.1, 124.3, 123.3, 121.6, 20.8 ppm.

3.4.3 Synthesis of Ir-Nap complex

The synthesis was started with the preparation of Ir dimer complex (Nonoyama, 1974), a solution of $\text{IrCl}_3 \cdot x\text{H}_2\text{O}$ (224.36 mg, 0.75 mmol) and 2-phenyl pyridine (350 mg, 1.58 mmol) in 2-methoxyethanol/ H_2O (3:1, v/v%) was refluxed at 90°C for 24 h, under argon atmosphere. After the reaction, the solution was cooled down to room temperature and poured into 50 mL of water. The precipitated yellow solid (compound 2), was filtered and washed with n-hexane (5 mL x 3) and cold diethyl ether (5 mL x 3). The next step was preceded without any further purification of the obtained crude product. A mixture of obtained dimer (250 mg, 0.1866 mmol) and naphthalene appended bipyridine (160 mg, 0.48 mmol) in $\text{CH}_2\text{Cl}_2/\text{CH}_3\text{OH}$ (1:1, v/v%) was refluxed under an argon atmosphere for 12 h. Upon completion of the reaction, the solution was cooled down to room temperature and the solvent was removed under reduced pressure. The residue obtained was subjected to column chromatography in silica gel (100-200 mesh) column with chloroform/Methanol system, giving the intermediate compound as an orange solid. Yield 68%. **^1H NMR (500 MHz, CDCl_3):** δ 8.50 (s, 2H), 8.03 – 7.99 (m, 4H), 7.93 (d, $J = 8.5$ Hz, 2H), 7.86 (t, $J = 7.5$ Hz, 2H), 7.78 – 7.75 (m, 4H), 7.67 (d, $J = 8$ Hz, 2H), 7.53 (d, $J = 5.5$ Hz, 2H), 7.49 (t, $J = 8.2$ Hz, 4H), 7.44 (t, $J = 7.5$ Hz, 2H), 7.36 (d, $J = 7$ Hz, 2H), 7.31 (t, $J = 6.5$ Hz, 2H), 6.99 (t, $J = 7.5$ Hz, 2H), 6.88 (t, $J = 7.5$ Hz, 2H), 6.30 (d, $J = 7.5$ Hz, 2H), 2.65 (s, 6H) ppm. **^{13}C NMR (125 MHz, CDCl_3):** δ 167.7, 155.8, 152.4, 150.3, 150.1, 149.0, 143.6, 138.6, 137.2, 131.8, 130.9, 129.6, 128.1, 127.1, 126.5, 126.4, 125.7, 125.1, 124.9, 124.7, 124.1, 122.8, 119.8, 19.7 ppm. **HRMS-ESI-MS** Calculated for Ir-Nap: 937.29, Found Ir-Nap: 937.29

3.4.4 Synthesis of PDA nanoparticle

A solution composed of 40 mL of ethanol and 90 mL of water was prepared. To this solution, 4 mL of ammonium hydroxide (containing 25% ammonia in water) were added, and the mixture was agitated for approximately 10 minutes. Following this, 500 milligrams of polydopamine (PDA) dissolved in 10 mL of water were introduced. The reaction mixture was continuously stirred for a period of 24 hours. Subsequently, the resulting mixture underwent a centrifugation process at 10,000 rpm for 20 minutes. This centrifugation procedure was repeated three times to obtain highly purified PDA nanoparticles. The purified nanoparticles were then stored at a temperature of 4⁰C for future use or analysis.

3.4.5 Photothermal effect of PDA nanoparticle

The effectiveness of PDA nanoparticles in photothermal applications was assessed by exposing them to different concentrations (6.25, 12.5, 25, 50, 100 µg/mL) and irradiating them with an 808 nm laser operating at a power density of 0.5 W/cm² for a duration of 10 minutes.

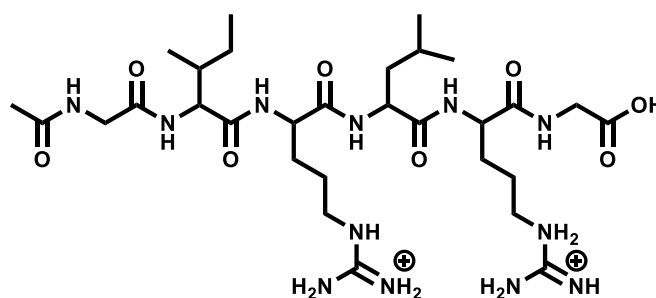
3.4.6 Loding of Ir-Nap-endo to the PDA nano particle

To a solution of 1mg/mL PDA nanoparticle in water mixed with calculated amount of the Ir-Nap-endo in acetonitrile: water 2:3 mixture. The mixture was incubated for about 24 h at 25⁰C. The PDA-Ir-Nap-endo was purified via centrifugation at 10000 rpm in 4⁰C. The purified nanoparticle was kept in fried for further use.

3.4.7 Synthesis of MnO₂ coated PDA-Ir-nap nanoparticle

To a solution of 1 mg/mL PDA-Ir-Nap in 10 ml water was stirred at 600 rpm at 25⁰C. To this 40 mg KMnO₄ was added and stirred for about 5 minutes. Tho the mixture 50 mg polyallylamine was added and stirred bout 4 h. The solution was centrifuged at 10000 rpm for 10 minutes and the residue was washed 3 times with water. The MnO₂ coated nanoparticle was purified via repeated centrifugation and stored at 4⁰C.

3.4.8 Synthesis of GRP-78 peptide



Synthesis of GRP-78 targeted peptide sequence was performed using solid-phase peptide synthesis with HMPB-MBHA resin as the solid support. Firstly, the Fmoc-Gly-COOH (338 mg, 1.36 mmol) was activated using DIC (219 mg, 1.79 mmol) in DCM-DMF (2 drops) to obtain the activated ester. The resin was swelled in S6 dry dichloromethane (DCM) which was then washed with N, N-dimethyl formamide (DMF) (3×3ml). After washing with DMF (3×3ml), activated Fmoc-Gly-COOH (165mg, 0.426mmol) was charged to the resin bed after activating with HBTU (161mg, 0.426mmol), diisopropylethylamine (DIPEA) (2 or 3 drops). The reaction was continued for 12 hrs under a mechanical shaker and the progress of the reaction was monitored by Kaiser test. After completion of the coupling reaction, the resin was washed with DMF (3×3ml) and the Fmoc group was deprotected by treatment with 20% piperidine in DMF in the same manner. The reaction cycle was continued in a similar manner with Fmoc-Arg (Pbf)-OH (276mg, 0.426mmol), Fmoc-Leu-OH (150mg, 0.426mmol), Fmoc-Arg (Pbf)-OH (276mg, 0.426mmol), Fmoc-Ile-OH (150mg, 0.426mmol), and Fmoc-Gly-OH (276mg, 0.426mmol) amino acids were charged to the resin to yield resin-bound peptide. Finally the NH₂ part of the final Gly-NH₂ was acetylated using pyridine and acetic anhydride (10% in DMF) to obtain the resin-bound N-acetyl peptide.

3.4.9 Conjugation of GRP-78 peptide to PDA-Ir-Nap-MnO₂ NP

An equal mixture of 10 mM solutions of EDC and Sulfo-NHS in DCM (100 μL each) were added to a 100 μL (2.5 mg/mL) peptide solution at room temperature and stirred for about 1 to 1.5 h for the activation. The activated peptide (100 μL) was then added to 1.5 mL of the nanoparticle solution (1mg/mL) and stirred for about 6h. Finally, the peptide bound nanoparticles were carefully isolated via centrifugation and washed with MQ water, and stored in the refrigerator.

3.4.10 Measurement of preliminary photophysical properties.

In general, the UV-Vis absorption and emission spectra were obtained on a Shimadzu UV-2600 UV-Vis spectrophotometer and Fluoromax-4 Spectrofluorometer respectively. The excitation/emission slit width was set to 4 nm with medium scan speed. Stock solutions of the complex were made in spectroscopic grade acetonitrile (1 mM) were used to prepare the working solutions acetonitrile: water mixture. Absorbance spectra were recorded from 300-700 nm while the emission spectra were from 490-750 nm. All the experiments were repeated three times to confirm the reproducibility of the results.

3.4.11 Stability and selectivity

The stability of Ir-Nap was assessed through UV/Vis spectroscopy by monitoring freshly prepared 10 μ M solutions of Ir-Nap in both acetonitrile and water over a 24-hour period. Additionally, the photostability of a 10 μ M Ir-Nap solution in acetonitrile was evaluated by subjecting it to irradiation with a 532 nm long pass laser at 37°C, with UV/Vis absorption measurements taken over the course of 1 hour to confirm its resistance to photodegradation.

3.4.12 Singlet oxygen generation studies

The research aimed to examine the production of singlet oxygen in solutions of Ir-Nap in acetonitrile. To assess this, the study employed 1,3-diphenylisobenzofuran (DPBF) as a substance that reacts with singlet oxygen. The concentration ratio of Ir(III) complexes to DPBF was set at 1:10, and the samples were exposed to a 532 nm long-pass laser. When singlet oxygen was generated, it caused DPBF to undergo photo-oxidation, disrupting its structure and leading to a decrease in its absorbance at 410 nm. The absorption of the Ir(III) complex, however, remained unaffected. These changes in absorbance were monitored every 10 seconds, and a known substance, [Ru(bpy)₃]Cl₂, with a quantum yield of 0.57 in acetonitrile, was used as a reference. The evaluation was conducted using the following formula:

$$\phi_c = \phi_s(S_c \times F_s / S_s \times F_c)$$

In this equation, ϕ_c and ϕ_s represent the singlet oxygen quantum yield of the complex and [Ru(bpy)₃]Cl₂, respectively. S denotes the slope obtained from plots of DPBF's absorbance at 410 nm against the irradiation time for both the complex and the reference. F represents the absorption correction factor for the complex and reference, which is calculated as $F = 1 - 10^{(-OD)}$, where OD represents the optical density of the complex and [Ru(bpy)₃]Cl₂ at 532 nm.

3.4.13 Cell culture methods

The human breast cancer cell line MDAMB-231 and murine cell 4-T1 were obtained from American Type Culture Collection (ATCC, Manassas, VA, USA). Cells were maintained in Dulbecco's modified Eagle medium (DMEM) with 10% fetal bovine serum and 5% CO₂ at 37 °C for MBA-MB and RPMI for 4-T1. Cells were cultured in glass-bottom, 96-well black plates, T-25 flasks, T-75 flasks, and 4-well chamber slides for various experiments 2

days prior to the conduction of experiments. All the experiments were performed in triplicate for accurate results.

3.4.14 Evaluation of cytotoxicity using MTT assay

MTT assay is based on the cleavage of a MTT (3-(4,5-dimethylthiazol-2-yl)-2,5-diphenyltetrazolium bromide) by mitochondrial dehydrogenases in viable cells. Quantities of 100 μL of the cell suspension of 1×10^4 cells/well were seeded in a 96-well plate and incubated at 37°C for 24 h in a CO_2 incubator. After the incubation cells were washed with 100 μL of PBS buffer (pH 7.4). The compound under investigation were diluted in plane DMEM media to a concentration 0 to 100 μM . Then 100 μL of each compound under investigation along with positive control (1 μM doxorubicin) was similarly added to the appropriate wells. The plates were then incubated for 24 and 48 h in a CO_2 incubator at 37°C . After incubation, 100 μL MTT (0.5 mg/mL) was added to each well and incubation was continued for an additional 2 to 4 h. The insoluble formazan crystals formed were solubilized by the addition of 100 μL DMSO followed by an incubation of 30 min and the absorbance was measured at 570 nm using a microplate spectrophotometer (BioTek, Power Wave XS).

The proliferation rate was calculated as : % Proliferation = $(A_{\text{sample}} / A_{\text{control}}) \times 100$

The Inhibition rate was calculated as : % Inhibition = $100 - \% \text{ Proliferation}$

3.4.15 *In-Vitro* oxygen generation studies

To assess the potential of PDA- MnO_2 to alleviate hypoxia, experiments were conducted on both normoxic and hypoxic MDA-MB-321 cells. These cultures were treated with the nanoparticle for a duration of 5 hours, and subsequently, a commercially available hypoxia detection probe known as $\text{Ru}(\text{Bpy})_3\text{Cl}_2$ (at a concentration of 50 μM) was applied to the cells for a 10-minute incubation period, and the samples were observed using an inverted fluorescence microscope equipped with both TRITC and filters (Olympus 1X51, Singapore).

3.4.16 Evaluation apoptotic potential

Evaluation of the mode of cytotoxicity exhibited by TNC was performed on cancer cells with various apoptotic assays after administration of TNC with and without laser via dual staining acridine orange –ethidium bromide assay, APO Percentage assay (Bicolor, Belfast, Northern Ireland) and finally by FITC-Annexin V staining (BD Pharmingen no.

556547, BD Biosciences, San Jose, CA). Assessment of apoptosis using the acridine orange-ethidium bromide dual staining procedure was performed as described in literature. The cells were observed under an inverted fluorescent microscope, using a FITC filter (Olympus 1X51, Singapore) to view the apoptotic or non-apoptotic cells. The apoptosis was further confirmed using APO Percentage dye (Biocolor, Belfast, Northern Ireland) as per manufacturer's instructions. Light microscopic images of APO Percentage dye-labelled cells, which stained pink under a light microscope, were used to quantify the extent of apoptosis. The dye uptake was further quantified using colorimetric method according to the manufacturer's instruction. The cells were lysed and the absorbance was measured at 550nm using a microplate reader (Biotech, USA).

3.4.17 In-Vivo studies

3.4.17.1 Acute toxicity profile

Acute toxicity analysis was conducted with 6-8 weeks old female Balb/c mice. A single dose (2000gm/Kg body weight) of drug was administered to three female Balb/C mice via intra-peritoneal administration. The mice were monitored initially for 4 hrs to observe any incidence of death and thereafter for 14 days for changes food water conception, body weight, physiological and behavioural patterns. At the end of 15th day, the animals were fasted overnight and sacrificed the internal viscera of each animal was observed for any organ abnormalities.

3.4.17.2 Sub-acute toxicity profile

Balb/c mice were used for the sub-acute toxicity analysis of TNC. Both male and female Balb/c mice (6-8 weeks old) were divided in to four groups, each group having five males and 5 female animals. TNC was intra-peritoneally administered in three doses to three groups viz., low dose (50 gm/Kg body weight), medium dose (100 gm/ Kg body weight) and high dose (200 gm/ Kg body weight) and one group was kept as untreated control. Treatment was continued consecutively for 28 days. The mice were monitored during this period for any adverse reactions to the TNC (through changes in behavior and mortality). Animals were weighed periodically and their food and water consumption were also monitored daily. At the end of the experimental period, the animals were sacrificed and blood and serum collected for biochemical analyses. Hematological paramters like total WBC count, RBC count, differential count, haemoglobin level etc., were measured along with the serum liver and kidney

function parameters and lipid profile. Organs were collected, weighed and organ somatic index (OSI) determined.

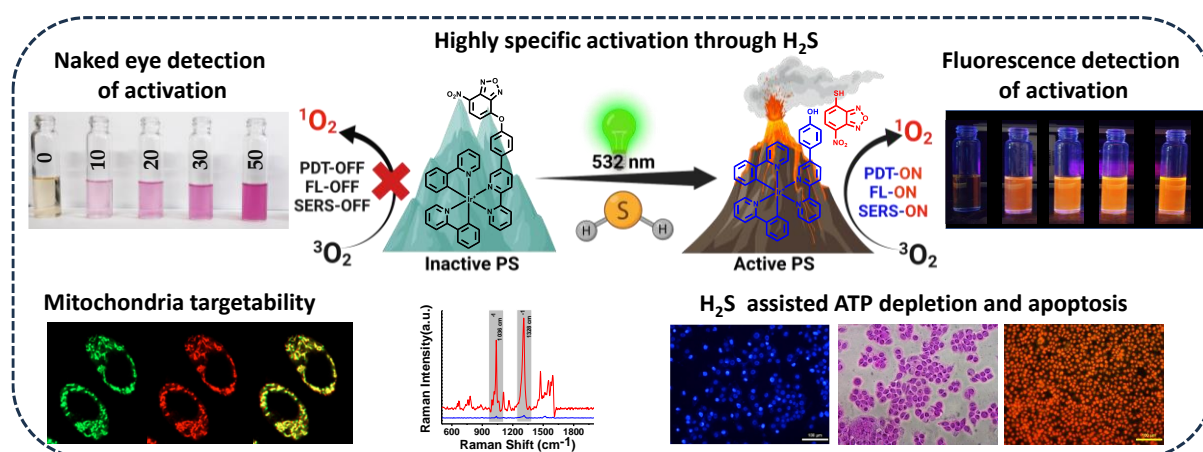
3.5 References

- (1) Harris, A. L. Hypoxia - A Key Regulatory Factor in Tumour Growth. *Nature Reviews Cancer*. European Association for Cardio-Thoracic Surgery 2002, pp 38–47. <https://doi.org/10.1038/nrc704>.
- (2) Lee, P.; Chandel, N. S.; Simon, M. C. Cellular Adaptation to Hypoxia through Hypoxia Inducible Factors and Beyond. *Nature Reviews Molecular Cell Biology*. Nature Research May 1, 2020, pp 268–283. <https://doi.org/10.1038/s41580-020-0227-y>.
- (3) Sørensen, B. S.; Horsman, M. R. Tumor Hypoxia: Impact on Radiation Therapy and Molecular Pathways. *Frontiers in Oncology*. Frontiers Media S.A. April 21, 2020. <https://doi.org/10.3389/fonc.2020.00562>.
- (4) Harris, A. L. Hypoxia - A Key Regulatory Factor in Tumour Growth. *Nature Reviews Cancer*. European Association for Cardio-Thoracic Surgery 2002, pp 38–47. <https://doi.org/10.1038/nrc704>.
- (5) Li, X.; Kwon, N.; Guo, T.; Liu, Z.; Yoon, J. Innovative Strategies for Hypoxic-Tumor Photodynamic Therapy. *Angewandte Chemie - International Edition*. Wiley-VCH Verlag September 3, 2018, pp 11522–11531. <https://doi.org/10.1002/anie.201805138>.
- (6) Ko, C. N.; Li, G.; Leung, C. H.; Ma, D. L. Dual Function Luminescent Transition Metal Complexes for Cancer Theranostics: The Combination of Diagnosis and Therapy. *Coordination Chemistry Reviews*. Elsevier B.V. February 15, 2019, pp 79–103. <https://doi.org/10.1016/j.ccr.2018.11.013>.
- (7) Wei, X.; Zhang, C.; He, S.; Huang, J.; Huang, J.; Liew, S. S.; Zeng, Z.; Pu, K. A Dual-Locked Activatable Phototheranostic Probe for Biomarker-Regulated Photodynamic and Photothermal Cancer Therapy. *Angewandte Chemie - International Edition* **2022**, *61* (26). <https://doi.org/10.1002/anie.202202966>.
- (8) Sung Jung, H.; Hong Lee, J.; Kim, K.; Koo, S.; Verwilt, P.; Sessler, J. L.; Kang, C.; Seung Kim, J. *A Mitochondria-Targeted Cryptocyanine-Based Photothermogenic Photosensitizer*; 2017. <http://pubs.acs.org>.
- (9) Li, X.; Lovell, J. F.; Yoon, J.; Chen, X. Clinical Development and Potential of Photothermal and Photodynamic Therapies for Cancer. *Nature Reviews Clinical Oncology*. Nature Research November 1, 2020, pp 657–674. <https://doi.org/10.1038/s41571-020-0410-2>.
- (10) Desai, D. A.; Mehta, F. A. *A Review on Photothermal Therapy (PTT) to Treat Cancer*; 2020; Vol. 1.
- (11) Liu, C.; Cao, Y.; Cheng, Y.; Wang, D.; Xu, T.; Su, L.; Zhang, X.; Dong, H. An Open Source and Reduce Expenditure ROS Generation Strategy for

- Chemodynamic/Photodynamic Synergistic Therapy. *Nat Commun* **2020**, *11* (1). <https://doi.org/10.1038/s41467-020-15591-4>.
- (12) Liu, D.; Liu, M.; Wan, Y.; Zhou, X.; Yang, S.; An, L.; Huang, G.; Tian, Q. Remodeling Endogenous H₂S Microenvironment in Colon Cancer to Enhance Chemodynamic Therapy. *Chemical Engineering Journal* **2021**, *422*. <https://doi.org/10.1016/j.cej.2021.130098>.
- (13) Ma, B.; Wang, S.; Liu, F.; Zhang, S.; Duan, J.; Li, Z.; Kong, Y.; Sang, Y.; Liu, H.; Bu, W.; Li, L. Self-Assembled Copper-Amino Acid Nanoparticles for in Situ Glutathione “aND” H₂O₂ Sequentially Triggered Chemodynamic Therapy. *J Am Chem Soc* **2019**, *141* (2), 849–857. <https://doi.org/10.1021/jacs.8b08714>.
- (14) Ou, J.; Tian, H.; Wu, J.; Gao, J.; Jiang, J.; Liu, K.; Wang, S.; Wang, F.; Tong, F.; Ye, Y.; Liu, L.; Chen, B.; Ma, X.; Chen, X.; Peng, F.; Tu, Y. MnO₂-Based Nanomotors with Active Fenton-like Mn²⁺ Delivery for Enhanced Chemodynamic Therapy. *ACS Appl Mater Interfaces* **2021**, *13* (32), 38050–38060. <https://doi.org/10.1021/acsami.1c08926>.
- (15) Yuan, H.; Han, Z.; Chen, Y.; Qi, F.; Fang, H.; Guo, Z.; Zhang, S.; He, W. Ferroptosis Photoinduced by New Cyclometalated Iridium(III) Complexes and Its Synergism with Apoptosis in Tumor Cell Inhibition. *Angewandte Chemie - International Edition* **2021**, *60* (15), 8174–8181. <https://doi.org/10.1002/anie.202014959>.
- (16) Koo, S.; Park, O. K.; Kim, J.; Han, S. I.; Yoo, T. Y.; Lee, N.; Kim, Y. G.; Kim, H.; Lim, C.; Bae, J. S.; Yoo, J.; Kim, D.; Choi, S. H.; Hyeon, T. Enhanced Chemodynamic Therapy by Cu-Fe Peroxide Nanoparticles: Tumor Microenvironment-Mediated Synergistic Fenton Reaction. *ACS Nano* **2022**, *16* (2), 2535–2545. <https://doi.org/10.1021/acsnano.1c09171>.
- (17) Huang, Y.; Wu, S.; Zhang, L.; Deng, Q.; Ren, J.; Qu, X. A Metabolic Multistage Glutathione Depletion Used for Tumor-Specific Chemodynamic Therapy. *ACS Nano* **2022**, *16* (3), 4228–4238. <https://doi.org/10.1021/acsnano.1c10231>.
- (18) He, T.; Qin, X.; Jiang, C.; Jiang, D.; Lei, S.; Lin, J.; Zhu, W. G.; Qu, J.; Huang, P. Tumor PH-Responsive Metastable-Phase Manganese Sulfide Nanotheranostics for Traceable Hydrogen Sulfide Gas Therapy Primed Chemodynamic Therapy. *Theranostics* **2020**, *10* (6), 2453–2462. <https://doi.org/10.7150/thno.42981>.
- (19) Escudero, A.; Carrillo-Carrión, C.; Castillejos, M. C.; Romero-Ben, E.; Rosales-Barrios, C.; Khiar, N. Photodynamic Therapy: Photosensitizers and Nanostructures. *Materials Chemistry Frontiers*. Royal Society of Chemistry May 21, 2021, pp 3788–3812. <https://doi.org/10.1039/d0qm00922a>.
- (20) Correia, J. H.; Rodrigues, J. A.; Pimenta, S.; Dong, T.; Yang, Z. Photodynamic Therapy Review: Principles, Photosensitizers, Applications, and Future Directions. *Pharmaceutics* **2021**, *13* (9). <https://doi.org/10.3390/pharmaceutics13091332>.
- (21) Callaghan, S.; Filatov, M. A.; Sitte, E.; Savoie, H.; Boyle, R. W.; Flanagan, K. J.; Senge, M. O. Delayed Release Singlet Oxygen Sensitizers Based on Pyridone-Appended Porphyrins. *Photochemical and Photobiological Sciences* **2017**, *16* (9), 1371–1374. <https://doi.org/10.1039/c7pp00244k>.

-
- (22) Lv, W.; Xia, H.; Zhang, K. Y.; Chen, Z.; Liu, S.; Huang, W.; Zhao, Q. Photothermal-Triggered Release of Singlet Oxygen from an Endoperoxide-Containing Polymeric Carrier for Killing Cancer Cells. *Mater Horiz* **2017**, *4* (6), 1185–1189. <https://doi.org/10.1039/c7mh00726d>.
- (23) Kolemen, S.; Ozdemir, T.; Lee, D.; Kim, G. M.; Karatas, T.; Yoon, J.; Akkaya, E. U. Remote-Controlled Release of Singlet Oxygen by the Plasmonic Heating of Endoperoxide-Modified Gold Nanorods: Towards a Paradigm Change in Photodynamic Therapy. *Angewandte Chemie* **2016**, *128* (11), 3670–3674. <https://doi.org/10.1002/ange.201510064>.
- (24) Celli, J. P.; Spring, B. Q.; Rizvi, I.; Evans, C. L.; Samkoe, K. S.; Verma, S.; Pogue, B. W.; Hasan, T. Imaging and Photodynamic Therapy: Mechanisms, Monitoring, and Optimization. *Chem Rev* **2010**, *110* (5), 2795–2838. <https://doi.org/10.1021/cr900300p>.
- (25) Dermime, S. Cancer Diagnosis, Treatment and Therapy. *J Carcinog Mutagen* **2013**, *S14*. <https://doi.org/10.4172/2157-2518.s14-007>.
- (26) Wang, Z.; Li, P.; Jiang, Y.; Jia, Z.; Tang, P.; Lu, X.; Ren, F.; Wang, K.; Yuan, H. Mussel-Inspired Nanostructured Coatings Assembled Using Polydopamine Nanoparticles and Hydroxyapatite Nanorods for Biomedical Applications. *Biosurf Biotribol* **2017**, *3* (1), 1–10. <https://doi.org/10.1016/j.bsbt.2017.01.001>.
- (27) Chen, Y.; Chen, M.; Zhai, T.; Zhou, H.; Zhou, Z.; Liu, X.; Yang, S.; Yang, H. Glutathione-Responsive Chemodynamic Therapy of Manganese(III/IV) Cluster Nanoparticles Enhanced by Electrochemical Stimulation via Oxidative Stress Pathway. *Bioconjug Chem* **2022**, *33* (1), 152–163. <https://doi.org/10.1021/acs.bioconjchem.1c00512>.
- (28) Chakraborty, S.; Agrawalla, B. K.; Stumper, A.; Vegi, N. M.; Fischer, S.; Reichardt, C.; Kögler, M.; Dietzek, B.; Feuring-Buske, M.; Buske, C.; Rau, S.; Weil, T. Mitochondria Targeted Protein-Ruthenium Photosensitizer for Efficient Photodynamic Applications. *J Am Chem Soc* **2017**, *139* (6), 2512–2519. <https://doi.org/10.1021/jacs.6b13399>.
-

Harnessing Hydrogen Sulphide-Induced Activation for Site-Specific Photodynamic Therapy: Disrupting Glycolysis as a Strategy for Selective and Enhanced Anticancer Effects



Abstract

The development of targeted and activatable photosensitizers holds great promise in the field of photodynamic therapy (PDT) for cancer treatment. Herein, design, synthesis, and comprehensive characterization of a novel cyclometalated iridium complex is demonstrated which is an activatable photosensitizer termed P-NBD and has been engineered for precise molecular control and functionality. The rationale involves the incorporation of an electron-deficient and hydrogen sulphide (H_2S)-responsive 7-nitrobenzofurazan (NBD) unit, covalently linked to a hydroxy appended iridium complex. Under normal physiological conditions, the NBD unit quenches the photodynamic effect, minimizing off-target cytotoxicity. Upon exposure to H_2S , a biologically relevant signaling molecule, the NBD unit undergoes nucleophilic substitution, activating P-NBD into the photosensitizer P-OH. This activation mechanism offers exceptional specificity and controllability. The molecular response to H_2S enables targeted activation within H_2S -rich environments, relevant to certain disease states. In the In-vitro system, the activation causes the depletion of H_2S leading to the disruption of glycolysis and ATP production. Activated P-OH efficiently generates reactive oxygen species (ROS) upon laser irradiation, inducing selective cell death. The positively charged central iridium ion enhances mitochondrial targeting, reinforcing its therapeutic potential. Cellular studies in SKBR3 cells demonstrate the molecule's biocompatibility, specificity, and ability to modulate H_2S

levels. Activated P-NBD induces apoptosis, disrupts mitochondrial membrane potential, and generates singlet oxygen, culminating in a robust photodynamic effect. SERS and fluorescence imaging further confirm apoptotic events in dual-modality. This work highlights P-NBD's potential as an advanced platform for targeted and activatable PDT in cancer therapy.

4.1 Introduction

Photodynamic therapy (PDT) represents an exciting and precise therapeutic approach that holds great promise in the field of medicine. By harnessing the power of photosensitizing agents (PS), specific light, and molecular oxygen, PDT selectively targets and damages specific cells, offering a non-invasive treatment technique with exceptional spatiotemporal selectivity and limited drug resistance.¹ However, the persistent "always on" nature of most PS and the resultant off-target phototoxicity during light exposure have posed practical limitations to the widespread application of PDT.² To overcome these challenges, a novel class of phototherapeutic compounds known as Activatable PS has emerged.³⁻⁵ Unlike conventional PS, Activatable PS exhibit reduced photoactivity in its natural state even under light irradiation, making them less harmful to healthy cells.⁶ However, when appropriately stimulated, these compounds undergo a remarkable transformation, activating their potent phototoxic effects selectively within the desired target cells.⁷⁻⁹ This unique property enables the targeted destruction of cancer cells while minimizing damage to neighboring healthy cells. The advent of Activatable PS represents a significant advancement in the field of PDT, offering enhanced specificity, improved safety, and greater efficacy.^{6,10}

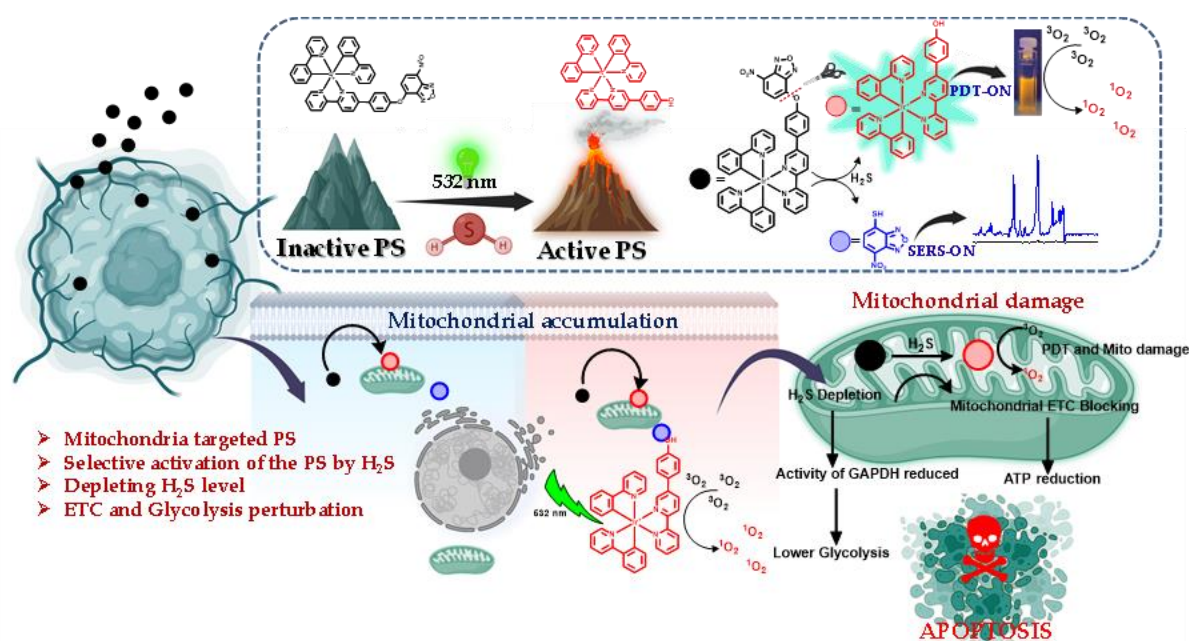
In order to induce a noticeable disruption in the cellular environment, the activation mechanism employed during PDT should effectively sequester the activator, thereby reducing its availability.¹¹ This sequestration event not only triggers the desired photodynamic response but also impairs the metabolic pathways reliant on the specific chemical. Consequently, the cellular environment experiences a severe imbalance, rendering the targeted cells vulnerable to destruction. The depletion of the activator resulting from the activation mechanism has two-fold effects on the cellular environment.¹²⁻¹⁴ Firstly, it enables an activatable PDT, where the photosensitizer becomes highly reactive upon activation, leading to enhanced cytotoxicity against the targeted cells. Secondly, the depletion impact affects the metabolic pathways that depend on the specific chemical, thereby exacerbating the cellular imbalance. This dual action reinforces the

therapeutic efficacy of PDT, achieving a more pronounced and comprehensive treatment outcome.^{15,16}

Hydrogen sulphide (H₂S) is a molecule of vital importance in various biological and physical processes. Its unique properties and versatile functions have attracted significant attention from researchers across different disciplines.¹⁷⁻¹⁹ In recent years, the association between elevated levels of H₂S and numerous diseases, including cancer, has emphasized the significance of H₂S -specific detection and monitoring.²⁰ Elevated levels of H₂S have been observed in various types of tumors, and studies suggest that it plays a crucial role in the development and progression of cancer.^{21,22} H₂S has been linked to tumor growth, angiogenesis, metastasis, and resistance to chemotherapy. Additionally, it has been found to modulate key signaling pathways involved in cancer cell proliferation, apoptosis, and inflammation. One particular area of interest is the role of H₂S in modulating the activity of glyceraldehyde-3-phosphate dehydrogenase (GAPDH), a central enzyme in cellular metabolism.²³ GAPDH participates in glycolysis and other vital pathways. Recent studies have highlighted a unique posttranslational modification called sulfhydration, where a sulphur atom is covalently added to specific cysteine residues. Emerging evidence suggests that sulfhydration dynamically regulates protein function. H₂S-mediated sulfhydration of GAPDH at cysteine 150 (Cys150) has been discovered to enhance its catalytic activity, providing a novel mechanism for the regulation of metabolic pathways. Increased GAPDH activity accelerates the conversion of glyceraldehyde-3-phosphate to 1,3-bisphosphoglycerate, thereby promoting a higher rate of glucose metabolism and glycolytic flux.²⁴ This enhanced enzymatic activity leads to an elevated ATP production rate through both substrate-level phosphorylation and subsequent oxidative phosphorylation. The elevation in GAPDH activity not only increases ATP availability but also fuels cellular processes such as active transport, biosynthesis, and muscle contraction. This allows cells to more efficiently meet their energy demands, especially during conditions of increased energy requirements, such as in rapidly dividing cells or under hypoxic conditions.²³

Herein, a newly evolved activatable photodynamic therapy (PDT) agent has been demonstrated based on a cyclometallated iridium complex, offering a multifunctional theranostic approach for cancer treatment. The agent is specifically activated in the presence of hydrogen sulphide (H₂S) through a specific nucleophilic substitution reaction within the tumor microenvironment. Upon activation, the photosensitizer (PS) not only initiates PDT-induced cell death but also depletes H₂S levels in the local cellular milieu. This H₂S depletion subsequently disrupts the activity of glyceraldehyde 3-phosphate

dehydrogenase (GAPDH), a key enzyme involved in glycolysis, leading to reduced glycolysis and ATP production within cancer cells. By harnessing the unique properties of H₂S and the specific activation of the cyclometallated iridium complex, our approach achieves a dual therapeutic effect. The activatable PDT selectively induces cell death while disrupting the glycolytic metabolism of cancer cells. This synergistic effect enhances the overall efficacy of the treatment, making it a promising strategy for cancer therapeutics. Additionally, the multifunctional nature of our approach allows for real-time visualization of the events in dual mode of Fluorescence and SERS platform (**Scheme 4.1**).



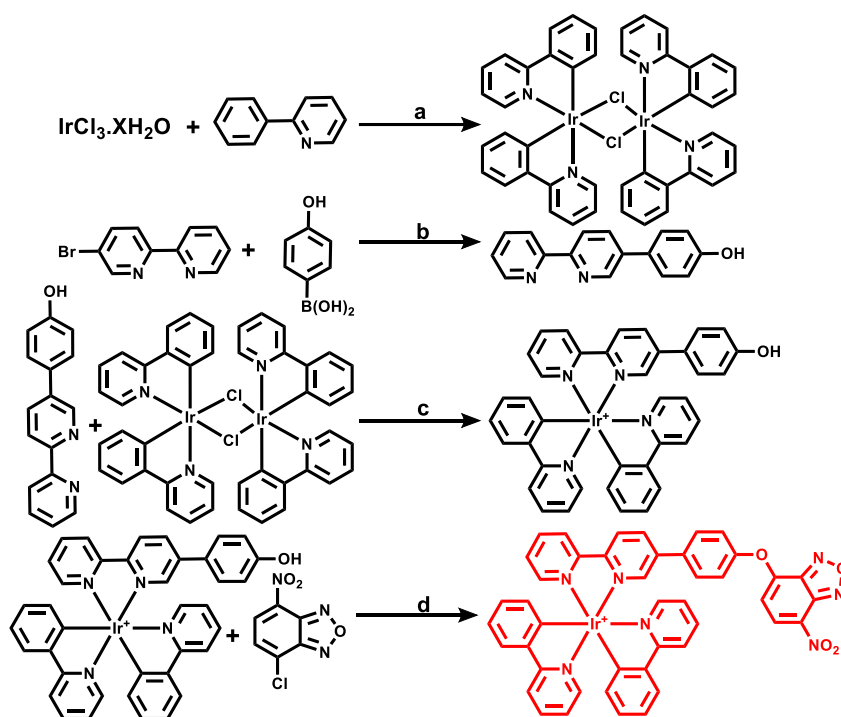
Scheme 4.1: Schematic depiction elucidating the cascade of processes elicited by the activatable photodynamic therapy (PDT) agent P-NBD within the cellular milieu.

4.2 Result and Discussion

4.2.1 Design and synthesis of P-NBD

Iridium complexes have garnered considerable attention due to their intriguing attributes within the realm of photochemistry. Their rising popularity renders them suitable materials for various biomedical applications, such as imaging and photodynamic therapy (PDT).²⁵ A key feature of these complexes is the high electron-donating capacity of the metal center, which readily facilitates the donation or transfer of electrons to electron-deficient acceptor molecules. This dynamic interplay between the electron acceptor and donor ultimately leads to the quenching of luminescent properties, accompanied by photoactive effects like PDT.²⁶ The restoration of luminescence and the generation of reactive oxygen species (ROS) occur only upon the removal of the electron acceptor.²⁷ This novel strategy has

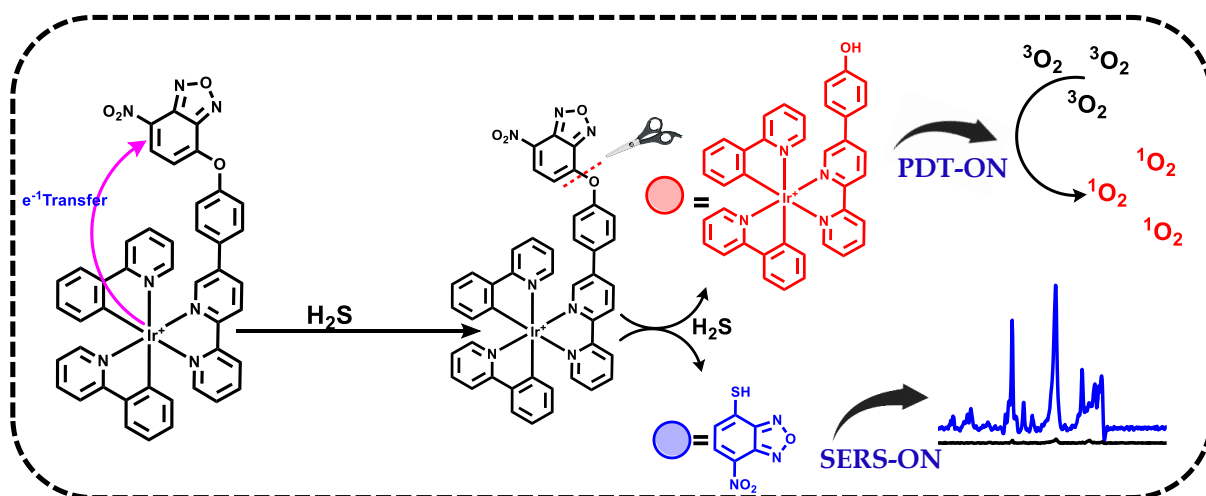
recently come to light, with researchers harnessing these properties to design sensor molecules across various fields, including cancer biology. The selective sensing process not only reinstates luminescence but also re-establishes PDT properties. Consequently, iridium metal complexes emerge as highly adaptable PDT agents, capable of selective activation in response to bio-related stimuli. This versatility opens new avenues for tailored therapies and targeted interventions in medical and biological contexts.²⁸



Scheme 4.2: Schematic illustration of the synthesis of P-NBD. Reagent and conditions: **(a)** 2-ethoxyethanol/water (8:2), reflux, 24 h. **(b)** Aq-K₂CO₃-Toluene, Pd (PPh₃)₄, TBAB-24 h, 90°C. **(c)** DCM/ethanol (1:3), Argon, 60°C, 12 h and NH₄PF₆. **(d)** DIPEA-DMF-2h, RT.

The cyclometalated iridium complex-based activatable photosensitizer, termed P-NBD, was synthetically engineered with precise control over its molecular structure and functionality. The design rationale involved the deliberate incorporation of an electron-deficient and H₂S-responsive NBD unit, covalently linked to a hydroxy appended iridium complex, P-OH, through an intermolecular reaction involving 4-Chloro-7-nitrobenzofurazan. The synthetic strategy was based on established methodologies reported in the literature, albeit with minor modifications to tailor the molecule for specific applications (**Scheme 4.2**). Under normal physiological conditions, the presence of the electron-deficient NBD unit efficiently quenches the photodynamic effect of P-NBD, ensuring minimal off-target cytotoxicity. However, upon encountering H₂S, a biologically relevant signaling molecule, the NBD moiety undergoes nucleophilic substitution, resulting in the cleavage of the NBD unit.²⁹ This event leads to the immediate activation of P-NBD,

generating the highly active photosensitizer, P-OH. The activation process is accompanied by distinct changes in the emission and absorption properties of the molecule. Upon activation, P-OH exhibits a pronounced turn-on emission at 615 nm, indicative of its photodynamic activity. Furthermore, the cleavage of the NBD unit simultaneously yields a Surface-Enhanced Raman Scattering (SERS) active species known as NBD-SH, which provides a reliable spectroscopic signature for monitoring the activation process in real-time (**Scheme 4.3**). The unique activation mechanism of P-NBD in the presence of H₂S endows it with exceptional specificity and controllability. This molecular responsiveness to H₂S enables targeted activation of the photosensitizer within H₂S-rich environments, such as those present in certain disease states or pathological conditions and cancer. Consequently, upon exposure to 532 nm laser irradiation, the activated P-OH efficiently generates reactive oxygen species (ROS), inducing selective cell death in the targeted tissue. The positive charge on the central Ir metal ion further enhances the molecule's mitochondrial-targeting capability, facilitating disruption of the cellular energy supply system and reinforcing its potential as a potent therapeutic agent.



Scheme 4.3: Mechanism of activation of the a-PDT agent P-NBD with H₂S

The PS complex P-NBD was synthesized and thoroughly characterized using advanced techniques like NMR and HRMS spectroscopic analysis. The NMR spectra showed the disappearance of the peak corresponding to the OH proton of the hydroxy group in the original iridium complex (P-OH) at 9.953 ppm after the reaction with NBD-Cl, and the appearance of new peaks at 7.33 and 7.53 ppm, confirming the successful reaction between P-OH and NBD-Cl. The HRMS spectra also provided evidence of the conversion, as the peak corresponding to P-OH at 749.1884 shifted significantly to 912.1941 in the P-NBD mass, further supporting the successful synthesis. To gain a comprehensive understanding

of the molecule, in-depth investigations were carried out to study its structural, photophysical, and electrochemical properties. These analyses involved UV-Visible, Fluorescence, and cyclic voltametric techniques, which are available in the experimental section.

4.2.2 Unlocking of P-NBD to activated PS P-OH by Hydrogen Sulphide (H₂S)

In our subsequent investigation, we explored the sensitivity of P-NBD to hydrogen sulphide (H₂S) by conducting a series of experiments. To initiate the process, P-NBD (10 μM in acetonitrile: water,3:2 mixture) was exposed to Na₂S (100 μM) in PBS buffer, and we monitored the reaction in real time through absorption and fluorescence measurements. The absorption spectra of P-NBD display distinct characteristics linked to various electronic transitions, including metal to ligand charge transfer (MLCT) and ligand-centred (LC) processes. Notably, there are strong and high-energy bands at around 286 nm attributed to ligand centred transitions originating from both Ppy and Bpy ligands. Additionally, moderately high-energy absorption shoulders in the range of 380-390 nm are thought to result from a combination of spin allowed ¹MLCT, dπ-π*(bpy) transitions, and ¹LLCT, π(bpy)-π*(bpy) processes (Figure 4.1 a).

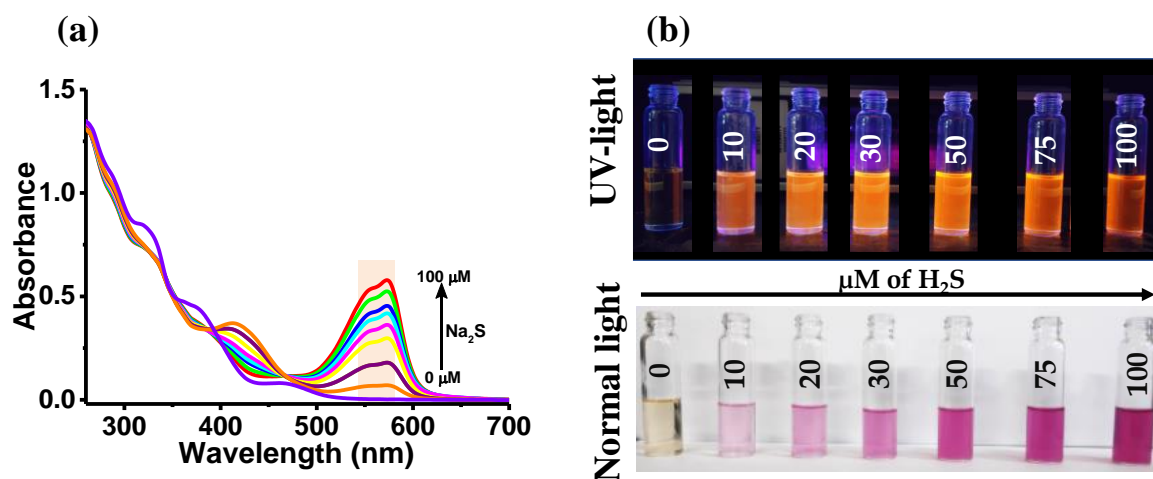


Figure 4.1: Absorption changes of P-NBD associated with varying concentrations of H₂S treatment. Photographs showing the activation of P-NBD with H₂S through naked eye visualisation and fluorescence.

Moreover, a less intense band at 475 nm is associated with spin-forbidden transitions related to ³MLCT and ³LLCT/³LC processes.^{30,31} Upon reaction with Na₂S, we observed a sharp increase in the absorption intensity at 565 nm, attributed to the formation of NBD-SH. By subjecting the same concentration of P-NBD solution to various amounts of Na₂S, ranging from 0 to 100 μM, we noted similar absorption changes, and the correlation

analysis yielded an R^2 value of 0.9981, signifying a consistent pattern in the data. Furthermore, the reaction rate between P-NBD and sulphide demonstrated a significant enhancement with higher concentrations of Na_2S . A time-dependent analysis revealed that the entire reaction process was nearly completed within approximately 2 minutes of incubation. Notably, this transformation was accompanied by a simultaneous change in colour from pale yellow to pink (Figure 4.1 b).

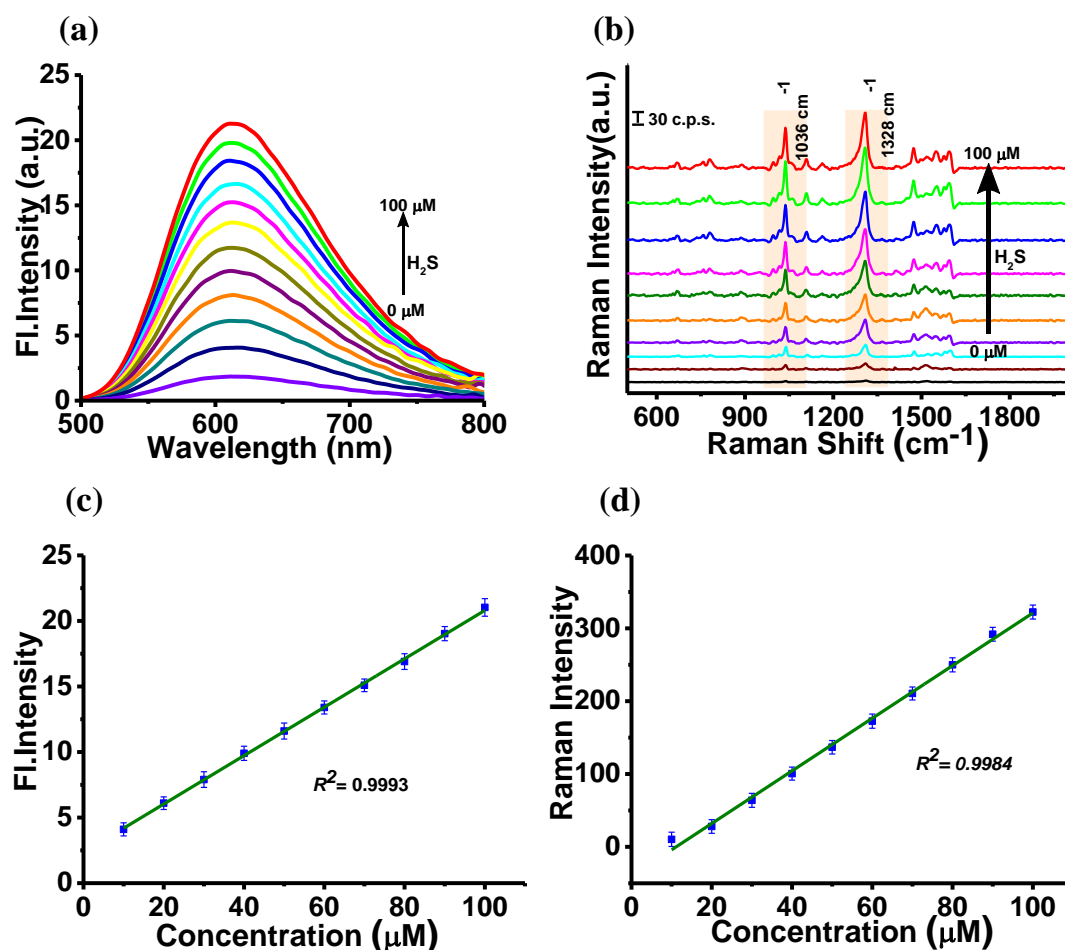


Figure 4.2: (a) Luminescence changes of P-NBD associated with varying concentrations of H_2S treatment. (b) The activation of P-NBD with H_2S tracked with SERS analysis (the peaks are corresponding to NBD-SH). (c&d) Corresponding linear response of PNBD with increasing H_2S concentration in Fluorescence and SERS.

Further, the fluorescence responsiveness of P-NBD has been evaluated in solution towards H_2S . Initially, the aqueous solution of P-NBD exhibited minimal or quenched fluorescence in its inactive bare form. However, upon the addition of increasing concentrations of Na_2S , the fluorescence intensity at 615 nm gradually increased (Figure 4.2 a). This fluorescence response was effectively suppressed when ZnCl_2 , a known H_2S scavenger, was present, indicating that P-NBD possesses excellent sensitivity and responsiveness towards H_2S . We hypothesize that this H_2S -responsive fluorescence change is attributed to the conversion of

P-NBD to P-OH through a nucleophilic substitution reaction with H₂S. To further investigate the sensitivity of P-NBD to Na₂S, we plotted the fluorescence intensity at 615 nm against the increasing concentrations of Na₂S. Notably, the activated fluorescence at 615 nm demonstrated a strong linear correlation with the Na₂S concentration within the range of 0 to 100 μM (R²=0.9993). Based on this linear relationship, the detection limit of 0.120 μM, was achieved highlights the high sensitivity of P-NBD toward H₂S detection (Figure 4.2 c). In light of the previously mentioned NBD elimination mechanism in the presence of H₂S, we conducted SERS measurements on P-NBD with H₂S to validate our hypothesis. To confirm this, we analyzed SERS spectra of P-NBD solutions with varying amounts of Na₂S, ranging from 0 to 100 μM, after a 2-minute incubation period. Subsequently, the solutions were mixed with Au Nanoparticles in a 1:9 ratio (2 μL of reaction mixture with 18 μL of AuNP).³² Remarkably, a significant enhancement was observed in the SERS peaks corresponding to the nitro vibration of the NBD component at 1328 cm⁻¹, providing evidence of the activation process (Figure 4.2 b).

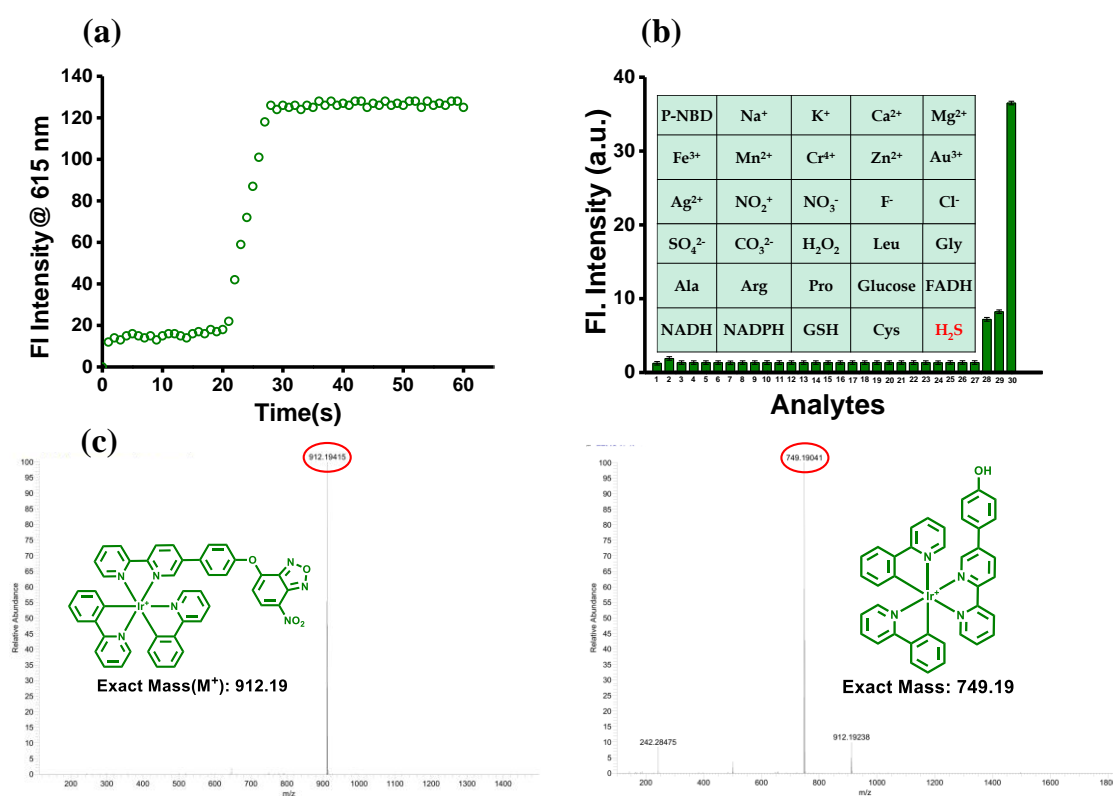


Figure 4.3: (a) Time of response of P-NBD associated with 100 μM of H₂S treatment. (b) The selective activation of P-NBD by H₂S, confirmed with selectivity studies over other analytes. (c&d) HRMS conformation of P-NBD to P-OH conversion by H₂S.

The appearance of a distinctive SERS band at 1328 cm⁻¹ also exhibited a strong linear relationship with the concentration of Na₂S, spanning from 0 to 100 μM (R²=0.9984).

Notably, we achieved an impressive detection limit of 0.567 nM (Figure 4.2d). Further, the response toward H₂S was accounted for by P-NBD demonstrates excellent responsiveness to varying concentrations of H₂S, exhibiting rapid and efficient fluorescence intensity increase upon the addition of 100 μM Na₂S, reaching its peak within just 30 seconds (Figure 4.3a). Additionally, it displays exceptional photostability, making it an ideal molecule for activatable PDT. To ascertain the precise and targeted activation of PS with H₂S, we undertook selectivity studies involving 30 different analytes, encompassing metal ions, amino acids, peptides, and various other biologically active molecules such as NADH, NADPH, GSH etc. Remarkably, our P-NBD demonstrated exceptional specificity and selectivity exclusively towards Na₂S under identical experimental conditions (Figure 4.3b). These findings unequivocally demonstrate the resistance of P-NBD against non-targeted and non-specific activations, substantiating its potential as a highly reliable and discriminating probe for H₂S-triggered activation. The reaction mechanism between P-NBD and H₂S was further confirmed using High-Resolution Mass Spectrometry (HRMS) analysis. As expected, the m/z peak of P-NBD alone exhibited a value of 912.1941 (in comparison to the calculated value of 912.194). However, after incubating the molecule with 100 μM of Na₂S for 1 minute, the HRMS analysis showed peaks at m/z 749.1884, corresponding to the activated PS P-OH (matching the calculated value of 749.1884) (Figure 4.3c&d).

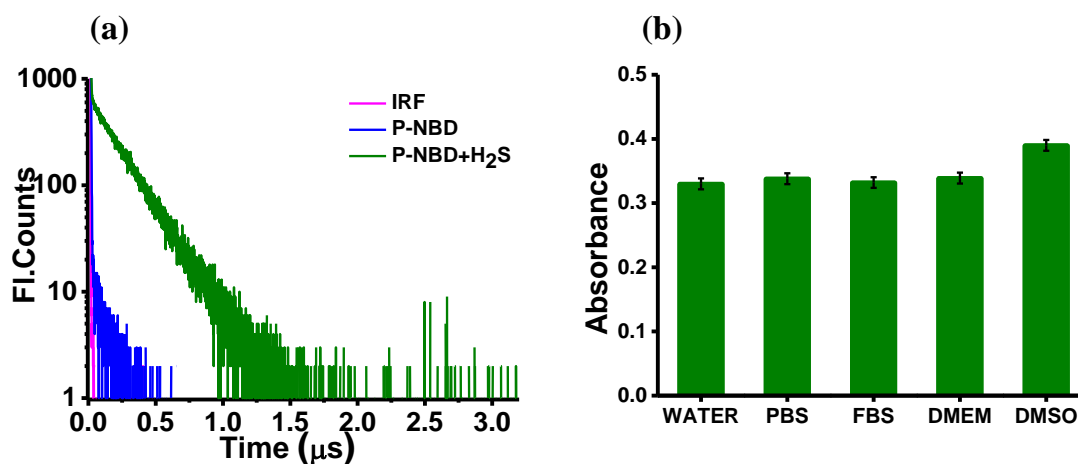


Figure 4.4: (a) Time Correlated Single Photon Counting studies of P-NBD and P-NBD with 100 μM of H₂S treatment. (b) The stability studies of P-NBD in various solvents.

To enhance the precision of activation confirmation, we utilized Time Correlated Single Photon Counting for lifetime measurement analysis. Molecules with quenched emission consistently exhibit notably shorter lifetimes compared to their fluorescent counterparts. However, when the probe molecule P-NBD was introduced and incubated with Na₂S, a

remarkable increase in lifetime from 14 ns to 209 ns was observed. This substantial prolongation of lifetime indicates that H₂S-mediated activation impedes the electron transfer between the metal and the NBD portion (Figure 4.4a). The molecule also exhibits excellent stability in solvents related to the cellular environment (Figure 4.4b). Taken together, these findings strongly suggest that P-NBD holds significant promise for H₂S-based activation with exceptional sensitivity and selectivity *In vitro*.

4.23 Conformation of *In-Vitro* activation through Fluorescence and SERS imaging of H₂S in SKBR3 cells.

With the exciting findings mentioned above, our focus shifted toward investigating the potential of P-NBD for activating H₂S in living cells.

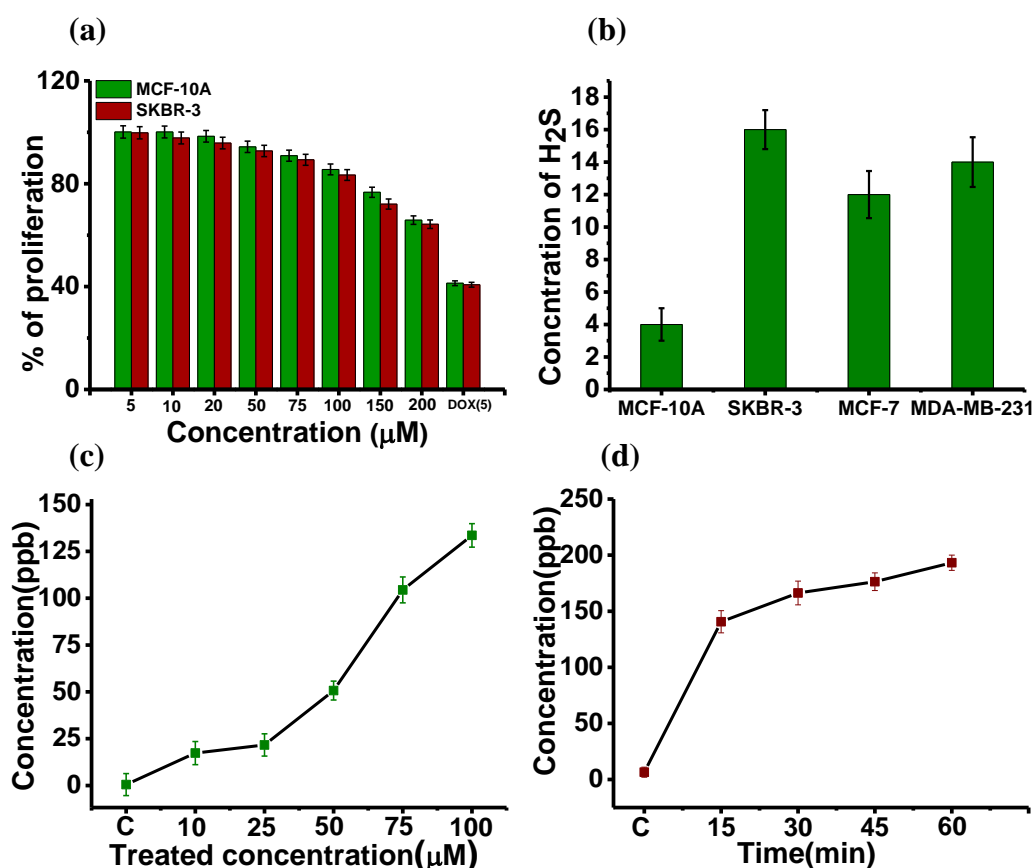


Figure 4.5: (a) MTT assay of P-NBD in normal MCF-10A and SKBR-3 cancer cells at 24 h. (b) The estimation of H₂S level in various cancer and normal cells using methylene blue assay. (c&d) ICPMS quantification of the Ir metal content in SKBR-3 cells concentration and time dependent manner.

Before delving into the cellular applications, we conducted MTT assays to assess the cytotoxicity of P-NBD on human breast cancer cell line SKBR3 and normal epithelial breast cell line MCF-10A. Remarkably, even at the concentration of 100 μ M, P-NBD

incubation for 24 hours had negligible cytotoxic effects on SKBR3 cells, with cell viability remaining above 78% (Figure 4.5a). Furthermore, no significant cytotoxicity was observed in normal epithelial breast cell MCF-10A even at the same concentration and incubation time, indicating excellent biocompatibility and the non-toxic nature of P-NBD. For further experiments, SKBR3 cells were chosen due to their higher H₂S levels compared to normal MCF-10A cells (Figure 4.5b). To quantitatively confirm the internalization process, we performed ICPMS studies, which clearly showed the presence of Ir³⁺ ions in cells treated with P-NBD, confirming the internalization process (Figure 4.5 c&d).

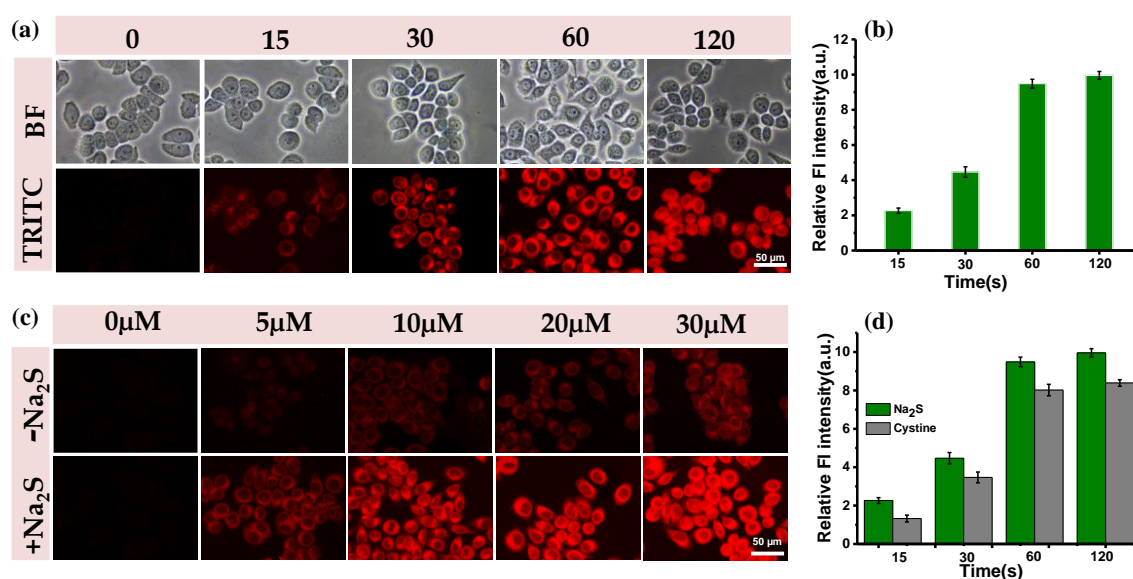


Figure 4.6: (a) MTT assay of P-NBD in normal MCF-10A and SKBR-3 cancer cells at 24 h. (b) The estimation of H₂S level in various cancer and normal cells using methylene blue assay. (c&d) ICPMS quantification of the Ir metal content in SKBR-3 cells concentration and time dependent manner.

To validate the optimization of time and concentration, we employed fluorescence microscopic imaging in living SKBR3 cells after incubation with P-NBD. Within 1 hour of treatment with 10 μM P-NBD, clear red fluorescence was observed in SKBR3 cells. To confirm that this fluorescence was indeed activated by endogenous H₂S, we preincubated SKBR3 cells with Na₂S, which led to enhanced fluorescence signals compared to the control cells both in time and concentration-dependent studies (Figure 4.6 a-d). Together, these findings strongly suggest that the fluorescence enhancement observed in P-NBD is specifically triggered by H₂S. To further assess the capability of P-NBD for detecting SKBR3 cells through SERS, cellular pellets from both the treated and control groups were collected, lysed to obtain aqueous solutions, and subjected to SERS signal measurement. The results depicted in Fig. 3c indicate that the treated samples displayed a prominent band

at 1328 cm^{-1} corresponding to the NO_2 vibration of NBD-SH, along with the cell peaks, while the peaks representing the NO_2 component were absent in the control sample. To verify the internalization and activation of P-NBD, a time-dependent SERS imaging was performed. As the time increased from 0 to 2 hours, complete activation was observed, clearly visualized through SERS using the 1328 cm^{-1} peak (**Figure 4.7**).

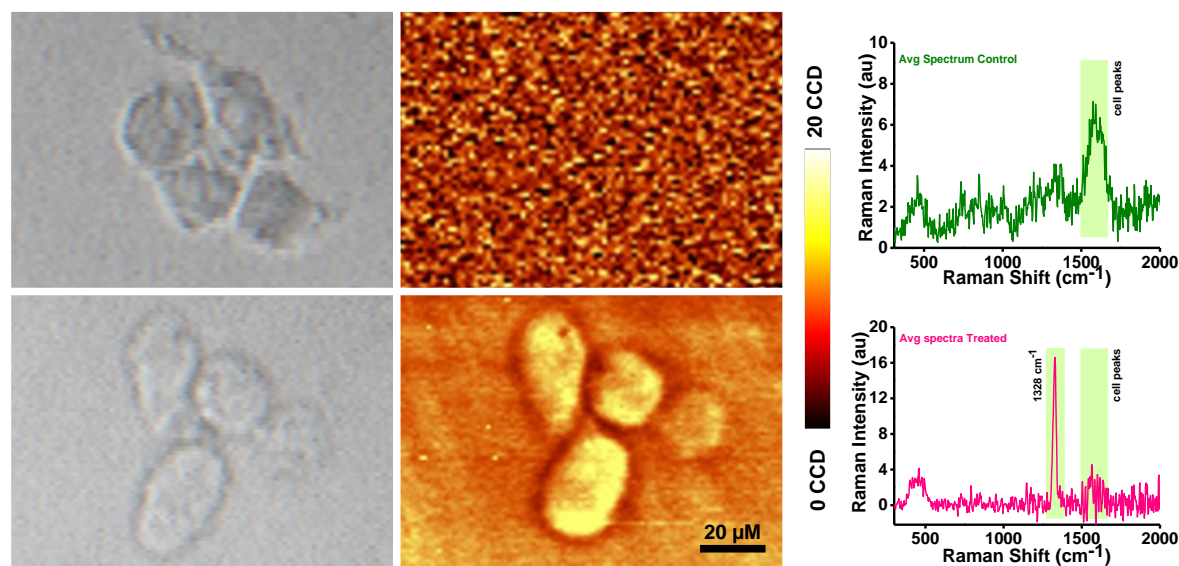


Figure 4.7: SERS imaging of the SKBR-3 control cells and cells treated with P-NBD (images were obtained by scanning using the 1328 cm^{-1} peak) and corresponding average spectra from the image.

In order to demonstrate the effectiveness of P-NBD in accurately assessing small variations in H_2S levels resulting from metabolic activities and various pretreatments, we conducted experiments involving inhibitor and activator studies. These investigations aimed to validate the ability of P-NBD to precisely detect and quantify the subtle fluctuations in H_2S levels caused by different factors. Pre-treating the cells with L-Cysteine (0.5 mM), a biochemical intermediate that participates in enzymatic reactions within the metabolic pathway responsible for the synthesis of H_2S , to stimulate intracellular H_2S expression resulted in significantly higher red fluorescence, which was effectively inhibited by adding AOAA (50 μM) to suppress CSE activity. Furthermore, pre-incubation with ZnCl_2 , an H_2S scavenger, suppressed the fluorescence signals, while preincubation with thiol scavenger NEM reduced the fluorescence intensity, both indicating H_2S -mediated activation of the molecule. Collectively, these findings present compelling proof that P-NBD is efficiently triggered by H_2S in In-vitro systems (**Figure 4.8 a-c**).

4.24 Untangling Mitochondrial Co-localization: Revealing Subcellular Relationships

Precise subcellular localization of a molecule is of paramount importance, especially in the context of its application as a Photosensitizer in PDT. When designing PDT agents, strategically aiming for mitochondria as the subcellular target has emerged as a superior choice. By selectively directing the PDT agent to accumulate within mitochondria, it becomes possible to disrupt this vital energy production system. As a result, the cellular respiration process is impaired, leading to an elevated and targeted therapeutic effect. Mitochondria possess a negative transmembrane potential, making them highly receptive to positively charged substances. The P-NBD molecule's naturally positive charge, stemming from the central iridium metal, aids in the accumulation of the PDT agent specifically on the mitochondria.

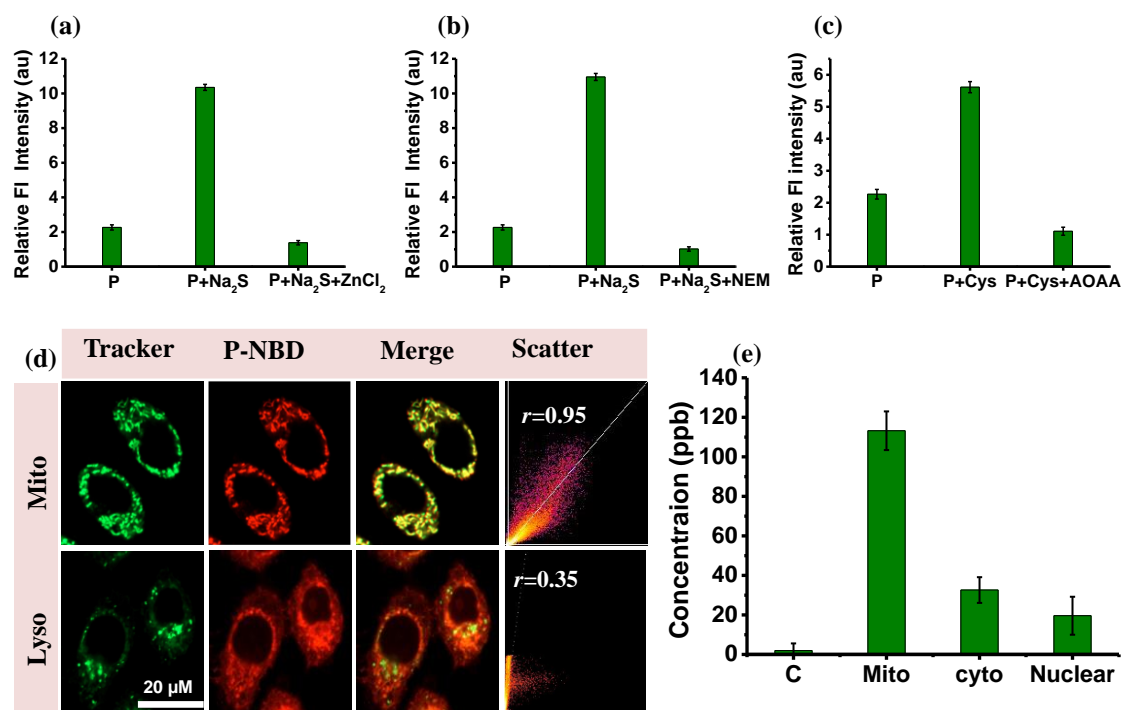


Figure 4.8: Inhibitor based studies to confirm the selective activation of P-NBD through H₂S (a) ZnCl₂ based studies. (b) Thiol inhibitor NEM based studies. (c) CBS and CBE inhibitor aminoxy acetic acid-based studies. (d) Confocal images of the P-NBD incubate with 1h followed by Mito and lysotracker dyes to confirm the subcellular localisation.

Prior to investigating the potential activated phototoxicity of P-NBD in vitro, the intracellular localization of P-NBD in SKBR3 cells was determined using fluorescence confocal microscopy, employing various commercially available organelle-selective trackers. **Figure 4.8d** shows that the fluorescence image of activated P-NBD exhibits a substantial overlap with that of a commercially available mitochondrial tracking dye, Mito Tracker Green FM, yielding a high Pearson Correlation coefficient (PC) of 0.95. In contrast,

poorer overlaps were observed with Lyso-Tracker, resulting in PC coefficients of 0.45 (Figure 4.8 d). These findings provide support for the hypothesis that P-NBD localizes and becomes activated within the mitochondria, likely due to the presence of a cationic centre that facilitates its specific targeting to this organelle. To further confirm the mitochondrial localization of P-NBD, an ICPMS analysis was conducted. The treated cells were isolated, and their mitochondrial, cytosolic, and nuclear fractions were separated, lysed, and subjected to ICPMS analysis. The results clearly demonstrated a significant elevation in iridium content in the mitochondrial fraction compared to the cytosolic and nuclear portions, unequivocally confirming the preferential accumulation of the molecule within the mitochondria (Figure 4.8 e).

4.25 Modulation of Glycolytic Metabolism in SKBR3 Cells through Endogenous H₂S Depletion using P-NBD Treatment

The activation of P-NBD by H₂S leads to a decline in intracellular H₂S levels, resulting in the inhibition of cellular energy production. To confirm this H₂S depletion effect, solution state measurements were conducted using the well-established DTNB assay. The introduction of 100 μ M Na₂S effectively neutralized the peak of DTNB at 324 nm, leading to the appearance of a new peak at 412 nm, indicating the formation of the nitro thiophenol moiety. Subsequent incubation of 100 μ M Na₂S with varying concentrations of P-NBD, followed by the addition of DTNB, showed a diminished attenuation of the 324 nm peak, suggesting reduced availability of Na₂S to facilitate depletion.

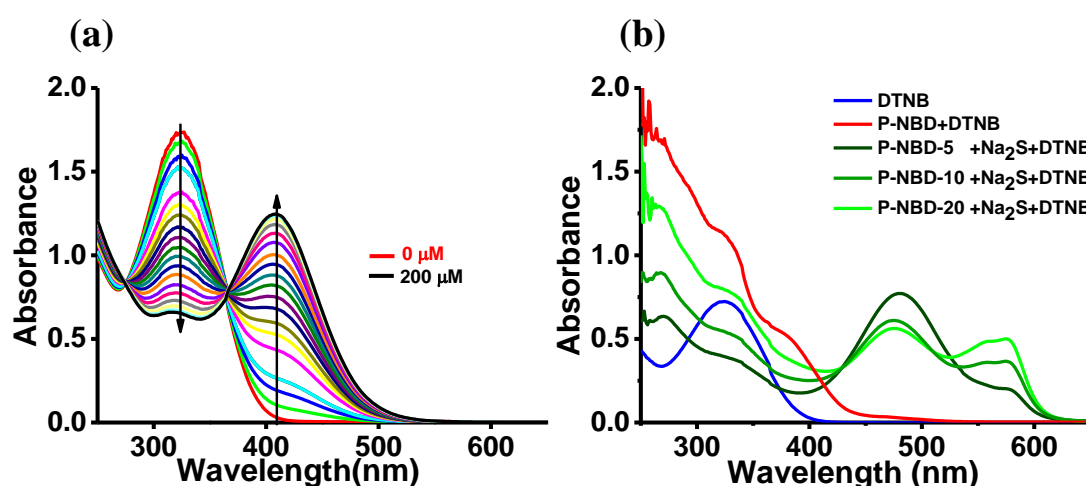


Figure 4.9: (a) Absorption spectra of DTNB with different concentration of Na₂S as the sulphide source ZnCl₂ based studies. (b) The absorption spectra of DTNB treated with reaction mixtures of different concentrations of P-NBD and 200 μ M H₂S.

Concurrently, the new 412 nm peaks displayed a slight red shift to 450 nm and reduced intensity, signifying a decrease in Na_2S concentration. These observations clearly support the occurrence of an interaction between Na_2S and P-NBD, which contributes to the reduction in Na_2S concentration. The visual confirmation of this interaction was evident through the colour transformation of the DTNB solution from deep yellow to dark orange upon incubation with P-NBD-treated samples. This orange colour arises from the combination of the cleaved thiol portion from P-NBD (displaying a pink-coloured NBD-SH) and DTNB (exhibiting a yellow-coloured nitro thiophenol), providing a readily observable method to validate the activity of the molecule. Importantly, neither P-NBD alone nor its combination with DTNB elicited any noticeable colour change, underscoring the molecule's specificity in depleting H_2S (**Figure 4.9**). These findings underscore the potential of the molecule as a promising candidate for modulating cellular H_2S levels and its impact on energy production. In the cellular environment, we conducted experiments to confirm the impact of P-NBD on the levels of H_2S . To do this, we incubated cells with 0, 10, 20 and 50 μM concentrations of P-NBD and measured the amount of residual H_2S using the methylene blue assay, a well-established method.

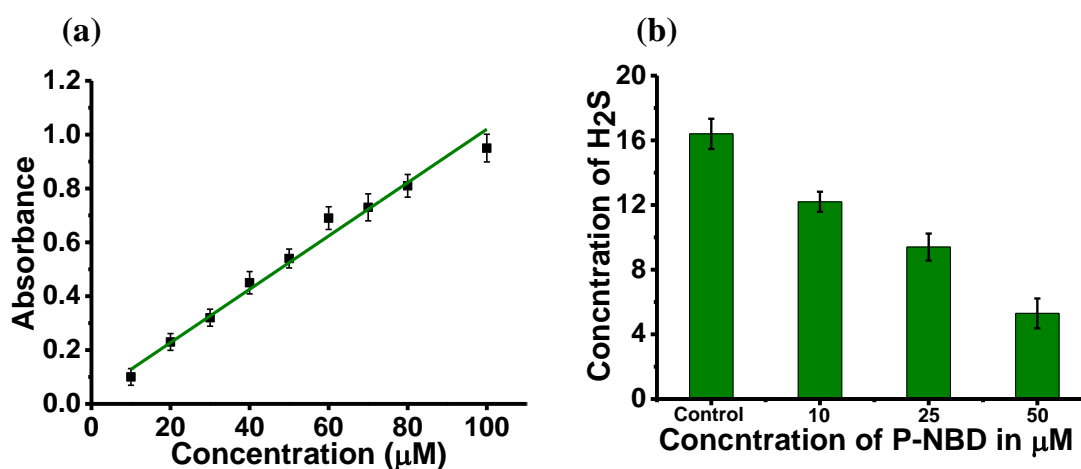


Figure 4.10: (a) The concentration dependent linear plot of methylene blue assay for H_2S estimation. (b) The intracellular H_2S depletion from SKBR-3 cells after treating with different concentrations of P-NBD.

Remarkably, compared to the control cells, the group treated with different concentrations of P-NBD exhibited a significant and sharp reduction in the H_2S levels. This validation clearly demonstrates the potent capability of P-NBD to effectively deplete H_2S in the cellular milieu (**Figure 4.10**). Further, explored the impact of depleting endogenous H_2S using P-NBD on the glycolysis of SKBR3 cells. Our findings revealed that the treatment with various concentrations of P-NBD led to a concentration-dependent inhibition of

GAPDH activity, a key enzyme involved in glycolysis. These compelling findings collectively demonstrate that P-NBD-induced H₂S depletion can adversely affect mitochondrial function and glycolysis in SKBR3 cells, leading to a significant suppression of cell proliferation leading to induce an enhanced effect during the therapy stage.

4.26 Activatable Photodynamic effect of P-NBD and singlet oxygen generation

Motivated by the promising outcomes illustrated above, our exploration focused deeper into the photodynamic effect of P-NBD in conjunction with the singlet oxygen (¹O₂) sensor DPBF under controlled in vitro conditions. Initially, we investigated the alterations in DPBF's absorption behaviour in response to P-NBD, both in the presence and absence of Na₂S, while subjecting them to laser irradiation at 532 nm with an intensity of 50 mW/cm² over a defined time span. In scenarios where Na₂S was absent, minor fluctuations in absorption intensities at 415 nm were observed, indicative of negligible ¹O₂ production. However, a distinct transformation occurred when Na₂S was introduced (**Figure 4.11 a&b**).

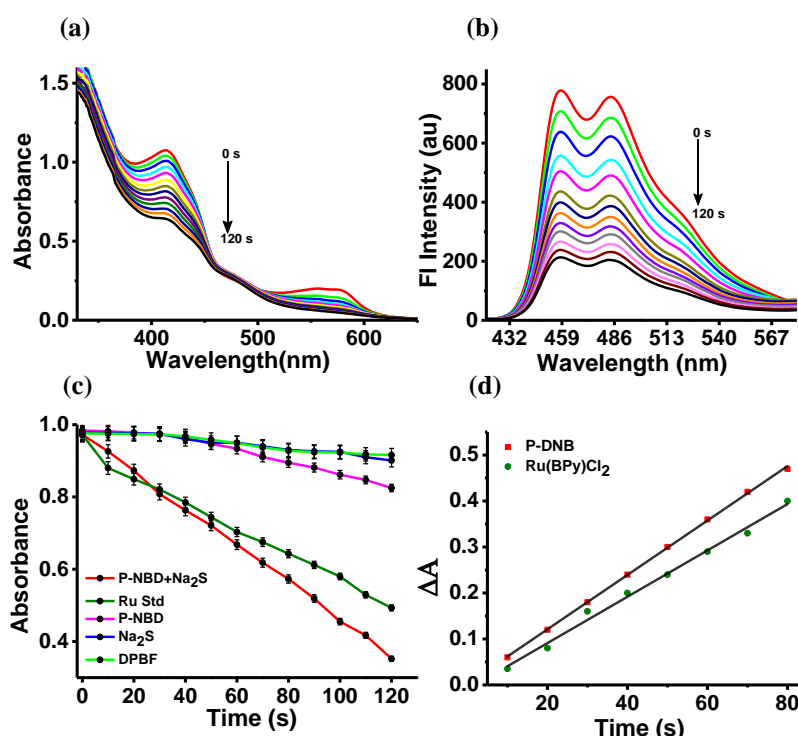


Figure 4.11: (a) Singlet oxygen generation capability of P-NBD with 100 μ M H₂S using the absorbance changes of DPBF at 410 nm from 0 to 120 seconds and the (b) corresponding emission spectrum. (c) Comparative depletion of DPBF absorbance with other combinations. (d) Linear plot for singlet oxygen quantum yield of QAIC+NADH with [Ru(Bpy)₃]Cl₂.

The absorption intensities exhibited a remarkable reduction over a 120-second timeframe, establishing a evident correlation with the presence of Na₂S whereas other combinations were unable to produce the effect due to their inactive state (**Figure 4.11 c**), thus unveiling

a notable singlet oxygen quantum yield of 0.76 (**Figure 4.11 d**) on compare to standard molecule $[\text{Ru}(\text{Bpy})_3]\text{Cl}_2$. The foregoing outcome distinctly elucidated the molecule's notably elevated singlet oxygen quantum yield following activation, in stark contrast to the instances involving DPBF alone with laser irradiation, Na_2S alone with laser irradiation, and other experimental cohorts exhibiting either negligible or exceedingly minimal quantum yields in the generation of singlet oxygen. To substantiate the engagement of singlet oxygen in the process during laser irradiation, we enlisted the aid of the renowned singlet oxygen sensor molecule SOSG (Singlet Oxygen Sensor Green). Employing fluorescence spectroscopy, we assessed the response of a $5\ \mu\text{M}$ SOSG solution under various conditions involving laser exposure. Strikingly, the combination featuring P-NBD, Na_2S , and laser irradiation demonstrated the rekindling of quenched SOSG fluorescence (**Figure 4.12 a**). This strongly indicated the initiation of P-NBD prompted by H_2S . In pursuit of an independent validation of our findings, we adopted a direct approach to affirm singlet oxygen generation.

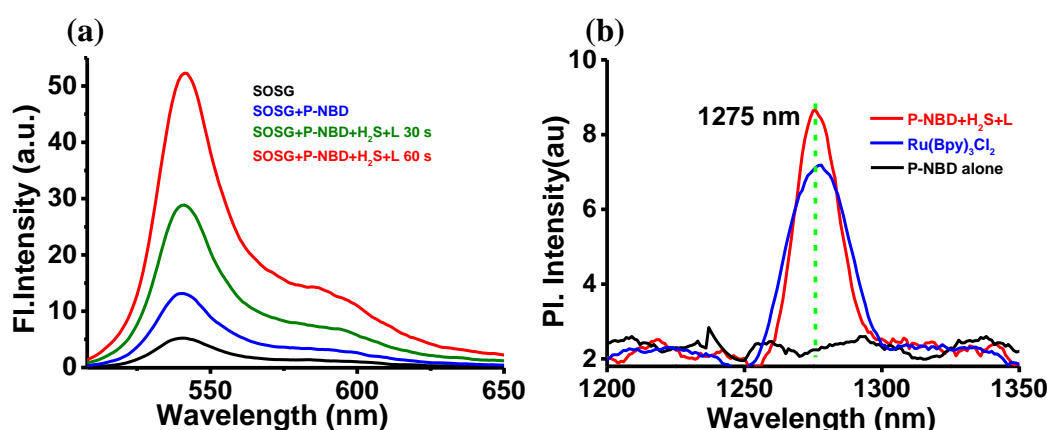


Figure 4.12: (a) Singlet oxygen generation capability of P-NBD with $100\ \mu\text{M}$ H_2S using the emission changes of SOSG. (b) The singlet oxygen generation of activated PS confirmed with direct method, The singlet oxygen phosphorescence measurement at 1275nm.

By employing NIR phosphorescent measurements, we were able to discern the inherent singlet oxygen phosphorescence at 1275 nm emanating from the P-NBD and Na_2S composite when exposed to 532 nm laser light (**Figure 4.12b**). This distinctive signal was meticulously compared against the recognized benchmark molecule $[\text{Ru}(\text{Bpy})_3]\text{Cl}_2$. In essence, our comprehensive investigation underscores the synergistic effect between P-NBD and Na_2S , their proficient induction of singlet oxygen generation, and the unequivocal involvement of this reactive oxygen species in our experimental conditions. Subsequently, we conducted a more in-depth assessment of the photodynamic effects of P-NBD within the live SKBR3 cells. To gauge the levels of intracellular singlet oxygen ($^1\text{O}_2$), we

employed SOSG, a widely recognized scavenger designed to selectively respond to singlet oxygen activation. The outcomes were observed across various cell groups subjected to distinct treatments. Illustrated in **Figure 4.13a**, upon exposure to P-NBD followed by 532 nm laser irradiation, a notably intensified green fluorescence emerged within the SKBR3 cells. This fluorescence vividly confirmed the generation of singlet oxygen within the cellular environment.

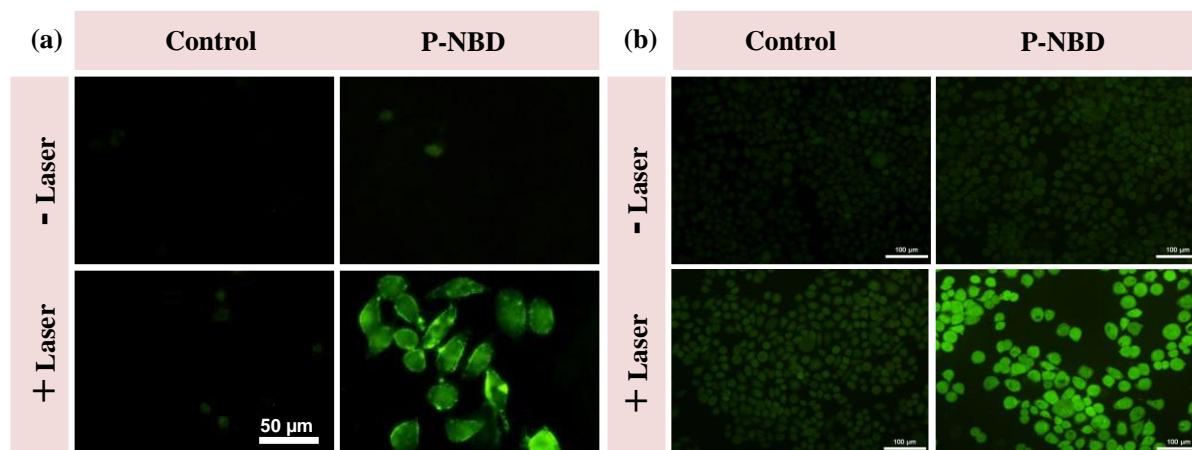


Figure 4.13: (a) Fluorescence imaging of SKBR-3 cells with SOSG to confirm the Singlet oxygen generation capability of P-NBD in cells. (b) The ROS generation of the molecule using DCF-DA assay.

Furthermore, the elevation in reactive oxygen species (ROS) generation was confirmed using 2,7-dichlorodihydrofluorescein diacetate (DCFH-DA), a molecule devoid of fluorescence that can permeate cell membranes and subsequently undergo oxidation by ROS, giving rise to a distinguishable green-fluorescent DCF. As depicted in **Figure 4.13b**, subsequent to P-NBD treatment and 660 nm irradiation, the SKBR3 cells exhibited markedly more potent green fluorescence in comparison to other treatment combinations. This outcome conclusively affirmed the excessive ROS production during the photodynamic therapy (PDT) process.

4.27 Establishing the apoptotic potential of activated P-NBD in the cellular milieu

The assessment of the apoptotic capability of activatable PDT was conducted utilizing various biological assays. Activation of the PDT was achieved by subsequent laser irradiation, revealing the molecule's PDT efficacy. This intervention notably induced a substantial decline in the cellular population when compared to control cells. To substantiate this effect, we performed the MTT assay both with and without laser assistance. The molecule exhibited potent toxicity in a concentration-dependent manner under 532 nm laser exposure (for 2 minutes), resulting in approximately 70% suppression

of cell proliferation in comparison to the control group. To validate and visualize the apoptotic potential of the P-NBD molecule, we executed live-dead assays (**Figure 4.14 a&b**).

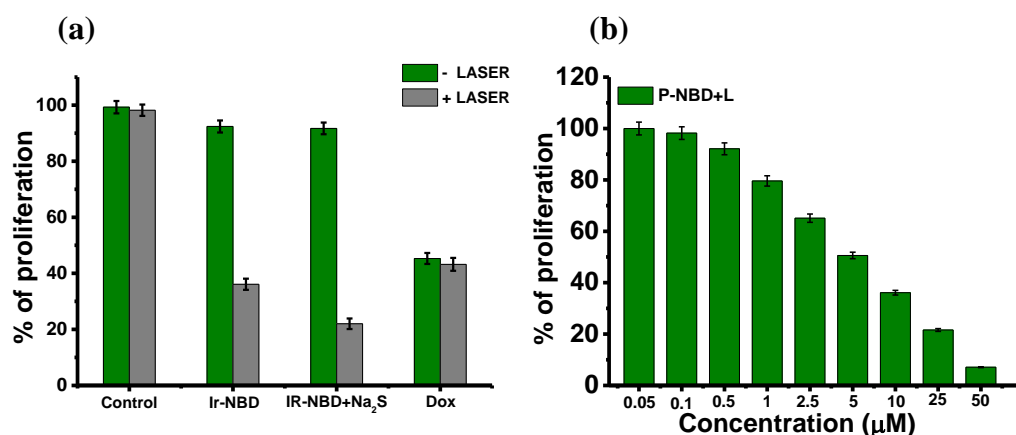


Figure 4.14: (a) MTT assay of the SKBR-3 cells with and without laser after incubating with P-NBD. (b) Dose dependent MTT assay on SKBR-3 cells after incubating with P-NBD and laser irradiation.

Typically, during the early stages of apoptosis, cell membrane integrity is compromised, permitting the passage of specific impermeable molecules. These marker molecules aid in discerning between live and dead cells. Initially, the loss of membrane integrity was assessed using trypan blue staining, which revealed a prominent dark blue staining in the P-NBD treated group following laser irradiation, substantiating this point (**Figure 4.15a**).

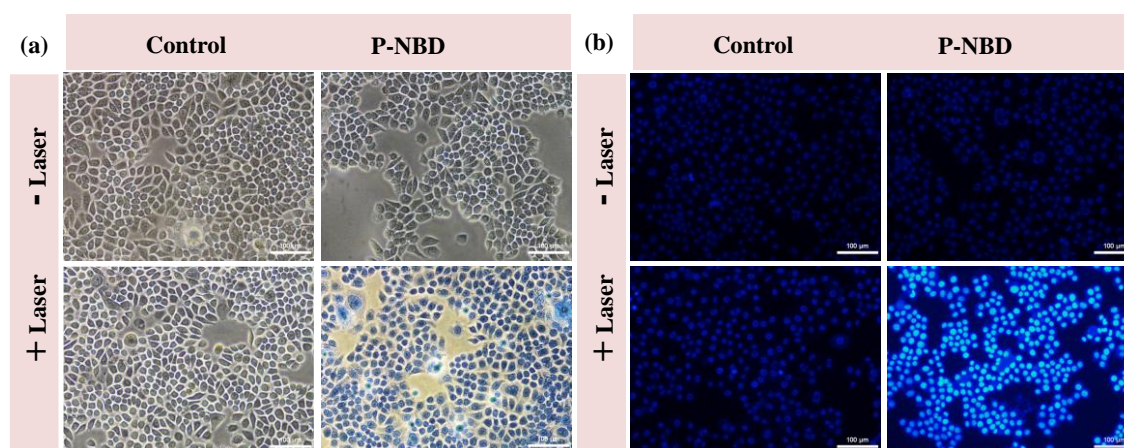


Figure 4.15: (a) Trypan blue staining to confirm the loss of membrane integrity during apoptosis. (b) The nuclear damage associated with apoptosis with Hoechst staining in the fluorescent platform.

The verification of nuclear DNA damage associated with PDT was achieved through Hoechst staining clearly indicated the damaged nucleus with bright blue fluorescence (**Figure 4.15b**). Furthermore, to assess the apoptotic potential of the probe molecule, we employed the Acridine Orange/Propidium Iodide live-dead staining technique on a

fluorescent platform. Activation of P-NBD led to a complete disruption of membrane integrity, resulting in intense orange fluorescence, indicative of late-stage apoptosis (Figure 4.16a). In contrast, both the control group and the laser-treated control group exhibited green labeling due to the presence of viable cells. In a non-fluorescent context, the APO percentage staining assay was carried out to capture the same phenomenon. The APO dye specifically entered deceased cells, imparting a pink coloration. The vivid pink hue observed in the group treated with P-NBD followed by laser irradiation further confirmed this process (Figure 4.16b). Collectively, these findings provide robust evidence for the potential of H₂S-activated PDT as demonstrated by the P-NBD probe molecule.

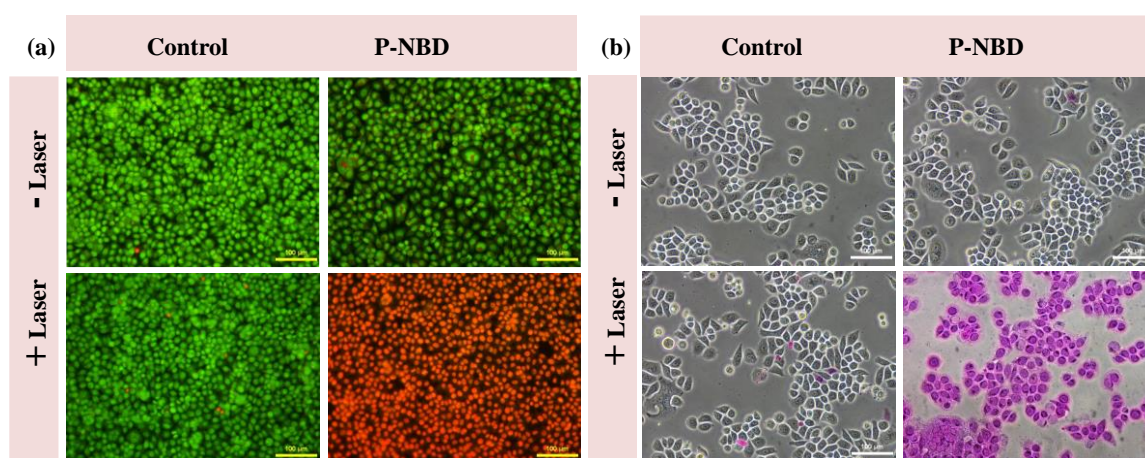


Figure 4.16: (a) Apoptotic evaluation in fluorescent platform using AO/EtBr live dead assay. (b) The evaluation of apoptosis in nonfluorescent platform using APOPercentage assay.

The highly localized photodynamic therapy (PDT) effect took place within the mitochondria due to the selective accumulation of the P-NBD compound in this cellular compartment. This occurrence resulted in a significant disruption of the mitochondrial membrane potential, ultimately leading to depolarization. To assess this phenomenon, the JC-1 dye, a well-established marker, was utilized. In this experimental process, SKBR3 cells were exposed to 10 μ M of P-NBD for approximately 24 hours, followed by conducting the JC-1 assay. The outcomes presented in Figure 4.17 revealed that untreated SKBR3 cells emitted strong red fluorescence, indicative of the presence of JC-1 aggregates within their mitochondria, suggesting the organelles' healthy state. In contrast, cells treated with P-NBD and subsequently subjected to laser irradiation exhibited distinct green fluorescence, signifying the existence of JC-1 monomers. The depolarization process led to reduced accumulation of JC-1 dye, causing it to exist in a non-aggregated, green-emitting state (Figure 4.17). These observations collectively provide strong evidence that the P-NBD

probe effectively triggers a photodynamic response when exposed to H₂S, resulting in the targeted eradication of breast cancer cells upon illumination with light.

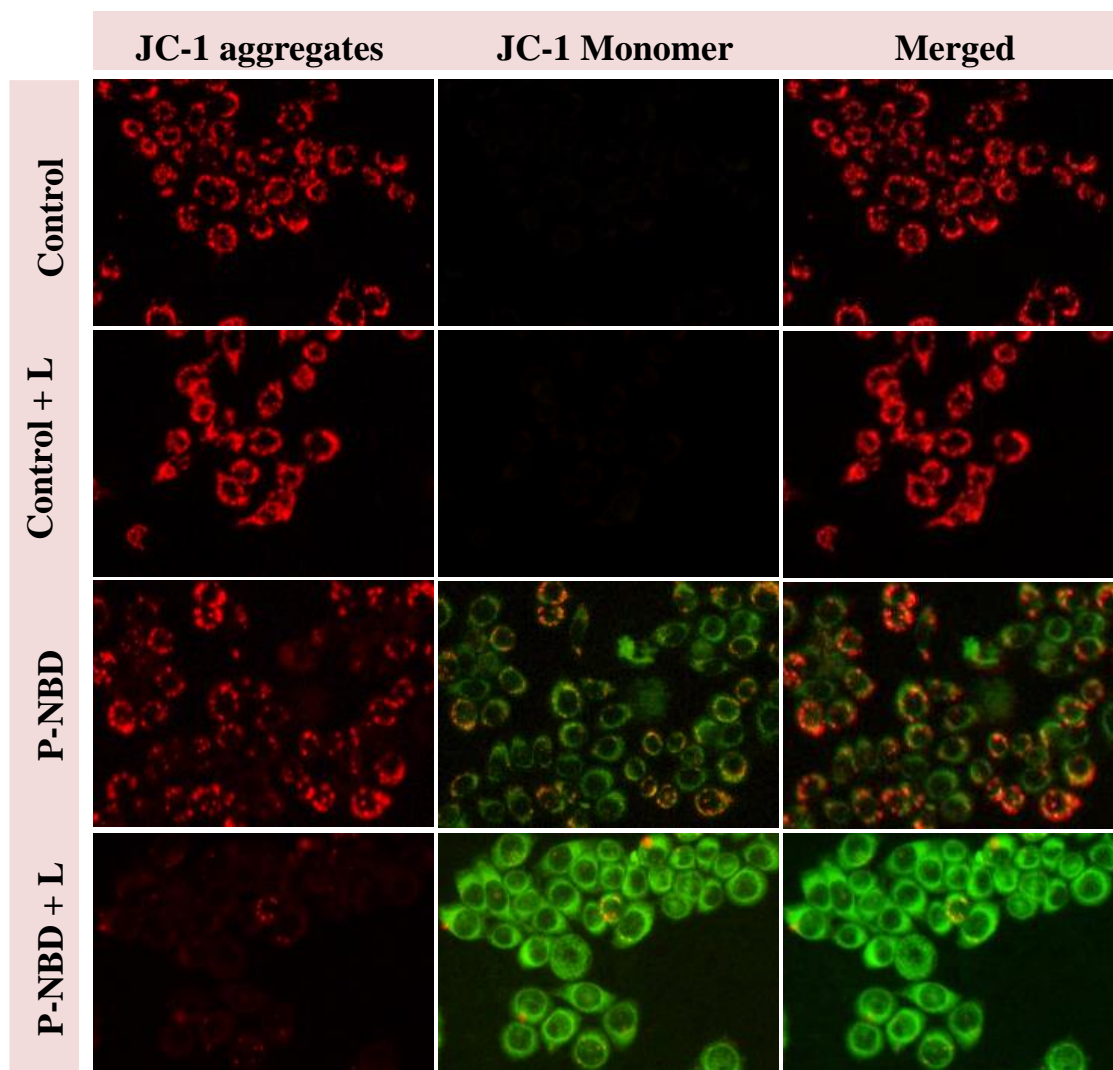


Figure 4.17: JC-1 assay for confirming the mitochondrial membrane depolarization after treatment with P-NBD followed by laser irradiation.

To validate the occurrence of mitochondrial depolarization, the TMRM assay was employed. The reduction in TMRM fluorescence in P-NBD treated samples exposed to laser light, as compared to other groups, distinctly indicates mitochondrial depolarization associated with PDT (**Figure 4.18a**). Furthermore, to confirm the involvement of the intrinsic apoptotic pathway and the role of mitochondria in apoptosis, the levels of caspases were analyzed. The increased expression of caspase 3 and 9 in the treated samples, as opposed to the control, strongly supports the notion of mitochondria-mediated intrinsic apoptotic pathway activation (**Figure 4.18b**).

Apoptotic changes become noticeable when phosphatidylserine is exposed on the outer layer of the cell's plasma membrane. To evaluate the distribution of cells at various stages

of cell death (early apoptosis, late apoptosis, or necrosis) based on phosphatidylserine exposure, an Annexin V apoptotic assay was executed. This assay involved co-staining annexin-FITC with PI, providing a clear insight into the extent and type of apoptosis. Notably, in the P-NBD laser combination, a distinct 68% of cells were found in the late apoptosis stage, undeniably confirming the activated PDT's apoptotic potential. In contrast, other combinations produced mostly healthy cells with minimal apoptosis (**Figure 4.18c**).

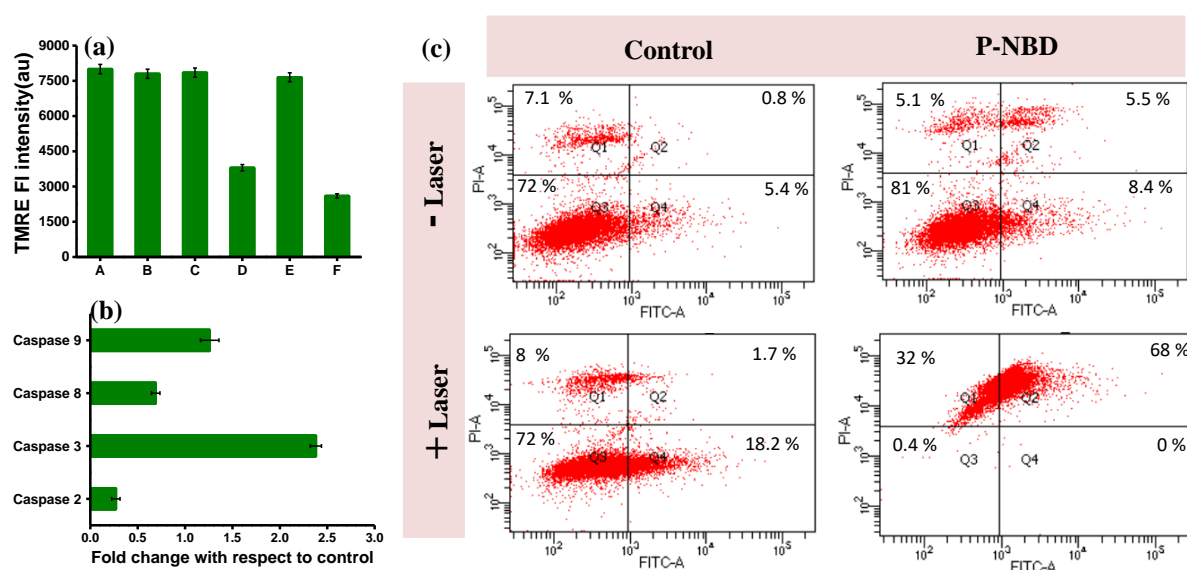


Figure 4.18: (a) The evaluation of mitochondrial membrane potential using TMRM assay. (b) Caspase assay to confirm the mitochondria-mediated apoptosis. (c) Extent of apoptosis and quantification with flowcytometric analysis (Annexin V assay).

4.28 SERS tracking of apoptotic events in the cellular milieu

SERS holds promise in monitoring cellular apoptosis through the detection of vibrational shifts associated with fundamental and altered cellular molecules. Throughout the apoptosis process, key biomolecules such as proteins, DNA, and specialized compounds like cytochromes exhibit noticeable modifications in their vibrational patterns due to structural alterations. These variations have been effectively identified and quantified by contrasting them against control specimens. The distinct visualization of cellular morphology resulting from apoptosis becomes readily comprehensible through the utilization of SERS imaging on SKBR3 cells subjected to P-NBD treatment, succeeded by PDT. In comparison to the cellular configuration of the control group, conspicuous apoptotic characteristics such as membrane blebbing and perturbed cell membrane integrity manifest prominently within the images, meticulously delineated by the assistance of the 1328 cm^{-1} spectral peak. The

average spectra originating from the treated and control specimens also unveil marked differentials in apoptotic progression, concomitant with the discernible NBS-SH peak. The application of cluster mapping to these cellular entities further elucidates the apoptotic attributes, fortifying the validity of the initial observations (**Figure 4.19a**).

To further evaluate the occurrence of apoptosis resulting from PDT, we conducted an in-depth analysis using Raman spectroscopy to observe distinct changes in the spectral characteristics of specific biomolecules. The induction of programmed cell death triggers noticeable alterations in the spectral patterns of proteins and DNA when compared to their normal states. Notably, a prominent indicator of apoptosis is DNA fragmentation, where the DNA molecule's phosphate backbone becomes disrupted, intensifying the N7-H vibrations on the nucleic bases. Following the administration of P-NBD and subsequent PDT, a comparative examination of Raman signatures before and after the therapy revealed significant peaks. The presence of peaks at 1476 cm^{-1} , indicating damaged DNA backbone, and the increased intensity of N7-H vibrations from nucleic bases at 1585 cm^{-1} strongly suggest an apoptotic nature in the observed sample (**Figure 4.19b**).

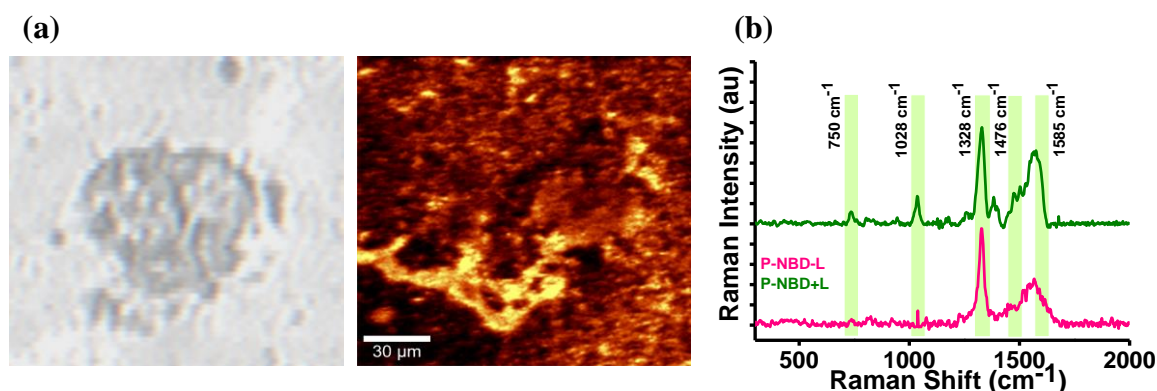


Figure 4.17: (a) Morphology changes associated with apoptosis tracked with SERS imaging of control and treated cells after laser irradiation. (b) Apoptotic features obtained from Raman spectra from the control and treated cells after laser irradiation.

These observations provide compelling evidence to support the occurrence of apoptotic cell death. Furthermore, the presence of a peak at 1028 cm^{-1} corresponds to the phenylalanine in degraded peptides and protein denaturation.³³ Importantly, these distinctive alterations were absent in the control groups. Furthermore, we traced the release of Cyt-C from the inner mitochondrial membrane to the cytoplasmic region using Surface-Enhanced Raman Spectroscopy (SERS). The presence of Cyt-C in the cytoplasmic space serves as a significant indicator of apoptosis.³⁴ The observed 750 cm^{-1} band in the Raman spectra originates from the core pyrrole vibration of Cyt-C. This signal exhibited a high intensity

exclusively in SKBR3 cells treated with P-NBD followed by PDT. In line with the intricate traditional in vitro assays for apoptosis, the SERS analysis introduces an additional method for validating these processes.

4.3 Conclusion

The design of the cyclometalated iridium complex P-NBD has resulted in a versatile activatable photosensitizer with precise control and functional adaptability. By integrating an electron-deficient NBD unit with a hydroxy-appended iridium complex, a harmonious molecular arrangement has been achieved. This design enables the photosensitizer to respond to hydrogen sulphide (H₂S) in specific environments, such as cancerous conditions, leading to its transformation and activation. This activation is marked by distinct changes in spectral characteristics, including turn-on emission and Surface-Enhanced Raman Scattering (SERS), allowing for sensitive detection. The strategic design not only ensures specificity but also provides a means for controlled therapeutic activation. In vitro, studies underscore the significant impact of P-NBD on cellular processes. Its fluorescence response triggered by H₂S and its targeted localization within mitochondria showcase its potential for precise therapeutic interventions, particularly in mitochondrial-focused treatments. The activation process disrupts the glycolytic activity of cancer cells through the selective depletion of H₂S, leading to reduced ATP production and an energy-depleted state that promotes apoptosis. The orchestrated interplay between P-NBD and H₂S ultimately leads to potent photodynamic effects. Through mitochondrial targeting, it triggers a cascade of events, including mitochondrial depolarization(Φ M), the release of Cyt-C, caspase activation, and exposure of phosphatidylserine, resulting in a pronounced apoptotic effect. SERS imaging provides detailed insights into these processes, enhancing our understanding. In conclusion, P-NBD's tailored synthesis, responsiveness, targeted action, and apoptotic effectiveness through activated PDT mark a paradigm shift in activatable photosensitizers, holding great promise for targeted therapeutic applications and warranting further investigation.

4.4 Experimental section

4.4.1 Materials and Methods

The reagents, such as 4-bromo-2,2'-bipyridine, 4-hydroxyphenylboronic acid, Potassium carbonate, TBAB, Pd(PPh₃)₄, IrCl₃·xH₂O, 2-phenyl pyridine, 2-methoxyethanol, methyl iodide, and diphenylisobenzofuran, were purchased from TCI Chemicals. Reagent-grade

solvents were obtained from local suppliers and were dried and distilled prior to use following standard procedures. ^1H NMR spectra were recorded at 25°C on a Bruker 500 MHz FT-NMR spectrometer, with chemical shifts (δ) and coupling constant (J) values reported in ppm and Hz, respectively. High-resolution mass spectra (HRMS) were obtained using a Thermo Scientific Exactive ESI-MS spectrophotometer. UV/vis spectra were acquired using a Shimadzu UV-2600 UV-Vis spectrophotometer, and emission spectra were recorded with a Fluoromax-4 Spectrofluorometer using a 1 cm quartz cuvette. All experiments were conducted at 298 K unless specified otherwise. Surface-enhanced Raman spectroscopy (SERS) experiments were performed using a WITec Raman microscope (WITec, Inc., Germany) equipped with a 600 g/mm grating and a Peltier-cooled charge-coupled device detector. Samples were excited using a 633 nm laser with a power of 10 mW, and the Raman spectra were collected in the range of 300 to 2000 cm^{-1} with a resolution of 1 cm^{-1} and an integration time of 1 s, averaging over 10 accumulations. Prior to each measurement, calibration was performed using a silicon standard with a Raman peak at 520 cm^{-1} . Data analysis was carried out using the WITec Project Plus (v5.2) software package. Excited state lifetimes were measured using a picosecond single-photon counting system (TCSPC) from Horiba, DeltaFlex.

4.4.2 Synthesis of 4-Hydroxy bipyridine ligand (compound 1)

4-bromo-2,2'-bipyridine (500 mg, 2.12 mmol) and 4-hydroxyphenylboronic acid (291 mg, 2.12 mmol) were dissolved in a mixture of 60 mL toluene and 10 mL 2 M aqueous potassium carbonate. To this TBAB (2.5 g, 6.36 mmol) in water (10 mL) was added. The mixture was stirred at room temperature for 30 minutes under Argon followed by adding $\text{Pd}(\text{PPh}_3)_4$ (0.020 g, 1.74×10^{-3} mmol) and then heated to 90°C for 24 h. After the completion of the reaction indicated by TLC, the mixture was poured into water and extracted three times with ethyl acetate. The organic layer was dried over anhydrous sodium sulphate. After removing the solvent under reduced pressure, the residue was chromatographed on a silica gel column with $\text{CHCl}_3:\text{CH}_3\text{OH}$ as eluent giving the compound as a pale-yellow solid. Yield: 68%.

^1H NMR (500 MHz, CD_3OD): δ 8.73 (s, 1H), 8.54 (d, $J = 4.5$ Hz, 1H), 8.21-8.20 (m, 2H), 8.00 – 7.98 (m, 1H), 7.85-7.80 (m, 1H), 7.47 (d, $J = 8.5$ Hz, 2H), 7.32 (t, $J = 6.5$ Hz, 1H), 6.82 (d, $J = 8.5$ Hz, 2H) ppm.

^{13}C NMR (125 MHz, CD_3OD): δ 158.0, 155.6, 153.4, 148.8, 146.5, 137.3, 136.8, 134.5, 128.0, 127.8, 123.7, 121.1, 115.7 ppm.

4.4.3 Synthesis of P-OH complex (compound 3)

The synthesis was started with the preparation of Ir dimer complex (Nonoyama, 1974), a solution of $\text{IrCl}_3 \cdot x\text{H}_2\text{O}$ (224.36 mg, 0.75 mmol) and 2-phenyl pyridine (350 mg, 1.58 mmol) in 2-methoxyethanol/ H_2O (3:1, v/v%) was refluxed at 90°C for 24 h, under argon atmosphere. After the reaction, the solution was cooled down to room temperature and poured into 50 mL of water. The precipitated yellow solid (compound 2), was filtered and washed with n-hexane (5 mL x 3) and cold diethyl ether (5 mL x 3). The next step was preceded without any further purification of the obtained crude product. A mixture of obtained dimer (250 mg, 0.1866 mmol) and compound 1 (207 mg, 0.48 mmol) in $\text{CH}_2\text{Cl}_2/\text{CH}_3\text{OH}$ (1:1, v/v%) was refluxed under an argon atmosphere for 12 h. Upon completion of the reaction, the solution was cooled down to room temperature and the solvent was removed under reduced pressure. The residue obtained was subjected to column chromatography in silica gel (100-200 mesh) column with chloroform/Methanol system, giving the intermediate compound as an orange solid. Yield 68%. **^1H NMR (500 MHz, DMSO- d_6):** δ 10.18 (brs, 1H), 8.89 (t, $J = 9.5$ Hz, 2H), 8.47 (d, $J = 8.5$ Hz, 1H), 8.27 (dd, $J_1 = 15.5$ Hz, $J_2 = 8$ Hz, 3H), 7.96 (s, 2H), 7.94 (d, $J = 5$ Hz, 3H), 7.88 (d, $J = 5$ Hz, 1H), 7.79 (d, $J = 5.5$ Hz, 1H), 7.67 (dd, $J_1 = 12.5$ Hz, $J_2 = 6.5$ Hz, 2H), 7.22 (d, $J = 8.5$ Hz, 2H), 7.19-7.15 (m, 2H), 7.09-7.02 (m, 2H), 6.97-6.91 (m, 2H), 6.85 (d, $J = 8.5$ Hz, 2H), 6.26 (t, $J = 8.5$ Hz, 2H) ppm.

^{13}C NMR (125 MHz, DMSO- d_6): δ 167.3, 159.4, 154.9, 152.8, 151.3, 150.9, 150.2, 149.7, 149.4, 146.8, 144.3, 140.1, 139.8, 139.3, 139.2, 136.2, 131.7, 131.6, 130.8, 130.7, 128.7, 128.4, 125.5, 125.3, 125.0, 124.5, 120.6, 116.8 ppm.

4.4.4 Synthesis of P-NBD molecule

The orange red Ir-OH (540 milligrams, 0.7207 millimoles, 1 equivalent) was dissolved in dimethylformamide (DMF) under a nitrogen (N_2) atmosphere, followed by the addition of diisopropylethylamine (DIPEA, 20 microliters, 2 equivalents) and stirring for 1-2 minutes. Subsequently, NBD-Cl (215 milligrams, 1.081 equivalents) was introduced into the solution, and the reaction was allowed to proceed for approximately 2-3 hours. After the reaction solvents were removed and the residue obtained was subjected to column chromatography in silica gel (100-200 mesh) column with chloroform/Methanol system, giving the intermediate compound as a red brown solid. Yield 89%

¹H NMR (500 MHz, DMSO-d₆): δ 8.98 (t, J = 9.5 Hz, 2H), 8.65 – 8.63 (m, 2H), 8.31 – 8.25 (m, 3H), 8.07 (s, 1H), 7.94 (d, J = 6.5 Hz, 3H), 7.90 (d, J = 7.5 Hz, 2H), 7.82 (d, J = 6 Hz, 1H), 7.73– 7.65 (m, 3H), 7.59 (s, 1H), 7.52 (d, J = 8 Hz, 1H), 7.35 (d, J = 8 Hz, 1H), 7.20 – 7.14 (m, 2H), 7.04 (t, J = 7.5 Hz, 1H), 6.91 (m, 3H), 6.77 (d, J = 8.5 Hz, 1H), 6.28 (d, J = 7 Hz, 1H), 6.22 (d, J = 7.5 Hz, 1H) ppm.

¹³C NMR (125 MHz, DMSO-d₆): δ 167.2, 155.4, 155.2, 154.2, 153.0, 151.0, 150.6, 150.4, 149.9, 149.4, 147.7, 145.8, 144.8, 144.4, 144.3, 140.2, 139.4, 139.2, 139.0, 138.4, 137.9, 137.4, 135.8, 132.4, 131.7, 131.6, 131.1, 130.7, 125.8, 125.6, 125.2, 124.6, 122.7, 122.4, 120.6, 120.5, 119.8, 110.8 ppm.

4.4.5 Measurement of preliminary photophysical properties.

In general, the UV-Vis absorption and emission spectra were obtained on a Shimadzu UV-2600 UV-Vis spectrophotometer and Fluoromax-4 Spectrofluorometer respectively. The excitation/emission slit width was set to 4 nm with medium scan speed. Stock solutions of the complex P-NBD were made in spectroscopic grade acetonitrile (1 mM) were used to prepare the working solutions acetonitrile:water mixture. Absorbance spectra were recorded from 300-700 nm while the emission spectra were from 490-750 nm. All the experiments were repeated three times to confirm the reproducibility of the results.

4.4.6 Activation of P-NBD with H₂S using UV-vis titration and Photoluminescence

To study how P-NBD responds to varying concentrations of H₂S, we prepared a 10 μM P-NBD solution in a mixture of acetonitrile and water (3:2 ratio) and incubated it at 37°C for 1 minute. We then exposed this solution to different concentrations of H₂S ranging from 0 to 100 μM. We measured the absorption of light in the wavelength range of 200 to 800 nm and the photoluminescence at 626 nm using an excitation wavelength of 475 nm and a slit width of 2 nm. To determine the limit of detection (LOD) for the complex in the fluorescent channel, we used the following formula: $LOD = 3\sigma/S$. Here, S represents the slope of the linear relationship between concentration and response, and σ is the standard deviation of the blank measurements.

4.4.7 Activation of P-NBD using SERS analysis

To investigate the interaction between P-NBD and H₂S using surface-enhanced Raman spectroscopy (SERS). Initially, a solution containing 2 μL of P-NBD at a concentration of 10 μM was then mixed with 18 μL of gold nanoparticles (AuNP) and allowed to incubate for approximately 2 minutes. During this incubation period, the molecules in the solution

interacted with the AuNP surface, setting the stage for subsequent SERS measurements. SERS spectra were recorded using a 633 nm laser for excitation, with the laser power set to 10 mW. Each measurement consisted of 5 accumulations, with a 5-second integration time for each accumulation. To assess the linear response of the P-NBD Probe to varying concentrations of H₂S, we prepared a 10 μM solution of the Probe in a buffer solution. This solution was then subjected to a 2-minute incubation at a controlled temperature of 37°C in the presence of different Na₂S concentrations, ranging from 0 to 100 μM. Following the incubation period, 2 μL aliquots of the resulting samples were mixed with 18 μL of highly concentrated AuNP. Subsequently, measured the SERS signals from these mixtures using the same laser excitation conditions and accumulation settings mentioned earlier.

4.4.8 Mass spectroscopic proof of H₂S aided activation

P-NBD and H₂S were mixed in acetonitrile and incubated for 2 minutes. Subsequently, HRMS analysis was performed, and the peak of P-NBD at 912.19 was transformed into the peak corresponding to 749.19, indicating the presence of the product P-OH.

4.4.9 Stability and selectivity

The stability of P-NBD was assessed through UV/Vis spectroscopy by monitoring freshly prepared 10 μM solutions of P-NBD in both acetonitrile and water over a 24-hour period. Additionally, the photostability of a 10 μM P-NBD solution in acetonitrile was evaluated by subjecting it to irradiation with a 475 nm long pass LASER at 37°C, with UV/Vis absorption measurements taken over the course of 1 hour to confirm its resistance to photodegradation. Furthermore, the selectivity of the iridium complex P-NBD towards various reactive analytes was investigated. This involved treating different species (with glutathione (GSH) concentration set at 1 mM) with 10 μM of P-NBD and incubating them for 2 hours at 37°C. Subsequently, the corresponding photoluminescence at 565 nm was measured using an excitation wavelength of 475 nm and a slit width of 4 nm. These experiments provided valuable insights into the stability, photostability, and selectivity of P-NBD, offering crucial information for its potential applications.

4.4.10 Singlet oxygen generation studies

The study aimed to assess singlet oxygen generation in solutions of P-NBD and P-NBD incubated with H₂S in acetonitrile. This assessment was conducted by utilizing 1,3-diphenylisobenzofuran (DPBF) as a singlet oxygen scavenger. The total concentration ratio of Ir(III) complexes to DPBF was set at 1:10, and the samples were irradiated using a 475

nm long-pass LASER. Singlet oxygen, when generated, induced the photo-oxidation of DPBF, causing a disruption in its conjugation, resulting in a decrease in its absorbance at 410 nm, while leaving the absorption of the complex unaffected. These changes in absorbance were monitored every 10 seconds. The quantum yields for singlet oxygen ($^1\text{O}_2$) production by the P-NBD and P-NBD+H₂S complexes under irradiation in acetonitrile were determined using a steady-state method. The absorption change of DPBF served as the indicator for $^1\text{O}_2$, and [Ru(bpy)₃]Cl₂ was used as the standard (with a known quantum yield of 0.57 in acetonitrile). This evaluation was carried out using the following equation:

$$\phi_c = \phi_s(S_c \times F_s / S_s \times F_c)$$

In this equation, the subscripts ϕ_c and ϕ_s denote the singlet oxygen quantum yield of the complex and [Ru(bpy)₃]Cl₂, respectively. S represents the slope obtained from plots of the absorbance of DPBF at 410 nm against the irradiation time for both the complex and the standard. F represents the absorption correction factor for the complex and standard, calculated as $F = 1 - 10^{(-\text{OD})}$, where OD represents the optical density of the complex and [Ru(bpy)₃]Cl₂ at 475 nm.

4.4.11 Singlet oxygen generation studies of H₂S

To ascertain the limited capability of H₂S in the generation of singlet oxygen upon activation by a 475 nm laser, we conducted an experiment involving the exposure of a 10 μM H₂S solution to DPBF (1,3-diphenylisobenzofuran) and monitored the spectral characteristics over a time span ranging from 0 to 180 seconds.

4.4.12 Photostability study of DPBF up on LASER

The photo inertness of DPBF up on 475 nm LASER trigger was screened by checking the spectral parameters (absorption and emission) of the compound under light illumination from 0 to 5 minutes.

4.4.13 Singlet oxygen generation study using SOSG

To assess the production of singlet oxygen when activated P-NBD and P-NBD are in a solution state, we combined a 5 μM solution of P-NBD with H₂S and a 5 μM solution of P-NBD in acetonitrile. Subsequently, we introduced 10 μM of singlet oxygen sensor green into the mixture and exposed it to irradiation using a 475 nm long-pass LASER. The resulting photoluminescence emitted by SOSG at 525 nm was quantified for analysis.

4.4.14 Singlet oxygen generation study using Oxygen phosphorescence

Approximately 10 μM of P-NBD and P-NBD incubated with H_2S were dissolved in acetonitrile, followed by their excitation at 532 nm via laser irradiation. Subsequently, the samples were promptly subjected to analysis of oxygen phosphorescence at 1275 nm utilizing a spectrofluorometer.

4.4.15 Time Correlated Single Photon Counting (TCSPC) analysis for excited state lifetime.

The excited state lifetime of P-NBD before and after the reaction with H_2S in the presence and absence of oxygen was measured. Briefly, a solution of P-NBD and P-NBD incubated with H_2S in acetonitrile was analyzed using TCSPC with IRF as the standard (excitation wavelength 510 nm, time range 3.2 μs , energy 250 KHz)

4.4.16 Cell culture methods

The human breast cancer cell line SKBR-3 was obtained from American Type Culture Collection (ATCC, Manassas, VA, USA). Cells were maintained in Dulbecco's modified Eagle medium (DMEM) with 10% fetal bovine serum and 5% CO_2 at 37 $^\circ\text{C}$. Cells were cultured in glass-bottom, 96-well black plates, T-25 flasks, T-75 flasks, and 4-well chamber slides for various experiments 2 days prior to the conduction of experiments. All the experiments were performed in triplicate for accurate results.

4.4.17 Evaluation of cytotoxicity using MTT assay

MTT assay is based on the cleavage of a MTT (3-(4,5-dimethylthiazol-2-yl)-2,5-diphenyltetrazolium bromide) by mitochondrial dehydrogenases in viable cells. Quantities of 100 μL of the cell suspension of 1×10^4 cells/well were seeded in a 96-well plate and incubated at 37 $^\circ\text{C}$ for 24 h in a CO_2 incubator. After the incubation cells were washed with 100 μL of PBS buffer (pH 7.4). The compound under investigation were diluted in plane DMEM media to a concentration 0 to 100 μM . Then 100 μL of each compound under investigation along with positive control (1 μM doxorubicin) was similarly added to the appropriate wells. The plates were then incubated for 24 and 48 h in a CO_2 incubator at 37 $^\circ\text{C}$. After incubation, 100 μL MTT (0.5 mg/mL) was added to each well and incubation was continued for an additional 2 to 4 h. The insoluble formazan crystals formed were solubilized by the addition of 100 μL DMSO followed by an incubation of 30 min and the absorbance was measured at 570 nm using a microplate spectrophotometer (BioTek, Power Wave XS).

The proliferation rate was calculated as : % Proliferation = (A_{sample} / A_{control})x 100

The Inhibition rate was calculated as : % Inhibition = 100 - % Proliferation

4.4.18 ICP-MS Analysis of iridium content

The cellular uptake capacity of the complexes was measured by determination of intracellular iridium contents through ICP-MS, Briefly, cells were seeded into 6 well plate for 24 h. The medium was removed and replaced with medium/DMSO (v/v, 99:1) containing P-NBD (10,25,50,75 and 100 μ M). After 2 h incubation, the cells were trypsinized, collected in PBS (3 mL) and counted. The cells were pelletized and lysed in radio immunoprecipitation assay (RIPA) Buffer. HNO₃ (65%, 1 mL) was added to the lysates of the whole cell and the mixture was incubated at room temperature for 24 h to digest entirely. The solution was then diluted to a final volume of 10 mL with Milli-Q water. The same experiment was repeated in time dependent manner by varying the incubation time from 15 minutes to 2 h. Finally, the

4.4.19 Endogenous H₂S stimulated live cell imaging via fluorescence

SKBR-3 cells were seeded into 96 well plate and treated with 10 μ M concentration of P-NBD incubated at 37⁰C with different time period. After required incubation time the cells were washed with PBS and time dependent fluorescence images were taken from 0 to 60 minutes.

4.4.20 Endogenous H₂S stimulated live cell imaging via SERS

Cells were cultured in 16 well chamber slide made of glass at a seeding density of 7 x 10³ cells /well. Cells were incubated with P-NBD followed by AuNP and time dependent SERS spectral mapping was carried out using confocal Raman microscope (alpha300R, WITec Inc. Germany) with a laser beam directed to the sample through 20X objective and a Peltier cooled CCD detector. For this, can range was given as 50 μ m X 50 μ m with 100 X 100 pixel. The sample was excited by a power of 10 mW from 633 nm laser and mapping was done based on 1328 cm⁻¹ peak using 600 g/mm grating. Integration time was fixed as 0.05 s and the intensity-modulated images were prepared by image processing option in control 5.2 software. A minimum of three independent measurements were made for each sample.

4.4.21 Action of exogenous H₂S

SKBR-3 cells were seeded into 96 well plate and treated with 10 μ M concentration of P-NBD and incubated at 37⁰C for 45 minutes. After the incubation cells were washed with

PBS and added fresh media followed by different concentrations of H₂S (10 and 20 μM) and incubated for 40 minutes. Washed with PBS and fluorescence images were taken using green filter.

4.4.22 Aminoxy acetic acid dependent study

SKBR-3 cells were incubated with different concentrations of aminoxy acetic acid (10 and 20 μM) for 60 minutes followed by 10 μM of P-NBD at 37°C for 45 minutes, washed with PBS and fluorescence images were taken.

4.4.23 ZnCl₂ and NEM dependent study

SKBR-3 cells were seeded into 96 well plate and incubated with varying concentrations of ZnCl₂ (10 and 20 μM) for 60 minutes followed by treating with 10 μM of P-NBD and incubated at 37°C for 45 minutes. After the incubation cells were washed with PBS and images were taken. The same procedure was repeated in case of NEM also (incubation time 30 minutes).

4.4.24 Phototoxicity of P-NBD via MTT assay

SKBR-3 human liver cancer cells were seeded into 96 well plates and incubated for 24 h (at 37 °C 5% CO₂). After the incubation cells were treated with varying concentrations of P-NBD (0.1-100 μM) for 12 h., MTT (0.5 mg /ml) was added to each well and kept at 37°C for 4 h, and finally the so formed formazan crystals were dissolved in DMSO and the OD was measured at 570 nm using a microplate reader. To validate the photodynamic effect SKBR-3 human liver cancer cells were seeded into 96 well plates and incubated for 24 h (at 37 °C 5% CO₂) at normoxic (20% O₂) and hypoxic (1% O₂) conditions. After the incubation cells were treated with 25 μM of P-NBD followed by irradiation of 532nm LASER for 5 minutes. After 12 h incubation, MTT (0.5 mg /ml) was added to each well and kept at 37°C for 4 h and finally, the so formed formazan crystals were dissolved in DMSO and the OD was measured at 570 nm using a microplate reader.

4.4.25 Intracellular ROS generation by DCFDA assay

The DCFDA assay is a method used to measure oxidative stress by observing the conversion of 2',7'-dichlorofluorescein diacetate (DCFDA) into the fluorescent compound 2',7'-dichlorofluorescein (DCF) in the presence of reactive oxygen species. To perform this assay, SKBR-3 cells (1 x 10⁵) were initially plated onto a 96-well plate and allowed to grow overnight. Following this, the cells were rinsed and exposed to 10 μM P-NBD and

incubate for 2h. After another wash step, the cells were irradiated with 532 nm laser followed by treated with 10 μ M DCFDA reagent. Subsequently, the cells were washed again, and fluorescence imaging experiments were conducted using an inverted fluorescence microscope. Images were captured within the 500-540 nm range, with an excitation wavelength of 485 nm.

4.4.26 Mitochondrial Membrane Potential Assay

The mitochondrial membrane depolarization was analysed using TMRM mitochondrial membrane potential assay in which a lipophilic, cationic dye that accumulates in the negatively charged mitochondrial matrix is utilized. The SKBR-3 cells were plated onto 12-well plates (1 \times 10⁵ cells/well) on a 5% CO₂ incubator at 37°C. When the cells attained almost 70% confluency, they were subjected to 10 μ M P-NBD treatment followed by laser irradiation for 5 minutes. Then the cells were treated with TMRM reagent and incubated for 30 minutes, cells were trypsinized, washed with ice cold phosphate buffered saline (PBS, pH 7.4) thrice, lysed, and mitochondrial membrane potential estimation was performed as per the kit protocol (TMRM-Mitochondrial Membrane Potential Assay Kit, ab113852, Abcam, Cambridge, UK). Further, measurements were made with a fluorimeter (FLx800, Bio-Tek, Winooski, VT, USA) at an excitation wavelength of 490 nm and an emission wavelength of 510 nm.

4.4.27 Mitochondrial Membrane Potential JC1 assay

The cationic dye JC-1 (5,5',6,6'-tetrachloro-1,1',3,3'-tetraethylimidacarbocyanine iodide) obtained from Sigma was used for the analysis. In this experimental setup, cells were initially seeded at a density of 8,000 cells per well. P-NBD at a concentration of 10 μ M was introduced into the cell culture and incubated about 2 h, followed by irradiation with a 532 nm laser. Subsequently, the cells were incubated for 24 hours, carefully washed, and then treated with JC-1 at a concentration of 5 μ M for 10 minutes. The cells were then observed using a Nikon-TS100 inverted microscope equipped with red and green channel filters to evaluate mitochondrial health and functionality. This assessment was made by observing changes in the red and green fluorescence signals emitted by JC-1 within the mitochondria. To quantify the results, ImageJ software was utilized to calculate the JC-1 aggregate/monomer ratio, a critical indicator of mitochondrial membrane potential. This ratio reflects the balance between the aggregated and monomeric forms of JC-1 dye within the mitochondria and provides insights into the state of the mitochondria and their potential impact on cellular health and function.

4.4.28 Evaluation apoptotic potential

Evaluation of the mode of cytotoxicity exhibited by P-NBD was performed on cancer cells with various apoptotic assays after administration of 10 μ M of P-NBD with and without laser via dual staining acridine orange –ethidium bromide assay, APO Percentage assay (Biocolor, Belfast, Northern Ireland) and finally by FITC-Annexin V staining (BD Pharmingen no. 556547, BD Biosciences, San Jose, CA). Assessment of apoptosis using the acridine orange-ethidium bromide dual staining procedure was performed as described in literature. The cells were observed under an inverted fluorescent microscope, using a FITC filter (Olympus 1X51, Singapore) to view the apoptotic or non-apoptotic cells. The apoptosis was further confirmed using APO Percentage dye (Biocolor, Belfast, Northern Ireland) as per manufacturer's instructions. Light microscopic images of APO Percentage dye-labelled cells, which stained pink under a light microscope, were used to quantify the extent of apoptosis. The dye uptake was further quantified using colorimetric method according to the manufacturer's instruction. The cells were lysed and the absorbance was measured at 550nm using a microplate reader (Biotech, USA).

4.5 References

- (1) Dolmans, D. E. J. G. J.; Fukumura, D.; Jain, R. K. Photodynamic Therapy for Cancer. *Nature Reviews Cancer*. 2003. <https://doi.org/10.1038/nrc1071>.
- (2) Zhang, Y.; Fang, J.; Ye, S.; Zhao, Y.; Wang, A.; Mao, Q.; Cui, C.; Feng, Y.; Li, J.; Li, S.; Zhang, M.; Shi, H. *Supplementary Information A Hydrogen Sulphide-Responsive and Depleting Nanoplatform for Cancer Photodynamic Therapy*.
- (3) Escudero, A.; Carrillo-Carrión, C.; Castillejos, M. C.; Romero-Ben, E.; Rosales-Barrios, C.; Khiar, N. Photodynamic Therapy: Photosensitizers and Nanostructures. *Materials Chemistry Frontiers*. Royal Society of Chemistry May 21, 2021, pp 3788–3812. <https://doi.org/10.1039/d0qm00922a>.
- (4) Sai, D. L.; Lee, J.; Nguyen, D. L.; Kim, Y. P. Tailoring Photosensitive ROS for Advanced Photodynamic Therapy. *Experimental and Molecular Medicine*. Springer Nature April 1, 2021, pp 495–504. <https://doi.org/10.1038/s12276-021-00599-7>.
- (5) Correia, J. H.; Rodrigues, J. A.; Pimenta, S.; Dong, T.; Yang, Z. Photodynamic Therapy Review: Principles, Photosensitizers, Applications, and Future Directions. *Pharmaceutics* **2021**, *13* (9). <https://doi.org/10.3390/pharmaceutics13091332>.

-
- (6) Shamjith, S.; Joseph, M. M.; Murali, V. P.; Remya, G. S.; Nair, J. B.; Suresh, C. H.; Maiti, K. K. NADH-Depletion Triggered Energy Shutting with Cyclometalated Iridium (III) Complex Enabled Bimodal Luminescence-SERS Sensing and Photodynamic Therapy. *Biosens Bioelectron* **2022**, *204*. <https://doi.org/10.1016/j.bios.2022.114087>.
- (7) Liu, M.; Li, C. Recent Advances in Activatable Organic Photosensitizers for Specific Photodynamic Therapy. *ChemPlusChem*. Wiley-VCH Verlag May 1, 2020, pp 948–957. <https://doi.org/10.1002/cplu.202000203>.
- (8) Yuan, B.; Wang, H.; Xu, J. F.; Zhang, X. Activatable Photosensitizer for Smart Photodynamic Therapy Triggered by Reactive Oxygen Species in Tumor Cells. *ACS Appl Mater Interfaces* **2020**, *12* (24), 26982–26990. <https://doi.org/10.1021/acsami.0c07471>.
- (9) Ichikawa, Y.; Kamiya, M.; Obata, F.; Miura, M.; Terai, T.; Komatsu, T.; Ueno, T.; Hanaoka, K.; Nagano, T.; Urano, Y. Selective Ablation of β -Galactosidase-Expressing Cells with a Rationally Designed Activatable Photosensitizer. *Angewandte Chemie* **2014**, *126* (26), 6890–6893. <https://doi.org/10.1002/ange.201403221>.
- (10) Sun, J.; Du, K.; Diao, J.; Cai, X.; Feng, F.; Wang, S. GSH and H₂O₂ Co-Activatable Mitochondria-Targeted Photodynamic Therapy under Normoxia and Hypoxia. *Angewandte Chemie - International Edition* **2020**, *59* (29), 12122–12128. <https://doi.org/10.1002/anie.202003895>.
- (11) Huang, Y.; Wu, S.; Zhang, L.; Deng, Q.; Ren, J.; Qu, X. A Metabolic Multistage Glutathione Depletion Used for Tumor-Specific Chemodynamic Therapy. *ACS Nano* **2022**, *16* (3), 4228–4238. <https://doi.org/10.1021/acsnano.1c10231>.
- (12) Li, X.; Kwon, N.; Guo, T.; Liu, Z.; Yoon, J. Innovative Strategies for Hypoxic-Tumor Photodynamic Therapy. *Angewandte Chemie - International Edition*. Wiley-VCH Verlag September 3, 2018, pp 11522–11531. <https://doi.org/10.1002/anie.201805138>.
- (13) Lovell, J. F.; Liu, T. W. B.; Chen, J.; Zheng, G. Activatable Photosensitizers for Imaging and Therapy. *Chem Rev* **2010**, *110* (5), 2839–2857. <https://doi.org/10.1021/cr900236h>.
-

- (14) Yuan, B.; Wang, H.; Xu, J. F.; Zhang, X. Activatable Photosensitizer for Smart Photodynamic Therapy Triggered by Reactive Oxygen Species in Tumor Cells. *ACS Appl Mater Interfaces* **2020**, *12* (24), 26982–26990. <https://doi.org/10.1021/acsami.0c07471>.
- (15) Li, Y.; Zhang, X.; Zhang, Y.; Zhang, Y.; He, Y.; Liu, Y.; Ju, H. Activatable Photodynamic Therapy with Therapeutic Effect Prediction Based on a Self-Correction Upconversion Nanoprobe. *ACS Appl Mater Interfaces* **2020**, *12* (17), 19313–19323. <https://doi.org/10.1021/acsami.0c03432>.
- (16) Wei, X.; Zhang, C.; He, S.; Huang, J.; Huang, J.; Liew, S. S.; Zeng, Z.; Pu, K. A Dual-Locked Activatable Phototheranostic Probe for Biomarker-Regulated Photodynamic and Photothermal Cancer Therapy. *Angewandte Chemie - International Edition* **2022**, *61* (26). <https://doi.org/10.1002/anie.202202966>.
- (17) Wallace, J. L.; Wang, R. Hydrogen Sulfide-Based Therapeutics: Exploiting a Unique but Ubiquitous Gasotransmitter. *Nature Reviews Drug Discovery*. Nature Publishing Group May 5, 2015, pp 329–345. <https://doi.org/10.1038/nrd4433>.
- (18) Szabó, C. Hydrogen Sulphide and Its Therapeutic Potential. *Nature Reviews Drug Discovery*. November 2007, pp 917–935. <https://doi.org/10.1038/nrd2425>.
- (19) Youness, R. A.; Gad, A. Z.; Sanber, K.; Ahn, Y. J.; Lee, G. J.; Khallaf, E.; Hafez, H. M.; Motaal, A. A.; Ahmed, N.; Gad, M. Z. Targeting Hydrogen Sulphide Signaling in Breast Cancer. *Journal of Advanced Research*. Elsevier B.V. January 1, 2021, pp 177–190. <https://doi.org/10.1016/j.jare.2020.07.006>.
- (20) Szabo, C.; Papapetropoulos, A. International Union of Basic and Clinical Pharmacology. CII: Pharmacological Modulation of H₂S Levels: H₂S Donors and H₂S Biosynthesis Inhibitors. *Pharmacogn. Rev.* **2017**, *69*.
- (21) Liu, D.; Liu, M.; Wan, Y.; Zhou, X.; Yang, S.; An, L.; Huang, G.; Tian, Q. Remodeling Endogenous H₂S Microenvironment in Colon Cancer to Enhance Chemodynamic Therapy. *Chemical Engineering Journal* **2021**, *422*. <https://doi.org/10.1016/j.cej.2021.130098>.
- (22) Fiorucci, S. The Third Gas: H₂S Regulates Perfusion Pressure in Both the Isolated and Perfused Normal Rat Liver and in Cirrhosis. *Hepatology* **2005**, *42*. <https://doi.org/10.1002/hep.20817>.

-
- (23) Mustafa, A. K.; Gadalla, M. M.; Sen, N.; Kim, S.; Mu, W.; Gazi, S. K.; Barrow, R. K.; Yang, G.; Wang, R.; Snyder, S. H. HS Signals through Protein S-Sulfhydration. *Sci Signal* **2009**, *2* (96). <https://doi.org/10.1126/scisignal.2000464>.
- (24) Paul, B. D.; Snyder, S. H. H₂S: A Novel Gasotransmitter That Signals by Sulfhydration. *Trends in Biochemical Sciences*. Elsevier Ltd 2015, pp 687–700. <https://doi.org/10.1016/j.tibs.2015.08.007>.
- (25) Celli, J. P.; Spring, B. Q.; Rizvi, I.; Evans, C. L.; Samkoe, K. S.; Verma, S.; Pogue, B. W.; Hasan, T. Imaging and Photodynamic Therapy: Mechanisms, Monitoring, and Optimization. *Chem Rev* **2010**, *110* (5), 2795–2838. <https://doi.org/10.1021/cr900300p>.
- (26) Wragg, A.; Gill, M. R.; Turton, D.; Adams, H.; Roseveare, T. M.; Smythe, C.; Su, X.; Thomas, J. A. Tuning the Cellular Uptake Properties of Luminescent Heterobimetallic Iridium(III)-Ruthenium(II) DNA Imaging Probes. *Chemistry - A European Journal* **2014**, *20* (43), 14004–14011. <https://doi.org/10.1002/chem.201403693>.
- (27) Zhao, J.; Yan, K.; Xu, G.; Liu, X.; Zhao, Q.; Xu, C.; Gou, S. An Iridium (III) Complex Bearing a Donor–Acceptor–Donor Type Ligand for NIR-Triggered Dual Phototherapy. *Adv Funct Mater* **2021**, *31* (11). <https://doi.org/10.1002/adfm.202008325>.
- (28) Zhang, K. Y.; Liu, S.; Zhao, Q.; Li, F.; Huang, W. Phosphorescent Iridium(III) Complexes for Bioimaging. *Struct Bond* **2015**, *165*, 131–180. https://doi.org/10.1007/430_2014_166.
- (29) Ramya, A. N.; Joseph, M. M.; Karunakaran, V.; Ahammed, C. V. S.; Samanta, A.; Maiti, K. K. An Efficient Molecular Luminophore Based on Tetraphenylethylene (TPE) Enabling Intracellular Detection and Therapeutic Benefits of Hydrogen Sulfide in Alzheimer’s Disease. *Sens Actuators B Chem* **2022**, 355. <https://doi.org/10.1016/j.snb.2021.131118>.
- (30) Liu, Z.; Bian, Z.; Huang, C. Luminescent Iridium Complexes and Their Applications. *Top Organomet Chem* **2010**, *28*, 113–142. https://doi.org/10.1007/978-3-642-01866-4_4.
-

- (31) Park, J.; Kim, T.; Kim, H. J.; Hong, J. I. Iridium(III) Complex-Based Electrochemiluminescent Probe for H₂S. *Dalton Transactions* **2019**, 48 (14), 4565–4573. <https://doi.org/10.1039/c8dt04901g>.
- (32) Ramya, A. N.; Arya, J. S.; Madhukrishnan, M.; Shamjith, S.; Vidyalekshmi, M. S.; Maiti, K. K. Raman Imaging: An Impending Approach Towards Cancer Diagnosis. *Chemistry - An Asian Journal*. John Wiley and Sons Ltd March 1, 2021, pp 409–422. <https://doi.org/10.1002/asia.202001340>.
- (33) Karunakaran, V.; Saritha, V. N.; Joseph, M. M.; Nair, J. B.; Saranya, G.; Raghu, K. G.; Sujathan, K.; Kumar, K. S.; Maiti, K. K. Diagnostic Spectro-Cytology Revealing Differential Recognition of Cervical Cancer Lesions by Label-Free Surface Enhanced Raman Fingerprints and Chemometrics. *Nanomedicine* **2020**, 29. <https://doi.org/10.1016/j.nano.2020.102276>.
- (34) Arya, J. S.; Joseph, M. M.; Sherin, D. R.; Nair, J. B.; Manojkumar, T. K.; Maiti, K. K. Exploring Mitochondria-Mediated Intrinsic Apoptosis by New Phytochemical Entities: An Explicit Observation of Cytochrome c Dynamics on Lung and Melanoma Cancer Cells. *J Med Chem* **2019**, 62 (17), 8311–8329. <https://doi.org/10.1021/acs.jmedchem.9b01098>.

ABSTRACT

Name of the Student: **Mr. Shamjith S.**
Faculty of Study: **Chemical Sciences**
AcSIR academic center/CSIR Lab: **CSIR-National
Institute for Interdisciplinary Science
and Technology (CSIR-NIIST)**

Registration No.: **10CC18A39018**
Year of Submission: **2023**

Name of the Supervisor: **Dr. Kaustabh Kumar Maiti**

Title of the thesis: **Design and Synthesis of Cyclometallated Iridium Molecular Probes with Targeted Image-Guided Therapeutic Capabilities for Cancer Management**

The concept of theranostics, which seamlessly merges therapy and diagnostics, is brimming with potential for translational research and clinical application. One promising non-invasive cancer treatment is Photodynamic Therapy (PDT), which harnesses the power of photosensitizers and light to selectively target and eliminate cells, notably cancer cells while sparing healthy tissue and minimizing toxicity. Nevertheless, PDT faces notable challenges, including limited light penetration and selectivity. Researchers are actively working on modulating photosensitizers and exploring combination therapies like a-PDT. **In Chapter 1**, readers can dive into a comprehensive review of the exploration of molecular probes in the context of PDT and bioimaging applications. Additionally, the chapter underscores the unique effectiveness of iridium-based molecular probes in PDT, serving as an indispensable primer on the significance and utilization of molecular probes, particularly within PDT and bioimaging techniques.

Chapter 2 delves into the intricate design and production of a unique cationic cyclometallated Ir(III) complex, which utilizes a quinoline-appended bipyridine as an auxiliary ligand. This complex is engineered for targeted activation through nicotinamide adenine dinucleotide-reduced (NADH), a crucial hydride (H^-) carrier in maintaining cellular homeostasis. The quinoline-appended iridium complex (**QAIC**) serves a pivotal role as a molecular probe in both SERS and fluorescence techniques. Its purpose is to assess the state of endogenous NADH within the cellular environment. Subsequently, the activated **QAIC** or **N-QAIC** is explored for its potential as a photosensitizer with the capacity to generate singlet oxygen and NAD radicals by inhibiting photo-induced electron transfer (**PeT**).

In Chapter 3, a novel strategy has been proposed, involving the integration of a sophisticated singlet oxygen delivery system known as **Ir-Nap**. This complex can autonomously generate singlet oxygen and undergo a cycloaddition reaction, forming an endoperoxide species, which induces photodynamic therapy (PDT) effects at higher temperatures. Ir-Nap-Endo has been incorporated into the **PDA** nanosystem, serving as both a controlled release agent and a photothermal therapy (PTT) agent. Encapsulation within glutathione (**GSH**)-responsive manganese dioxide (**MnO₂**) nanoparticles enhances chemodynamic therapy by reducing intracellular GSH levels and promoting oxygenation. To target triple-negative breast cancer (**TNBC**) cells selectively, the construct is conjugated with a **GRP78**-targeting peptide, enabling preferential recognition and uptake. This approach combines GSH depletion, singlet oxygen generation, **PTT**, chemodynamic therapy, and tumor-specific targeting for advanced cancer treatment.

Chapter 4 unveils a novel cyclometallated iridium complex, serving as an **H₂S**-activated photodynamic agent for targeted cancer cell treatment. Initially, it remains in a weakly luminescent **PDT-OFF** state but intensifies fourfold upon exposure to H₂S, disrupting the **PeT** process. PDT activation relies on PeT cessation, fostering a triplet state. Exceptional selectivity for **H₂S** is confirmed through rigorous tests with various molecules. This innovative probe not only detects endogenous H₂S but also transforms it into a potent PDT agent, reducing cellular **ATP levels** through H₂S depletion. This approach promises to revolutionize cancer therapy by depleting-assisted activatable **PDT**, enhancing sensitivity to apoptosis, and offering a groundbreaking paradigm in cancer treatment.

List of Publications Emanating from the Thesis

1. **Shamjith S**, Joseph MM, Murali VP, Remya GS, Nair JB, Suresh CH, Maiti KK. NADH-depletion triggered energy shutting with cyclometalated iridium (III) complex enabled bimodal Luminescence-SERS sensing and photodynamic therapy. *Biosens Bioelectron.* 2022; 204: 114087. PMID: 35182836.
2. **Shamjith S**, Joseph MM, Nair JB, Murali VP, and Maiti KK. GSH-assisted self-degrading singlet oxygen delivery system for light-triggered ablation of deep tumors. (Manuscript to be submitted)
3. **Shamjith S**, Joseph MM, Nair JB, Murali VP, Fathima T S and Maiti KK. Harnessing Hydrogen Sulphide-Induced Activation for Site-Specific Photodynamic Therapy: Disrupting Glycolysis as a Strategy for Selective and Enhanced Anticancer Effects. (Manuscript Submitted)

List of Publications not Related to Thesis Work

1. Neelambaran Nishna; **Shamjith S.**; Murali, Vishnupriya; Maiti Kaustabh; Joseph Joshy. Exploring a Mitochondria Targeting, Dinuclear Cyclometalated Iridium (III) Complex for Image-Guided Photodynamic Therapy in Triple-negative Breast Cancer Cells; ACS Appl. Bio Mater. 2023, 6, 12, 5776–5788
2. Chandana Reghukumara; **Shamjith S.**; Vishnu Priya Murali; Pilankatta K.Ramya; Kokkuvayil Vasu Radhakrishnan, Kaustabh Kumar Maiti. Cyclometalated Ir(III) Theranostic Molecular Probe Enabled Mitochondria Targeted Fluorescence-SERS-Guided Phototherapy in Breast Cancer Cells; Journal of Photochemistry and Photobiology B: Biology, 2024,250, 112832
3. Archana Panthalattu Parambil, **Shamjith S.**, Jais Kurian, Akila Kesavan, Ashis K. Sen, Paul R. Thangaraj, Kaustabh Kumar Maiti* and Muraleedharan K. Manheri*; Dual Mode ‘Turn-on’ Fluorescence-Raman (SERS) Response probe based on 1H-pyrrol-3(2H)-one scaffold for Monitoring H₂S Levels in Biological Samples; Analytical Methods, DOI: 10.1039/D3AY00282A, 2023
4. Narayanan N, Kim JH, Santhakumar H, Joseph MM, Karunakaran V, **Shamjith S**, Saranya G, Sujai PT, Jayasree RS, Barman I, Maiti KK. Nanotheranostic probe built on

methylene blue loaded cucurbituril [8] and gold nanorod: Targeted phototherapy in combination with SERS imaging on breast cancer cells. *J Phys Chem B*. 2021; 125:13415-13424. PMID: 34871005.

5. Sujai PT, **Shamjith S**, Joseph MM, Maiti KK. Elucidating gold–MnO₂ core–shell nanoenvelope for real time SERS-guided photothermal therapy on pancreatic cancer cells. *ACS Appl Bio Mater*. 2021; 4: 4962–4972. PMID: 35007044 (**Equal Authorship**)
6. Sujai PT, Joseph MM, Karunakaran V, Saranya G, Ramya AN, **Shamjith S**, Thomas R, Nair JB, Swathi RS, Maiti KK. Biogenic cluster-encased gold nanorods as a targeted three-in-one theranostic nanoenvelope for SERS-guided photochemotherapy against metastatic melanoma. *ACS Appl Bio Mater*. 2019; 2: 588-600. PMID: 35016322

Review Articles

1. Ramya AN, Arya JS, Madhukrishnan M, **Shamjith S**, Vidyalekshmi MS, Maiti KK. Raman Imaging: An Impending Approach Towards Cancer Diagnosis. *Chem Asian J*. 2021 Mar 1;16(5):409-422. doi: 10.1002/asia.202001340. Epub 2021 Jan 28. PMID: 33443291.
2. **Shamjith S**, Manu M Joseph, and Kaustabh Kumar Maiti; The Recent Development of Fluorescence-Based Chemo Sensors for Nicotinamide Adenine Dinucleotides and Its Biological Applications. (Review under Preparation)

List of Papers/Posters Presented in Conferences

1. Advanced Materials and Manufacturing Technologies (AMMT 2023), Held at CSIR-NIIST Trivandrum. (Participation)
2. NS-DPHM-2022 National Seminar on Recent Trends in Disease Prevention and Health Management CSIR-National Institute for Interdisciplinary Science and Technology, Thiruvananthapuram, Kerala (Participation)

3. Co-Enzyme Driven Targeted Phototherapy for Effective Cancer Management; Shanmughan Shamjith, Manu M. Josepha, Vishnu Priya Murali, Cherumuttathu H. Suresh* and Kaustabh Kumar Maiti*; Indian Analytical Science Congress held at MUNNAR 2022 march (**Best oral presentation award**)
4. INCD- International Conference on Nutraceuticals and Chronic Diseases conference is designed to explore the scientific basis for the 'Pharmaceuticals and Nutraceuticals for Cancer and Other Chronic Diseases, Delhi (**Poster presentation**)
5. International Conference on Chemistry for Human Development (ICCHD-2020) Date: 9th -11th January 2020, Venue: Heritage Institute of Technology, Kolkata (**Poster presentation**)
6. International Conference on Eco materials (ICEM-14 2019), organized by CSIR-NIIST, Thiruvananthapuram. (**Poster presentation**)
7. 8th Annual Meeting of Indian Academy of Biomedical Sciences, (IABS 2019) held at CSIR-NIIST, Thiruvananthapuram, Kerala. (Participation)



NADH-depletion triggered energy shutting with cyclometalated iridium (III) complex enabled bimodal Luminescence-SERS sensing and photodynamic therapy

Shanmughan Shamjith^{a,b}, Manu M. Joseph^a, Vishnu Priya Murali^a, Geetha S. Remya^{a,b}, Jyothi B. Nair^a, Cherumuttathu H. Suresh^{a,b,**}, Kaustabh Kumar Maiti^{a,b,*}

^a Chemical Sciences & Technology Division (CSTD), Organic Chemistry Section, CSIR-National Institute for Interdisciplinary Science & Technology (CSIR-NIIST), Industrial Estate, Pappanamcode, Thiruvananthapuram, 695019, Kerala, India

^b Academy of Scientific and Innovative Research (AcSIR), Ghaziabad, 201002, India

ARTICLE INFO

Keywords:

Iridium complex
NADH-Sensing
Computational modelling
Multiphase-PDT
NAD radical
Enhanced therapeutic

ABSTRACT

The nicotinamide adenine dinucleotide-reduced (NADH) function as a hydride (H) carrier to maintain cellular homeostasis. Herein, we report a quinoline appended iridium complex (QAIC) as a molecular probe in fluorescence and surface-enhanced Raman spectroscopy (SERS) modalities to evaluate the endogenous NADH status. NADH-triggered activation of QAIC enabled luminescence (turn-ON) and SERS (turn-OFF) switching phenomenon with a detection limit of 25.6 nM and 15 pM for NADH in luminescence and SERS respectively. Transition state modelling using density functional theory calculations proved that a facile migration of H from NADH to QAIC transformed the activated QAIC (N-QAIC) with an energy span of 19.7 kcal/mol. Furthermore, N-QAIC is probed as a photosensitizer to source singlet oxygen by blocking the photo induced electron transfer (PeT) and generate NAD radicals. Therefore, an efficient light triggered cyclometalated iridium-based molecular probe has been divulged to promote bimodal NADH sensing and multiphase photodynamic therapy.

1. Introduction

Altered cellular metabolism is a hallmark of cancer (Hanahan and Weinberg, 2011) where, the excess energy required for various anaerobic reactions is managed by the intracellular levels of nicotinamide adenine dinucleotide (NADH) (Yaku et al., 2018). As a coenzyme, NADH performs vital roles in the metabolic activities of cells and regulates the redox homeostasis (Chiarugi et al., 2012). The classical Warburg theory and the modern symbiotic theory of cancer metastasis eventually spotlight the significance of NADH in cancer progression and hence can be considered as a marker for tumorigenesis (Kim, 2018). Selective depletion of NADH can shut down the energy production, forcing the cells into a redox uncertainty (Xiao et al., 2018). Therefore, it is worth exploring NADH detection using new generation molecular probes that enable both sensing and therapy (Wang et al., 2016). The fascinating photo-physical features, high quantum yield, ease of synthesis and tunable emission characteristics of cyclometalated iridium complexes satisfy the requirements of a molecular sensor for sensing pH, metabolites,

biomarkers, ions, and much more. Moreover, the activated singlet oxygen conversion efficiency and elevated aqueous solubility are added advantages of iridium complexes over other organic sensor moieties due to their cationic nature (He et al., 2015; Nam et al., 2016). So far, there is no reports on the selective detection of intracellular NADH using cyclometalated iridium complexes.

Photodynamic therapy (PDT) has received attention in precision medicine but the practical application depends on the availability of efficient photosensitizers (PS) capable of producing reactive oxygen species (ROS) in type-II and other free radicals in type-I upon light trigger (Brown et al., 2004; Dolmans et al., 2003). Therapeutic approaches for handling hypoxia by enhancing the efficiency of PDT is the hallmark of antitumor treatment (Li et al., 2018). Since reduced oxygen concentration is the major bottleneck of PDT, researchers are focusing on approaches that can establish oxygen independent PDT. Herein, we introduce an activatable PDT using an in-house iridium metal based complex wherein 1-methylquinoline moiety appended bipyridine was positioned as the ancillary ligand. The newly designed complex is named

* Corresponding author. CSIR National Institute for Interdisciplinary Science and Technology, Thiruvananthapuram, 695019, India.

** Corresponding author. Academy of Scientific and Innovative Research (AcSIR), Ghaziabad, 201002, India.

E-mail addresses: sureshch@gmail.com (C.H. Suresh), kkmaiti@niist.res.in (K.K. Maiti).

<https://doi.org/10.1016/j.bios.2022.114087>

Received 6 December 2021; Received in revised form 10 January 2022; Accepted 7 February 2022

Available online 13 February 2022

0956-5663/© 2022 Elsevier B.V. All rights reserved.

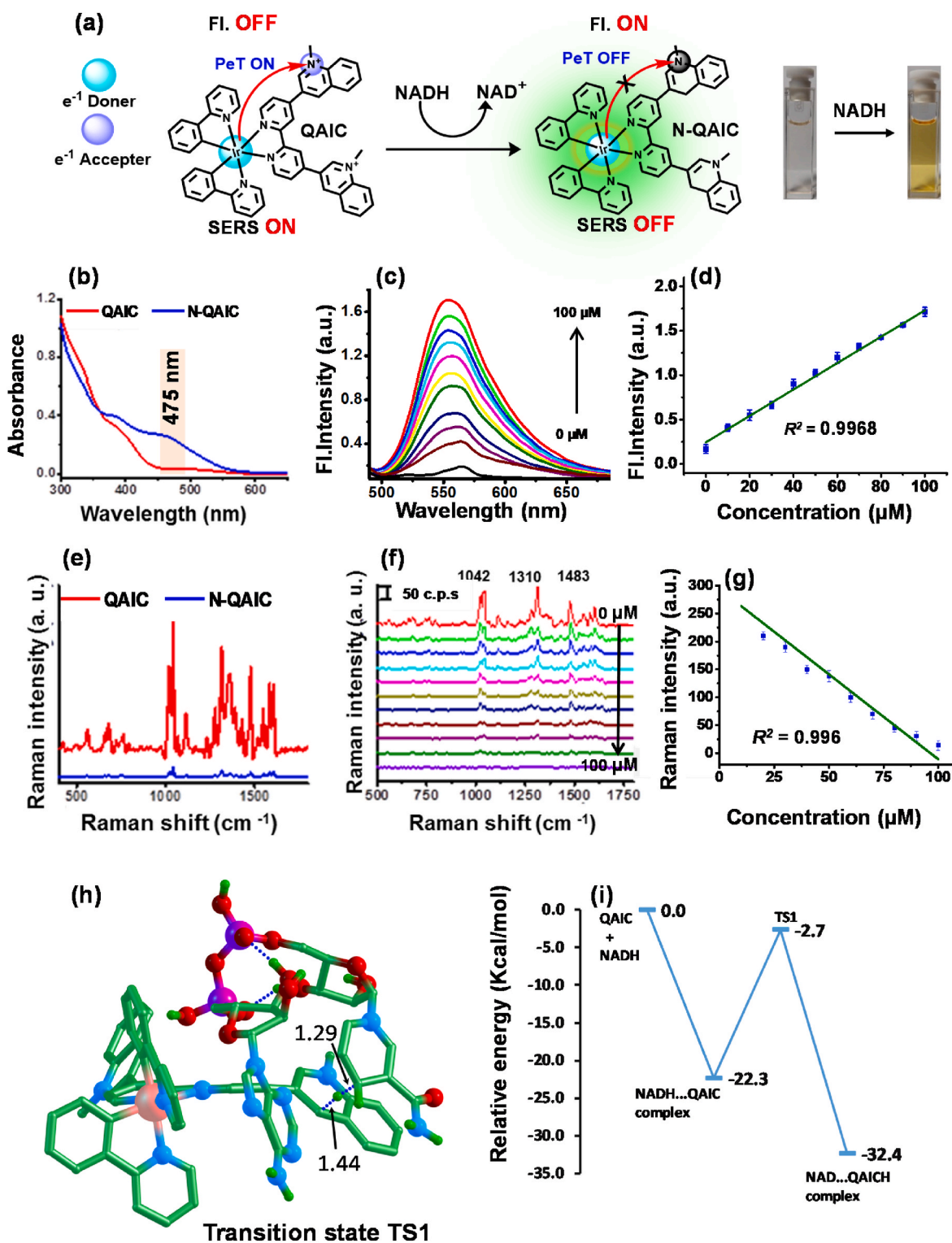


Fig. 1. (a) Schematic illustration of NADH-triggered activation of QAIC. (b) UV-Visible spectra of QAIC and QAIC with NADH (10 μM, 20-min incubation). (c) Emission characteristics of QAIC with increasing concentration of NADH (0, 10, 20, 30, 40, 50, 60, 70, 80, 90 and 100 μM) followed by incubation in HEPES (pH 7.4, excitation 475 nm, emission 555 nm, slit width: 4 nm/4 nm) and (d) linear correlation graph between emission intensities and concentrations of NADH. (e) SERS spectra of QAIC with and without NADH treatment. (f) The concentration dependent SERS OFF process with AuNP as SERS substrate with increasing concentration of NADH. (g) The linear correlation of SERS intensities and concentrations of NADH. (h) The optimized transition state TS1 of the hydride transfer reaction. (i) Energy profile diagram of the hydride transfer from NADH to through TS1 (The activated C-H distances are given in Å).

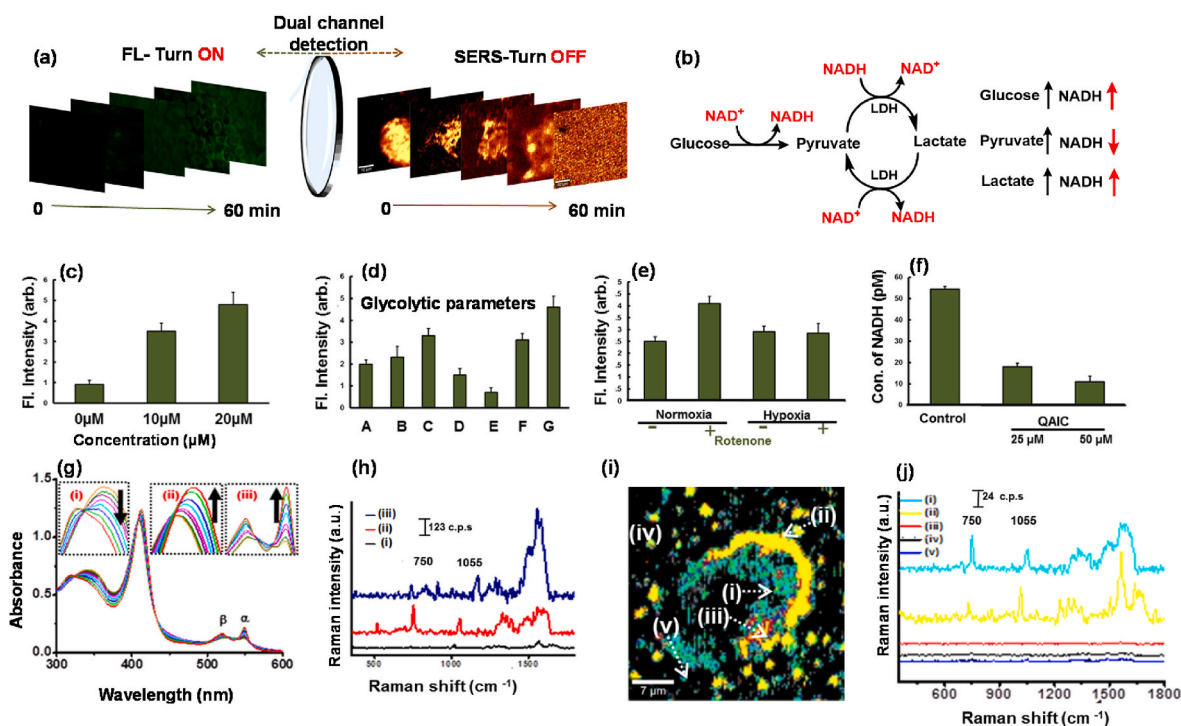


Fig. 2. (a) Time-dependent imaging of HepG2 cells showing the fluorescence-ON process (left panel) and SERS imaging showing the Raman-OFF process (right panel) via activation of QAIC by NADH. (b) Schematic illustration of the biochemical event causing the fluctuations of intracellular NADH. (c) Fluorescence enhancement of QAIC from cells incubated with exogenous NADH. (d) Effect of pre-incubation of various glycolytic intermediates on the NADH sensing by QAIC (A-control, B-10 mM glucose, C-20 mM glucose, D-5 mM pyruvate, E-10 mM pyruvate, F-5 mM lactate, G-10 mM lactate). (e) The activation of QAIC in the presence of rotenone in normoxic and hypoxic situation. (f) Quantification of intracellular NADH from HepG2 cells incubated with QAIC using a commercially available kit. (g) Confirmation of Fe^{3+} -cyt-c reduction by QAIC and NADH with laser via UV-Visible spectroscopy; insert shows the enlarged portion of absorption changes occurred in α , β (iii) and other bands. (h) Tracking of cytochrome c reduction via SERS mapping of HepG2 cells incubated with QAIC and NADH after laser irradiation: i-Control HepG2, ii-QAIC + NADH + L, iii-QAIC + NADH. (i) Cluster mapping of HepG2 cells using the 750 cm^{-1} peak and (j) Corresponding SERS spectra from the selected parts.

'1-methylquinoline Appended Iridium Complex' (QAIC). As-synthesized molecular probe is envisaged to exhibit the following processes, (i) real-time bimodal detection of endogenous NADH in cancer cells through turn-ON luminescence and turn-OFF SERS phenomenon, (ii) tracking the molecular events via SERS and luminescence modalities, (iii) NADH depletion triggered PDT, (iv) NAD radical generation capability and (v) inducing enhanced PDT towards both normoxic and hypoxic conditions. To the best of our knowledge, this is the first demonstration where the NADH triggered "ON-OFF" sensing approach synchronizes the detection as well as phototherapy with iridium-metal based molecular probe by SERS and fluorescence-based bimodal strategies.

2. Materials and methods

The detailed experimental procedures including synthesis and characterization of all the precursor molecules, singlet oxygen studies, radical generation assays, computational analysis, details regarding cell lines, cell viability assay, apoptosis assays, SERS studies, and fluorescence imaging are described in the Supporting Information.

3. Results and discussion

3.1. Design and synthesis of quinoline appended iridium complex (QAIC)

The cyclometalated iridium (III) complex QAIC was synthesized through a three-step process using precursor 4-(2-pyridyl)benzene (ppy) and bipyridine ligand which is appended with 1-methylquinoline unit at 4 and 4' positions. The quaternized N-centers of the quinoline moiety provide two positive charges to this ligand. We abbreviate this ligand as

(Nq^+Nq^+) where the N stands for the N-donor ligands of the bipyridine and q^+ stands for the 1-methylquinoline substituents at 4 and 4' positions. Thus QAIC can be written as $[\text{Ir}(\text{ppy})_2(\text{Nq}^+\text{Nq}^+)]^+$ with a total charge of +3 on the complex (Fig. 1a, Scheme S1 and Figs. S1a-d). We hypothesized that, NADH mediated activation of QAIC will promote turn-ON luminescence with simultaneous induction of localized PDT by blocking the PeT via selective shutting of electron transfer between iridium metal center (PeT donor) and the electron deficient nitrogen of quinoline moiety (PeT acceptor) (You et al., 2014).

3.2. Photophysical assessment and activation of QAIC by NADH

UV-Vis absorption spectrum of the complex showed energy absorption bands at 316–350 nm corresponding to the spin-allowed ligand-centered π - π^* transitions for cyclometalated (ppy) and ancillary (Nq^+Nq^+) ligands. The mixed singlet and triplet metal-to-ligand charge-transfer ($^1\text{MLCT}$ and $^3\text{MLCT}$) and ligand-to-ligand charge-transfer (LLCT) transitions are responsible for the weak and low-energy bands between 400 and 510 nm (He et al., 2015; Sudheesh et al., 2018). Upon incubation with NADH a change in the colour from pale yellow to orange was observed (Fig. 1b and Fig. S2a). QAIC displayed negligible luminescence (excitation 475 nm, slit width 4 nm), but after incubation with varying equivalents of NADH enhanced emission at 555 nm with a linear response R^2 value of 0.9968 was displayed (Fig. 1c&d, Fig. S2b). Remarkably, the response of QAIC to NADH at low concentrations (0–5 μM) also showed linearity with a detection limit as low as 25.6 nM with high selectivity and was stable over pH fluctuations (Figs. S2c–e).

Here, PeT switch-OFF mechanism occurs due to the hydride transfer from NADH to QAIC and subsequently eliminates the net charge on the nitrogen to convert activated QAIC (denoted as NAD-QAIC i.e., N-

QAIC) (Scheme S2). The diminished electron acceptance capacity of N-QAIC causes a decrease in PeT which facilitates the intersystem crossing (ISC) to improve the luminescent properties of the complex (T. H. Huang et al., 2019). The NADH-QAIC redox reaction in the sensing process was further confirmed by mass spectrometry analysis. HRMS peak at 315.157 (calcd for $C_{52}H_{40}IrN_6^{3+}$ with m/z 313.164, where $z = 3$) for QAIC was changed to 943.312 (calcd for $C_{52}H_{42}IrN_6^+$ with m/z 943.310) upon NADH addition which confirms the hydride transfer from NADH to QAIC (Fig. S3a&b). Additionally, SERS analysis was performed to trace the Raman fingerprints of QAIC (Table S1). (Narayanan et al., 2015) Upon treatment with 2 equivalents of NADH, a sharp quenching in the characteristic Raman peaks of QAIC at 1042, 1228 and 1310 cm^{-1} indicating a SERS turn-OFF response with a limit of detection of 15 pM (Fig. 1e and Fig. S3c). Further, a linear response of hydride transfer between QAIC and NADH was observed by recording the SERS spectra with increasing NADH concentration. The well resolved Raman spectra can be attributed to the strong electrostatic interaction between the positively charged ($Nq^+ Nq^+$) ligand in QAIC with the negatively charged citrate stabilized AuNPs. The reduction of QAIC by NADH converts the charged ($Nq^+ Nq^+$) to the neutral ($NqNq$) which weakens the interaction with AuNPs, rendering a SERS turn-OFF phenomenon with a linear response of $R^2 = 0.996$ (Fig. 1f&g). When AuNPs were treated with QAIC (0 to 100 nM), a change in the zeta potential from -30 to +13 was observed, validating the strong electrostatic interaction between AuNP and QAIC (Figs. S4a–d).

In another assessment, dispersion and solvation effect included density functional theory (DFT), viz. wB97xD/SMD/BS2//wB97xD/BS1 was used to derive the structures of NADH ... QAIC and NAD ... QAIC complexes and the transition state (TS1) for the redox reaction (Fig. 1h&i, Fig. S5). The interaction energy (E_{int}) for the NADH ... QAIC adduct formation was 22.3 kcal/mol which indicates strong electrostatic binding between the tri positively charge QAIC and neutral NADH. The structure of TS1 suggests the hydride migration from the nicotinamide ring of NADH to the 4th position of 1-methylquinoline unit of QAIC with an energy span of 19.7 kcal/mol. The product complex NAD ... QAIC is more stable than the reactant complex by 10.0 kcal/mol indicating that stronger electrostatic interaction exists between the cationic NAD and di-positively charged QAIC. The exothermic character of this reaction suggests spontaneous conversion of NADH to NAD due to the strong ability of QAIC to abstract a hydride from the C–H bond of NADH. The hydride transfer from NADH to QAIC, followed by the PeT turn-OFF behaviour suggests a novel sensing mechanism for NADH by QAIC.

3.3. NADH homeostasis by QAIC under cellular physiology

The intracellular concentration of NADH varies between cells of different origin (Da Veiga Moreira et al., 2016). Hence we evaluated the NADH level in different human cancer cell lines and normal fibroblast cells (WI-38) with the aid of a commercially available NADH quantification kit. Among all, hepatocellular carcinoma cells (HepG2) was chosen for further studies as it maintained the highest levels of NADH (Figs. S6a–d). QAIC was observed to be biocompatible and resistant against photobleaching in cells as well as in the solutions (Figs. S7a–d). Cellular uptake efficiency of QAIC was evaluated by ICPMS analysis which displayed a time and concentration-dependent uptake in HepG2 cells under ambient conditions (Fig. S8a&b).

QAIC exhibited a measurable, time-dependent luminescence turn-ON response towards endogenous NADH. Complementing the luminescence analysis, intense Raman signals were observed at the beginning (within 0–15 min) upon incubation of QAIC, which gradually decreases, and eventually SERS turn OFF occurred at around 1 h (Fig. 2a). The most intense peak around 1042 cm^{-1} , corresponding to the C–H bending mode of QAIC was utilized for Raman mapping (Fig. S9a&b). To further confirm NADH-mediated selective activation of QAIC, cells were treated with different metabolic precursors, that either promote or reduce intracellular NADH levels (Fig. 2b). We noticed a concentration-

dependent increase in the luminescence signals when HepG2 cells were pre-treated with NADH (Fig. 2c, Fig. S10).

Increase in the luminescence intensity from cells pre-incubated with glucose suggested redox reaction between NADH and QAIC. Also, the luminescence was reduced when the cells were treated with pyruvate due to the utilization of intracellular NADH by the enzyme lactate dehydrogenase. This enzyme elevates the NADH levels significantly when exogenous lactate is supplied (Fig. 2d & Fig. S11a). Cells pre-treated with glutathione (GSH) displayed a reduction in the luminescence intensity, while the administration of GSH inhibitor helps to regain the fluorescence. Recently our group reported that paclitaxel caused a reduction in the cellular GSH level (Saranya et al., 2017). An amplified luminescence with the paclitaxel treatment not only confirmed this drug mediated GSH reduction, but also displayed the efficiency of QAIC to precisely monitor NADH kinetics. When cells were treated with a GSH inducer α -Lipoic acid, a noticeable reduction in the luminescence was observed (Fig. S12). An increased luminescence from the cells maintained under hypoxic conditions proved the inflated NADH level in low oxygen conditions. The increased luminescence with low oxygen status is assumed to the interruption of partially preserved mitochondrial respiration that caused an accumulation of intracellular NADH. An electron transport chain blocking agent rotenone was employed to validate this hypothesis, which will elevate NADH concentration (Kim et al., 2013). Under normoxia, rotenone enhanced the luminescence of QAIC whereas in hypoxia, no notable changes were observed. Treatment of cells with resveratrol, a potent antioxidant enhanced the fluorescence in hypoxia whereas, no changes can be observed in normoxia (Fig. 2e, Figs. S13a–d). Further, intracellular NADH level upon treatment of QAIC was monitored using NADH quantification kit (Fig. 2f). Besides NADH sensing, QAIC played the role of NADH scavenger that ultimately enforced the redox imbalance with an energy shutting process via NADH depletion (Purohit et al., 2019).

3.4. Evaluation of photo-oxidation of NADH by QAIC

Upon treatment with QAIC, there was a decline in the absorption and emission band of NADH with an increasing time of laser irradiation, irrespective of temperature change. In this context, we envisage that in the presence of light where NADH activated QAIC (N-QAIC) is capable of generating NAD radicals. To confirm the radicals, semi-quantitative analysis was performed using 2,7-dichlorofluorescein diacetate (DCF-DA). A sharp increase in the emission intensity for DCF was monitored at 545 nm upon laser irradiation, which indicated the production of NAD radicals as it converts the DCFH to DCF. (Figs. S14a–b). Therefore, it is worth mentioning that the NAD radical generation occurs in the presence of excess NADH even after hydride transfer reaction in QAIC.

3.5. Photo-reduction of cytochrome c by QAIC and NADH

The NAD radicals play a critical role in the Fe^{3+} -cytochrome c reduction in the intracellular milieu (H. T. Huang et al., 2019). In the absence of oxygen, the Fe^{3+} -cyt c act as the terminal electron acceptor in the mitochondrial electron transport chain and can be converted to Fe^{2+} -cyt c with the help of single electron donors like NAD radicals. The UV-absorption band of cyt c showed an enhancement of β (520 nm) and α (550 nm) bands corresponding to the Fe^{2+} -cyt c, upon treatment with QAIC and NADH in argon purged solutions by laser irradiation. A liner enhancement of these bands with a R^2 value of 0.9939 confirmed the Fe^{3+} -cyt c reduction (Fig. 2g, Figs. S14c–e). We have further evaluated the Raman bands for oxidized and reduced forms of cyt c. An intense Raman peak at 750 cm^{-1} corresponding to the pyrrole breathing vibrations of the reduced form i.e., Fe^{2+} -cyt c was explicitly marked upon treatment of QAIC in the presence of NADH and laser irradiation. Similarly, time dependent SERS titration of oxidized Fe^{3+} -cyt c treated with QAIC and NADH under laser spark displayed fingerprint Raman peak at 750 cm^{-1} associated with the reduced cyt c with increasing order

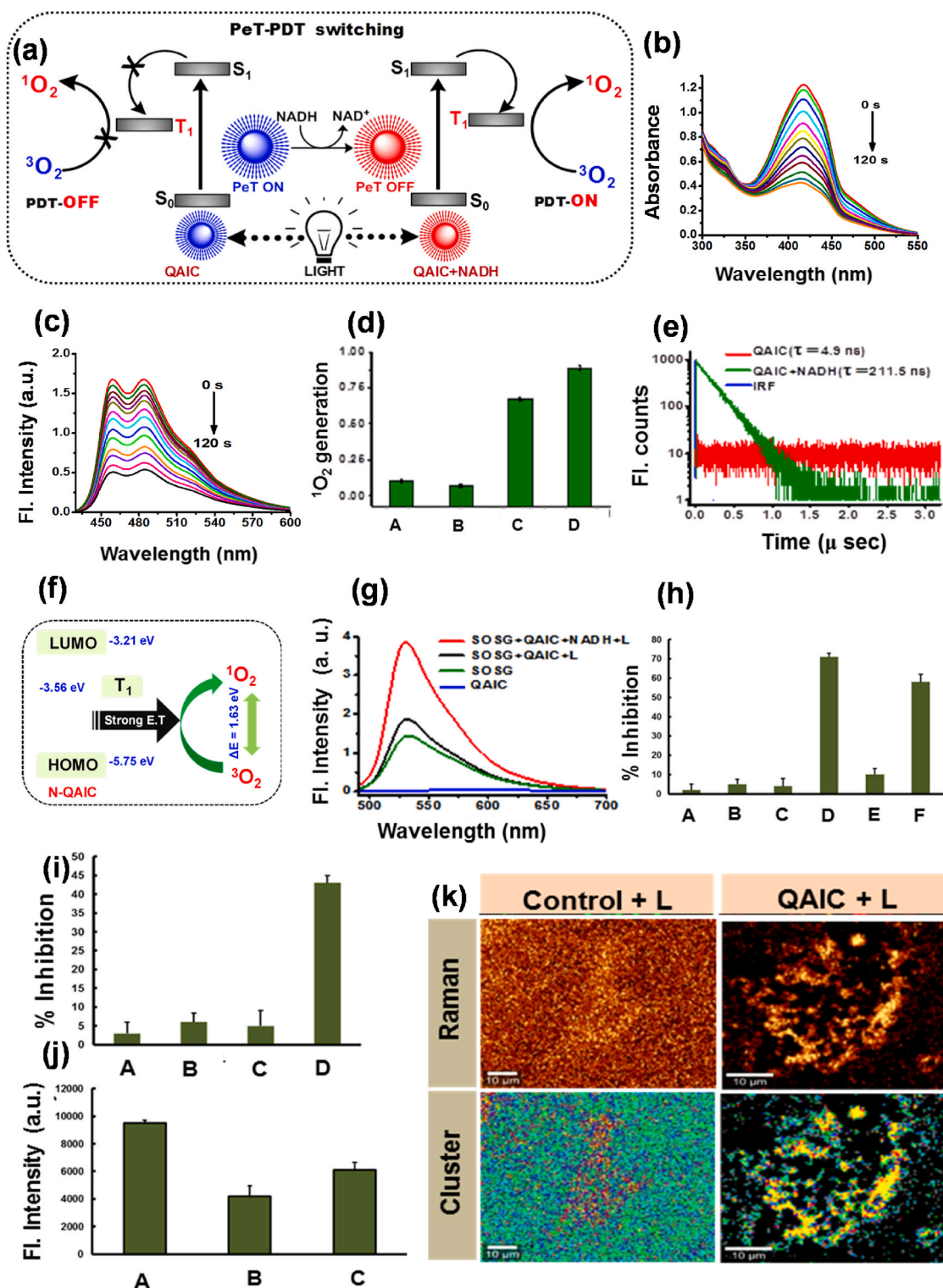
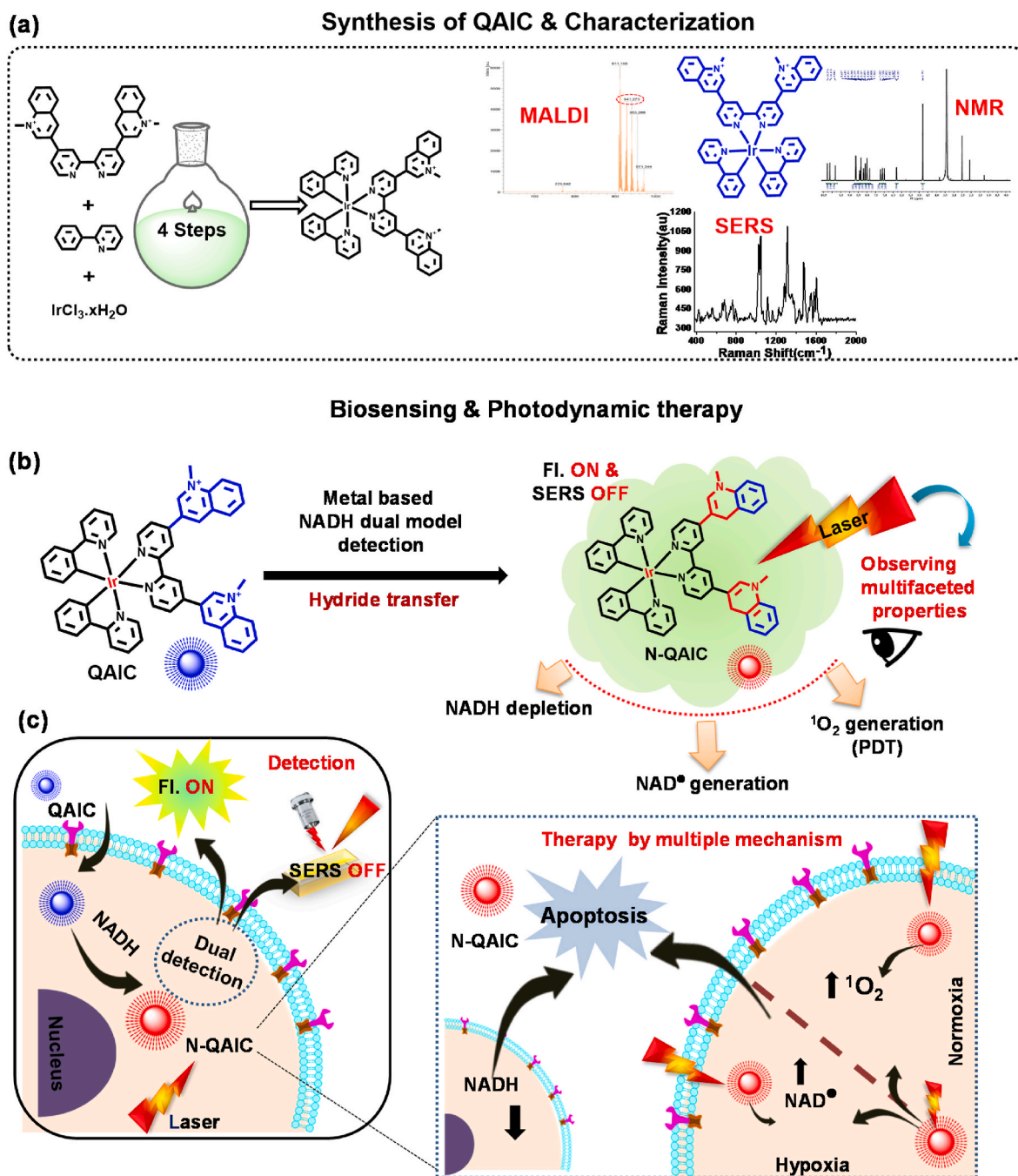


Fig. 3. (a) Schematic illustration of PeT-PDT switching process of QAIC. (b) Singlet oxygen generation capability of QAIC via NADH mediated PeT switching using the absorbance change of DPBF from 0 to 120 s with 10 s intervals and the (c) corresponding emission spectra. (d) Relative singlet oxygen generation capacity of the molecules under investigation (A-QAIC, B-NADH, C-(Ru(bpy)₃)Cl₂, D-N-QAIC). (e) Calculation of phosphorescent lifetime of QAIC and N-QAIC using TCSPC analysis without O₂. (f) HOMO-LUMO and triplet energy state diagram showing the conversion efficiency of ³O₂ to ¹O₂ via energy transfer calculated using Cyclic voltammetry analysis of N-QAIC using ferrocene as standard. (g) Confirmation of singlet oxygen generation using SO SG. Phototoxicity of the activated QAIC with and without laser in (h) normoxic (A-Control, B- Control + L, C-QAIC, D-QAIC + L, E-QAIC + NaN₃, F-QAIC + NaN₃ + L) and (i) hypoxic (A-Control, B- Control + L, C-QAIC, D-QAIC + L) conditions. (j) Evaluation of mitochondrial membrane potential associated with PDT in normoxic (A-Control + L, B-QAIC + L, C- QAIC + NaN₃+L) situations. (k) Evaluation of apoptotic inductions through PDT by the complex QAIC in HepG2 cells through SERS imaging with cluster mapping (using 1042 cm⁻¹ band of QAIC) under normoxic condition.



Scheme 1. (a) Schematic workflow of synthesis and characterization procedures of the biosensor. (b) The mechanism of NADH detection with QAIC. (c) Additional events monitored after the sensing process and laser triggered therapeutic mechanism of N-QAIC in normoxia and hypoxia.

of peak intensity but neither Fe^{3+} -cyt *c* alone or other combinations imparted this effect (Figs. S14f–h). Later, the cyt *c* dynamics in the cells were investigated based on SERS spectral assessment to track other metabolites (Joseph et al., 2018). The appearance of unique Raman peak at 750 cm^{-1} was traceable selectively in the treated cells. Intense Raman signal from the cells confirmed the QAIC mediated generation of NAD radicals followed by cyt *c* reduction (Fig. 2h–j).

3.6. Switching-OFF PeT to PDT during NADH sensing by QAIC

In the current scenario, NADH mediated reduction transforms the QAIC emissive and subsequently PeT off state modulate the production of singlet oxygen ($^1\text{O}_2$) in presence of laser irradiation (Yogo et al.,

2008). Therefore, PeT can be used as a switching mechanism to impart controllable PDT (Fig. 3a) caused by $^1\text{O}_2$. The $^1\text{O}_2$ generation capability of N-QAIC was tested by employing $[\text{Ru}(\text{bpy})_3]\text{Cl}_2$ as a standard reference material wherein a singlet oxygen quantum yield (Φ) of 0.86 was documented (Fig. 3b & c, Fig. S15) (Wu et al., 2013). Further, the relative $^1\text{O}_2$ generation of N-QAIC was also assessed in comparison with QAIC and other combinations (Fig. 3d & Fig. S16a). An amplified excited state lifetime of N-QAIC (211 ns) upon comparison with bare QAIC (4.9 ns) via Time-correlated single-photon counting (TCSPC) indicated a highly populated triplet state of the activated molecule, confirming the NADH mediated PeT-PDT switching mechanism (Fig. 3e, Fig. S16b). Cyclic voltammetry experiment was performed to evaluate the oxidation and reduction potential of N-QAIC by employing ferrocene as a standard.

The HOMO and LUMO calculations indicated the proximity between the energy levels of triplet state and with the molecular oxygen. This will promote the efficient transfer of energy from triplet state of N-QAIC to triplet of molecular oxygen to generate singlet oxygen (Fig. 3f, Figs. S16c–d). Finally, the singlet oxygen generation capacity was verified with help of singlet oxygen sensor green (SOSG). The emission profile of SOSG treated with QAIC followed by 475 nm laser irradiation didn't impart any characteristic change, while N-QAIC treatment instantly showed an enhanced emission maximum at 540 nm within 60 s of laser irradiation (Fig. 3g).

3.7. PDT evaluation by the activated N-QAIC in cellular milieu

Further, we investigated the *in vitro* phototherapeutic potential of QAIC in cellular milieu. Initially, the phototoxicity of N-QAIC was evaluated where eight-fold enhanced cytotoxicity was recorded in normoxia upon laser trigger wherein the presence of a singlet oxygen scavenger caused a reduction in the laser-assisted cytotoxicity (Fig. 3h). This observation confirmed that the cytotoxicity imparted by NAD radicals alone without the aid of $^1\text{O}_2$. In the presence of excess NADH, QAIC generates toxic NAD radicals that acted as apoptotic initiator (Fig. 3i). The laser-triggered production of ROS by N-QAIC promotes mitochondria-mediated cell death (Fig. 3j, Fig. S17a&b). In order to confirm the cell death mechanism, various apoptosis assays were carried out in both normoxic and hypoxic conditions (Arya et al., 2019; Liu et al., 2015). The extent of phototoxicity caused by activated QAIC in presence of 532 nm laser spark was evident with multiple studies confirming programmed execution of cell death (Fig. S17c–e&g). Additionally, SERS spectra corresponding to protein degradation and nuclear damage authenticated the orchestration of apoptosis (Joseph et al., 2020). More fingerprint changes were observed during normoxia due to the active involvement of singlet oxygen and NAD radicals in the process of PDT (Fig. 3k, Fig. S17f). Synergistically, QAIC recognize the dynamic fluctuations of NADH and impart NADH depletion assisted enhanced phototherapeutic effect in both in hypoxic and normoxic conditions (Scheme 1).

4. Conclusions

In summary, a newly designed cyclometalated iridium complex $[(\text{ppy})_2(\text{Nq}^+\text{Nq}^+)]^+$, QAIC was evaluated as an endogenous NADH sensing bimodal molecular probe which imparted multiphase PDT. The QAIC not only senses the dynamics associated with intracellular NADH via PeT switching process but also simultaneously transformed into a photoactivatable motif N-QAIC. The depletion of cellular NADH by QAIC exerted a redox imbalance and also triggers PDT in the cellular milieu. The QAIC generated NAD radical upon laser trigger endowed oxygen independent photodynamic effect in hepatocellular carcinoma cells. Considering the fact that oxygen deficiency and antioxidants are the major impediments of hypoxic PDT, our design strategy may produce a paradigm change in the management of hypoxic cancer.

CRediT authorship contribution statement

Shanmughan Shamjith: Conceptualization, Methodology, Validation, Formal analysis, Writing – original draft, Writing – review & editing. **Manu M. Joseph:** Validation, Formal analysis, Writing – review & editing. **Vishnu Priya Murali:** Validation, Formal analysis. **Geetha S. Remya:** Software, Formal analysis. **Jyothi B. Nair:** Methodology,

Validation, Formal analysis, Writing – review & editing. **Cherumuttathu H. Suresh:** Software, Formal analysis, Writing – review & editing. **Kaustabh Kumar Maiti:** Writing – review & editing, Project administration, Funding acquisition.

Declaration of competing interest

The authors declare that they have no known competing financial interests or personal relationships that could have appeared to influence the work reported in this paper.

Acknowledgments

K.K.M. thanks, CSIR and DBT (BT/PR26670/NNT/28/1367/2017), Government of India for funding. M.M.J. thanks CSIR, Government of India for the Senior Research Associate (SRA) fellowship [13(9128-A) 2020-Pool]. AcSIR Ph.D. student SJS thank UGC for the research fellowship and CHS acknowledges SERB(GAP160439). Thanks to all K. K. M. group members for their support.

Appendix A. Supplementary data

Supplementary data to this article can be found online at <https://doi.org/10.1016/j.bios.2022.114087>.

References

- Arya, J.S., Joseph, M.M., Sherin, D.R., Nair, J.B., Manojkumar, T.K., Maiti, K.K., 2019. *J. Med. Chem.* 62, 8311–8329.
- Brown, S.B., Brown, E.A., Walker, I., 2004. *Lancet Oncol.* 5, 497–508.
- Chiarugi, A., Dölle, C., Felici, R., Ziegler, M., 2012. *Nat. Rev. Cancer* 12, 741–752.
- Da Veiga Moreira, J., Hamraz, M., Abolhassani, M., Bigan, E., Pérès, S., Paulevé, L., Nogueira, M.L., Steyaert, J.M., Schwartz, L., 2016. *Metabolites* 6, 1–12.
- Dolmans, D.E.J.G.J., Fukumura, D., Jain, R.K., 2003. *Nat. Rev. Cancer* 3, 380–387.
- Hanahan, D., Weinberg, R.A., 2011. *Cell* 144, 646–674.
- He, L., Li, Y., Tan, C.P., Ye, R.R., Chen, M.H., Cao, J.J., Ji, L.N., Mao, Z.W., 2015. *Chem. Sci.* 6, 5409–5418.
- Huang, H., Banerjee, S., Qiu, K., Zhang, P., Blacque, O., Malcomson, T., Paterson, M.J., Clarkson, G.J., Staniforth, M., Stavros, V.G., Gasser, G., Chao, H., Sadler, P.J., 2019. *Nat. Chem.* 11, 1041–1048.
- Huang, T., Yu, Q., Liu, S., Zhang, K.Y., Huang, W., Zhao, Q., 2019. *ChemBiochem* 20, 576–586.
- Joseph, M.M., Narayanan, N., Nair, J.B., Karunakaran, V., Ramya, A.N., Sujai, P.T., Saranya, G., Arya, J.S., Vijayan, V.M., Maiti, K.K., 2018. *Biomaterials* 181, 140–181.
- Joseph, M.M., Ramya, A.N., Vijayan, V.M., Nair, J.B., Bastian, B.T., Pillai, R.K., Therakathinal, S.T., Maiti, K.K., 2020. *Small* 16, 2003309.
- Kim, S., Fujitsuka, M., Majima, T., 2013. *J. Phys. Chem. B* 117, 13985–13992.
- Kim, S.Y., 2018. *Biomol. Therapeutics* 26, 39–44.
- Li, X., Kwon, N., Guo, T., Liu, Z., Yoon, J., 2018. *Angew. Chem. Int. Ed.* 57, 11522–11531.
- Liu, K., Liu, P., Cheng, Liu, R., Wu, X., 2015. *Med. Sci. Monitor Basic Res.* 21, 15–20.
- Nam, J.S., Kang, M.G., Kang, J., Park, S.Y., Lee, S.J.C., Kim, H.T., Seo, J.K., Kwon, O.H., Lim, M.H., Rhee, H.W., Kwon, T.H., 2016. *J. Am. Chem. Soc.* 138, 10968–10977.
- Narayanan, N., Karunakaran, V., Paul, W., Venugopal, K., Sujathan, K., Kumar Maiti, K., 2015. *Biosens. Bioelectron.* 70, 145–152.
- Purohit, V., Simeone, D.M., Lyssiotis, C.A., 2019. *Cancers* 11, 955.
- Saranya, G., Anees, P., Joseph, M.M., Maiti, K.K., Ajayaghosh, A., 2017. *Chem. Eur J.* 23, 7191–7195.
- Sudheesh, K.V., Jayaram, P.S., Samanta, A., Bejoymohandas, K.S., Jayasree, R.S., Ajayaghosh, A., 2018. *Chem. Eur J.* 24, 10999–11007.
- Wang, L., Zhang, J., Kim, B., Peng, J., Berry, S.N., Ni, Y., Su, D., Lee, J., Yuan, L., Chang, Y.T., 2016. *J. Am. Chem. Soc.* 138, 10394–10397.
- Wu, W., Yang, P., Ma, L., Lalevé, J., Zhao, J., 2013. *Eur. J. Inorg. Chem.* 228–231, 2013.
- Xiao, W., Wang, R.S., Handy, D.E., Loscalzo, J., 2018. *Antioxidants Redox Signal.* 28, 251–272.
- Yaku, K., Okabe, K., Hikosaka, K., Nakagawa, T., 2018. *Front. Oncol.* 8, 1–9.
- Yogo, T., Urano, Y., Mizushima, A., Sunahara, H., Inoue, T., Hirose, K., Iino, M., Kikuchi, K., Nagano, T., 2008. *Proc. Natl. Acad. Sci. U.S.A.* 105, 28–32.
- You, Y., Cho, S., Nam, W., 2014. *Inorg. Chem.* 53, 1804–1815.